NANO-SCALE MECHANICAL AND TRIBOLOGICAL PROPERTIES OF MINERALIZED TISSUES

by

Griselda María Guidoni

A thesis submitted in fulfillment of the
requirements for the degree of
Doktor der montanistischen Wissenschaften
an der Montanuniversität Leoben (PhD)

Materialphysik Department, Montanuniversität Leoben

Financed by a Marie Curie Early Stage Training Netwok (ESTN) on Biomimetic Systems

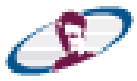

and
Erich Schmid Institut für Material Wissenschaften der Österreichische Akademie der Wissenschaften

February 2008

DECLARATION

Candidate's Certificate

This is to certify that due acknowledgement has been made in the text to all other material used. This thesis contains no material that has been submitted previously, in whole or in part, for the award of any other academic degree or diploma. Except where otherwise indicated, this thesis is my own work.

_____

Griselda María Guidoni, February 2008

Ithaca

When you set out on your journey to Ithaca,
pray that the road is long,
full of adventure, full of knowledge.
The Lestrygonians and the Cyclops,
the angry Poseidon -- do not fear them:
You will never find such as these on your path,
if your thoughts remain lofty, if a fine
emotion touches your spirit and your body.
The Lestrygonians and the Cyclops,
the fierce Poseidon you will never encounter,
if you do not carry them within your soul,
if your soul does not set them up before you.

Pray that the road is long.
That the summer mornings are many, when,
with such pleasure, with such joy
you will enter ports seen for the first time;
stop at Phoenician markets,
and purchase fine merchandise,
mother-of-pearl and coral, amber, and ebony,
and sensual perfumes of all kinds,
as many sensual perfumes as you can;
visit many Egyptian cities,
to learn and learn from scholars.

Always keep Ithaca on your mind.
To arrive there is your ultimate goal.
But do not hurry the voyage at all.
It is better to let it last for many years;
and to anchor at the island when you are old,
rich with all you have gained on the way,
not expecting that Ithaca will offer you riches.

Ithaca has given you the beautiful voyage.
Without her you would have never set out on the road.
She has nothing more to give you.

And if you find her poor, Ithaca has not deceived you.
Wise as you have become, with so much experience,
you must already have understood what these Ithacas mean.

Constantine Cavafy (1863-1933)

ACKNOWLEDGMENTS

My last, but not the least, remaining task is to acknowledge all those people who have contributed to the work described in this thesis. This thesis is the result of 40 months of work whereby I have been accompanied and supported by many people. This is my opportunity to express gratitude to all of them.

First of all, I would like to thank my supervisor, Professor Ingomar Jäger from Department of Materials Physics, Montanuniversity Leoben, Leoben, Austria. Ingomar accepted me as his PhD student, and offered me the opportunity to do a PhD in a subject I was always interested in: biomaterials. We had productive discussions -not only related to science but also about a wide range of subjects- which contributed to my education not only as a researcher but also as a person. Ingomar managed to tolerate my disorganization, impulsivity and constant questioning, and I kindly appreciate it. In addition, Ingomar has tremendous skills to model systems, to think abstractly and an insatiable curiosity on Biomaterials topics that contributed positively to my learning.

Dr. Thomas Schöberl from Department of Materials Physics, Montanuniversity Leoben, Leoben, Austria, collaborated to my introduction to the fascinating field of nanoindentation technique, showing me the experimental basis and participating in fruitful discussions.

I am also grateful to Professor Gerhard Dehm, Head of the Department of Materials Physics, Montanuniversity Leoben, and Erich Schmid Institute, from the Austrian Academy of Science, Leoben, Austria. His interest in my thesis, encouragement, trust, discussions and financial help - through the Austrian Academy of Science - were very valuable on the realization of my thesis.

I wish to express my warm and sincere thanks to Professor Michael Swain from Biomaterials Science Research Unit, Faculty of Dentistry, University of Sydney, United Dental Hospital, Sydney, Australia. I visited Michael in Australia for two months in 2007, and since then, we intensively worked on the organization and understanding of my experimental results. His enthusiasm and interest on Science are endless. Michael contributed also financially to the realization of my thesis through an ARC grant and Australian Dental Research foundation grant, paying my flight tickets to and from Australia, and allowing me to use their equipment. We have had tremendously interesting and enriching scientific discussions, which motivated me, and challenged me in this wonderful field of doing research. His predisposition and collaboration have gone far beyond the commitment of an external Professor. I am deeply grateful for his personal and scientific support.

My acknowledgements are extended to Prof. Christian Teichert from Department of Physics, Montauniversity Leoben, Leoben, Austria, for accepting being part of my PhD committee, but particularly for taking the effort of reading and providing me with valuable comments on a preliminary version of this thesis.

Prof. Peter Fratzl, Dr. Oskar Paris and Dr. Himadri Gupta from Department of Biomaterials, Max Planck Institute, Golm, Germany, are gratefully acknowledged for allowing me to spend 3 months with them. I had interesting scientific discussions with all of them which contributed to the development of my PhD.

I would like to thank all the people I met during my work at Erich Schmid Institute of Materials Science, Austrian Academy of Sciences/Department Materials Physics, University of Leoben, Leoben, Austria, for a nice working atmosphere and help. People from Biomaterials Science Research Unit, Faculty of Dentistry, University of Sydney, United Dental Hospital, Sydney, Australia are also included in my acknowledgement list, it was a joy to work with them. I wish to extend my thanks to all those who have helped me with my work in Department of Biomaterials, Max Planck Institute, Golm, Germany and Institute for Mechanics of Materials and Structures from Vienna University of Technology, Vienna, Austria.

People from the Marie Curie Early Stage Training Network on Biomimetics Systems are also acknowledged for the training and given scientific feedback. Having the possibility to meet other PhD students from Europe and other places, to travel and to establish collaborations was an invaluable chance during these years. In addition, more than 90% of this thesis was financed by this project through EC Contract No MEST-CT-2004-504465 and it is gratefully acknowledged.

I want to thank also my family and my close friends, who kept always faith in me, in spite of my crazy ideas and my particular way of taking and living my life. They encouraged and motivated me in different ways. I could not have gone through this process if they would not have given me their support.

TABLE OF CONTENTS

DECLARATION ..... **II**

Candidate's Certificate ..... *ii*

ACKNOWLEDGMENTS ..... **V**

TABLE OF CONTENTS ..... **VII**

SPECIFIC BIOLOGICAL DICTIONARY ..... **XIII**

BRIEF OVERVIEW ..... **XVI**

OBJECTIVES XVI

MATERIALS AND METHODS XVII

Teeth ..... *xvii*

Enamel xvii

Dentine xviii

Bone ..... *xix*

Nanoindentation ..... *xx*

Nanoscratching ..... *xxi*

FIGURES ..... **XXII**

1. LITERATURE REVIEW: MATERIALS **1**

ENAMEL, DENTINE AND COMPACT BONE: MICROSTRUCTURE AND MECHANICAL PROPERTIES . 2

1.1. ENAMEL 2

1.1.1. Microstructure *2*

1.1.1.1. Nanometer level 2

1.1.1.2. Micrometer level 2

1.1.2. Mechanical properties *3*

1.1.2.1. Indentation modulus and hardness 3

1.1.2.1.1. Orientation effects 3

1.1.2.1.2. Environment effects 4

1.1.2.1.3. Mineral content effects 5

1.1.2.1.4. Positional variations 6

1.1.2.1.5. Time dependent properties 6

1.1.2.2. Tribological properties 7

1.2. DENTINE 9

1.2.1. Microstructure *9*

1.2.2. Mechanical properties: indentation modulus and hardness *13*

1.2.2.1. Mineral content 13

1.2.2.2. Positional variations 13

1.2.2.3. Environmental effects 14

1.3. BONE 14
1.3.1. Microstructure *15*
1.3.2. Mechanical properties: indentation modulus and hardness *16*
1.3.2.1. Time dependent properties 16
1.3.2.2. Anisotropy effects (within different planes) 16
1.3.2.3. Positional effects (within the same plane) 16
1.3.2.4. Environmental effects 17
1.3.2.5. Mineral content 17

FIGURES OF CHAPTER 1 18

2. THEORETICAL BASIS 25

2.1. MINERALIZED TISSUE FROM A MATERIALS SCIENCE ENGINEERING PERSPECTIVE. 26
2.1.1. Simple composite mechanics *26*
2.1.2. Staggered arrangement of organic and inorganic components. Mechanical implications. *26*
2.1.3. Spears' model *27*
2.1.4. Contact induced deformation in enamel *27*
2.1.5. A model for the toughness of enamel *28*
2.1.6. Realignment of the mineral single crystals induced by the indenter. *28*
2.2. CONTACT MECHANICS 28
2.2.1. Different expected mechanical responses depending on the indenter tip geometry *28*
2.2.2. A special case: Hertz contact *29*
2.2.3. Oliver and Pharr approach *30*
2.2.4. Area function calibration *32*

FIGURES OF CHAPTER 2 33

SCOPE OF THIS WORK 43

MOTIVATION 44
AIMS OF THE STUDY 44
RESULTS AND SIGNIFICANCE 45
PUBLICATIONS AND SCIENTIFIC MEETING PRESENTATIONS ARISING FROM THIS RESEARCH. 47
Journal publications *47*
Scientific meetings *47*
Project meetings *48*
Abroad Collaborations *48*

3. INFLUENCE OF THE INDENTER TIP GEOMETRY AND ENVIRONMENT ON THE INDENTATION MODULUS OF ENAMEL 49

3.1. ABSTRACT 50
3.2. INTRODUCTION 50

3.3. MATERIALS 52
3.4. NANOINDENTATION TESTS 53
3.4.1. Sharp cube corner tip 53
3.4.2. Berkovich and 45° pyramidal indenter tips 53
3.4.3. Further details 54
3.5. SEM OBSERVATIONS 54
3.6. RESULTS 54
3.6.1. Sharp cube corner tip 54
3.6.2. 45° Pyramidal indenter tip 55
3.6.3. Berkovich indenter 55
3.7. DISCUSSION 56
3.7.1. Corrections 56
3.7.1.1. Creep 56
3.7.1.2. Recovery 57
3.7.1.3. Viscoelastic creep and recovery 58
3.7.1.4. Pile up 58
3.7.2. The sharp cube corner indenter: Cracking and micro-damage 61
3.8. CONCLUSIONS 62
3.9. ACKNOWLEDGEMENTS 62

FIGURES OF CHAPTER 3 64

TABLES OF CHAPTER 3 72

4. WEAR BEHAVIOUR OF ENAMEL AT THE NANO SCALE WITH A SHARP AND BLUNT INDENTER TIP 73

4.1. ABSTRACT 74
4.2. INTRODUCTION 74
4.3. MATERIAL 76
4.4. TRIBOLOGICAL TESTS 76
4.5. RESULTS 77
4.5.1. Conical indenter tip 77
4.5.2. Sharp cube corner indenter tip 79
4.6. DISCUSSION 80
4.6.1. Conical rounded indenter tip. 80
4.6.2. Sharp cube corner indenter tip 82
4.6.3. Damage mechanisms: Rounded conical versus Sharp cube corner indenter tips 83
4.7. CONCLUSIONS 85
4.8. ACKNOWLEDGEMENTS 86

FIGURES OF CHAPTER 4 87

TABLES OF CHAPTER 4 99

5. NANO-SCALE SLIDING CONTACT DEFORMATION BEHAVIOUR OF ENAMEL UNDER WET AND DRY CONDITIONS 101

5.1. ABSTRACT 102
5.2. INTRODUCTION 102
5.3. MATERIAL AND METHODS 103
5.3.1. Single scratches 103
5.3.2. Wear tests 104
5.4. RESULTS 104
5.4.1. Single scratches 104
5.4.2. Area scans 105
5.5. DISCUSSION 106
5.6. CONCLUSIONS 108
5.7. ACKNOWLEDGEMENTS 108

FIGURES OF CHAPTER 5 109

TABLES OF CHAPTER 5 118

6. ENAMEL: BRITTLE TO DUCTILE LIKE TRIBOLOGICAL RESPONSE 119

6.1. ABSTRACT 120
6.2. INTRODUCTION 120
6.3. MATERIALS 121
6.4. TRIBOLOGICAL TESTS 122
6.5. RESULTS 122
6.5.1. Glass sample 123
6.5.2. Enamel sample 123
6.5.3. Copper and Silver single-crystals 124
6.6. DISCUSSION 125
6.6.1. Glass like behaviour of enamel (low loads) 125
6.6.2. Metal like behaviour of enamel (high loads) 126
6.7. CONCLUSIONS 126
6.8. ACKNOWLEDGEMENTS 127

FIGURES OF CHAPTER 6 128

TABLES OF CHAPTER 6 135

7. NANOINDENTATION IN TEETH: THE INFLUENCE OF EXPERIMENTAL CONDITIONS ON LOCAL MECHANICAL PROPERTIES 136

7.1. ABSTRACT 137
7.2. INTRODUCTION 137
7.3. SAMPLE PREPARATION 138

7.4. NANOINDENTATION TESTS 139
7.5. RESULTS 140
7.6. DISCUSSION 141
7.7. CONCLUSIONS 142
7.8. ACKNOWLEDGEMENTS 143

FIGURES OF CHAPTER 7 144

TABLES OF CHAPTER 7 147

8. NANOINDENTATION OF WET AND DRY COMPACT BONE: INFLUENCE OF ENVIRONMENT AND INDENTER TIP GEOMETRY ON THE ELASTIC MODULUS 149

8.1. ABSTRACT 150
8.2. INTRODUCTION 150
8.3. SAMPLE PREPARATION 151
8.4. NANOINDENTATION TESTS 152
8.5. RESULTS 153
8.6. DISCUSSION 154
8.6.1. The influence of storage temperature on mechanical properties: lamellar level. 154
8.6.2. Anisotropy of the same type of compact bone: fibre level. 155
8.6.3. The influence of the hydration state on mechanical properties: constituents' level. 155
8.7. CONCLUSIONS 157
8.8. ACKNOWLEDGEMENT 158

FIGURES OF CHAPTER 8 159

TABLE OF CHAPTER 8 162

A. NANOINDENTATION IN TEETH: THE INFLUENCE OF EXPERIMENTAL CONDITIONS ON LOCAL MECHANICAL PROPERTIES. VERIFICATION ..... A

ABSTRACT ..... B
SAMPLE PREPARATION ..... B
NANOINDENTATION TESTS ..... B
RESULTS C
DISCUSSION C
CONCLUSIONS ..... F

FIGURES OF APPENDIX A ..... H

B. ABRASION TESTS ON HUMAN ENAMEL UNDER WET AND DRY CONDITIONS. ..... A

ABSTRACT ..... B

INTRODUCTION ..... B
MATERIAL C
NANOINDENTATION AND TRIBOLOGICAL TESTS ..... D
RESULTS ..... E
DISCUSSION ..... F
CONCLUSIONS I
ACKNOWLEDGEMENTS I

FIGURES OF APPENDIX B ..... J

TABLES OF APPENDIX B L

REFERENCES ..... O

SPECIFIC BIOLOGICAL DICTIONARY

Abrasion	*n,* superficial injury to skin or mucous membrane from scraping or rubbing.
Amalgam	The most common filling material used for fillings, also referred to as mercury or silver, which are often contained in the mixture. Alternatives are composite resins, and gold or porcelain inlays.
Apatite	Calcium phosphate, an insoluble mineral that confers hardness and rigidity to bone tissues.
Attrition	*n,* wear of the occlusal surfaces of the teeth by use.
Bruxism	Involuntary, "nervous" grinding of the teeth while the patient is asleep. Can eventually cause headaches, loss of tooth surface and cracking. Treatment includes a nightguard custom-made by a dentist from impressions made of the patient's teeth.
Buccal	*adj.* Pertaining to the cheek or mouth.
Canaliculi	Fine channels through bone that form an anastomising network between the osteocyte lacunae. In living bone the canaliculi are occupied by the cytoplasmic processes of the osteocytes.
Caries	The medical term for dental cavities.
Cavity	A decay lesion or hole in a tooth, usually caused by a diet which includes sugar, which allows bacteria to grow and secrete acid onto the enamel of the tooth.
Cervical	*adj.* Pertaining to the neck of an organ.
Collagen	A fibrous protein that constitutes the principal organic fraction of bone.
Cusp	*n* a projecting point, such as the edge of a tooth **-cuspal** *adj.*
Decussation	*n,* intersection, crossing of nerves fibres at a point beyond their origin.
Deciduous Teeth	A child's first set of twenty teeth that are eventually replaced by permanent teeth. (Also known as primary or baby teeth.)
Diaphysis	*n.* The shaft of a long bone.
Diaphysis, epiphysis, metaphysis	The long bones consist of a central, usually hollow, tubular region, the ***diaphysis*** linked to specialised ends (***epiphysis***) by a junctional region (***metaphysis***).
Epiphysis	*n.* The end of a growing bone.
Erupt, Eruption	When a new tooth comes in, the tooth is said to erupt when the tooth breaks through the surface of the gums, so the tooth is seen in the mouth.
Haversian Canal	Vascular channel at the centre of an osteon.
Haversian System	See osteon.
Incisors	*npl* the teeth first and second from the midline, four in each jaw used for cutting food.
Interstitial Lamellar Bone	Remnants of former osteons and circumferential lamellar bone that is visible in the spaces between more recently developed secondary osteons.
Lamellar Bone	Dense bone with fine collagen fibres organised into sheets of a few microns thickness (lamellae), within which the fibres are parallel in orientation.

Lingua	*n* , the tongue -**lingual** *adj.*
Mastication	*n,* the art of chewing.
Medullary Cavity	Central cavity within a long bone, usually filled with marrow (but air-filled in some bird bones).
Molar teeth	the teeth fourth and fifth in the deciduos dentition and sixth, seventh and eight in the permanent dentition, used for grinding food.
Occlusion	*n,* the closure of an opening, especially of ducts or blood vessels. In dentistry, the fit of the teeth as the two jaws meet -**occlusal** *adj.*
Osteocyte Lacuna	A round, ovoid or lenticular space within which an osteocyte resides in living bone tissue.
Osteon	Haversian system, consisting of a central vascular channel surrounded by concentric cylindrical layers of lamellar bone.
Pre molars	the teeth situated fourth and fifth from the midline of the jaws, used with the molars for gripping and grinding food.
Primary Osteon	Usually a small osteon that is not bounded by a reversal line, but instead is surrounded by conformable layers of interstitial or circumferential lamellar bone.
Reversal Line	Narrow zone of hypermineralisation that demarcates the boundary between the termination point of bone resorption and the initiation point of new bone formation. Sometimes referred to as a cement line.
Sagittal	*adj.* Resembling an arrow. In the anteroposterior plane of the body.
Secondary Osteon	An osteon that has developed in a resorption space within pre-existing bone tissue. Distinguished by its interception of pre-existing lamellae and by its hypermineralised border (reversal line).
Wisdom Teeth	The third set of molars, the last teeth to come in. For many people, wisdom teeth become impacted and must be removed by oral surgery.
Woven Bone	Highly vascularised bone tissue with coarse, undulating, interwoven and randomly orientated collagen fibre bundles and randomly distributed osteocyte lacunae. Found in embryonic and fetal bone, fracture callus, and in the medullary bone of egg-laying bird

If one way be better than another,
that you may be sure is Nature's way.

(Aristotle, fourth century B.C.E)

BRIEF OVERVIEW

Objectives

Nature has little range of substances to build up biological materials. These available materials include relatively weak organic molecules like collagen (proteins, in general) or cellulose and an even more restricted choice of inorganic compounds such as calcium hydroxyapatite found in hard tissue like bone and teeth and calcium carbonate in nacre. None of these materials would have been the obvious choices in man-made structures requiring stiffness and toughness, since metals and/or alloys offer stiff materials with the option of manipulating toughness by limiting the mobility of microscopic defects like dislocations.

However, it seems that nature runs far ahead of our knowledge on Materials Science since as it creates biological materials, with the above mentioned components, with outstanding properties (toughness, stiffness, etc) and at the same time light enough for their applications. How is that achieved?

Natural materials, such as tooth (Fincham et al., 1999, White et al., 2001, Tesch et al., 2001), or bone (Weiner and Wagner, 1998, Wenk and Heidelbach, 1999, Paris et al., 2000, Fratzl and Weinkamer, 2007), exhibit many levels of hierarchical structures from macroscopic to microscopic length scales. Most interesting to observe is that the smallest building blocks in such materials are generally on the nanometer length scale. The coupling between different levels of hierarchical structures to the final resultant mechanical properties is still not well understood issue but it is the clue to elucidate the mechanical success of mineralized tissue, like bone and teeth.

Understanding structure-function relations in these materials is therefore a challenge. We are easily able to measure bulk mechanical properties of some family members and in some special cases obtain information on certain of the intermediate hierarchical levels, but how can these be related to the structures themselves? An in-depth understanding of this subject ideally requires interpreting the bulk mechanical behaviour in terms of the contributions of the sub-structures at each hierarchical level.

Thus, in the present study, the relatively recently developed nano-indentation technique was chosen to characterize the elastic properties (elastic modulus) and plastic properties (hardness) at a nanometre scale of compact bone, dentine (the inner layer of teeth), and enamel (the outer layer of teeth). In addition, using the same instrumentation, nano-scratch and nano-abrasion tests were carried out in enamel to characterize tribologically this system in a nanometre scale.

These studies were complemented with observations using AFM (atomic force microscopy), and SEM (scanning electron microscopy); and to a lesser extent with FIB (focused ion beam) and TEM (transmission electron microscopy) techniques

Materials and methods

Enamel was the most characterized tissue in the present thesis although dentine and compact lamellar bone were also studied. A brief description and scheme of the structures and material systems orienting the study to the features treated in this thesis now follows.

Teeth

In Fig. 1 can be seen a scheme of a tooth. *Enamel* and *dentine* are both layers present in teeth and will be described next.

Enamel

Enamel, the outer cover of the tooth, is composed of about 97 % by weight of mineral, essentially carbonated apatite, 1 % organic material, mostly protein, which is not collagen, and 2 % water (Currey, 2002). Selvig and co-workers (Selvig and Halse, 1972) found that the crystals of rat incisor were as irregular in shape as in human enamel and that they occupied 85 % in volume.

Human enamel rarely undergoes catastrophic mechanical failure despite a lifetime of repeated masticatory, parafunctional, and occasional impact loading. The functional success of enamel is also somewhat surprising, given that it is largely composed of brittle hydroxyapatite (Hap) crystallites.

However nature, using the limited available materials, was wise enough to play with the microstructural arrangement of its components to achive the desired mechanical performance. Selvig and co-workers (Selvig and Halse, 1972) measured by scanning electron microscopy a crystal size of rat enamel incisor of 45 nm width and 25 nm in height. They were very densely packed with an electron lucent space of 1 to 2.5 nm. Gao and co-workers (Gao et al., 2003) recently showed that the nanometer size of the mineral crystals in bio-composites is selected to ensure optimum fracture strength and maximum tolerance of flaws. In addition, White and co-workers (White et al., 2001) found that enamel is 3 times tougher than its major component, crystalline Hap. They attributed this result to the organic component.

Most of the mineral crystals are bound together in bundles called prisms or rods. Each rod is 3-6 μm in diameter (Fig. 2). There is limited protein within the prisms “glueing” the apatite crystallites together, with more protein located at the interprism boundaries (Currey, 2002, White et al., 2001). This region is often called the enamel sheath, and also consists of apatite crystals that are inclined to the axis of the rods. Ge et al. (Ge et al., 2005) used a pyramidal (*Berkovich*) indenter tip to investigate the local mechanical properties variations between prisms and sheaths within an enamel rod. The nanohardness (H) and elastic modulus (E) of the sheaths were about 73.6% and 52.7% lower than those of the prisms, respectively.

Enamel has a truly 3D structure (Macho et al., 2003) starting with a crossed plywood-like form near the interface with dentine (DEJ) (Fig. 3, upper image and Fig. 4) and ending up

with almost parallel alignment of rods near the outer surface (Fig. 3, lower image). Depending on the analyzed section, e.g. occlusal or transversal, the mechanical response is expected to be different. Cuy et al. (Cuy et al., 2002) mapped the cross sectional properties of human enamel using a Berkovich tip. They reported significant differences in hardness and elastic modulus from the DEJ to the outer surface and also depending on the buccal or lingual region tested. In addition, Spears (Spears, 1997) developed a 3D finite element modeling of enamel in which triaxial anisotropy in a ratio of (3:1.5:1) for (Ez:Ey:Ex) could be predicted together with the dependence of the resultant elastic modulus on the mineral content. Xu et al. (Xu et al., 1998) measured also a dependence of tooth orientation in fracture toughness, elastic modulus and hardness by micro-indentations with a Vickers indenter. The maximum values were always obtained on the occlusal section.

In vivo enamel is mainly subjected to a fluidic environment, e.g. saliva. Staines et al. (Staines et al., 1981) used a spherical indenter for testing enamel under wet (immersed in water) and dry conditions. They reported an increase of 15 % in elastic modulus when going from wet to dry conditions and more substantial viscoelastic behaviour under wet than dry conditions, respectively. Habelitz and coworkers (Habelitz et al., 2002) used a cube corner indenter tip to study the influence of storage solutions on the local mechanical properties of enamel. Both water and $CaCl_2$ solution were shown to result in lower E modulus values and it was argued that these conditions lead to demineralisation of the tooth with time. Thus, in order to test enamel under near in vivo conditions, in our experiments the enamel was stored and tested immersed under Hank's balanced salt solution (HBSS), and its behavior compared with the same material in a dry condition.

Regarding tribology, the majority of wear studies in enamel have been made at the micrometer scale (Li and Zhou, 2002) and macroscopic scale (West et al., 1999, DeLong, 2006, Pintado et al., 1997, Sajewicz, 2006, Magne et al., 1999). However, there is some incipient literature on wear on enamel at the nanometre scale (Jandt, 2006, Habelitz et al., 2001b). Jandt et al. (Jandt, 2006) used AFM and nanoindentation to study the influence of erosion on enamel by measuring the change in mechanical properties after immersing enamel under different acidic soft drinks. Habelitz et al. (Habelitz et al., 2001b) studied the width of the dentine-enamel junction (DEJ) by nano-scratching.

Dentine

Dentine is also a mineralized tissue, containing approximately 50 % vol. mineral and 30 % vol. of collagen fibrils with fluid occupying the remaining tubular void space. It is the inner layer beneath enamel (Fig. 1).

Dentine contains many tubules (channels) typically radiating outwards from the root cavity, in which the dentinal fluid is located and the cytoplasmic processes of the cells that have formed the dentine, the odontoblasts, take place. Tubules are surrounded by a thin, hard, highly mineralized shell of peritubular dentine (Weiner et al., 1999), the contribution of which to the

overall mechanical properties of a tooth is not yet quite clear (Kinney et al., 1996, Balooch et al., 1998, Balooch et al., 2004). The tubules are embedded in a softer matrix named intertubular dentine. A SEM micrograph taken from (Weiner et al., 1999) showing all the above mentioned structures is shown in Fig. 5

As for the case of enamel, the mechanical properties of dentine are expected to be moisture content dependent (Angker et al., 2004, Balooch et al., 1998, Kahler et al., 2003, Kishen and Vedantam, 2007, Kitasakoa et al., 2001, Maciel et al., 1996, Nalla et al., 2005, Pashley et al., 2003, Pashley et al., 2001).

Bone

Bones are rigid organs that form part of the endoskeleton of vertebrates. They function to move, support, and protect the various organs of the body, produce red and white blood cells and store minerals. Because bones come in a variety of shapes and have a complex internal and external structure, they are lightweight, yet strong and hard, in addition to fulfilling their many other functions.

At a millimetre level, two types of bone can be distinguished:

- Compact bone: forms the hard outer layer of bones, so-called due to its minimal gaps and spaces. This tissue gives bones their smooth, white, and solid appearance, and accounts for 80% of the total bone mass of an adult skeleton. Compact bone may also be referred to as dense bone or cortical bone.
- Trabecular bone: Filling the interior of the organ is the trabecular bone tissue (an open cell porous network also called cancellous or spongy bone) which is comprised of a network of rod- and plate-like elements that make the overall organ lighter and allowing room for blood vessels and marrow. Trabecular bone accounts for the remaining 20% of total bone mass, but has nearly ten times the surface area of compact bone.

A scheme of bone types can be found in Fig. 6.

Cortical bone is a typically dense structure with porosity in the order of 6%, mainly due to the presence of blood vessels. The role of blood vessels is to supply nutrients and remove toxins and forms the basis of internal remodelling. This latter process involves the excavating of large tunnels by teams of specialized cells called osteoclasts. These tunnels are then refilled by osteoblasts, starting with the deposition of a thin layer of cement on the existing excavated surface, followed by layers of lamellar bone. The process stops when the tunnel is almost completely filled, leaving a narrow channel at the centre that functions as a blood vessel. In fact, other even smaller capillary-like features (canaliculi) are also built into the structure. These canaliculi are numerous and house the cells (osteocytes) that remain within the bone material itself. The canaliculi tend to radiate out from the central blood vessel. An example of an osteocyte lacuna is shown in Fig. 7.

Thus the structure of an osteon is basically onion-like in cross-section with layers of lamellae surrounding a central hole; in longitudinal section they are cylindrical (Weiner and

Wagner, 1998). The osteon also contains many elongated pores. The secondary osteons (to distinguish them from the primary osteons which are deposited before remodelling) are the basic building block of compact bone.

The bone lamellae forming the secondary osteons are around 3-6 μm in width (Currey, 2002). Each lamella consists of a series of fibril layers oriented at different angles to the osteon axis, having a right-handed helicity (Fratzl and Weinkamer, 2007). This particular helicoidal structure imparts the osteons extensibility (and compressibility) like a spring along its long axis. The elastic extensibility is useful in absorbing energy during mechanical loading, and may help in protecting the blood vessels.

The lamellas are organized in alternating thick and thin layers (Fig. 8). Each of the lamellas has different mechanical properties, not merely due to anisotropy (Hengsberger et al., 2002) but also to composition (Gupta et al., 2006b).

As dentine and enamel, bone is mainly composed of an organic (22-25%) and an inorganic phase (70%). The organic phase is mainly Type I collagen (90+%), but there are also non-collagenous proteins (10%) and proteoglycans. The inorganic phase is mainly non-stochiometric hydroxyapatite (95%) and impurities (5%). It also contains water (5-8%). The minerals have plate-like crystal form of ~20-80nm length and 2-5nm thickness.

Nanoindentation

Nanoindentation is a powerful technique that provides a set of tools for investigating the mechanical properties of materials in small dimensions. In such a test, a hard tip, typically a diamond is pressed into the sample with a known load.

Instrumented indentation (nanoindentation) is a widely used technique for studying the mechanical response of biomaterials mainly due to the small amount of material needed and the complexity of preparing samples for conventional mechanical testing (Gupta et al., 2006a, Gupta et al., 2005). Using this method, the load and displacement of the indenter are recorded during the indentation process and such data are analyzed to obtain the contact area and unloading compliance from which the mechanical properties may be derived (Fischer-Cripps, 2005, Fischer-Cripps, 2004).

Many indenter tip geometries and testing conditions may be found in the literature for enamel (Staines et al., 1981, Ge et al., 2005, Xu et al., 1998, Cuy et al., 2002), dentine (Angker et al., 2004, Angker et al., 2005, Balooch et al., 1998, Kinney et al., 1996, Maciel et al., 1996, Moscovich et al., 1999, Poolthong et al., 2001, Xu et al., 1998) and compact bone (Fan et al., 2002, Gupta et al., 2006b, Hengsberger et al., 2002, Hoffler et al., 2000, Mullins et al., 2007, Zysset et al., 1999). The data is commonly analyzed using the Oliver & Pharr method (Oliver and Pharr). Analysing the data by the method given in (Oliver and Pharr, 1992) assumes implicitly the material sinks in and behaves in a elastic-perfectly plastic way.

Nanoscratching

The indenter tip can be scanned across the surface at imaging loads (2-4 μN) to record the topography of the surface before indenting, thanks to the add-on AFM facility housing the nanoindenter transducer. This movement leads to square sized scanned areas.

In this thesis, nanoscratching is referred to the sliding of the indenter tip on the surface of the sample (as described above) but with higher loads than imaging loads. Thus, the surface is either plastically deformed and/or material is removed. In this way the tribological behavior at a nanometer scale of the systems was characterized.

FIGURES

Fig. 1

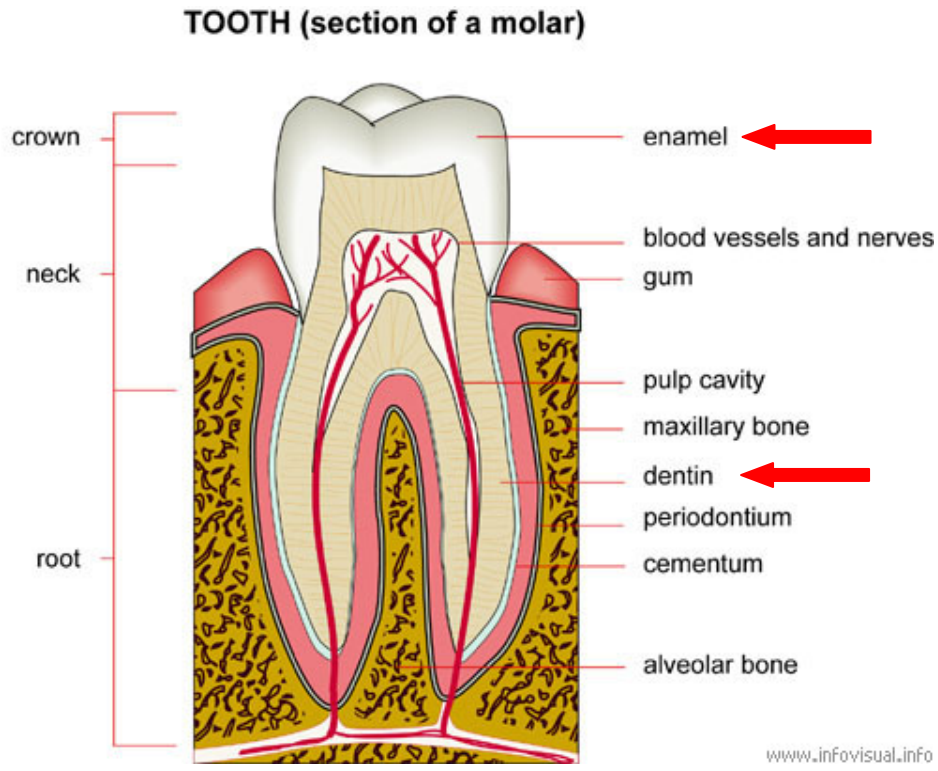

Fig. 1 Scheme of the cross section of a tooth. The two zones of interest are enamel (outer layer in contact with the external environment) and the immediately inner layer: dentine. Both structures are marked with a red arrow on the graph. The scheme also showed the cut section tested in this thesis: parallel to the main axial direction of the tooth.

Fig. 2

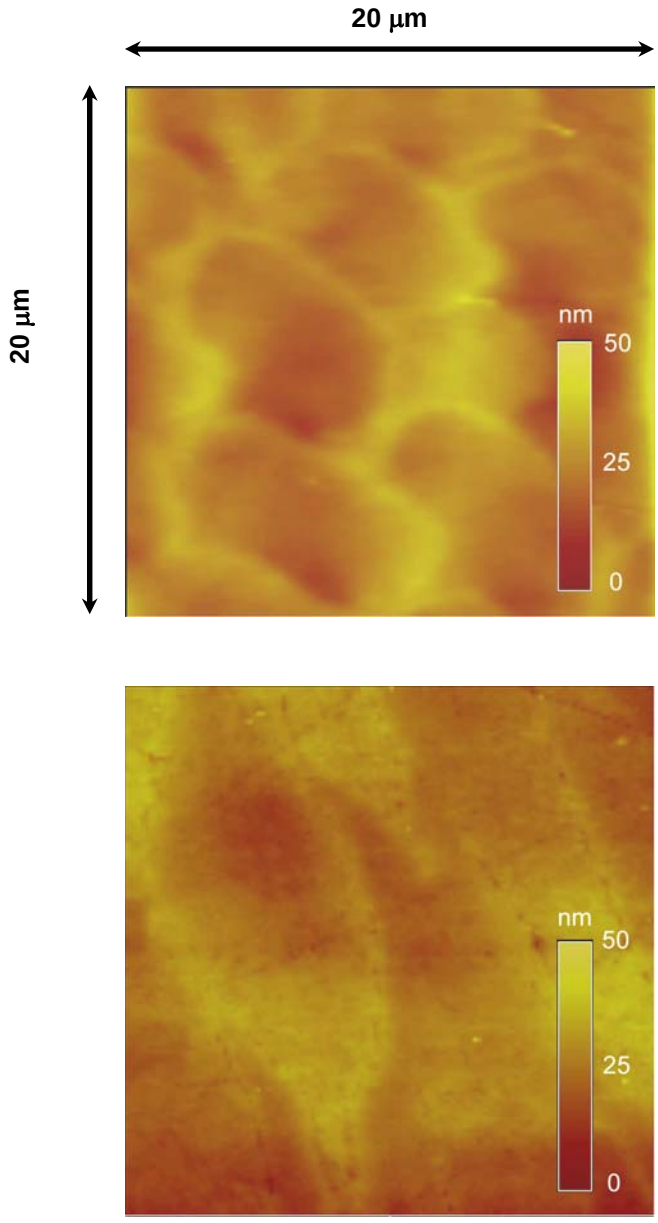

Fig. 2 Upper image: AFM 20 x 20 μm image of a cross sectional sample of human enamel tested under wet conditions. Max Z = 47 nm. Image taken with a rounded conical nanoindenter tip (400 nm nominal radius) in contact mode. Lower image: AFM 20 x 20 μm image of a cross sectional sample of human enamel tested under dried conditions. Max Z = 37 nm. Image taken in tapping mode with the AFM cantilever tip.

Fig. 3

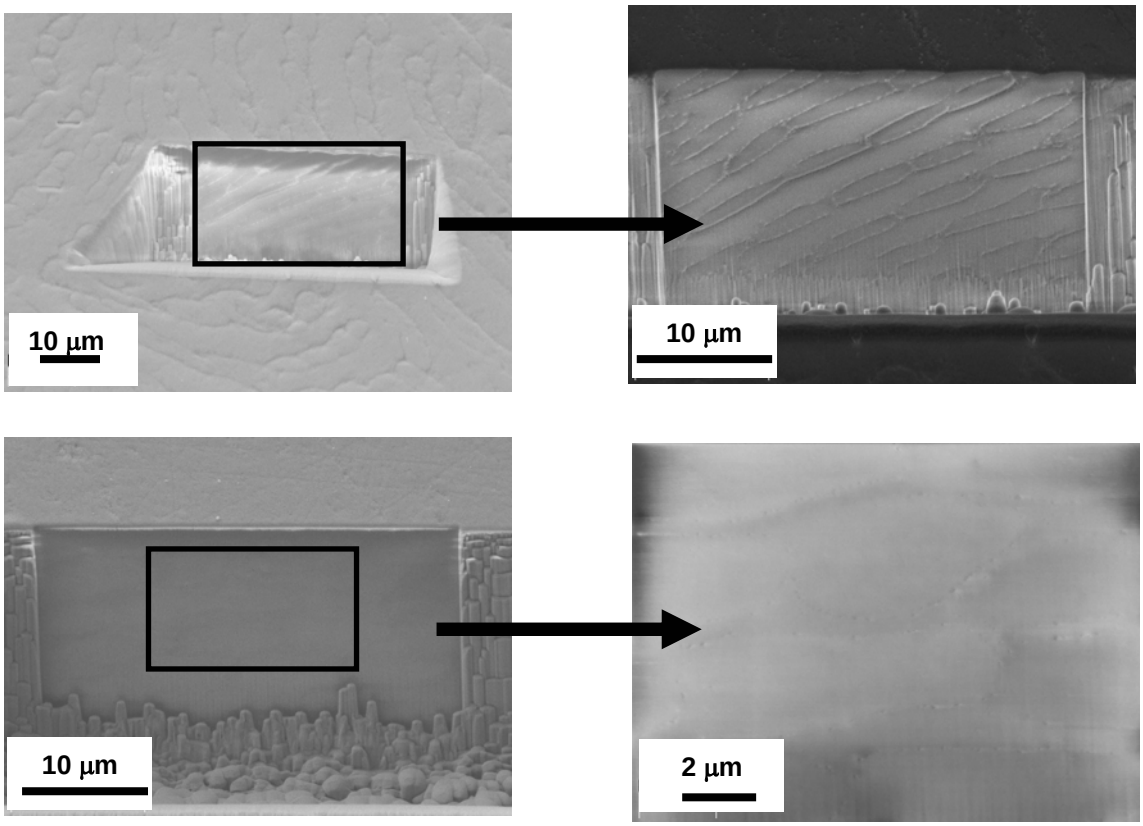

Fig. 3 Combined FIB (Focused Ion Beam) and SEM (Scanning Electron Microscopy) of the cross surface of bovine enamel. The sample was pre-coated with carbon. The holes were rough milled with 10 nA current superimposing a SEM windows with high current, 10 kV and 120 μm aperture to compensate charging of the sample. The last polishing step was done with 1 nA to 500 pA. The upper two pictures correspond to the region close to the DEJ (Dentine Enamel Junction) and the bottom two images correspond to the same sample of bovine enamel but close to the outer surface. On the right, the images are higher resolution back scatter electron images of the marked rectangle on the left images. The contrast is attributed to differences in orientation. As shown, the microstructure close to the DEJ shows a twisted orientation while close to the outer surface the absence of different contrast may indicate a highly oriented structure.

Fig. 4

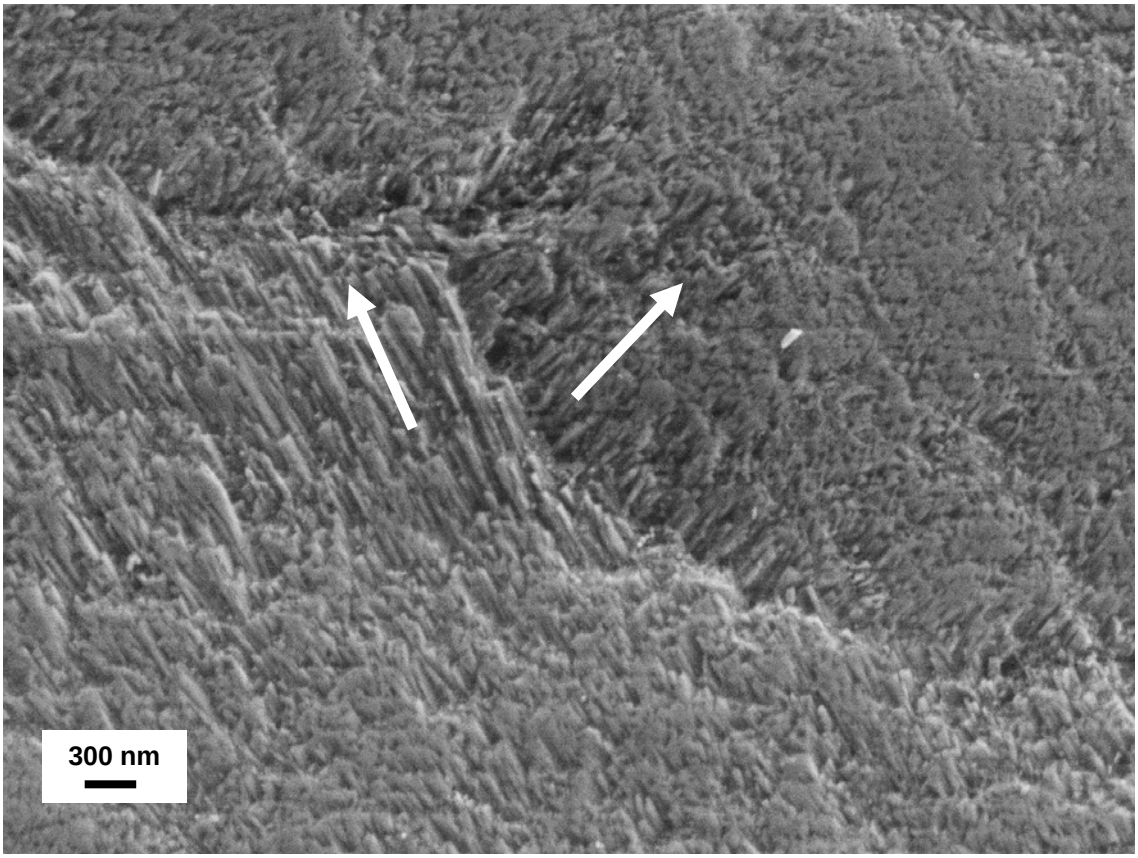

Fig. 4. High resolution SEM image, without carbon coating, of a cross section of a human enamel sample close to the DEJ. The change in orientation of the enamel fibers from one rod to the adjacent are clearly seen and indicated with white arrows.

Fig. 5

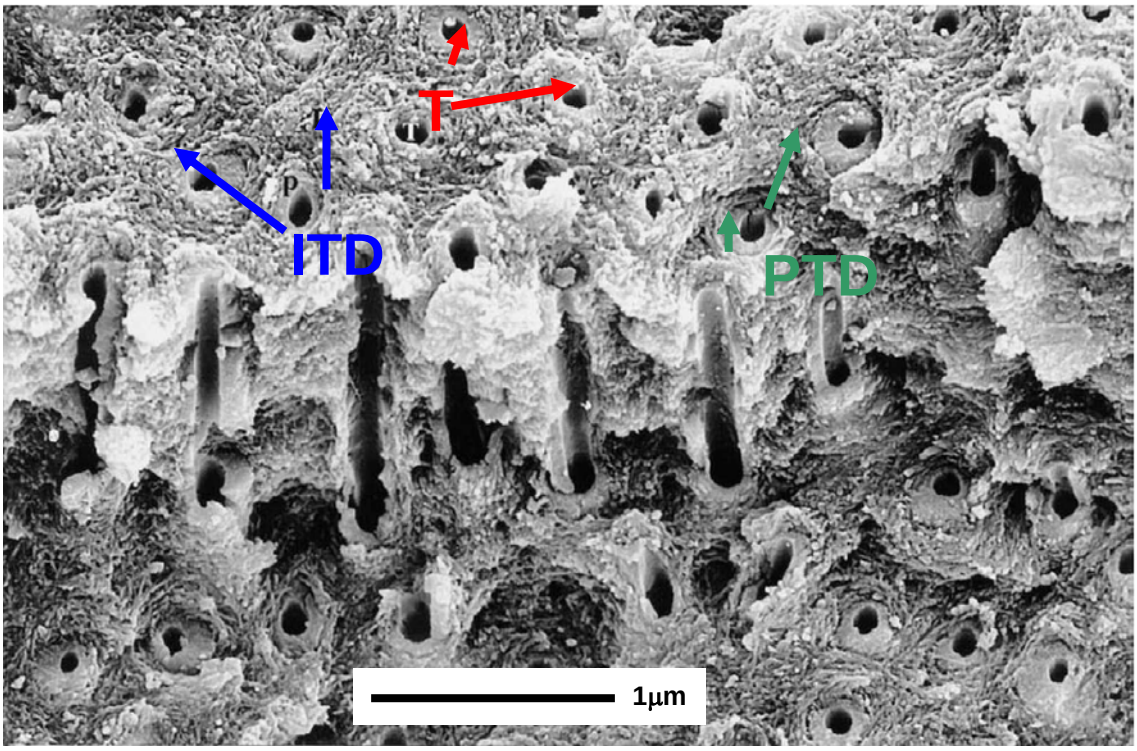

Fig. 5 SEM micrograph of the fracture surface of human coronal dentine, showing the tubules (T) surrounded by relatively dense peritubular dentine (PTD), and the intervening space occupied by intertubular dentine (ITD). ITD has a fibrous texture with the fibrils being oriented tangentially around the tubules and the fibril axes are aligned mainly in the plane perpendicular to the tubule directions. Extracted from (Weiner et al., 1999)**.**

Fig. 6

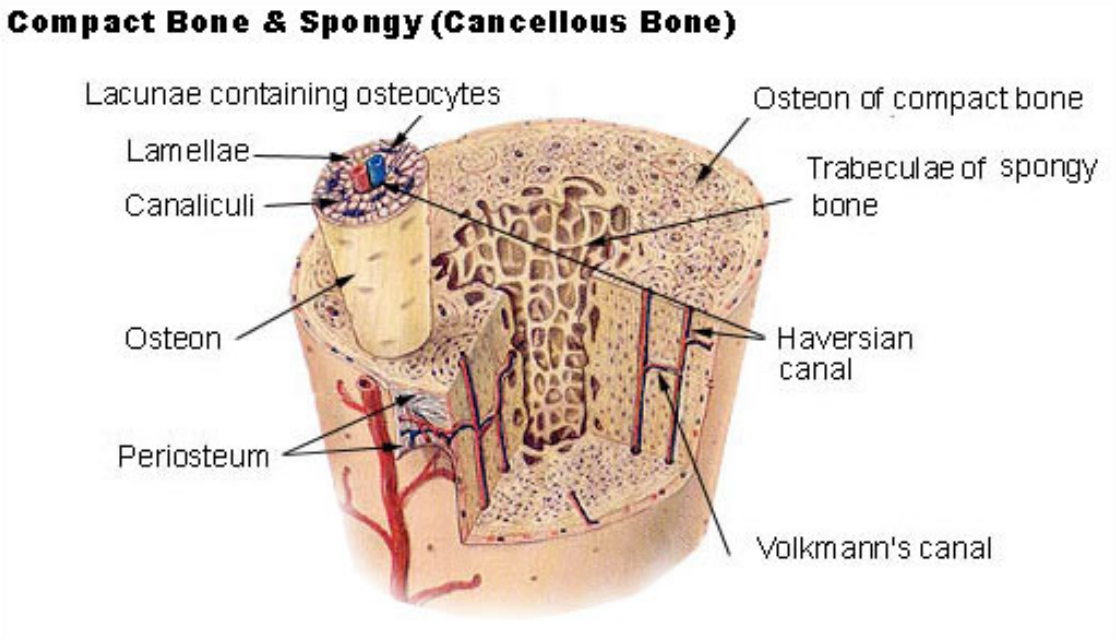

Fig. 6 Scheme of a section of a bone, showing the main constituent of compact and trabecular bone at a micrometer level.

Source: http://en.wikipedia.org/wiki/Image:Illu_compact_spongy_bone.jpg#file

Fig. 7

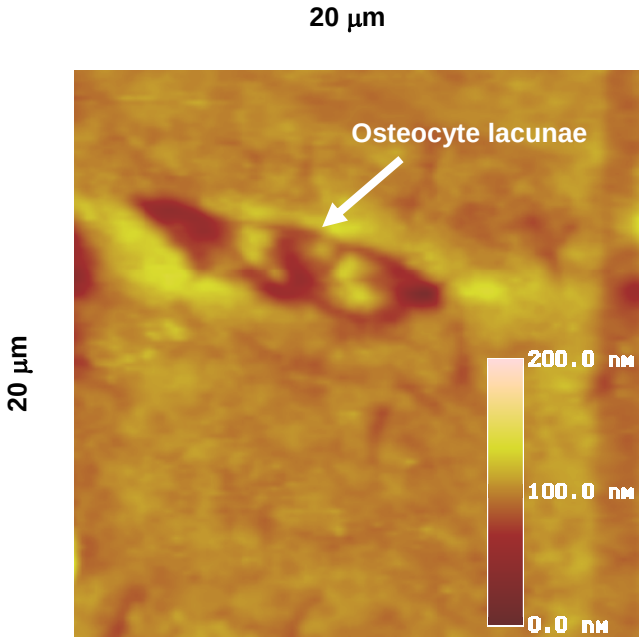

Fig. 7 AFM 20 x 20 μm image of a cross sectional sample of bovine compact bone sample tested under wet conditions. Image taken with the rounded conical nanoindenter tip (400 nm nominal radius) in contact mode. The normal vector of the imaged area is parallel to the longitudinal direction of a long bone.

Fig. 8

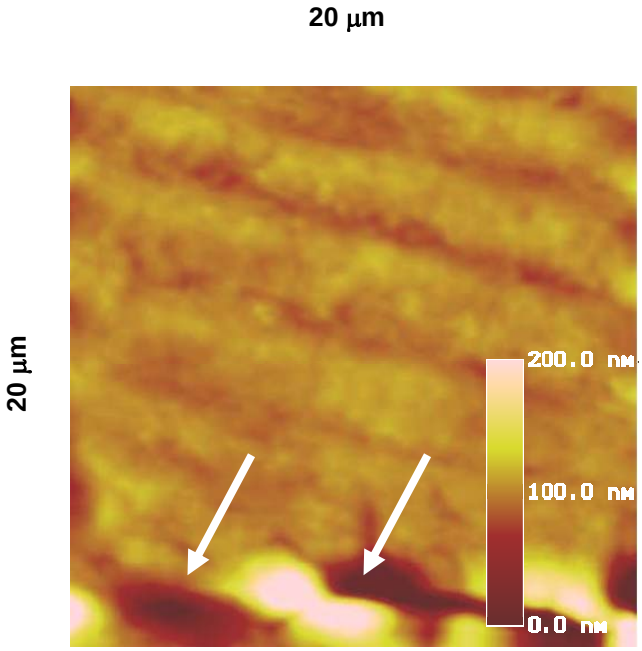

Fig. 8 AFM 20 x 20 μm image of a cross sectional sample of bovine compact bone sample tested under wet conditions. Image taken with the rounded conical nanoindenter tip (400 nm nominal radius) in contact mode. The white arrows mark osteocyte lacunae. Dark and bright areas correspond to thick and thin lamellas respectively. The normal vector of the image area is parallel to the longitudinal direction of a long bone.

CHAPTER 1

1. LITERATURE REVIEW: MATERIALS

Chapter 1 provides a short overview of the knowledge of enamel, dentine and compact lamellar bone, oriented to the scale and methods studied in this thesis. This chapter is an extension of the description of materials already presented in the introductory section above.

Enamel, dentine and compact bone: microstructure and mechanical properties

1.1. Enamel

1.1.1. Microstructure

1.1.1.1. Nanometer level

In enamel, the proteins form an organic matrix ‘‘framework’’ most of which disappears after it completes its function, leaving behind the highly oriented, largely inorganic, unique mineralised structure (Fincham et al., 1999). Fincham and co-workers (Fincham et al., 1999) presented a complete review of the composition of the matrix (which exceeds the scope of this thesis) and proposed a mechanism for organic mediated mineralization which is schematically presented in Fig. 9.

Habelitz et al. (Habelitz et al., 2001a) measured by AFM after etching human third molars enamel for 5 s with 0.005 mol% citric acid, single apatite crystals of about 50 nm width, separated by a thin cuticle of enamelin. Selvig and Halse (Selvig and Halse, 1972) measured in completely mineralized enamel of rat incisor, mineral crystals of irregular contours, densely packed with 1-2.5 nm separation space, and 45 nm in width and 25 nm in thickness. White et al. (White et al., 2001) measured individual crystallites of approximately 100 nm in diameter in adult human incisor teeth.

1.1.1.2. Micrometer level

Rods are bundles of crystallites approximately 4.5 μm in diameter (White et al., 2001). Currey (Currey, 2002) reported a wider range of 3-6 μm in diameter. The rods have a honeycomb arrangement as shown in Fig. 10

White et al. (White et al., 2001) found a mis-orientation between the dominant crystallite orientations in rod and interrod (60° in this plane). Poole and Brooks (Poole and Brooks, 1961) measured by X-Ray diffraction the particular orientation of the crystallites inside the enamel rods which is also schematically represented in Fig. 10. Crystallites on the cuspal sides of the prism are almost parallel with prism axis, those cervically deviate by 20-40º, whilst between these two extremes is a gradual transition from one to the other.

Human enamel contains Hunter-Schreger bands Fig. 11. Each band is composed of approximately 10 layers of rods (White et al., 2001). Each band had a large angle of mis-orientation with adjacent bands. Within single bands, adjacent layers of rods have a small angle of mis-orientation. Therefore, human enamel has two separate levels of mis-orientation (commonly called decussation).

Macho and co-workers (Macho et al., 2003) developed a computer model which is based on mathematical algorithms derived from biophysical processes in order to elucidate the 3D arrangement of rods in enamel. The model makes it possible to recreate small enamel pieces from broken surfaces. Because the rods have an undulating path both in the longitudinal and transversal plane Fig. 12, a crack travelling along the structure will be deflected and be more likely to be arrested. Enamel decussation may indeed be an adaptation to functional demands (e.g., a crackstopping mechanism in large-bodied, thick-enamelled animal species, such as the orangutan, which are capable of high bite forces).

1.1.2. Mechanical properties

1.1.2.1. Indentation modulus and hardness

All the mechanical properties in this section refer to the local elastic modulus and hardness measured by nanoindentation. Unless specially stated, all the references analyzed the data with the Oliver and Pharr method (Oliver and Pharr, 1992), which will be described in Chapter 2.

Although the following effects are inter-related, in order to give a better indication of each of them, they are described separately.

1.1.2.1.1. Orientation effects

Habelitz et al. (Habelitz et al., 2001a) measured by nanoindentation with a *sharp cube corner* indenter tip the Young's moduli of four individual human premolar enamel samples. Elastic moduli were in the range of 85–90 and 70–77 GPa in directions parallel and perpendicular to the rod axis, respectively. They explained the dependence of the mechanical properties on the orientation of the tooth due to the texture of fibre-like apatite crystals in the enamel rods. The observed anisotropy of up to 30% is attributed to the anisotropy and alignment of fibre-like apatite crystals within the rods and to the composite architecture of enamel.

Habelitz and co-workers (Habelitz et al., 2001a) also reported lower Young's modulus and hardness in the tail area in all teeth studied, which they attributed to the change in crystal orientation in this area. However, the differences for the Young's modulus were not statistically significant. In addition, Young's moduli and hardness were lower in the inter-rod enamel, which they attributed mostly to the higher content of elastic and soft organic tissue in this area. However, the Young's moduli values were not significantly different, which might be due to the fact that the inter-rod space shows high variability of mineral content and is so small that indentations did not lie exclusively within the organic soft tissue. Ge et al. (Ge et al., 2005) used a *Berkovich* tip to investigate the local mechanical properties variations between prisms and sheaths within an enamel rod. The nanohardness (H) and elastic modulus (E) of the sheaths

were about 73.6% and 52.7% lower than those of the prisms, respectively. They reported cracking and pile up around the indents.

He and Swain (He et al., 2006) also reported anisotropic properties of enamel. Nano-indentation with a *Berkovich* and two *spherical* indenters with nominal tip radii of 5 and 20 μm were used to determine the elastic modulus and stress–strain response of human enamel. The top surface is stiffer and has higher stress–strain response than an adjacent cross-section surface. They proposed that the difference arises from the rod like prism-sheath structure. Indentation modulus perpendicular to enamel rod is more compliant because of the greater influence of the prism sheaths, according to the authors.

Interestingly, Cuy and co – workers concluded that prism alignment and loading direction appear to have limited influence on the values of H and E they measured (see Section 1.1.2.4 for more details). Braly et al. (Braly et al., 2007) also reported that the impact of prism orientation on mechanical properties measured by nanoindentation appears to be minimal. They carried out nanoindentation tests at two different orientations relative to the hydroxyapatite prisms: parallel and perpendicular. The resulting data show 1.5–3.0% differences between the two orientations for both hardness and Young's modulus. They attributed the variations in hardness and Young's modulus on cross-sectional samples of human molar to changes in local chemistry (varying levels of mineralization, organic matter, and water content) and changes in microstructure (varying volume fractions of inorganic crystals and organic matrix).

1.1.2.1.2. Environment effects

Enamel works under a fluidic environment, i.e. saliva. Thus, it is important to measure its mechanical properties as close as possible to in vivo conditions.

The chosen solution for testing does influence the mechanical properties measured by nanoindentation (Habelitz et al., 2002, Barbour et al., 2003). Nanoindentation is a surface sensitive technique and is capable of detecting changes in the surface properties. Although a surface sensitive technique, its results are thought to be representative of the bulk properties.

Barbour and co-workers (Barbour et al., 2003) measured elastic modulus and hardness of unerupted human third molars stored in tap water with thymol for at least a month after removal of the roots and pulp using a *Berkovich* indenter tip. Volvic mineral water (solution 1) was chosen as the control, and as it has a pH of 7.48 was not expected to cause enamel dissolution. The test solutions were citric acid solution (solution 2), and citric acid containing calcium hydroxide and phosphoric acid (solution 3). Solution 1 caused no statistically significant change in hardness or elastic modulus of enamel at any time, compared to untreated enamel. Solutions 2 and 3 did reduce the measured mechanical properties. Dissolution affected enamel hardness in a different way to elastic modulus. Hardness approached a plateau while elastic modulus did not. There was no statistically significant difference in the hardness and elastic modulus of enamel samples treated with solutions 2 and 3 at any time. Thus, the presence of calcium or phosphorous ions may have no influence.

Following the same method of analysis, Lippert et al. (Lippert et al., 2004) found while studying demineralization/re-mineralization effects of enamel by means of nanoindentation with a *Berkovich* indenter tip that the acid resistance of softened enamel can be improved by an exposure to a mineral water, and, in fact, was indistinguishable to the one observed with a remineralizing solution.

For both measurements above (Barbour et al., 2003) and (Lippert et al., 2004), it is not clear whether the indentations were done under the solutions or under atmospheric conditions following removal from the environments.

Staines et al. (Staines et al., 1981) reported the elastic modulus of enamel increased by 15 % when drying when comparing it with under water. They used a *spherical* tungsten carbide indenter and also reported visco-elastic moisture dependent properties of enamel.

He and Swain (He and Swain, 2007c) calculated the shear modulus of the protein phase of enamel by nano-indenting enamel with a *Berkovich* indenter. It was also found to be significantly changed in the various environments: distilled water, chemically dehydration (ethanol), burnt at 300 ºC and re-hydrated in distilled water. They argued that pure ethanol partially blocked functions of matrix proteins by dehydrating the system, while heat treatment destroyed matrix proteins inside enamel. As a result, without deformable matrix proteins, the mechanical behaviour of different enamel samples noticeably changed. Comparing sound and treated enamel samples, matrix proteins endow enamel better performance as a load bearing calcified tissue. These observations suggest that, although proteins are only a minor part of the enamel composition, however with their biopolymer and perhaps sacrificial bond characteristics, they may regulate the mechanical properties of enamel by redistributing stresses inelastically.

1.1.2.1.3. Mineral content effects

Mahoney et al. (Mahoney et al., 2004) have shown that hypo-mineralised enamel from first permanent molar teeth has a hardness and modulus of elasticity of 0.537 $\pm$ 0.31 GPa and 14.497 $\pm$ 7.56 GPa, respectively. These results correspond to a decrement change of up to 85 % when comparing with sound enamel. They measured local mechanical properties with a *Berkovich* indenter tip and using distilled water as environment. They complemented the study by the determination of the morphological structural influence of hypo-mineralised defects using scanning electron microscopy (SEM): they found an increase in porosity and a consistently disorganised rod structure in the hypo-mineralised enamel, by the determination of the chemical composition and crystalline structure of the hypo-mineralised areas using Energy Dispersive X-ray Spectrometer (EDX) and Xray diffraction: the only calcium phosphate phase present in the hypo-mineralised enamel was calcium apatite; and finally to measure the mineral content of the hypo-mineralised tissue in comparison to unaffected enamel using Back Scatter Electron (BSE) images: the Ca/P ratio for hypo-mineralised enamel was found to be 2.07 which was not significantly different to that of the control tissue. Thus, they were not able to give an explanation for the dramatic reduction of mechanical properties in hypo-mineralized enamel.

Xie et al. (Xie et al., 2007) used focused ion beam (FIB) milling for the preparation of site-specific cross-sectional samples of sound and defective dental enamel for SEM and TEM observations. These observations have revealed a reduction in density of the enamel as a result of hypomineralization both within the prisms and, most markedly, at the sheath regions. It was hypothesized that this observed reduction in density is a result of a decrease in the fraction of mineral phase and a corresponding increase in protein fraction both within the prisms and, most significantly, at the sheath regions. Nano-indentation tests were carried out over a wide range of peak loads in a direction perpendicular to the enamel prisms with a *Berkovich* indenter. The degradation of structural integrity was believed to be responsible for the continuing reduction in measured mechanical properties of hypomineralized enamel with increasing contact area.

1.1.2.1.4. Positional variations

Cuy and co-workers (Cuy et al., 2002) mapped the elastic modulus, E, and hardness, H, of cross sectional areas of enamel by using a *Berkovich* indenter under atmospheric conditions. They found significant decreases in H and E on going from the enamel surface to the junction with dentine, particularly for the lingual side. The extreme variations are well over 50% for both H and E. They supported the hypothesis that the mechanical properties of enamel are strongly dependent on its degree of mineralization (CaO/P_2O_5 content) and only weakly dependent on its microstructure. In general, both H and E were higher along the surface of the lingual cusp than along the buccal cusp. The lingual side, which experiences higher surface loads during mastication, has higher values of *H* and *E* at its occlusal surface and lower values at the enamel–dentine junction than the buccal side, they argued this latter is a functional adaptation.

As already presented in Section 1.1.2.1.1, Ge and co-workers (Ge et al., 2005) used presumably a *Berkovich* indenter (it was not clearly stated in the manuscript) to characterize the local mechanical properties of the rod cores and interfaces. They found that the nanohardness, H, and elastic modulus, E, of the enamel sheaths were about 73.6% and 52.7% lower than those of the prisms, respectively. The variations of mechanical properties in these domains are considered to be mainly relative to their different component and fibrils arrangement. In addition, they recorded pile-up and cracking for both structures, although the patterns were different.

1.1.2.1.5. Time dependent properties

Zhou et al. (Zhou and Hsiung, 2006a) found that deformation on enamel is dependent upon strain rate. They explained such rate dependence from the rate dependent unfolding behaviour of macromolecules in protein matrix. They reported a rising elastic modulus and enhanced resistance to penetration deformation with increasing strain rate.

He and Swain (He and Swain, 2007d) could not record a elastic contact behaviour when loading enamel with spherical indenters of 5 and 20 μm nominal radii even at 5 mN load. In a later paper, He and Swain (He and Swain, 2007a) suggested that these results may be explained by the fact that the protein layers bears most of deformation in the form of shear

strain, which is 16 times greater than the contact strain. Being an organic phase, the protein layer behaves as a visco-elastic material.

He and Swain (He and Swain, 2006) recorded only a slight difference in energy absorption between two force tests despite a 100-fold difference in the loading rates. The slower loading rates for all indenters (one *Berkovich*, and two *spherical* of 5 and 20 μm radii) resulted in a slightly greater penetration depth. This indicates that the energy loss ratio for enamel is almost strain rate independent. This independence of energy loss as a consequence of loading rate suggests that enamel viscous behavior is not the major basis of the energy loss mechanism. Three different mechanisms were considered to contribute to the measured energy absorption, namely fluid flow within the sheath structure as proposed by Fox (Fox, 1980), protein ''sacrificial bond'' extension as proposed for nacre and bone, or nanoscale friction within sheaths associated with the ply-wood organization of enamel rods (Macho et al., 2003). Fox's mechanism could not explain the independence of energy loss with loading rate.

In addition, He and Swain (He and Swain, 2007b) showed that although the major component of enamel is brittle hydroxyapatite, it behaved more metallic like with respect to its stress–strain curves, creep and crack initiation behaviour. Four metals used in dentistry: cast alloy, gold alloy, titanium and amalgam, were compared with enamel. Pure hydroxyapatite (HAP) was used as the ceramic analogue of enamel. A *Berkovich* and a *spherical* indenter were selected for nanoindentation tests. This investigation indicated that dental metallic alloys may have better mechanical compatibility than ceramics with respect to enamel. Enamel acquires its metallic-like properties as a consequence of the limited presence of proteins within it.

Recently, He et al. (He et al., 2007) used Raman spectroscopy to measure residual stresses around indents done with a *Berkovich* and *spherical* indenters made with a force of 100 mN in enamel and hydroxyapatite samples. For HAP samples the residual stress was mainly limited within the indent impression. In contrast, residual stress fields for the enamel samples extended well beyond the indent impressions. Rod units were believed to redistribute the stress in a more complex manner.

Table 1 summarizes some of the elastic moduli and hardness of enamel found in literature.

1.1.2.2. Tribological properties

Wear -simply defined- is a loss of anatomic contour. The reason for loss of hard tissue could be caries, erosion, attrition, or abrasion. Pintado and co-workers (Pintado et al., 1997) reported a steady wear rate of 0.04 mm^3 per year by volume and 10 μm per year by depth, averaged over all teeth, over a 2-year period in a population of 18 young adults. Only attrition on the occlusal surfaces was considered. They also recorded important differences on the basis of anatomic position in the arch, with the canines showing the most wear. Although not as severe as attrition, in this thesis, abrasion will be studied. Abrasion is the result of two-body interactions. It occurs in the mouth during mastication and other normal daily functions (i.e. tooth brushing with tooth paste which usually contains hard particles).

Reeh and co-workers (Reeh et al., 1995) compared the tribological response of bovine and human enamel under different environments. They concluded that the high correlations between widely different lubricants on the two enamel substrates gives confidence in the use of bovine enamel as a model for human enamel in salivary lubrication studies. Thus, in the present study the enamel from the different origins (human or bovine) was considered representative of enamel and no further distinctions were made.

Fernandes et al. (Fernandes et al., 2003) measured in vivo forces between 50 to 300 N for among 3 female and 3 male individuals. The results were dependent on position and test subject. Anderson (Anderson, 1956) measured masticatory stresses in 4 subjects using a resistance wire strain gauge apparatus accommodated in inlays in lower molars. The pressure was roughly 20 MPa. Loads are variable and are cyclic and they will affect the expected wear response of enamel.

Wear depends on the environment chosen for testing (Turssi et al., 2006, West et al., 1999, Li and Zhou, 2002, Sarrett et al., 2000). It is in general accepted that an absence of lubrication generates more wear. Turssi et al. (Turssi et al., 2006) found that over the whole testing period (carried out in a wear simulator after 250000 cycles), the unlubricated condition provided the greatest wear. They stated that under dry condition, an initial period elapsed where the surface roughness profile was reduced to a state that supported relatively uniform contact. In addition, during dry sliding, adhesive wear might have operated simultaneously with abrasive mechanisms. As the load and tangential force (sliding) were applied, adhesively-bonded contact junctions made between the two unlubricated surfaces which may have been ruptured and detached. They found that at 250,000 cycles, wear of the composite ranked as follows: MC<HS<CM<DW<UN, where human saliva (HS), mucinbased artificial saliva (MC), carboxymethylcellulose-containing saliva (CM), deionized water (DW) or with no lubrication (UN). The better lubrication of mucin based artificial saliva in comparison with Human saliva was attributed to the saliva collected in vitro might have shown precipitation or degradation of proteins adversely affecting its lubricating properties. West et al. (West et al., 1999) studied in vivo and in situ the influence of mean losses of enamel in situ for orange juice, water, experimental blackcurrant juice drink with calcium and blackcurrant juice drink. Even though the wear trends were retained, the absolute values obtained in vivo and in vitro differed considerably, the latter being higher. In addition, Sarret et al. (Sarrett et al., 2000) showed that alcoholic beverages with at least 9 vol% ethanol increased the wear of enamel in comparison with water. Li and Zhou (Li and Zhou, 2002) concluded that the artificial saliva they used could play both a cooling and lubricant effect during wear process in comparison to their dry measurements.

Sajewicz et al. (Sajewicz and Kulesza, 2007) presented a new device for characterizing wear of dental materials and reported that the outer enamel was subjected to some transformation during sliding and a new structure was formed, then its delamination occurred and finally wear debris was produced. They used artificial saliva as environment. They obtained

a friction coefficient of ~ 0.5 at the end of their tests. Understanding wear mechanisms is important for the design of clinical therapies and selection of new prostheses.

Sajewicz (Sajewicz, 2006) found a linear dependency of wear volume on dissipated friction energy of dental materials. The lower the slope of wear volume vs. dissipated energy obtained for a material during sliding, the higher the wear resistance of the material. Why is the characterization of enamel and dental materials regarding tribology so interesting? Wear, among other properties (Kelly et al., 1996), is one of the important considerations taken while choosing the right prosthesis for each particular case. For example, Magne et al. (Magne et al., 1999) simulated with an artificial mouth masticatory movements and forces and found that depending on the ceramic used the antagonistic healthy tooth could become more worn that against normal enamel. Thus, repairing one problem (for example, caries) may lead to another future problem (wear of the opposite healthy teeth).

All the above investigations studied wear mechanism on the micro to millimetre range; however, knowing the inherent hierarchical structure of enamel, understanding wear mechanisms at a nanometre scale may help to elucidate the outstanding performance of enamel even under the adverse operation conditions like fluidic environments of varying pH, repeated loads, etc. In this respect, incipient research is emerging at the nanometre scale. Jandt (Jandt, 2006) studied the role of soft drink induced erosion (demineralisation) and remineralisation by means of atomic force microscope (AFM), measuring changes in depth and a Berkovich indenter tip, measuring changes in hardness. Although less related to wear mechanisms, Habelitz et al. (Habelitz et al., 2001b) determined the width of the dentine enamel junction (DEJ) by using the different friction coefficients of dentine and enamel while scratching the AFM tip across the interface. A new field of research is now opening regarding the wear behaviour of enamel at the nanometre scale.

1.2. Dentine

Although compact bone and dentine were not the main systems studied here, a short literature review on these systems is also given.

1.2.1. Microstructure

Dentine, the most abundant mineralized tissue in the tooth, is composed largely of type-I collagen fibrils and nanocrystalline apatite mineral, with composition similar to that of human bone. At the smallest length scales the constituent materials are: a carbonated nanocrystalline apatite mineral phase (approximately 50% by volume) and a felt-structure of type I collagen fibrils (Kinney et al., 2003b). The collagen fibrils, approximately 30% by volume, are roughly 50-100 nm in diameter; they are randomly oriented in a plane perpendicular to the direction of dentine formation. The mineral crystallites are needle-like near the pulp; the shape continuously progresses to plate-like with proximity to the enamel (Porter et al., 2005). The crystallite thickness, ~ 5 nm, is not invariant with location. Porter et al. (Porter et al., 2005) found that the mineral crystal decreases from the upper root (5.54 nm) to the apex (4.84 nm). Tesch et al.

(Tesch et al., 2001) measured a strong variation of the mineral particle thickness (T), which decreased with the distance from the DEJ.

At a higher level of organization is an intermediate, or composite, length scale. At this length scale, dentine can be modelled as a continuous fibre-reinforced composite, with the intertubular dentine forming the matrix and the tubule lumens with their associated cuffs of peritubular dentine forming the cylindrical fibre reinforcement. Based on ESEM data Elbaum et al. (Elbaum et al., 2007) found that the averaged radius of the lumen is about 0.9 μm. Weiner et al. (Weiner et al., 1999) showed that the crystals of peritubular dentine are plate-shaped and that they are locally aligned in layers. The crystal organization is similar to that found in intertubular dentine and bone.

The tubules run continuously from the dentine-enamel junction to the pulp in coronal dentine, and from the cementum-dentine junction to the pulp canal in the root. The regular, almost uni-axial, alignment of the tubules has led some to suggest that they play an important function in the orientation dependence of the mechanical properties. However, there is controversy in literature regarding the last point: Qin and Swain (Qin and Swain, 2004) developed an anisotropic mechanical model that took into account fluidic flow within capillaries for this system while Kinney et al. (Kinney et al., 1999) predicted that the intertubular dentine matrix governs the elastic behaviour of dentine, in both studies it was found that the tubules did not introduce elastic anisotropy.

Schilke et al. (Schilke et al., 2000) found that the number of dentinal tubules per mm^2 determined by SEM is similar between human and bovine coronal dentine. However, the diameters of dentinal tubules in bovine coronal and root dentine both close to and remote from the pulp were larger than in human coronal dentine. Schilke and co-workers suggested that - provided standardized preparations are used- bovine incisor crown dentine is a suitable substitute for human molar dentine in adhesion studies.

Table 1 Elastic modulus and hardness of enamel.

Author(s)	Surface and site	Test method	Test load ()	Hardness (GPa)	Elastic modulus (GPa)	Environment
Xu et al. (Xu et al., 1998)	Top surface Cross section	Standard Vickers indentation	2-50 N	3.23±0.38 3.03±0.09	\	Atmosphere
	Top surface Cross section	Modified Vickers indentation	1.9 N	3.62±0.2 3.37±0.15	94±5 80±4	Atmosphere
Cuy et al. (Cuy et al., 2002)	Cross section: Outer enamel DEJ	nanoindentation (Berkovich)	Depth control (400 & 800 nm)	2.7-6.4 >6 <3	47-120 >115 <70	Atmosphere
Zhou et al. (Zhou and Hsiung, 2006b)	Top surface	nanoindentation (Berkovich)	Depth control (100-2000 nm)	5.7-3.6	104-70	Atmosphere
Ge et al. (Ge et al., 2005)	Top surface: rod Interrod	nanoindentation (Sharp Cube Corner)	1 mN 0.3 mN	4.3±0.8 1.1±0.3	83.4±7.1 39.5±4.1	Atmosphere
Mahoney et al. (Mahoney et al., 2000)	Cross section (primary molar)	nanoindentation (Berkovich)	50 & 150 mN	4.9±0.4	80.4±7.7	HBSS
Fong et al.(Fong et al., 2000)	Top surface Cross Section	nanoindentation (Berkovich)	0.3-2.5 mN	4.78±0.36 4.53±0.26	98.3±5.9 95.6±4.9	Atmosphere
Habelitz et al. (Habelitz et al., 2001a)	Top surface Cross section Head of rod Tail of rod interrod	nanoindentation (Sharp Cube Corner)	1.5 mN	3.8±0.31 3.3±0.35 4.3±0.4 3.7±0.4 3.9±0.4	87.5±2.1 72.7±4.4 88.0±8.6 80.3±7.2 86.4±11.7	Atmosphere
Habelitz et al. (Habelitz et al.,	Cross section	nanoindentation (Sharp Cube	0.75 & 1.5 mN	3.2±0.4 – 3.7±0.5	74±4 - 80±9.1	HBSS Water

2002)		Corner)		(time 0) 4 1 1 (time 15d)	(time 0) 80 30 30 (time 15d)	$CaCl_2$ solution HBSS Water $CaCl_2$ solution
Barbour et al.(Barbour et al., 2003)	Top surface	nanoindentation (Berkovich)	3 mN 5 mN 7 mN	4.81±0.15 4.77±0.13 4.75±0.12	99.6±1.8 101.9±1.6 105.2±1.3	Atmosphere (?)
Balooch et al. (Balooch et al., 2004)	Cross section	nanoindentation (Berkovich)	2.5 μN		60-70	Atmosphere
He et al. (He et al., 2006)	Top surface Cross Section	nanoindentation (Berkovich & Spherical)	1 to 450 mN	-	100-60 80-40	Distilled water
He et al. (He and Swain, 2007b)	Top surface	nanoindentation (Berkovich & Spherical)	1 – 400 mN	4.2 ± 0.2	94.1 ± 5.4	Distilled water
He et al. (He and Swain, 2007c)	Top Surface	nanoindenter (Berkovich)	10 – 250 mN	4.497 ± 0.15	115-95	Distilled water

Elbaum et al. (Elbaum et al., 2007) found that tubule density increases from the dentine enamel junction (DEJ) towards the pulp. They also found that some of the collagen fibrils are oriented perpendicularly to the tubules in the bulk dentine, forming lumps of ordered collagen fibrils along the tubules. Collagen fibrils oriented along the tubules long axis were found close to the DEJ. Garberoglio et al. (Garberoglio and Brännström, 1976) reported the same trend in tubule density and they also observed that there is no peritubular dentine near the pulp.

1.2.2. Mechanical properties: indentation modulus and hardness

1.2.2.1. Mineral content

Angker et al. (Angker et al., 2005) found that hardness and elastic modulus of carious dentine decreased significantly (compared to sound dentine) and progressively toward the lesion cavity floor where the lowest values were generally found ranging from 0.002 to 0.56 GPa and 0.015 to 14.55 GPa, respectively, while those of sound dentine ranged from 0.527 ± 0.24 to 0.917 ± 0.15 GPa and11.59 ± 3.95 to 17.06 ± 3.09 GPa, respectively. The exceptionally low values found in the outer region were explained by the significant demineralisation with the mineral content reported to be less than 10 % by weight and mostly comprised of denatured collagen.

Kinney et al. (Kinney et al., 1996) reported that the average modulus of peritubular dentine was 29.8 ± 8.9 GPa, and did not depend upon the site within the dentine. The average modulus of the intertubular dentine near the junction was 21.1 ± 1.3 GPa, whereas, the modulus of the intertubular dentine near the pulp was 17.7 ± 0.3 GPa.

1.2.2.2. Positional variations

Tesch et al. (Tesch et al., 2001) found that the hardness and the elastic modulus increase from the DEJ towards the coronal dentine. A decreasing thickness of mineral particles was found to correlate with increasing mineral content and increased hardness and elastic modulus. This fact agreed with the staggered model developed by (Jäger and Fratzl, 2000) since the highest elastic moduli were obtained for the thinnest crystals. The reason is that shear forces in the matrix are an important contribution to the mechanical response of the tissue and they are more effectively used with many thin crystals than with fewer but thicker ones. The same trend was also found by Angker et al. (Angker et al., 2003), explaining their results by changes in both the inorganic content and the histological structure of dentine (tubuli density variations).

Kinney et al. (Kinney et al., 1996) suggested that the decrease in dentine hardness on approaching the pulp can be attributed to changes in the hardness of the intertubular dentine, and not to an increase in the number of tubules as previously suggested.

1.2.2.3. Environmental effects

Kishen et al. (Kishen and Vedantam, 2007) studied theoretically and experimentally the role of environment on mechanical properties of dentine. The compression testing of sagittal dentine sections highlighted conspicuous difference between the stress – strain responses of fully hydrated dentine and dentine dehydrated at 20 ºC for 72 h. The fully hydrated dentine demonstrated high strain at failure compared to the partially dehydrated dentine specimens. They also confirmed that the mechanical response observed in the fully hydrated dentine samples was a discrete response produced by the free water in the dentinal tubules and root canal lumen, and is not caused by any inorganic or organic phase alterations.

Moscovich et al. (Moscovich et al., 1999) found that conventional freezing at -18ºC for 12 days in water appeared to have no short term effects on the hardness of human coronal dentine. They used Vicker's indentation with 30 kg load and 2.1 mm thick disks. However, they made no precise positioning of the indents.

Kinney et al. (Kinney et al., 2003a) reported that the indentation Young's modulus of dry normal dentine was 23.9 (SD = 1.1) GPa; the modulus decreased by 15%, or 3.9 GPa, with wetting. Values measured with a Berkovich indenter tip. On the other hand, the hardness of normal dentin did not appear to depend on water content.

Habelitz et al. (Habelitz et al., 2002) also found by nano-indenting intertubular dentin with a sharp cube corner indenter tip that storage in deionized water or $CaCl_2$-buffered saline solution significantly altered its elastic modulus, while storage in HBSS did not induce significant changes. The reduced elastic modulus of human dentin had average values between 22.8 (± 2.5) and 24.5 (± 1.5) GPa prior to storage. If stored in deionized water, the modulus dropped by 15% after 1 day, which was a significant change. It decreased to 5 GPa after 14 days. Storage of dentin in the $CaCl_2$-solution resulted in a significant drop of the elastic modulus to about 18.5 GPa after 1 day and continued to fall to 40% after 14 days. Storing the specimen in HBSS, however, did not significantly alter the elastic response of dentin.

Maciel and co-workers (Maciel et al., 1996) measured the effect of different solvents on the stiffness of decalcified dentin. The results indicate that the stiffness of decalcified human dentin matrix is very low (ca. 7 MPa), if the specimens are wet with water. As they are dehydrated, either chemically in water-miscible organic solvents or physically in air, the stiffness increases 20- to 38-fold at low strains or three- to six-fold at high strains. These increases in modulus were rapidly reversed by rehydration in water. They claimed their finding is due to the plasticizing effect of water.

1.3. Bone

As already pointed out in the introduction, the term "bone" is a quite general terminology since there are several types of bone in the millimetre scale (compact and trabecular bone) and there are more distinctions inside these categories (woven, lamellar, etc). Thus, since the work done here was done in compact lamellar bone, the literature review presented here will be limited to this type of bone.

1.3.1. Microstructure

Dahllite (carbonated apatite) crystals, type I collagen fibrils, and water are the major components of the bone family of materials. Whereas dahllite is the only mineral type in mature bone, type I collagen is by no means the only protein present (Weiner and Wagner, 1998). The crystals of bone are plate-shaped, with average lengths and widths of 50 x 25 nm (Weiner and Wagner, 1998). Type I collagen is characterized by its fibrous nature, with the fibrils in bone generally 80–100 nm in diameter.

Mineralized collagen fibres form into planar arrangements called lamellae (3–7 μm wide). In some cases these sheets (lamellae) of mineralized collagen fibres wrap in concentric layers (3–8 lamellae) around a central canal to form what is known as an *osteon* or a *Haversian* system. The osteon looks like a cylinder about 200 – 250 μm in diameter running roughly parallel to the long axis of the bone. Other forms of cortical bone where the mineralized collagen fibres are less well registered and no pattern can be distinguished are called *woven* bone (Rho et al., 1998). The microstructure of bone is schematically shown in Fig. 13.

Lee and Glimcher (Lee and Glimcher, 1991) found that the equatorial distance of collagen is 1,5 nm in the wet state and 1,1 nm in the dry state and they were 1,3 and 1,2 nm respectively in higher mineralized regions. These data indicate that collagen is more closely packed in heavily mineralized regions.

Wesch et al. (Wenk and Heidelbach, 1999) measured by synchrotron X-ray investigation that for bovine bone apatite, the c axes are aligned parallel to the bone surface; that is, parallel to the collagen fibril direction in their measurement. In addition, in bovine bone there is a significant portion of apatite crystallites randomly oriented (i.e., half of the crystals are strongly textured and the other half are not). In spite of the above mentioned mis-orientation, compact bone is generally modelled as being mainly oriented in the longitudinal direction. Fig. 14 summarizes dimensions and arrangement of mineral and organic phase in the longitudinal direction of bone.

Marotti (Marotti, 1992) carried out a complete characterization of lamellar compact bone. He reported that bone lamellation was due to a different density of the fibrillar matrix and not to a different orientation of collagen fibers in adjacent lamellae. In fact, all thick and thin lamellae showed a highly interwoven texture with collagen bundles running in transverse, longitudinal, and various oblique directions. Bone lamellation was due to the alternation of collagen-rich (thick) and collagen-poor (thin) layers, all having an interwoven arrangement of fibres. In addition, by means of X-ray microprobe analysis he found that calcium and phosphorus concentration in collagen-poor layers (thin lamellae) is 10-15% higher than in collagen-rich layers (thick lamellae).

Wagermaier et al. (Wagermaier et al., 2006b) carried out scanning texture analysis using a 1 μm-sized synchrotron X-ray beam on human Haversian Systems and found that the fibril orientation in osteons oscillates around a mean direction, but all layers show the same chirality. In an earlier work, Wagermaier et al. (Wagermaier et al., 2006a) used the same technique to find that the orientation angle of the fibrils relative to the osteon axis in successive

cholesteric layers (spacing of 1 μm) changes in a regular sequence of about 5° – 25°, and just at about every sixth cylinder there is a jump in the angle of more than 30°. The sense of the helical winding is right-handed and the chirality is the same for all lamellae except for the outermost one. A scheme is shown in Fig. 15

1.3.2. Mechanical properties: indentation modulus and hardness

1.3.2.1. Time dependent properties

Tang et al. (Tang et al., 2007) reported visco-elastic of dry compact mice bone, although they did not distinguish between the different sub-structures of compact bone. They used the correction for visco-elastic creep developed by one of the authors, Ngan et al. (Ngan et al., 2005).

Rho and Pharr (Rho and Pharr, 1999) reported considerably recovery of their lamellar compact bone samples during the 200 s duration of the second lower load holding period with a Berkovich indenter.

1.3.2.2. Anisotropy effects (within different planes)

Fan and co-workers (Fan et al., 2002) studied the anisotropy of compact lamellar bone by nanoindentation with a Berkovich indenter tip under dry conditions. They included in the analysis the anisotropy of the material tested by using ultrasonic measurements. They found 40 % difference between 0 and 90º mis-orientation and no differences between transversal and radial elastic modulus. Similar results were shown in a study by Swadener et al. (Swadener et al., 2001).

Ji and Gao (Ji and Gao, 2006) reported besides some mechanical models at the nanometre level of bone, a description for the anisotropy of Poisson's ratio of these systems, which is scarcely experimentally considered and may influence the determination of the elastic moduli.

1.3.2.3. Positional effects (within the same plane)

Xu et al. (Xu et al., 2003) found by nano-indenting lamellar bone with a Berkovich indenter tip under dry conditions that higher elastic modulus values were observed for thick lamella in microtomed samples compared with that of thin lamellae, whereas measured elastic modulus differences between thick and thin lamellae in polished samples were found to be statistically insignificant. Microtome samples were less rough than mechanical polished samples (grounded using carbide paper in ascending grit order. After grinding, the sample was washed and polished using 0.05 μm alumina suspension on micro-cloths)

Zysset et al. (Zysset et al., 1999) found that the elastic modulus of human bone tissue depends strongly on tissue type, anatomical location and individual. They found considerable differences between the femoral neck and the diaphysis of the same individual. They also

reported differences between interstitial and osteonal lamellar bone. In diaphyseal femoral bone, the average elastic moduli were 19.1 ± 5.4 GPa in osteonal and 21.2 ± 5.3 GPa in interstitial lamellae. In the neck, the average moduli were 15.8 ± 5.3 GPa in osteonal, 17.5 ± 5.3 GPa in interstitial lamellae. Rho et al. (Rho et al., 1997) found the same trend in their dry indentations with a Berkovich indenter tip: the average results show that Young's modulus is greatest for the tibial interstitial lamellae (E = 25.8GPa), followed in decreasing order by the tibial osteons (E = 22.5 GPa). On the other hand, Hoffler et al. (Hoffler et al., 2000) reported that interstitial bone did not always have greater properties than osteonal tissue, by measuring with a Berkovich indenter tip under a solution not specified. Only the femoral neck interstitial tissue had a greater elastic modulus than its osteonal counterpart. Elastic moduli of osteonal and interstitial microstructures in the femoral diaphysis and distal radius were indistinguishable. They suggested that the discrepancy may result from differences in the average tissue age of the three cortical bone locations.

1.3.2.4. Environmental effects

Bembey et al. (Bembey et al., 2006) used the nanoindentation technique to characterize the influence of different alcohol grading in the elastic modulus of compact bone. Although they did not state which structure in particular was tested, they did find an inverse relationship between elastic modulus and water content.

Gupta et al. (Gupta et al., 2006a) also reported an influence of the environment on the elastic modulus of fibrolamellar bone measured by in situ micro-tensile experiments. They found a 20 % decrement when going from dry to wet conditions.

Rho and Pharr (Rho and Pharr, 1999) found that drying increased the elastic modulus by 9.7% for interstitial lamellae and 15.4% for osteons when comparing with the same structures tested under deionized water (with the incorporation of an antibacterial agent). They used a Berkovich indenter.

1.3.2.5. Mineral content

Tai et al. (Tai et al., 2005) carried out a complete characterization by AFM, SEM, GSE (gaseous secondary electron), BSE, and Raman spectroscopy and nanoindentation with a Berkovich indenter tip of osteonal bone in the direction of the Haversian systems. They found a non-linear increment of elastic modulus with mineral content of the samples.

FIGURES OF CHAPTER 1

Fig. 9

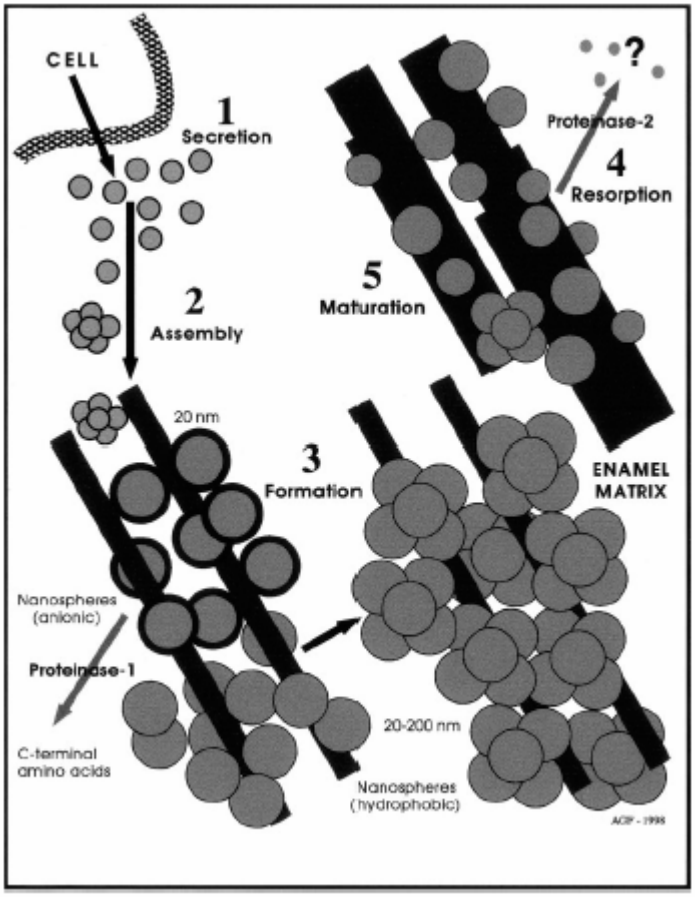

Fig. 9 Schematic diagram for enamel biomineralization. (1) Amelogenins are synthesized by the ameloblasts and secreted extracellularly. (2) Amelogenin monomers assemble to generate nanosphere structures of some 20 nm diameter with the hydrophilic (anionic) carboxy-terminals externalized. (3) Anionic nanospheres initially interact electrostatically with the crystallite faces parallel to the c axis, preventing crystal–crystal fusions and acting as ‘‘20-nm spacers.’’ Proteinase-1 then processes the exposed amelogenin carboxy-terminals progressively reducing their anionic character. Hydrophobic nanospheres further assemble, stabilizing the matrix containing the initial enamel crystallites, which continue to grow by ion accretion on their exposed 001 faces. (4) Proteinase-2 action degrades the hydrophobic nanosphere amelogenins generating smaller fragments and other unidentified products, which are eventually resorbed by ameloblasts. (5) As amelogenin nanosphere ‘‘protection’’ is removed, crystallites thicken and eventually may fuse to generate the mature enamel. Taken from (Fincham et al., 1999)

Fig. 10

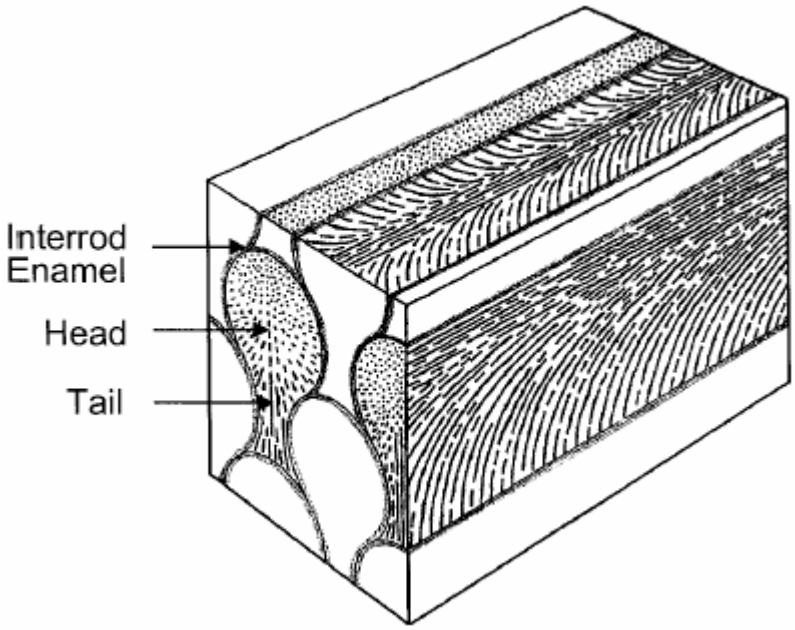

Fig. 10 Schematic drawing of enamel microstructure, showing keyhole-like rods of about 5 μm diameter aligned in parallel. Enamel rods are over 95% mineralized and contain aligned fiber-like apatite crystals with different orientations in the head and tail area. Inter-rod enamel is enriched in organic matter. Taken from (Habelitz et al., 2001a)

Fig. 11

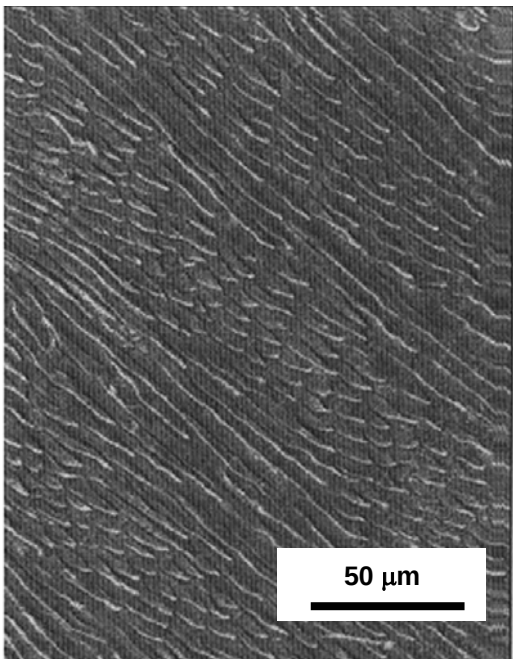

Fig. 11 Sagittal section SEM showing the large angle of decussation between Hunter-Schreger bands (approximately 10 rods). Taken from (White et al., 2001)

Fig. 12

Fig. 12 3D reconstruction of enamel from the dentin enamel junction (DEJ) to the outer enamel surface (OES). The decussating arrangement is shown. Taken from (Macho et al., 2003).

Fig. 13

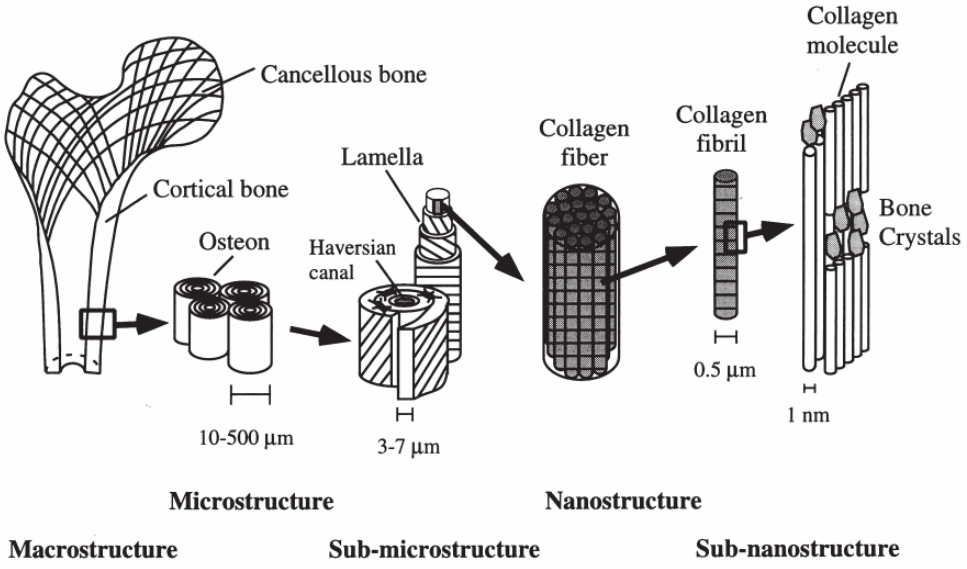

Fig. 13 Hierarchical structural organization of bone: (a) cortical and cancellous bone; (b) osteons with Haversian systems; (c) lamellae; (d) collagen fiber assemblies of collagen fibrils; (e) bone mineral crystals, collagen molecules, and non-collagenous proteins. Taken from (Rho et al., 1998)

Fig. 14

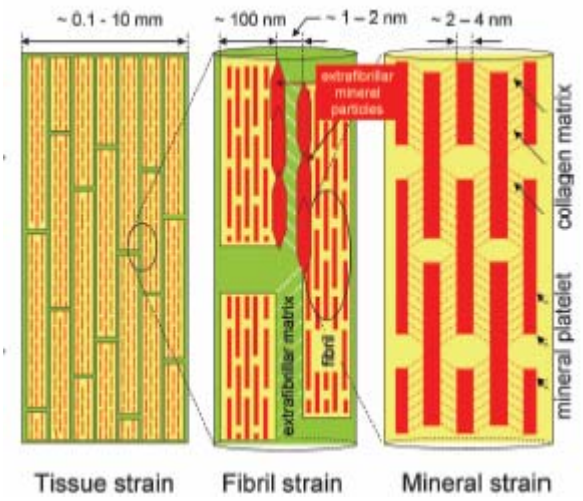

Fig. 14 Detailed scheme showing the hierarchical organization of bone at a nanometer scale. Taken from (Gupta et al., 2006a).

Fig. 15

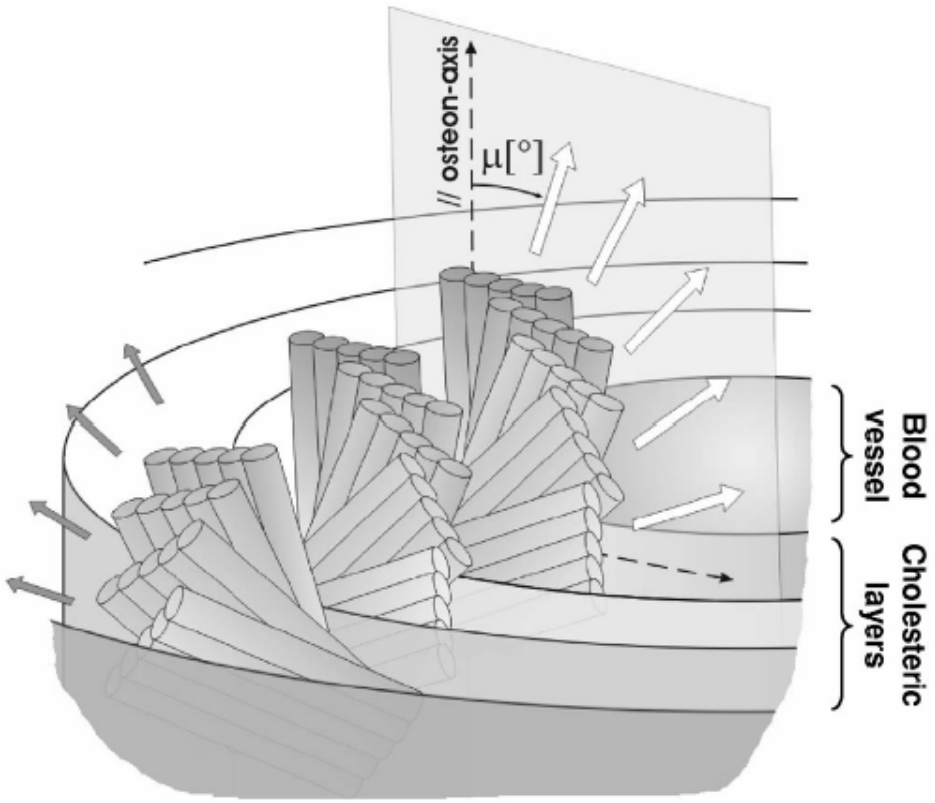

Fig. 15 Model of fibrillar orientation relative to the osteon axis. The orientation of the fibrils changes with a periodicity of 5–7 μm, which corresponds to one single dark or bright lamellae in a polarized light microscopy image. Only the fibrils of the outermost lamella show a different chirality in orientation. Taken from (Wagermaier et al., 2006a).

CHAPTER 2

2. THEORETICAL BASIS

Chapter 2 sums up the basic knowledge to follow and understand this thesis. This thesis was developed in the frame work of Materials Science and Engineering perspective. The present chapter introduces the importance of studying the contact between indenter tip and tested surface in order to interpret the measurements. To describe this contact it is necessary to develop models which represent the mechanisms involved. Therefore, the models proposed in the literature for the biological systems tested plus the existing deformation mechanism during indentation will be introduced in this Chapter. They will be the basis to explain the results presented in Chapters 3 to 8.

2.1. Mineralized tissue from a Materials Science Engineering perspective.

The outstanding mechanical properties of biological tissues such as teeth or bone are mainly due to their hierarchical structure and to their optimization at all levels of hierarchy. It is therefore essential to characterize the structure at all levels to understand the complex behavior of such tissues. The mechanical properties cannot be understood without taking into account all these structural levels.

Thus, since in the present thesis the systems were evaluated on a nanometer scale, the tested materials (dentin, enamel and bone) will be described mechanically on the nanometer scale. The proposed deformation mechanisms at this level are described in the next section.

At the smallest hierarchical level enamel, dentin and bone can be considered as a nano-composite consisting of organic fibrils and small mineral particles.

2.1.1. Simple composite mechanics

For an elastic two-phase composite, the stiffness of Voigt and Reuss composites represent rigorous upper and lower bounds on the Young's modulus for a given volume fraction of one phase Fig. 16. There is no restriction on the shape of the two phases. The modulus for the *Voigt* composite is

$$E_c = E_1 V_1 + E_2 V_2 \qquad \text{Eq. 1}$$

in which E_c, E_1 and E_2 refer to the Young's modulus of the composite, phase 1 and phase 2, and V_1 and V_2 refer to the volume fraction of phase 1 and phase 2 with $V_1+V_2 = 1$. This is an exact analytical form for this morphology. The modulus of the *Reuss* composite is

$$\frac{1}{E_c} = \frac{V_1}{E_1} + \frac{V_2}{E_2} \qquad \text{Eq. 2}$$

These composite properties are attainable for the structures given. Such laminates are anisotropic since they represent an identical structure subjected to a different orientation of stress (Lakes).

2.1.2. Staggered arrangement of organic and inorganic components. Mechanical implications.

In Fig. 17 the proposed staggered arrangement of collagen and mineral at the nanometer scale of bone can be seen. A similar arrangement is thought to be found in dentin and enamel. The outstanding properties of the mineralized tissues studied here cannot be described by the above simple composite models.

Jäger and Fratzl (Jäger and Fratzl, 2000) developed a mechanical model for the behavior of this type of systems. They proposed a model with a staggered array of platelets that

is in good agreement with results on molecular packing in collagen fibrils and that accounts for an increase of both elastic modulus and fracture stress with the amount of mineral in the fibril. Although the mineral and organic phase arrangement resembles a parallel model, the deformation is assumed to be transmitted through shear of the organic phase into the mineral phase (tensile) leading to a simplified one-dimensional serial spring system (Fig. 18).

One of the main results is also that the stiffest tissue is obtained for the thinnest possible crystals spaced laterally as tightly as possible. The large aspect ratio of mineral platelets compensates for the low modulus of the protein phase (Gao et al., 2003).

Based on the work of Jäger and Fratzl (Jäger and Fratzl, 2000), Gao et al. (Gao et al., 2003) proposed a one-dimensional composite model to study the nanoscale effective stiffness of bone and dentin. They found that the stiffness of the composite could be described as:

$$\frac{1}{E} = \frac{1}{\Phi_{mineral} E_{mineral}} + \frac{4(1-\Phi)D^2}{\Phi^2 L^2 G_{matrix}} \qquad \text{Eq. 3}$$

where $E_{mineral}$ is the Young's modulus of mineral, G_{matrix} is the shear modulus of protein, Φ is the volume concentration of mineral, and ρ=D/L is the aspect ratio of the mineral platelets.

Gupta et al. (Gupta et al., 2006a) extended the model to the next hierarchical level of fibrils and extra-celullar matrix, resulting in:

$$E = (1-\Phi)E_{matrix} + \Phi E_{mineral}\left(1 + \frac{4(1-\Phi)D^2 E_{mineral}}{\Phi L^2 G_{matrix}}\right)^{-1} \qquad \text{Eq. 4}$$

2.1.3. Spears' model

Spears (Spears, 1997) developed a 3D finite element model of enamel in which crystal orientation within prismatic enamel is taken into account. He incorporated the prismatic arrangement of enamel plus the variation on mineral orientation within each particular prism.

The basis of this model is schematically shown in Fig. 19. $E_{parallel}$ and $E_{perpendicular}$ referred to the composite models, Voigt and Reuss respectively, already introduced above in section 2.1.1.

In this study, Spears (Spears, 1997) has demonstrated that enamel is likely to behave anisotropically, the ratio of anisotropy being (E_Z:E_y:E_x.) of the model (3:1.5:1). The main output of the model is shown in Fig. 20.

2.1.4. Contact induced deformation in enamel

Another proposed model for the deformation of mineralized tissue (enamel particularly) was recently published (He and Swain, 2007a), in which it is assumed that shear strain of protein layer is the primary microdeformation response during contact deformation of enamel. A scheme of the deformation proposed with point indenters is shown in Fig. 21.

This model may be used to explain the inelastic contact response, the excellent antifatigue, and the large energy absorption abilities of enamel. Based on the model, all of these characteristics are related to the thin protein layers between crystallites. This model agrees with

the Jäger and Fratzl model (Jäger and Fratzl, 2000) and with the sacrificial bond theory proposed for various mineralized tissues (Thompson et al., 2001).

2.1.5. A model for the toughness of enamel

Fox (Fox, 1980) proposed a mechanism for the toughness of enamel based on the transport of fluids through thin channels in enamel (he presented data of nanometre size channels in enamel). He suggested that the work done in forcing liquids through the small channels between the minerals is one of the mechanisms responsible for the toughness of enamel. Enamel is considered as a ‘‘stiff sponge’’ in which fluid flow occurs in the narrow sheath channels between the enamel prisms. Liquid is expelled in compression and drawn in again when the load is released.

Staines et al. (Staines et al., 1981) also invoke Fox’s theory to explain the 15 % increment in elastic modulus on enamel after 72 h drying when compared with the wet condition.

He and Swain (He and Swain, 2006) considered Fox’s approach while trying to explain the energy loss they measured by nanoindentation on enamel, although it could not explain the fact that the rate of loading had little influence on the indentation force–displacement and energy loss response of enamel. Fox also mentioned this discrepancy with loading rate in his original measurements although he attributed it to the difficulty in the comparison of results because of differences in shape and structure from one tooth to the other.

2.1.6. Realignment of the mineral single crystals induced by the indenter.

Zhou et al. (Zhou and Hsiung, 2006b) reported that both the hardness and elastic modulus values incessantly decrease with increasing penetration depth. In a depth range from 100 to 2000 nm, the elastic modulus decreased by 30% from 104 to 70 GPa, and the hardness decreased by more than 30% from 5.7 to 3.6 GPa. The decreasing values are speculated to be associated with microstructure evolution that is induced by the nanoindenter tip (Fig. 22).

2.2. Contact mechanics

Contact mechanics is the study of the deformation of solids that touch each other at one or more points. The physical and mathematical formulation of the subject is built upon the mechanics of materials and theory of elasticity. Work in this field dates back to the publication of the paper "On the contact of elastic solids" by Heinrich Hertz in 1882 (Wikipedia).

2.2.1. Different expected mechanical responses depending on the indenter tip geometry

Johnson (Johnson, 2003, Johnson, 1970), Hill et al. (Hill et al., 1947), Aktins and Tabor (Atkins and Tabor, 1965), Hirst and Howse (Hirst and Howse, 1969) were the pioneer researchers studying the influence of the indenter tip angle on the hardness of ductile materials.

They found indeed that the response of the studied material system depends not only on the mechanical properties of the particular material investigated (elastic modulus, E, and Yield strength, Y) but also on the geometry of the indenter (indenter tip half angle, β).

Hill (Hill et al., 1947) predicted the formation of pile up on the sides of the indentation for plastic rigid solids and wedge indenters of 30º half face angle. Dugdale (Dugdale, 1953) supported Hill's theory by examining the impressions made in cold worked metals by wedge indenters with various angles.

Hirst and Howse (Hirst and Howse, 1969) found for the case of wedge indenters and a wide range of materials (from metals to polymers) the scheme of deformation mechanisms presented in Fig. 23.

One year later, Johnson (Johnson, 1970) extended the theoretical description and limitations of the elastic, expansion of a cylindrical cavity and plastic rigid deformations also to point indenters, normalizing the scope of each mechanism with a parameter (E/Y tanβ), where β is the inclination of the face of the indenter.

Although the above presented deformation mechanisms assume frictionless contact, Grunzweig et al. (Grunzweig et al., 1954) have analyzed the wedge indentation problem allowing for friction and showed that the effect is to raise the apparent indentation pressure by an amount which depends upon the angle of the wedge and the coefficient of friction. The influence of friction on the penetration is much greater at small (sharper), than at large, wedge (blunter) angles.

2.2.2. A special case: Hertz contact

Hertz is well known for his contributions to the field of electrodynamics. However, most papers that consider into the fundamental nature of contact cite his work as a source for some important ideas. His work basically summarises how two axi-symmetric objects placed in contact will behave under loading, he obtained results based upon the classical theory of elasticity and continuum mechanics (Wikipedia).

Fig. 24 shows a scheme of the contact of a spherical indenter and a flat surface.

The radius of contact circle, *a*, can be calculated as (Johnson, 2003),

$$a^3 = \frac{3}{4}\frac{PR}{E_{eff}} \qquad \text{Eq. 5}$$

where *a* is the radius of contact, *P* is the normal contact load, *R* is the nominal radius of the indenter and E_{eff} is $\frac{1}{E_{eff}} = \frac{1-\nu^2}{E} + \frac{1-\nu_i^2}{E_i}$ in which, E, E_i and ν, ν_i are Young's modulus and Poisson's ratio of specimen and indenter (usually diamond).

The total depth of penetration, h_t, is given by:

$$h_t^3 = \left(\frac{3}{4E_{eff}}\right)^2 \frac{P^2}{R} \qquad \text{Eq. 6}$$

Contact pressure, P_m, can be calculated by the definition of the pressure,

$$P_m = \frac{P}{\pi a^2} \quad \text{Eq. 7}$$

Hertz also established the simple relationship between the elastic total displacement into the sample, h_t, and the contact depth, h_c,

$$h_t = 2h_c \quad \text{Eq. 8}$$

Thus, combining Eq. 6 and Eq. 7 the relationship between the contact pressure, P_m, and the contact radius, a, is,

$$P_m = \left(\frac{4E_{eff}}{3\pi}\right)\frac{a}{R} \quad \text{Eq. 9}$$

where E_{eff} is the reduced or indentation elastic modulus and R is the nominal radius of the indenter tip. This expression establishes the linear relationship between contact pressure and contact strain, a/R, during the elastic loading of a material.

At the same time, a relationship between the indenter radius, R, contact radius, a, and contact depth h_c, can be derived from Fig. 24,

$$a = \sqrt{2h_cR - h_c^2} \quad \text{Eq. 10}$$

From Fig. 24, it is not difficult to show that the contact area of a spherical indenter with a specimen can be described by the h_c-a curve (He and Swain, 2007d). The tangent angle of this curve, θ, may also be easily calculated from the derivative of the function $h_c(a)$. Moreover, to facilitate calculation, the equation of the curve can be expressed as $a = f(h_c)$ and its derivative as $a' = \tan\beta = f'(h_c)$, in which β is the tangent angle of the curve. For $\theta + \beta = 90^\circ$, $\tan\theta$ can be calculated as,

$$\tan\theta = 1/\tan\beta = 1/f'(h_p) \quad \text{Eq. 11}$$

Another geometrical relationship illustrated in Fig. 24 is

$$a/R = \sin\theta = 1/\sqrt{(\tan^{-2}\theta + 1)} \quad \text{Eq. 12}$$

Tabor (Tabor, 1970) estimated the strain produced by indentation as

$$\varepsilon_r = 0.20\frac{a}{R} \quad \text{Eq. 13}$$

were the proportional constant (0.20) was determined experimentally.

2.2.3. Oliver and Pharr approach

The most accepted model for calculating elastic modulus, E, and hardness, H, from the load-displacement curves generated during indentation is the well known Oliver and Pharr method (Oliver and Pharr, 1992). It is shown that the load–displacement curves during unloading are not linear. An analysis technique is presented that accounts for the curvature in the unloading data and provides a physically justifiable procedure for determining the depth which should be used in conjunction with the indenter shape function to establish the contact

area at peak load. During unloading, it is assumed that only the elastic displacements are recovered.

Oliver and Pharr (Oliver and Pharr, 1992), based in the expressions of Sneddon (Sneddon, 1965), recommended to fit the unloading nanoindentation loading-displacement (P-h) curve with

$$P = \alpha(h - h_r)^m \qquad \text{Eq. 14}$$

where *P* is the indenter load, *h* is the elastic displacement, h_r is the residual impression depth of the indenter, while *α* and *m* are constants. This method applies to all axi-symmetric indenters, including spheres (Oliver and Pharr, 2004). With this equation, *dP/dh*, the slope of the upper portion of the unloading curve during the initial stages of unloading (also called the contact stiffness, *S*) can be calculated.

m is a parameter which depends on the indenter geometry used being *m* = 1 for flat cylinders, *m* = 1.5 for spheres in the limit of small deformations and for paraboloids of revolution and *m* = 2 for cones. In (Oliver and Pharr, 2004), the same authors Oliver and Pharr introduced the concept of a effective indenter and suggested a general value of m = 1.5 for all the indenter geometries.

The procedure used to measure *H* and *E* is based on the unloading processes shown schematically in Fig. 25. *The basic assumption is that the contact periphery sinks-in.* This assumption limits the applicability of the method because it does not account for the pile-up of material at the contact periphery that occurs in some elastic–plastic materials.

Assuming, however, that pile-up is negligible, the elastic models show that the amount of sink-in, *h*s, is given by:

$$h_s = \varepsilon \frac{P_{max}}{S} \qquad \text{Eq. 15}$$

where ε is a constant that depends on the geometry of the indenter. However, based on the empirical observation that the unloading curves are best approximated by an indenter that behaves like a paraboloid of revolution (Oliver and Pharr, 2004), the value ε = 0.75 was recommended.

It follows from the geometry of Fig. 25 that the depth along which contact is made between the indenter and the specimen, $h_c = h_{max} - h_s$, is:

$$h_c = h_{max} - \varepsilon \frac{P_{max}}{S} \qquad \text{Eq. 16}$$

Letting F(h) be an “area function” that describes the projected (or cross sectional) area of the indenter at a distance h back from its tip, the contact area A is then

$$A_{(h)} = F_{(h)} = \pi a^2 \qquad \text{Eq. 17}$$

where *a* is the radius of contact.

The area function must carefully be calibrated by independent measurements so that deviations from non-ideal indenter geometry are taken into account.

Once the contact area is determined, the hardness is estimated from:

$$H = \frac{P_{max}}{A_{(h_c)}} \qquad \text{Eq. 18}$$

Measurement of the elastic modulus follows from its relationship to contact area and the measured unloading stiffness through the relation

$$\frac{dP}{dh} = \beta \frac{2}{\sqrt{\pi}} E_{eff} \sqrt{A} \qquad \text{Eq. 19}$$

where E_{eff} is the effective elastic modulus (or indentation modulus) defined by

$$\frac{1}{E_{eff}} = \frac{1-\nu^2}{E} + \frac{1-\nu'^2}{E'} \qquad \text{Eq. 20}$$

The effective elastic modulus takes into account the fact that elastic displacements occur in both the specimen, with Young's modulus E and Poisson's ratio ν, and the indenter, with elastic constants E_i and ν_i. β is a constant dependent upon indenter shape. Traditionally, β has been used to account for deviations in stiffness caused by the lack of axial symmetry for pyramidal indenters. However, it has been shown that even for indentation of an elastic half-space by axisymmetric rigid cone, β can deviate significantly from unity. In (Oliver and Pharr, 2004) a value of β = 1.05 is recommended. Although in this thesis it was taken equal to 1 for simplicity.

Oliver and Pharr published a refining on their first theory basing their argument on an effective indenter shape (Oliver and Pharr, 2004).

2.2.4. Area function calibration

Although it does not belong to a theoretical model, area function calibration is an important issue when dealing with nanoindentation. The contact between indenter and sample is done at a nano to micro meter scale; therefore, the real shape of the indenter must be taken into account when using nanoindentation technique. All values obtained from a quasi-static nanoindentation analysis depend on accurate knowledge of the shape of the indenter tip

A very precise but almost impractical method to measure the residual contact area is the TEM replica method. In this case acetate replicas of a range of indentations are made and their area is measured. Another approach is to image the indenter tip with a scanning force microscope (SFM). In this case the shape of the SFM tip must be known well enough in order to deconvolute the indenter shape from the image.

A commonly used and practical method to determine the tip shape is to carry out indents in a material with known elastic properties. The mostly used standard sample for calibrations is a fused silica specimen (elastic modulus = 72.5 GPa). Afterwards an iterative procedure is used to find the tip shape function (Oliver and Pharr, 1992). In this case the experimental data are often modeled with a function according to equation:

$$A_{(h_c)} = C_0 h_c^{\,2} + C_1 h_c + C_2 h_c^{\,1/2} + C_3 h_c^{\,1/4} + \ldots \qquad \text{Eq. 21}$$

The first term of Eq. 21 describes the ideal area function of the indenter tip.

FIGURES OF CHAPTER 2

Fig. 16

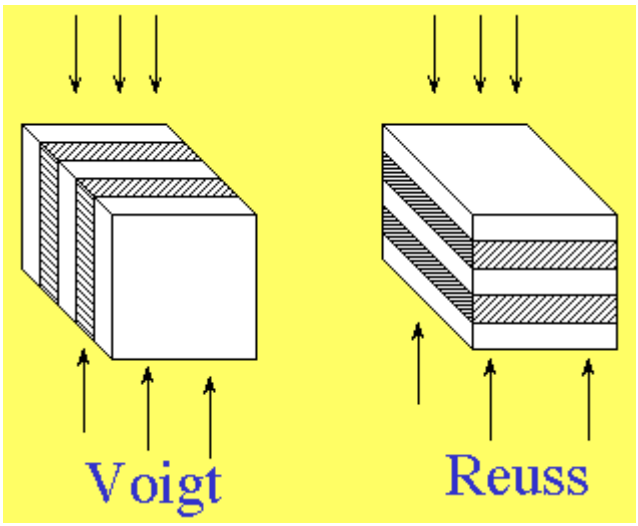

Fig. 16 Parallel (Voigt) and serial (Reuss) arrangement of a two-phase composite. Taken from (Lakes)

Fig. 17

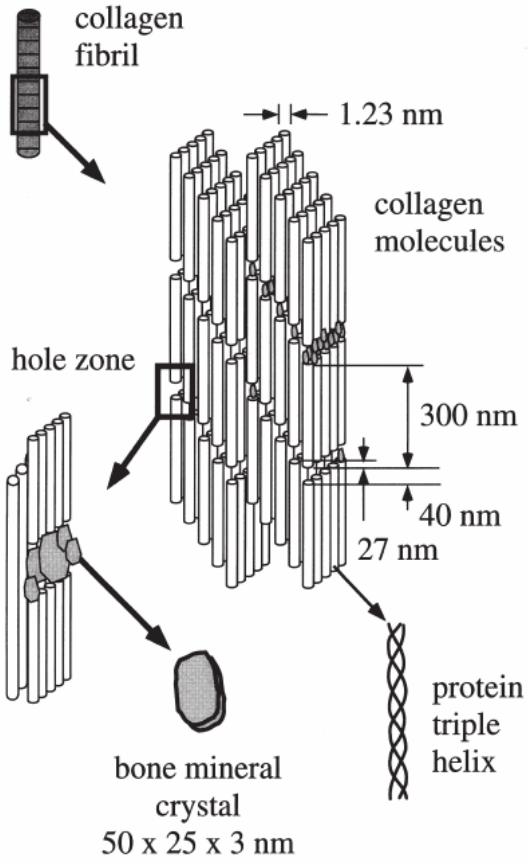

Fig. 17 A schematic diagram illustrating the assembly of collagen fibrils and fibers and bone mineral crystals. The well known 67 nm periodic pattern results from the presence of adjacent hole (40 nm) and overlap (27 nm) regions of the assembled molecules. Taken from (Rho et al., 1998).

Fig. 18

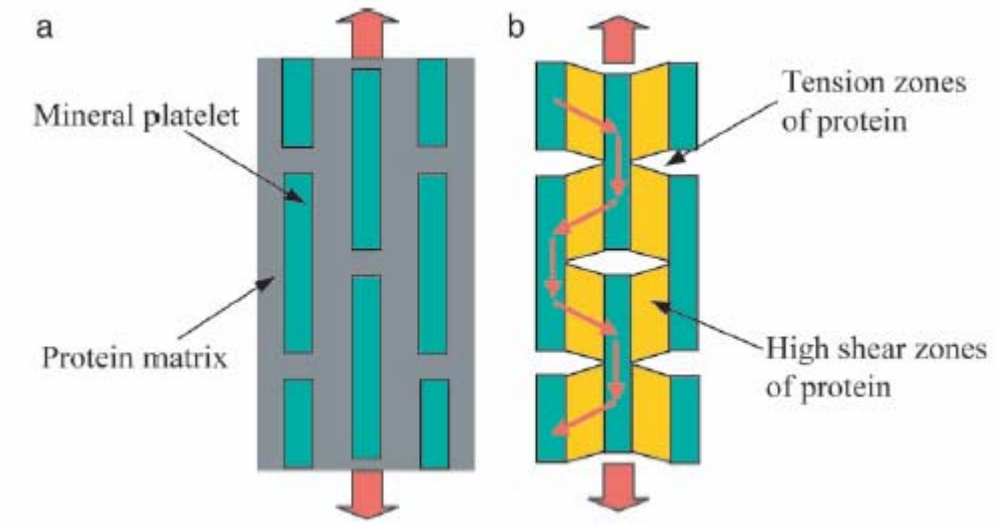

Fig. 18 A model of biocomposites. (*a*) A schematic diagram of staggered mineral crystals embedded in protein matrix. (*b*) A simplified model showing the load-carrying structure of the mineral–protein composites. Most of the load is carried by the mineral platelets whereas the protein transfers load via the high shear zones between mineral platelets. Taken from (Gao et al., 2003).

Fig. 19

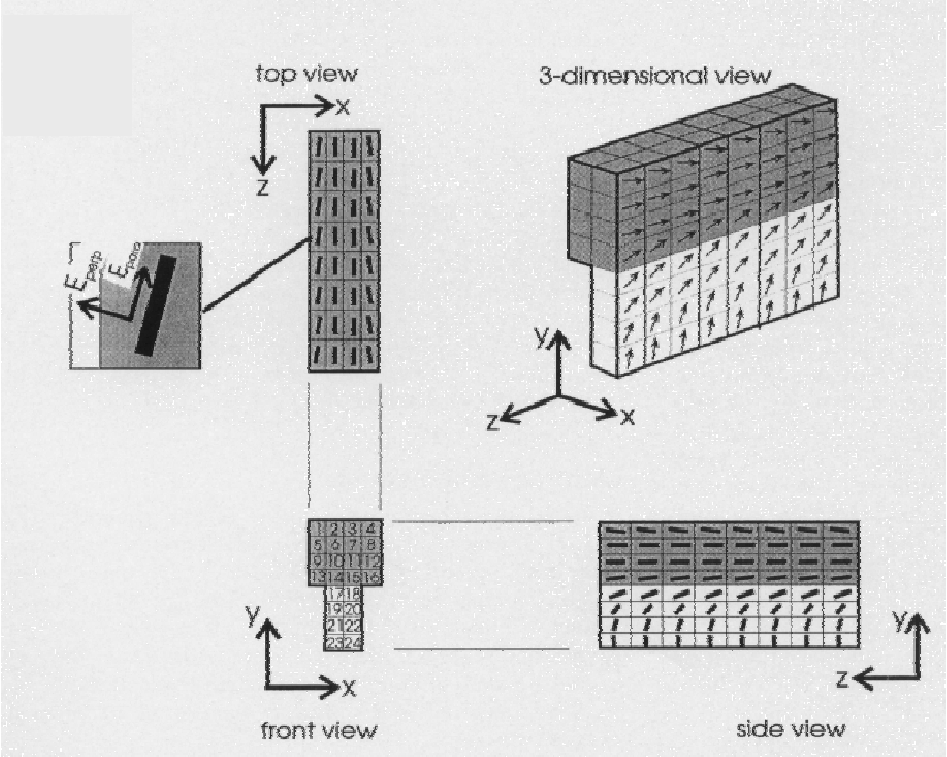

Fig. 19 The elements at the surface of an individual prism model as seen from top, front, side, and three-dimensional views. The vector directions illustrate the assumed crystal orientations, and thus, the assigned directions of high stiffness (E_{para}).

Fig. 20

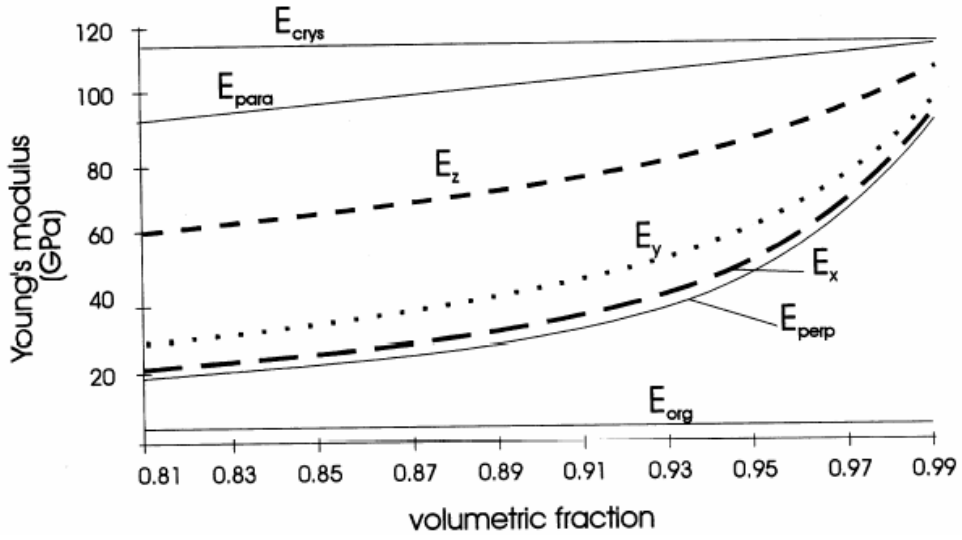

Fig. 20 Predicted Young's modulus along (E_z), horizontally across (E_x), and vertically across (E_Y) the directions of prisms. Also shown are the calculated values of stiffness along (E_{para}) and across (E_{perp}) crystals. Taken from (Spears, 1997)

Fig. 21

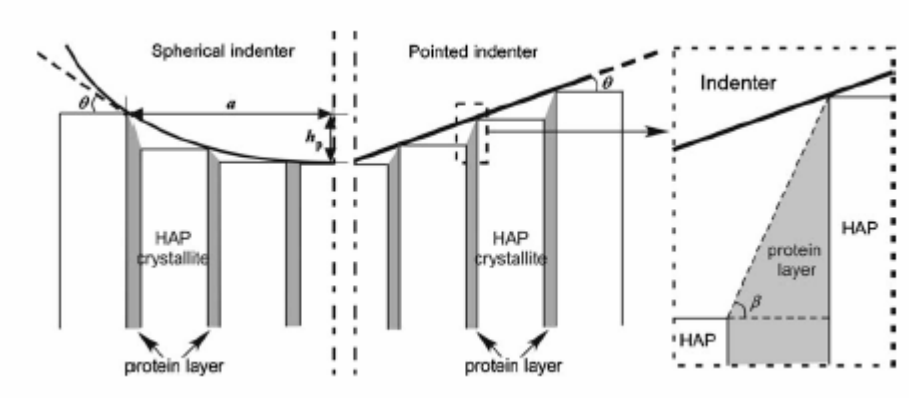

Fig. 21 Schematic illustration of contact induced deformation of enamel with pointed and spherical indenters. Taken from (He and Swain, 2007a)

Fig. 22

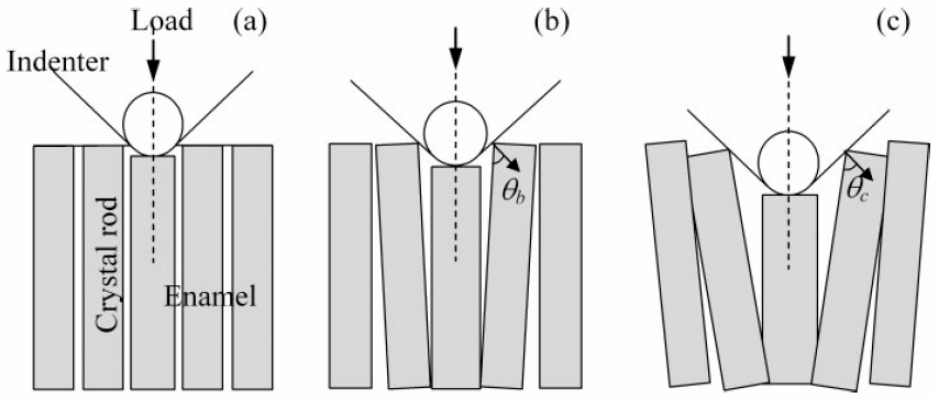

Fig. 22 Schematic illustration of the tip-induced realignment of HAP single crystals, as test proceeds and indent depth increases. Note that $\theta_b < \theta_c$. Taken from (Zhou and Hsiung, 2006b).

Fig. 23

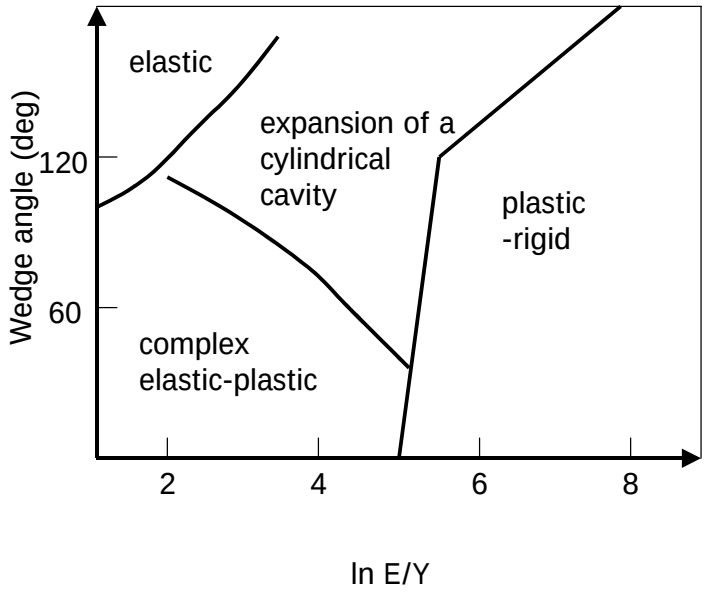

Fig. 23 Regions of operation of different deformation mechanisms proposed by Hirst and Howse for wedge indenters (Hirst and Howse, 1969)

Fig. 24

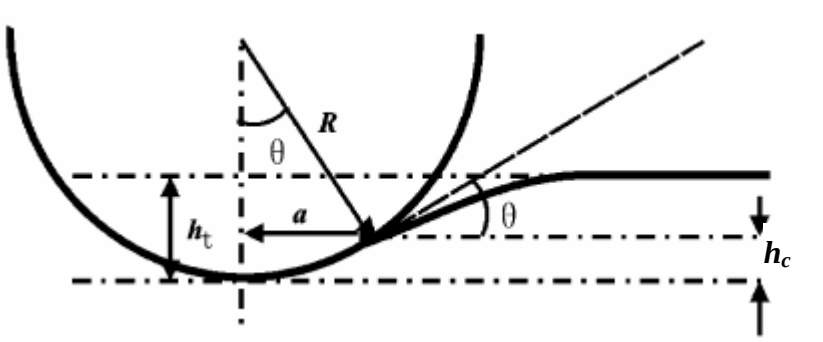

Fig. 24 Schematic diagram of the contact between a spherical indenter and an originally flat specimen. Taken from (He et al., 2006)

Fig. 25

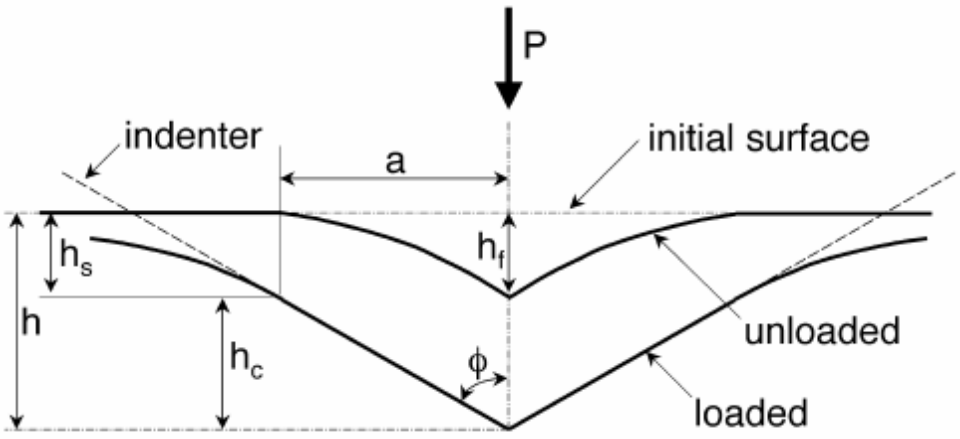

Fig. 25 Schematic illustration of the unloading process showing parameters characterizing the contact geometry. Taken from (Oliver and Pharr, 1992)

SCOPE OF THIS WORK

Starting from Chapter 3, each following chapter (except Appendix A) is a manuscript submitted or already published as a result of this thesis. This section aims to introduce them in the frame of this thesis.

Motivation

Compositional and hierarchical microstructural characteristics of enamel, dentin and compact lamellar bone have been documented. Although their microstructures at the nanometer level are still in constant investigation, the assumption that hierarchical microstructure significantly regulates the mechanical behavior of the biocomposite is well accepted, although it is not well understood. Therefore, in this thesis efforts have made in order to contribute to the knowledge of the relation between microstructure and local mechanical properties.

A range of indenter tip geometries was found in the literature but detailed studies of the contact mechanics and its influence on the measured local mechanical properties of complex anisotropic composite materials like the ones here studied was rarely found. With nanoindentation mainly two mechanical properties can be obtained: indentation modulus and hardness. The first corresponds to an elastic property and it is intimately related to the electronic bonds present in the structure. The second one corresponds to a plastic property and it is an extrinsic property which depends on the structure and composition of the tested material. That is why, in this thesis, most of the analyses were carried out solely on the variations of the elastic modulus with the testing conditions since the structural effects that the different environments impart to the studied biological materials are still not well understood.

The role of the organic phase, although the minority component, in the final mechanical properties of these systems is becoming of importance these days and it was one of the key factors in understanding and analyzing the experiments in this thesis. The visco-elastic character that this component contributes to the biological systems studied here is a feature that still needs to be clarified.

The study was extended from point indentations (0D) to single scratches (1D) and area scratches (2D) for the particular case of enamel. As shown in the literature review and throughout the thesis, most of the wear characterization found in literature was done on the micro to millimeter scale. The in house AFM device together with the transducer for nanoindentation tests gave us a wide range of possibilities for studying these systems at a nanometer scale. The choice of enamel for the wear tests was the obvious choice since it is the major structure exposed to this kind of operational demands.

In addition, the extraordinary possibility of carrying out nanoindentations and nanoscratching tests under fluidic environments together with the high resolution positioning given by the AFM mode provided us the opportunity to move a step further in the mechanical knowledge of these systems and it may contribute to our understanding of the existing gap discovered during the literature review.

Aims of the study

The aims of the study are summarized as follows:

- To determine the influence of environment on the local mechanical properties of enamel, dentine and compact lamellar bone by nanoindentation;

- To explore the influence of the hierarchical structures of these biological systems on its mechanical properties;
- To understand the function of the organic components of enamel and compact bone and dentine in regulating the mechanical properties of these biocomposites;
- To develop a nanoindentation based technique to characterize the tribological behavior of enamel.

Results and significance

The contribution of this PhD thesis to the existing knowledge of mineralized tissue and mechanical properties on a nanometer scale may be summed up as follows:

A detailed experimental study of the influences of storage conditions on the elastic modulus and hardness of intertubular dentine was carried out by means of nanoindentation **(Chapter 7 and Appendix A)**. The influence of storage solution, temperature of storage, reversibility of the conditions and time of storage were analyzed by means of nanoindentation. It was found that chemical dehydration seems to be a reversible process. Hank's balanced salt solution (HBSS) (SIGMA and Product_Information) is a suitable fluid for storing teeth, even after two years of storage. The mechanical properties of dehydrated dentine differ considerably from the near in vivo condition (immersed in HBSS), although the trends are preserved. The temperature of storage is likely to be an important factor for storing teeth in HBSS.

Regarding enamel, the elastic mechanical response dependence on the indenter tip angle under wet and dry conditions when making nanoindentations was studied **(Chapter 3)**. Three different pyramidal indenters were tested. The study was complemented with AFM and SEM imaging. A marked dependence of elastic modulus on indenter tip angle was found, which was explained by inherent visco-elastic effects of enamel and a change in deformation mechanism depending on the indenter tip angle.

The influence of viscoelastic effects in wet and dry conditions on the elastic properties of compact bone were investigated by means of nanoindentation with the rounded conical indenter tip **(Chapter 8)**. The anisotropic behaviour in two different directions was also measured together with the influence of storage temperature on the elastic modulus. The discrepancy between wet and dry results was attributed to the non mineralized phase contribution and rationalized by a simple mechanical model (Jäger and Fratzl, 2000). Anisotropy effects could be explained in terms of deformation mechanisms inherent to the particular fibre like arrangement of lamellar bone. The effect of sub-zero storage temperatures could be clarified by the helicoidal arrangement of lamellar bone.

Regarding wear, the wear mechanism of enamel was characterized under dry conditions and the different response obtained with the two different indenter tips (rounded conical and sharp cube corner) was evaluated and described **(Chapter 4)**. Two different wear mechanisms were proposed depending on the indenter tip geometry: the rounded tip generates a predominantly elastic contact that mainly compresses and plastically deforms the superficial material and generates severe shear deformation on the sub-surface material which, under

certain conditions, fractures and removes material from the sample; on the other hand, the sharp tip cuts into and ploughs the enamel creating a wedge or ridge of material ahead of itself which eventually detaches. The investigation was complemented with TEM, SEM, AFM and single scratch measurements (the latter was performed at Institute for Mechanics of Materials and Structures from Vienna University of Technology, Vienna, Austria).

A comparison of the wear response of enamel under wet and dry conditions with a rounded indenter tip was also conducted **(Chapter 5 and Appendix B)**. The wear mechanism for both conditions was identical. Single scratches were more sensitive to microstructural anisotropic arrangement than abrasion tests. Recovery effects were also present during sliding deformation in enamel for both wet and dry conditions, although wet (HBSS) favours this behaviour. SEM and AFM observations also indicate a better abrasion resistance for the wet than for the dry condition.

A comparison between the wear behaviors of enamel and three materials, namely copper, silver and glass was conducted **(Chapter 6).** The materials were chosen in order to have a wide range of different mechanical responses: from brittle (glass) to plastic (copper and silver). Under the conditions tested all the materials irreversibly deformed presenting very similar wear mechanisms. However, enamel behaves in a brittle manner (glass like) at low loads and ductile (copper and silver like) at higher loads. SEM and AFM provided the basis to critically access the deformation behaviors.

Publications and scientific meeting presentations arising from this research.

Journal publications

- ***Griselda GUIDONI, Julia Denkmayr, Thomas Schöberl, Ingomar Jäger.*** *"Nanoindentation in Teeth: the influence of experimental conditions in local mechanical properties"* **Philosophical Magazine. Volume 86 Number 33-35 (2006) 5705 – 5714***.*
- ***Griselda GUIDONI, M. Swain and I. Jäger.*** *Nano-scale sliding contact deformation behaviour of enamel under wet and dry conditions,* **Journal of Biomedical Research (2007)** ***Submitted.***
- ***Griselda GUIDONI, M. Swain and I. Jäger.*** *"Wear behaviour of enamel at the nano scale with a sharp and blunt indenter tip".* **Wear (2007)** ***Submitted*****.**
- ***Griselda GUIDONI, L. H. He, T. Schöberl, I. Jäger, G. Dehm and M. Swain.*** *"Influence of indenter tip geometry and enironment on the indentation modulus of enamel",* **Journal of Materials Research (2008)** ***Submitted.***
- ***Griselda GUIDONI, M. Swain and I. Jäger.*** *"Nanoindentation in wet and dry compact bone: influence of environment and indenter tip geometry on the elastic modulus"* **Journal of Biomechanics (2008)** ***Submitted.***
- ***Griselda GUIDONI, M. Swain and I. Jäger.*** *"Enamel: from brittle to ductile like tribological behaviour"* **Journal of dentistry (2008)** ***Submitted.***

Scientific meetings

The fifth IASTED international conference on Biomedical Engineering ~Biomed 2007~

Innsbruck, Österreich (Austria). 14th to 16th February, 2007. (Talk)

- ***G. M. GUIDONI, T. Schöberl, G. Dehm and I. Jäger,*** *Abrasion tests on human enamel under wet and dry conditions,* **The fifth IASTED international conference on Biomedical Engineering "Biomed 2007" (2007)**

2. Wiener Biomaterialsymposium

Wien, Österreich (Austria). 22nd to 24th November, 2006. (Poster)

2006 Hysitron Europe User Meeting & Nanomechanical Workshop

Ismaning, Deutschland (Germany). 26th to 27th October, 2006. (Poster)

Nanomech 7. The 7th European Symposium on nano-mechanical Testing

Hückelhoven, Deutschland (Germany). 5th to 7th September, 2006. (Talk)

Bio-Systems Conference

Berlin, (Germany). 26th to 30th June, 2006. (Poster)

Instrumented Indentation Testing in Materials Research and Development

Crete, (Greece). 9th to 14th October, 2005. (Talk)

Project meetings

Biomimetic Systems - Work Shop

Toulouse (France). 19th to 21st September, 2007. (Talk)

Biomimetic Systems - Work Shop

Ischia, Italia (Italy). 18th to 19th September, 2006. (Talk)

Biomimetic Systems - Work Shop

Leoben, Österreich (Germany). 29th to 30th September, 2005. (Talk)

Biomimetic Systems - Work Shop

Postdam, Deutschland (Germany). 7th to 8th April, 2005. (Talk)

Abroad Collaborations

January 2005 — ***Max Planck Institute of Colloids and Interfaces, Biomaterials' Department, Golm, Deutschland (Germany)***

Under the supervision of: Prof. Peter Fratzl and Dr. Oskar Paris.

April 2007 – Juni 2007 — ***University of Sydney, Sydney, New South Wales, Australia***

Under the supervision of: Prof. Michael Swain

October 2007 – December 2007 — ***Max Planck Institute of Colloids and Interfaces, Biomaterials' Department, Golm, Deutschland (Germany)***

Under the supervision of: Prof. Peter Fratzl and Dr. Himadri Gupta.

CHAPTER 3

3. INFLUENCE OF THE INDENTER TIP GEOMETRY AND ENVIRONMENT ON THE INDENTATION MODULUS OF ENAMEL

◆ ***Griselda GUIDONI, L. H. He, T. Schöberl, I. Jäger, G. Dehm and M. Swain.*** *"Influence of indenter tip geometry and environment on the indentation modulus of enamel"* **Journal of Materials Research (2007)** ***Submitted.***

3.1. Abstract

The aim of the study was to study the influence of indenter tip geometry on the conventionally obtained indentation modulus of enamel by nanoindentation. Indentation tests on bovine enamel using three different diamond pyramidal indenters with half face angles 65.27º, 45º and 35.26º were conducted to evaluate the indentation modulus using the Oliver & Pharr method (Oliver and Pharr, 1992). In addition, three different dehydration conditions were studied: wet under Hank's balanced salt solution, laboratory dried and vacuum dehydrated. For the Berkovich indenter (65.27º) and 45º pyramidal indenters there was only a small difference between indentation modulus values whereas for the sharp cube corner indenter (35.26º) a ratio of 2.4 between laboratory dry and wet samples was found. A detailed evaluation including indentation creep and recovery as well as pile-up resulted in a reduction of this latter ratio to 1.7. This still large difference was rationalized on the basis of the different deformation mechanisms generated by indenters of different face angles.

Keywords: Enamel, nanoindentation, creep, recovery, pile up, effective cone angle, Hank's balanced salt solution (HBSS), Berkovich indenter, sharp cube corner indenter (SCC).

3.2. Introduction

Enamel, the outer cover of the tooth, is composed of about 97 % by weight mineral, essentially carbonated apatite, 1 % organic material, mostly protein, which is not collagen, and 2 % water (Currey, 2002). Most of the mineral crystals are bound together in bundles called prisms or rods. Each rod is 3-6 μm in diameter. There is limited protein within the prisms "glueing" the apatite crystallites together, with more protein located at the interprism boundaries (Currey, 2002). This region is often called the enamel sheath, and also consists of apatite crystals that are inclined to the axis of the rods. Enamel has a truly 3D structure (Macho et al., 2003) starting with a crossed plywood-like form near the interface with dentin (DEJ) and ending up with almost parallel alignment of rods near the outer surface.

In vivo enamel is mainly subjected to a fluidic environment, e.g. saliva. Habelitz and coworkers (Habelitz et al., 2002) used a cube corner indenter tip to study the influence of storage solutions on the local mechanical properties of enamel. In order to maintain the physical properties of dental tissues Habelitz and coworkers (Habelitz et al., 2002) recommended short-term storage of the specimens in Hank's balanced salt solution (HBSS). Thus, in order to test enamel under near *in vivo* conditions, in our experiments the enamel was stored and tested immersed under the above solution (plus an antibacterial agent), and its behaviour compared with the same material in a dry condition.

Instrumented indentation (nanoindentation) is a widely used technique for studying the mechanical response of enamel mainly due to the small amount of material needed and the complexity of preparing samples for conventional mechanical testing. Many indenter tip geometries and testing conditions may be found in the literature (Staines et al., 1981, Ge et al., 2005, Xu et al., 1998, Cuy et al., 2002, Braly et al., 2007). The data is commonly analyzed using

the Oliver & Pharr method (Oliver and Pharr, 1992) in which the geometry of the indenter tip is taken into consideration by the indenter form factor. Analysing the data in this manner (Oliver and Pharr, 1992) assumes implicitly the material behaves in a elastic-perfectly plastic way. Staines et al (Staines et al., 1981) used a spherical indenter for testing enamel under wet (immersed in water) and dry conditions. They reported an increase of 15 % in indentation modulus when going from wet to dry conditions and more substantial viscoelastic behaviour under wet than dry conditions, respectively. Ge et al (Ge et al., 2005) used a Berkovich tip to investigate the local mechanical property variations between prisms and sheaths within an enamel rod. Xu and coworkers (Xu et al., 1998) stored their samples in water but they tested them dry and indicated that enamel showed mechanical property differences regarding prism orientation, when using a Vickers indenter. Cuy et al (Cuy et al., 2002) mapped the cross sectional properties of human enamel using a Berkovich tip. They reported significant differences in hardness and indentation modulus from the DEJ to the outer surface and also depending on the buccal or lingual region tested. On the other hand, in a recent work, Braly et al (Braly et al., 2007) found no influence of prism orientation on the indentation modulus of enamel measured with a Berkovich indenter under atmospheric conditions.

Indentation with different tip geometries is, however, well studied for (macroscopic) hardness measurements in metals and other materials (Hill et al., 1947, Hirst and Howse, 1969, Atkins and Tabor, 1965, Johnson, 1970). In the pioneering work of Hill et al (Hill et al., 1947) a model for a slip-line deformation mechanism associated with sharp wedge indentations in ductile materials was developed. Included in this model for sharp wedges was the occurrence of pile up to accommodate the volume of material displaced by the indenter. Hirst and Howse (Hirst and Howse, 1969) studied the change in deformation mechanism under wedge indenters considering the indenter angle and also the ratio of the elastic modulus to the yield stress Y of the tested material. They identified four different deformation mechanisms depending on the indenter angle and the ratio of E/Y, namely: elastic, expansion of a cylindrical cavity for large angles, plastic rigid and complex elastic-plastic response for the sharper wedges at low E/Y, schematically shown in Fig. 26. This concept developed by Hill was also taken up by Marsh (Marsh, 1964) to explain the indentation response of glasses. Atkins and Tabor (Atkins and Tabor, 1965) studied the dependence of hardness with conical indenter tip angle. They explained the variations found by changes in mechanisms of deformation of strain hardening metals depending on the tip angle of the conical indenter they used. Johnson (Johnson, 1970) proposed an approach to correlate material deformation (not specifically for metallic materials) under blunt like (both pointed and spherical) indenters. For blunter indenters he advocated there is no upward movement of material since the material is mainly compressed, in other words, pile up is not expected. Johnson determined that the product (E/Y) tanΘ was the major determinant of deformation response, where θ is the complement angle of the indenter tip.

In the case of nano-indentation the effect of tip geometry on the determination of the elastic response of enamel when using the well known Oliver-Pharr method (Oliver and Pharr, 1992), has, to the knowledge of the authors, not been questioned. Only He and coworkers (He

et al., 2006) used a Berkovich and two spherical indenters to determine the indentation modulus of human enamel in two orthogonal directions to the prisms. The indentation modulus showed load dependence for both orientations of the enamel rod structure that depended on the indenter shape. They were able to normalize these differences by considering the contact diameter relative to the rod diameter and to rationalise this behaviour because of differences in prism versus sheath contributions to the mechanical response as shown by Ge et al (Ge et al., 2005). In a previous study Guidoni et al (Guidoni et al., 2006) found considerable differences in the hardness and indentation modulus of dentin when tested wet with a conical rounded tip (~400 nm radius) and dry using a cube corner indenter. They found a 1.6 fold difference between the indentation modulus wet versus dry.

Since representative values of elastic properties of enamel may be found in the literature (Ge et al., 2005, Staines et al., 1981, Cuy et al., 2002, He et al., 2006, Habelitz et al., 2002), this paper is not intended to give universal elastic properties of enamel but attempts to understand the different mechanisms active while indenting enamel with different indenter tip geometries. Thus, nanoindentation tests with a sharp cube corner tip (20-50 nm radius) and ultra-micro indentations with a blunter pyramidal tip (45º) and a Berkovich indenters were done on the same local tooth structure and on the same sample under both wet and dry conditions to study the influence of tip geometry and environment on the elastic response of enamel in a endeavour to exclude any inter-sample scatter.

3.3. Materials

For the investigation reported here one incisor of a 1.5 year old steer was used. The sample was cut with a diamond saw in two sections along the crown-root direction, carefully avoiding any overheating. One half of the incisor was immediately immersed in Hank's balanced salt solution (HBSS) plus 0.001 wt % NaN_3 as an antibacterial to prevent sample degradation ("wet"). The other part was dehydrated in air ("dry").

For nanoindenter testing and handling purposes, the pieces were glued to a plastic stub with cyanoacrylate glue. In all cases, the transversal section of the incisor consisting of enamel and dentin was accessible for preparation. The exposed area was ground and polished to a 2500 P grit finish with silicon carbide cloths, followed by polishing in 0.3 µm alumina suspension. The 'wet' sample was permanently rinsed with HBSS while polishing, and stored under HBSS at all times to avoid accidental dehydration. This is essential especially in the last stages of preparation.

All the samples were again polished with 0.3 µm alumina suspension and thoroughly cleaned with HBSS plus antibacterial a short time before testing to avoid any possible superficial film formation. For the case of the dry samples, a period longer than 12 hours in air was allowed for stabilization.

After the tests, the "dry" sample was further dehydrated in a vacuum chamber at ~10^{-6} mbar, then coated with a few nanometer thick layer of carbon for Scanning Electron Microscopy (SEM) viewing. This sample was then once more tested under atmospheric laboratory

conditions ("vacuum dry") and these imprints imaged with the SEM in order to detect possible cracking and to check positioning.

3.4. Nanoindentation tests

All nanoindentation tests were carried out in several loading-unloading steps. Since different devices were used, details of the load, hold and unload times or rates are given for the individual cases. The maximum force was chosen in each case to achieve similar indentation depths. Typically 8 measurements per condition were taken. All tests were made in a region approximately 500 microns from the dentine-enamel junction and the area of placement of the tests in the different environments overlapped.

Thermal drift was corrected by measuring the indenter drift for a maximum of 25 s before the start of every indent, taking the drift during the last 5 s and applying this correction to the measured data, for the Triboscope measurements. For the case of the UMIS measurements, the tests were only commenced when the thermal drift was lower than 0.1 nm/s.

Two configurations for indentations were used: 'dry', in which the samples were indented under atmospheric conditions, and, 'wet', in which the sample and indenter were immersed in HBSS during testing, in which case the indenter was mounted at the end of a tungsten rod ca. 9.5 mm long in order to maintain the transducer at a safe distance from the fluid.

3.4.1. Sharp cube corner tip

The nanoindentations were carried out using an add-on nanoindentation device (Hysitron Triboscope, Hysitron Inc., Minneapolis, MN, USA) mounted on the scanner head of an AFM stage (Veeco – Digital Instruments, Santa Barbara, CA, USA).

Load ramping data were: Open loop load control, loading rate of 1mN/sec to a maximum of 5 mN, holding maximum load for 60 seconds, unloading at a constant rate of 0.4 mN/sec to the second holding period at 1 mN for 20 seconds, then unloading to zero within 2 seconds. Before making an indent the indenter was used to scan the sample at imaging loads (2-4 μN) in order to choose suitable areas for indenting. In spite of the disadvantages of open loop measurements, this setup was chosen since double trapezoidal loading ramps can not be done with the closed loop control of the Hysitron system.

Afterward the atmospherically dry sample was vacuum dehydrated as described above and tested again under atmospheric conditions with the cube corner (35.26º). Finally, after indenting the vacuum dry samples, images of the residual imprints were taken with the nanoindenter tip.

3.4.2. Berkovich and 45° pyramidal indenter tips

The indentations were made using an Ultra Micro-Indentation System (UMIS-2000, CSIRO, Australia).

For the 45º pyramidal indenter tip the load ramping data were: Closed loop load control, load with constant rate to a maximum of 5 mN within 70 seconds, hold for 60 seconds, unload with constant rate to the second hold at 500 μN within 50 seconds, hold for 20 seconds, unload to zero within 2 seconds. For the Berkovich indenter a maximum load of 30 mN reached in 116 s was used in order to generate similar indentation depths and the sample was partially unloaded to 3 mN in 90 s prior to holding for 20 seconds and then rapidly unloading. The effects of the different loading and unloading rates chosen were corrected by explicitly incorporating viscoelastic effects in the analysis, see below.

3.4.3. Further details

The area functions for each of the three indenters used were calibrated with a fused quartz sample. Since the penetration depths during calibration are small due to the nature of the standard sample (fused quartz), the form of the area function was chosen to converge to the ideal area of the indenter at higher penetration depths (Fischer-Cripps, 2004). The types of indenters here used are made with 0.05º precision according to the manufacturers.

Indentation tests were also performed on the fused silica sample submerged in aqueous solution and results for hardness and indentation modulus were within the standard deviation of the calibration tests.

Since Poisson´s ratio of the material is not known (He et al. (He et al., 2006) used 0.33, Cuy et al (Cuy et al., 2002) chose 0.25, Ge et al. (Ge et al., 2005) mentioned a range from 0 to 0.5, but did not specify which value they used, if any) and the material is anisotropic, the values are given as the reduced indentation modulus, E_r (Oliver and Pharr, 1992).

3.5. SEM Observations

After the indents were done on the vacuum dry samples, images where taken with the Ultra high resolution SEM facility of a LEO XB 1540 Crossbeam FIB-Workstation. An acceleration voltage of 10-20 kV was used. The working distance was approx 5 mm. Secondary and backscattered electron images were simultaneously taken of the imaged area.

3.6. Results

The load-displacement data achieved from a number of indents under the same condition and indenter geometry were very similar. Thus, they were averaged and plotted as single curves, as shown in Fig. 27.

3.6.1. Sharp cube corner tip

P - h curves for the three dehydrated conditions are plotted in Fig. 28. The vacuum dry sample curve shows initially less penetration but has a marked pop in event at ~ 1mN during loading and then continues more or less smoothly until complete unloading, with the post pop-in displacement lying between the wet and dry tests. In the case of normal dry tests, the loading data show some minor discontinuities during the loading curves. The loading curve of the wet

tests initially overlaps the dry tests until approx. 1 mN where upon it diverges and shows further multiple small step-like increments in penetration depth at specific loads during loading. There were more steps evident for the wet measurements than the dry ones.

During the hold period at maximum load for the wet test the indenter continued to penetrate for approximately another 100 nm whereas for the dry tests this was only 30 nm. In the case of the vacuum dry tests the extent of creep at maximum load was 20 nm.

The average reduced elastic modulus (E) together with standard deviation is 31 ± 4 GPa and 74 ± 7 GPa, for the wet and atmospherically dry conditions respectively. These results indicate a factor of ~ 2.4 in indentation modulus, between both conditions respectively. For the case of the vacuum dry test, the reduced elastic modulus was 70 ± 10 GPa.

The extent of recovery during the 20 s of the second hold period in the case of wet condition was ~ 20 nm while for the case of the laboratory dry condition and same indenter tip it was ~2 nm.

In the case of the vacuum dry tests a scan was done in the AFM mode with the nanoindenter tip immediately after the indentation was done. This image plus the resultant surface profile are shown in Figs. 4a, b and c.

3.6.2. 45° Pyramidal indenter tip

At maximum load for the wet test the indenter continues to penetrate for approximately another 40 nm whereas for the dry test this was only 20 nm. There were no pop in events observed. During the second hold period, the measured recovery displacement was ~ 5 nm for the wet and ~2 nm for the dry condition (see Fig. 27).

The reduced elastic modulus was 63 ± 2 GPa and 56 ± 6 GPa, for the dry and wet tests, respectively. These results indicate a factor of ~ 1.12 in indentation modulus, between atmospherically dry and wet test conditions respectively.

3.6.3. Berkovich indenter

There is no large difference in the creep displacement at maximum load between the wet (30 nm) and dry (20 nm) test conditions. For the case of the second hold period, recovery was ~ 4 nm and ~ 2 nm, wet and dry, respectively. The loading curves for both conditions are almost identical, as is the contact stiffness (see Fig. 27).

The reduced elastic modulus was 56 ± 2 GPa and 54 ± 3 GPa, for the dry and wet tests, respectively. These results indicate a factor of ~ 1.04, for the ratio of the indentation modulus, between atmospherically dry and wet conditions respectively.

The various parameters derived from the force-displacement curves using the Oliver and Pharr approach (Oliver and Pharr, 1992) are listed in table 1.

As seen from the above obtained indentation moduli, the standard deviation of the results lies within 10 % of the average value. Therefore, the average curves showed in Fig. 27

were used as master curves for the corrections proposed in the Discussion section. As a result, the re-calculated values are presented as average values.

3.7. Discussion

Depending on the tip geometry, differences in elastic response between wet and dry conditions are observed when the data is analyzed following the standard Oliver and Pharr approach. The factor of ~ 2.4 in indentation modulus found between atmospherically dry and wet conditions in the case of a sharp cube corner tip appears to be very large, given the very high degree of mineralization of enamel. It is also considered that the elastic modulus of the mineral apatite component, which is typically greater than 95vol% in enamel, is unaffected by the presence of surface moisture.

Habelitz et al (Habelitz et al., 2002) reported a similar factor of two in the indentation modulus between the enamel samples stored in Hank´s solution compared with tests of mechanically polished specimens stored in water and $CaCl_2$ solution. They attributed this difference to demineralisation of the surface of enamel when not stored in Hank's solution. On the other hand, previous studies of wet versus dry enamel by He et al (He et al., 2006), and Poolthong et al (Poolthong et al., 2001, Poolthong, 2000), using blunter Berkovich indenters, did not observe large differences in the force-displacement curves between both conditions and Staines et al (Staines et al., 1981) reported only a 15 % increase of indentation modulus of human enamel between wet (water) and dry conditions when using a large 6.35 mm diameter tungsten carbide spherical indenter.

In order to understand the origin of the different results depending on the geometry of the indenter tip used, viscoelastic effects together with pile up and micro-damage are discussed. Their influences are considered after incorporating analysis methods to evaluate their significance.

3.7.1. Corrections

3.7.1.1. Creep

In the present work, even though the viscoelastic component in enamel is low, viscoelastic responses were observed, as Staines and coworkers also reported (Staines et al., 1981). Viscoelastic creep as well as recovery during the second hold period is more significant for the wet samples and the effect is more pronounced as the tip angle is reduced.

Zhou and Hsiung (Zhou and Hsiung, 2006a) investigated the indentation modulus of dry enamel and conducted tests at different strain rates using a Berkovich indenter. They reported that the indentation modulus not only is a function of penetration depth, similar to that reported by He et al (He et al., 2006), but also that it is strain rate sensitive, increasing from ~80 GPa to 100 GPa with a change in strain rate from 0.0005 to 0.05 s^{-1}. These authors argued on the basis of a relationship developed by Gao and coworkers (Gao et al., 2003) that the elastic modulus of the protein is strain rate dependent and that this explains the difference observed. Rho and Pharr (Rho and Pharr, 1999) studied the effects of drying of bone on the nanoindentation

response with a Berkovich tip. They used a multiple loading scheme to examine the extent to which the load-displacement data were influenced by viscoelastic deformation. They loaded and unloaded the sample three times. For the last loading step they kept the load at maximum load during 120 s and then unloaded to 10 % of maximum load for 300 s prior to the final unloading. They observed that viscoelastic recovery is significant during the initial portion of the latter hold period and viscoelastic deformation is also apparent in the creep displacements observed during the constant load hold period at peak load. However no allowance was made for this behaviour and they treated their data with the standard Oliver-Pharr method (Oliver and Pharr, 1992).

The effect of creep predominates at high loads and recovery at lower ones. Both influence the slope of the unloading curve especially for the case of wet samples. Ngan et al (Ngan et al., 2005) investigated the role of creep at maximum load on the resultant initial unloading slope of visco-elastic materials. They proposed that the elastic stiffness at the onset of unloading, S_e, should be corrected by including the creep rate just prior to unloading, using for a linear viscoelastic material with a Maxwell spring-dashpot model.

In the present work, the creep data (first holding period) was best fitted with a function of the type:

$$h = a - b \times c^t \qquad \text{Eq. 22}$$

where *a*, *b* and *c* are fitting parameters (c<1) and *h* and *t* are the measured penetration depth and the time, respectively (R^2 > 0.9 in all cases). Based upon the above correction the indentation modulus including creep is 31 GPa for the wet tests using the cube corner tip and 74 GPa for its corresponding dry condition. The corresponding elastic moduli for the 45º pyramidal tip considering viscoelastic creep were 51 GPa and 56 GPa for the wet and dry conditions, respectively. The similarly corrected elastic moduli for the Berkovich tip are 61 GPa and 58 GPa for the wet and dry tests. Thus it appears as if the 60 s hold period at maximum load was enough to exhaust most of the creep thereby minimizing its influence.

3.7.1.2. Recovery

The smaller recovery depths registered with the 45º and Berkovich indenters are a consequence of the longer unloading period for these two indenters than for the sharp cube corner tip. A negligible amount of recovery was also observed for the case of dry conditions. Since the recovery depths for these cases lie within the noise level of the devices used, the correction proposed below was only carried out for the case of cube corner indenter and the wet sample.

To our knowledge there does not appear to be an approach to incorporate the recovery during unloading on the resultant slope of the unloading curve. An approach to consider this effect for a sample that has almost exhausted its creep behaviour at the maximum load hold period is as follows. If during unloading the plastically deformed material were to behave totally elastically, then its unloading response would be independent of the unloading rate and the contact stiffness at maximum load a constant. Thus, if the recovery response during the second

hold period is extrapolated to the time when the unloading started, an estimation of how much recovery occurred during the unloading time is obtained. The recovery data was plotted as a depth vs time plot. The recovery behaviour follows an exponential decay response. The data was fitted to a first order exponential function and all the data points of the second hold period were considered in the fitting. This function was then extrapolated until the time when the unloading started, and the corresponding penetration depth, $h_{recovery}$, at that point was recorded. The last penetration point at maximum load and this new extrapolated penetration depth at the second hold load are fitted by Eq. 14, assuming a parabolic behaviour (Sneddon, 1965) . A schematic illustration of this procedure is shown in Fig. 30 and Fig. 31. $S_{recovery}$ was then calculated by deriving the latter unloading function at the maximum penetration depth. This procedure is equivalent to an extrapolation to infinite unloading rate yielding the instantaneous indentation modulus.

Thus, for the corrected cases (wet condition and sharp corner cube indenter tip), the new penetration depths at the second hold period calculated considering recovery effects were ~ 20 nm higher than the original ones, generating a 12 % increase in the corrected indentation modulus.

3.7.1.3. Viscoelastic creep and recovery

Visco-elastic creep and recovery were combined to calculate an indentation modulus taking into account both effects. The slope obtained with the recovery approach, $S_{recovery}$, was used in Ngan' creep correction (Ngan et al., 2005) as S. A new penetration depth and area of contact were calculated following Oliver and Pharr equations (Oliver and Pharr, 1992), but using the new corrected stiffness, $S_{recovery\&creep}$. The new indentation moduli considering both viscoelastic effects was 34 GPa for the wet tests and cube corner tip. The difference between the latter and the dry condition is still very high.

3.7.1.4. Pile up

It is important at this point that we consider the basis whereby the current results and all previous results for the properties of enamel are generated. The basic relationships were derived by Oliver and Pharr (Oliver and Pharr, 1992) assuming the indented material behaves as an elastic perfectly plastic material. In this instance the displacement of the contact surface below the reference surface is determined by the relationship developed by Sneddon (Sneddon, 1965) and is approximately 25% of that for a flat punch. If we consider the vacuum dry specimen indented with the cube corner indenter then the AFM scanned image of the surface in Fig. 29 shows that pile-up occurs around the impression. In other words the material does not behave as predicted by the Sneddon analysis (Sneddon, 1965) upon which the Oliver and Pharr (Oliver and Pharr, 1992) interpretation is derived and the contact area is much greater than that expected for an elastic-plastic solid.

Ge and coworkers (Ge et al., 2005) also reported the appearance of pile up while testing the prisms and sheaths of sound enamel. However, their treatment of the data followed

the classical Oliver and Pharr method. They found a 74 % difference in indentation modulus between prism and sheaths.

Pile up is predicted to occur as the indenter angle is reduced according to the indentation models found in the literature irrespective of material types (Hill et al., 1947, Johnson, 1970, Hirst and Howse, 1969, Atkins and Tabor, 1965).

Even though Fig. 26 was derived for a wedge indenter and ductile materials and hence has its limitations describing the present system, it appears that a change in deformation mechanism occurs between Berkovich and blunter 45º indenter tips and the sharp cube corner indenter tips.

The deformation mechanism corresponding to the Berkovich and blunter 45º indenters may be described by Johnson model (Johnson, 1970). That is, a hydrostatic core is attached to the indenter and is surrounded by an elastic-plastic region in which the deformation is radially symmetric. There is no upward movement of material since the material is mainly compressed. Pile up is expected to be insignificant both for the wet and dry tests. Thus, the projected area A is likely to be the same for both test conditions.

For sharper indenter angles, the response resembles that predicted by Hill et al (Hill et al., 1947) of the deformation produced by a rigid frictionless wedge (2D) penetrating a plastic material. In this model the material can escape toward the free surface and create a lip, thus the effect of elastic compressibility of the surrounding material in absorbing the displaced volume is small. It is then assumed that the volume of material above the original plane surface is equal to the volume of the impression below the surface. Based upon these geometrical and boundary conditions it is possible to estimate the height of the pile up as a function of penetration depth and angle of the indenter.

The 2D approximation for a wedge indenter generates a ~3 fold volume overestimation of pile up when generating a cone by rotating the area around the longitudinal axis in relation to the displaced volume by the indenter. Thus, an experimental approach was carried out in order to consider pile up effects for the dry samples and sharp cube corner indenter, as follows.

The plastic area was determined after examining the corresponding 3D plot of Fig. 29 and finding the point of inflection from the pile up to the flat surface. The radius of the plastic area around the imprint was measured by plotting circles and recording the corresponding radius. The measured contact area obtained from the load-displacement curves using the calibrated area function was approximated by a circular shape and its radius obtained from $\pi a^2 = A(h_{max})$. The ratio β between the radius of the plastic zone and the radius of the contact area is $\sim$ 2. The height of pile up needed to accommodate the same volume of material displaced by a conical indenter with an equivalent cone angle that provides the same contact area to depth relationship as the actual sharp cube corner indenter was calculated considering that the volume of material above the original plane surface is equal to the volume of the impression below the surface. That leads to

$$d\left[(\beta a)^2 - (a - d\tan(\alpha))^2\right] + d\left[(a + d\tan(\alpha))^2 - a^2\right] = \frac{2}{3}a^2 h \qquad \text{Eq. 23}$$

where *d* is the height of pile up, β is the plastic zone ratio, *a* is the contact radius, α is the indenter included (half effective cone) angle and *h* is the penetration depth at maximum load. A scaled cross-section through the calculated pile-up is shown in Fig. 32, together with the variables used for the calculation.

Thus, the corresponding height of pile up for Fig. 29 was 156 nm. The latter height is in good agreement with Fig. 29. That is, the above calculation provides an upper limit for the estimation of pile up, since the free surfaces of the pile up were taken as straight lines rather than convex profiles. The contact depth associated with such pile-up is 23 % higher than the contact depth obtained by the classical Oliver and Pharr analysis. As a first approach, a new contact depth is calculated using 1.23 h_{max} instead of h_{max} in $h_c = h_{max} - \varepsilon \frac{P_{max}}{S}$ (Oliver and Pharr, 1992). Its corresponding contact area is calculated and the resulting indentation modulus of the vacuum dry tests of Fig. 29 would be 61 GPa rather than 77 GPa without this correction. If the same plastic zone size ratio is assumed for the other, atmospherically dry tests, a value of 60 GPa for the indentation modulus is obtained for this condition and indenter tip. This estimation does not consider anisotropy effects and friction between indenter and indented material and it is limited by the lateral resolution of the scanning indenter tip used to generate the image shown in Fig. 29. Furthermore, the image of the indent was taken after complete unloading, and therefore cannot show the actual pile-up at maximum load. Since the amount of recovery of dry enamel has been shown to be small, this presumably introduces only a small error.

After all these three corrections (where appropriate), it can be seen that with all the indenters the dry values for indentation modulus fall in the range between 55 and 60 GPa. In the case of the Berkovich and blunter 45º pyramid the differences between wet and dry conditions were 6 and 8 %, respectively, whereas the sharp cube corner result under wet condition was far less, 34 GPa. The initial factor of 2.4 between wet and dry conditions and cube corner indenter was reduced to 1.7 after considering viscoelastic effects and deformation mechanisms. However, the indentation modulus measured with the cube corner and wet sample remains still very low.

It is worth to point out that the differences found with the cube corner could not be a result of the different loading rates when compared with the Berkovich and blunter 45º indenter rates, since in the former case the loading rate was faster than in the latter case. If the differences were due to viscoelastic effects they should be more evident at low loading rates. In addition, it may be shown very simply that the radius of contact of the Berkovich indenter under the conditions here tested is 3 and 2 times larger than that for the dry and wet measurements done with the cube corner. Therefore, the Berkovich measurements should be more susceptible to the influence of the more viscoelastic enamel interfaces (Ge et al., 2005) than the cube corner ones.

The indentations with the cube corner indenter were repeated under the same conditions on a human enamel sample (Guidoni (PhD thesis 2008)). These observations were very similar to similar tests on human enamel tested under wet and dry environments with the cube corner where the E modulus values were 30.7 ± 2.1 and 60.5 ± 7.3, respectively.

3.7.2. The sharp cube corner indenter: Cracking and micro-damage

Due to the small tip radius of the sharp cube corner indenter (20-50 nm) and smaller apical angle the consequent stress concentration, this indenter is presumably able to generate a different type of deformation to the material than the other indenters, namely wedging and splitting instead of compression.

Vacuum-dry sample: The loading curve in this state starts with a distinctly steeper gradient than in the two other states (Fig. 28) but shows a massive pop-in around 1 mN, followed by some minor pop-ins up to maximum load. In view of the SEM picture shown in Fig. 33 we interpret this pop-in as being connected with the formation of a major median radial crack (Schneider et al., 2005, Field et al., 2003), followed by some minor cracks not detected. This is the typical indentation behaviour of a very brittle material and agrees with the observation that totally dehydrated protein is indeed very brittle (Ntim et al., 2006, Vincent, 1990). The indentation modulus derived from the unloading curve, applying all the corrections outlined above, is 61 GPa. In order to check the influence of the cracking, the vacuum dry condition was again measured at indentation loads of 0.7 and 0.8 mN corresponding to indentation depths of 120 and 140 nm, respectively. There were no pop in events observed in this new loading condition. But the indentation modulus of these latter tests following the above corrections were 59 ± 2 GPa. Thus, the indentation modulus of dry enamel with and without large cracks is practically the same. This latter observation suggests that micro-damage may precede the appearance of cracks large enough to cause observable pop-ins and be observable, e.g., by SEM. In addition, it also suggests that in the case of the dry tests, the elastic constraint of the surrounded material partially restores the original compliance of the structure since, due to the higher yield stress, the plastic zone under the indenter is small and therefore there is a major elastic constraint of the surrounding area, causing presumably more pile up than in the case of wet conditions.

Laboratory dry tests: The loading curve in this state starts with a shallower gradient, almost identical to the one in the wet state, and shows no discernible pop-ins. Also, the elastic stiffness at the beginning of unloading and, therefore, the indentation modulus, were the same as “vacuum dry”.

Wet sample: The loading curve in this state starts almost parallel to the dry state, but starts deviating at about 1 mN, showing a series of well-developed pop-ins in addition to being more ductile generally. Those results could be interpreted as the gradual development of a much larger deformed volume, leading to a distributed “pile-up” located away from the indented

area. In addition, the high tensile strains generated by a sharp cube corner indenter ahead of the indenter tip combined with the plasticizing effect of the water on the strained protein layers between the apatite (He and Swain, 2007a) may lead to a spread-out of (micro) damage causing the series of small pop-in events. Since elastic stress fields associated with contact loading tend to be long-range, this distributed damage presumably does influence the indentation modulus more profoundly than the strictly localized damage observed in the dry state, thus explaining the lower indentation modulus unique to the sharp cube corner used on a wet sample. The fact that no damage could be detected in this case may be either due to the small size of these micro-cracks, most likely within the very thin protein layer between the individual nano-apatite crystallites and to the recovery mechanisms favoured under fluid.

3.8. Conclusions

The straightforward use of the well know Oliver and Pharr method for measuring indentation modulus of a visco-elastic biological tissue such as enamel has some limitations, especially when testing samples with a sharp cube corner indenter tip under wet and dry conditions.

The hold time used, 60 seconds in the case of enamel, appears to be sufficient for the creep to be exhausted, thus necessitating only minor corrections for visco-elastic effects. However, recovery during the unloading period may introduce significant errors, depending on the hydration state of the sample and the unloading rate, if not considered.

Pile-up – exclusively observed when using the sharp cube corner indenter – can introduce large errors. Unfortunately a quantitatively correct evaluation of the increment in projected area brought about by a pile-up is hampered by its complex geometric shape and the uncertainty with respect to its real load-bearing surface.

After correcting viscoelastic effects and pile up, the indentation modulus of dry enamel close to the dentine-enamel junction measured with any of the three indenter types used lies consistently between 55 and 60 GPa and the differences between dry and wet are about 6 – 8 % for the blunter indenters, which agrees with the very high degree of mineralization in enamel.

In spite of all the above corrections the indentation modulus of wet enamel measured with a sharp cube corner remains low. This leads to the assumption of a change in the deformation mechanism associated with the stress concentration under a sharp wedging nature of such a indenter tip.

The use of an ultra-sharp indenter for investigating inhomogeneous, nano-structured materials seems to be limited by its tendency towards splitting the material. The details of this mode of deformation as well as possible relationships between indenter tip radius and structure dimensions need further investigation.

3.9. Acknowledgements

Financial aid through EC Contract No MEST-CT-2004-504465, „Marie Curie Host Fellowships for Early Stage Research Training" and Austrian Academy of Science, are gratefully

acknowledged. ARC grant and Australian Dental Research foundation grant are also acknowledged.

FIGURES OF CHAPTER 3

Fig. 26

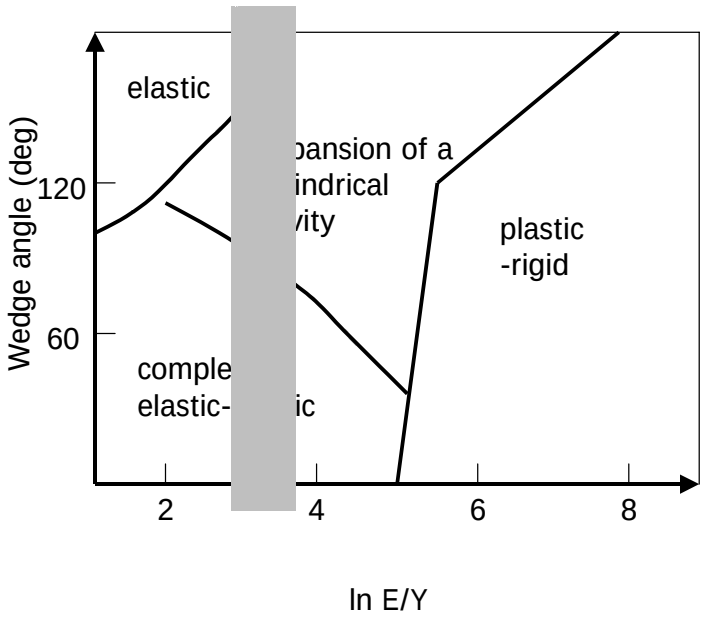

Fig. 26 Region of operation of the different indentation mechanisms according to Hirst and coworkers (Hirst and Howse, 1969), schematically redrawn. The grey area shows where the mechanical properties of enamel lie.

Fig. 27

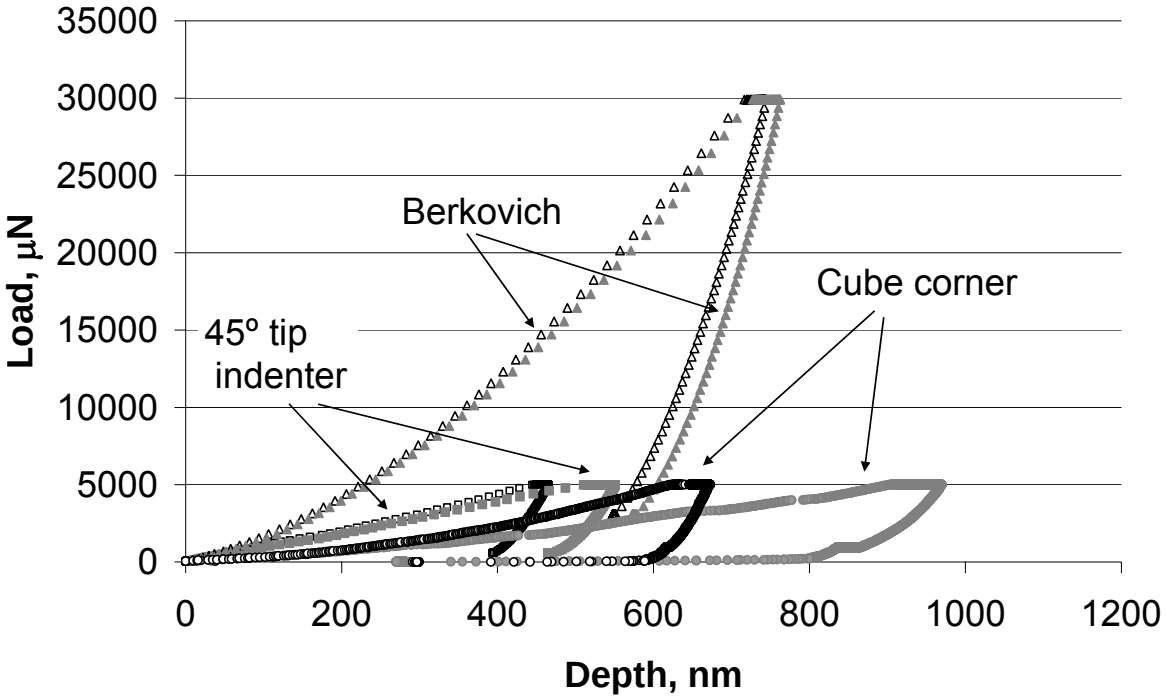

Fig. 27 Averaged load-displacement curves of bovine enamel for the dry and wet conditions for the three indenters used. The open black symbols correspond to the dry conditions and the filled grey ones to the wet measurements. Note the progressive dissimilarity among wet and dry conditions as the tip angle decreases.

Fig. 28

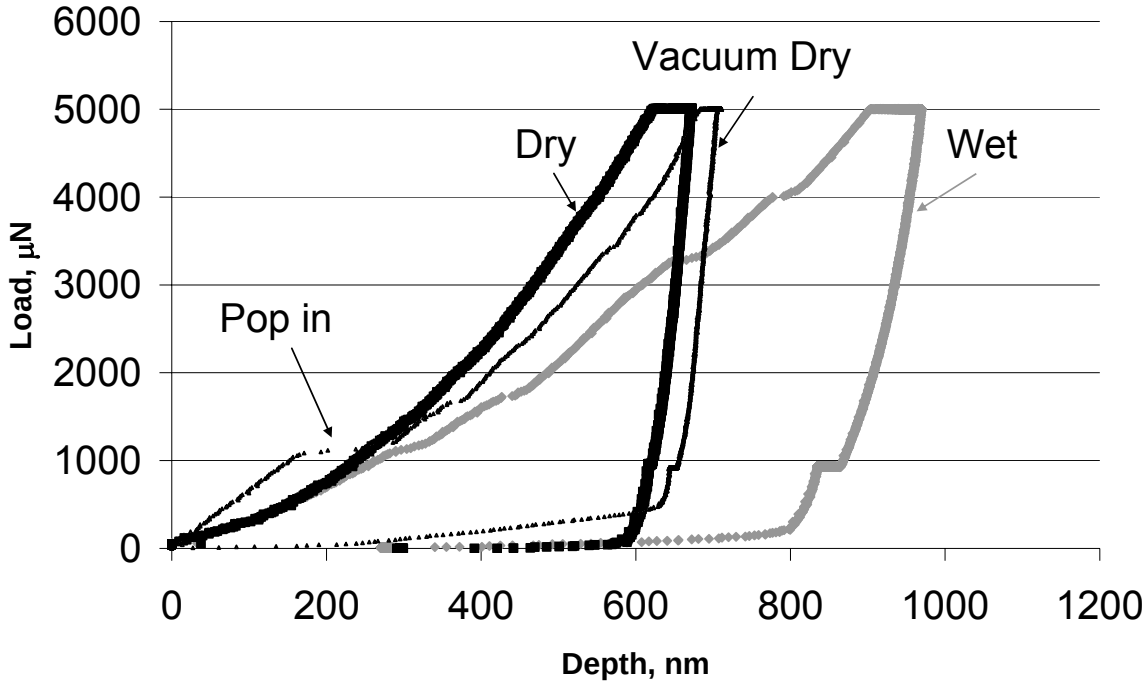

Fig. 28 Averaged load-displacement curves of bovine enamel for the three tested conditions with the cube corner tip. The grey filled diamond symbols correspond to the wet condition, the open black squares correspond to the dry condition and the black continuous line to the vacuum dry condition. The indents were placed in the transversal area of the incisor (perpendicularly to the main direction of the prisms). The prominent pop in event of the vacuum dry sample is indicated in the figure.

Fig. 29

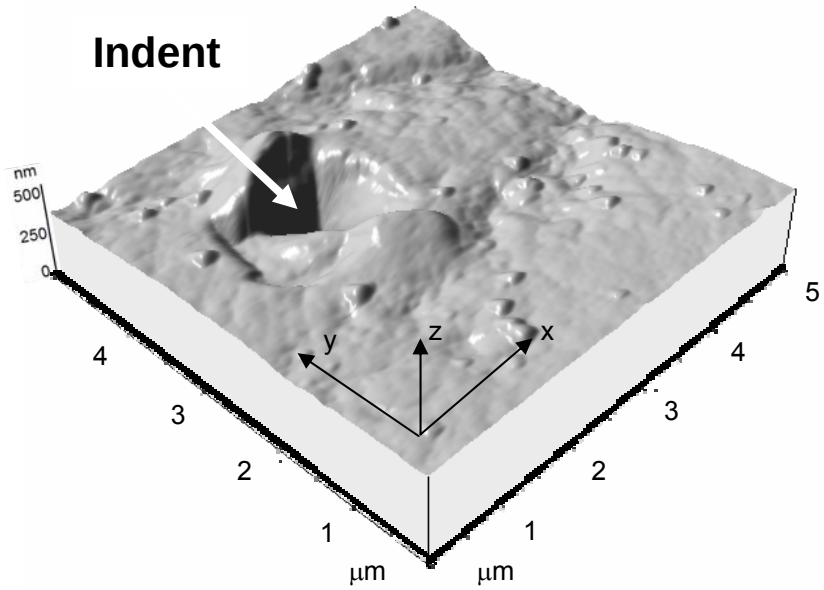

Fig. 29 3D simulation of an indentation done on a vacuum dry sample. It was obtained by scanning the nanoindenter tip on the indented area immediately after the test was done. By rotation and examination of this plot, the plastic zone was delimited.

Fig. 30

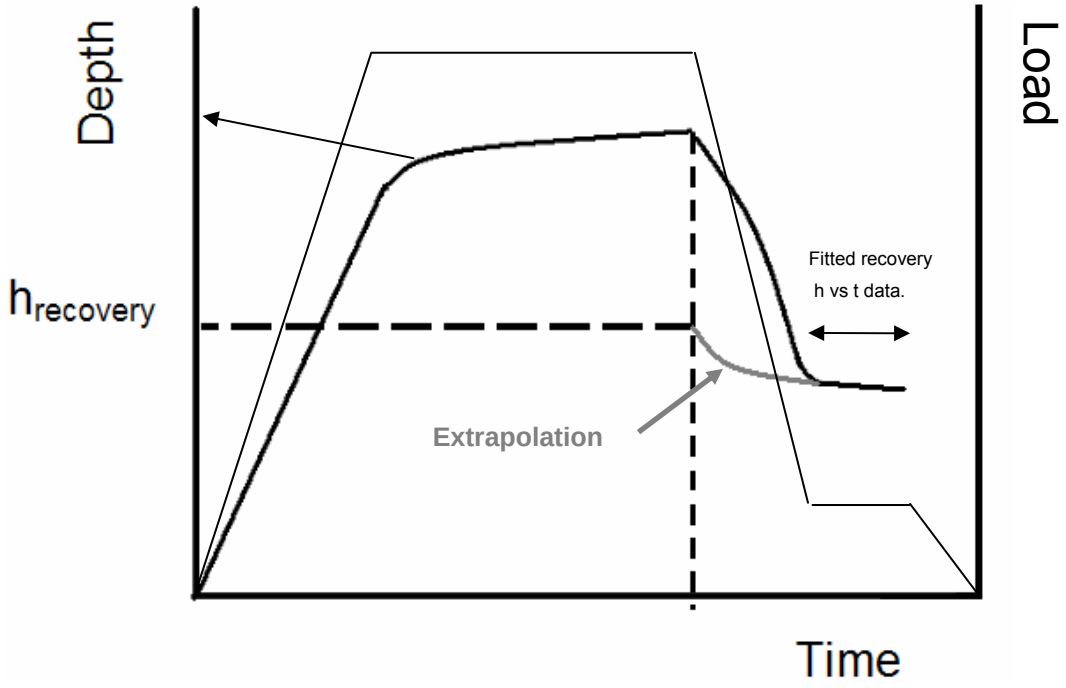

Fig. 30 Schematic of penetration depth, on the left axis, and load, on the right axis, vs. time curve. The first section of the second holding period was fitted with a first order exponential function and extrapolated to the time when the unloading started (gray plot). The $h_{recovery}$ is then the penetration depth the material would have in case of an instantaneous unloading.

Fig. 31

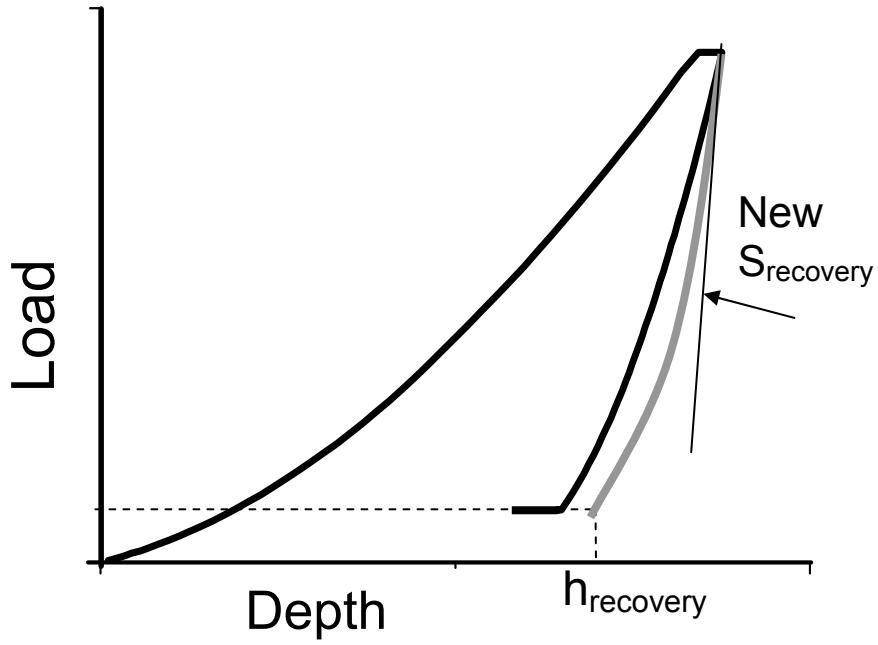

Fig. 31 Schematic of the modification of the load-displacement curve by the consideration of recovery. The unloading curve was re-fitted considering the new displacement at the second hold period calculated by the extrapolation of the exponential recovery curve shown in Fig. 30¡Error! No se encuentra el origen de la referencia..

Fig. 32

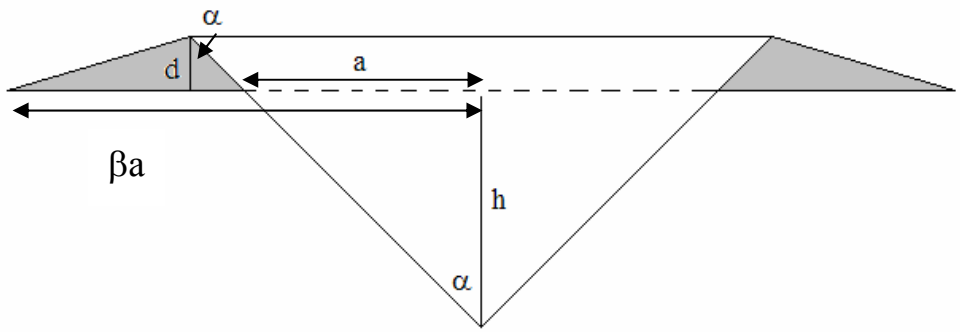

Fig. 32 2D projection of the system used to calculate the amount of pile up for a conical indenter. The parameters *a* and *h* are obtained using the contact area at maximum load and the maximum penetration depth. The ratio of plastic zone radius, β, was obtained from ¡Error! No se encuentra el origen de la referencia.**. α is the effective cone half angle.**

Fig. 33

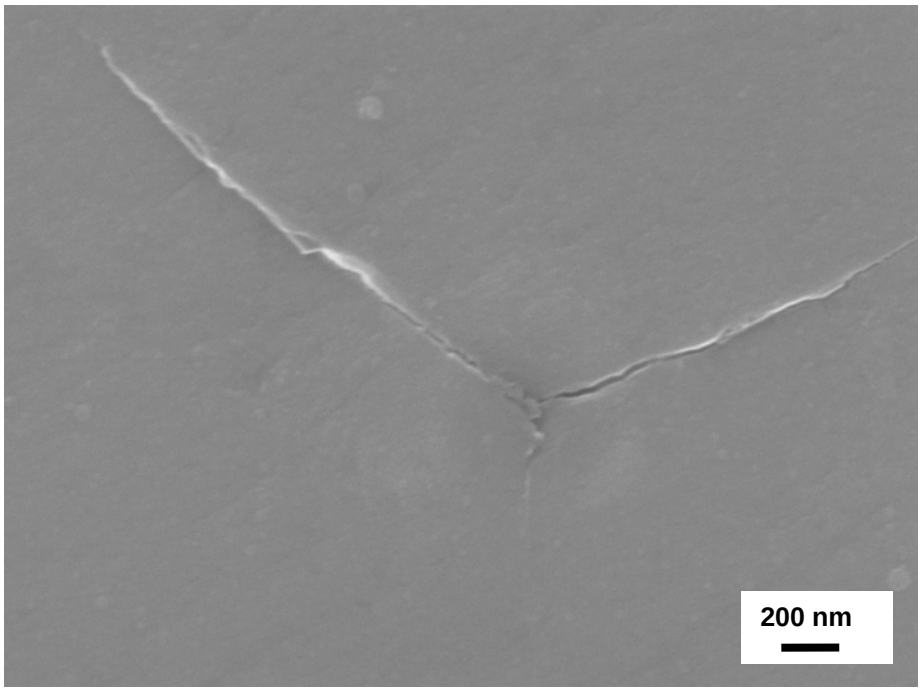

Fig. 33 Scanning electron micrograph of an imprint made on a vacuum dry sample. Radial cracks are shown emerging from the corners of the indentation.

TABLES OF CHAPTER 3

Table 2

	hc(nm)	S(μN/nm)	A(nm^2)	m
WET	908.38	58.13	2605680.71	2.55
Normal Dry	635.56	97.65	1384082.05	2.07
Vacuum Dry	684.81	100.27	1595670.19	1.85

Table 2 Averaged contact penetration depth (h_c), contact stiffness (S) contact area (A) and unloading slope exponent (m) used for the calculation of reduced elastic modulus, E_r, according to the Oliver-Pharr method, for the three tested conditions using the sharp cube corner tip.

CHAPTER 4

4. WEAR BEHAVIOUR OF ENAMEL AT THE NANO SCALE WITH A SHARP AND BLUNT INDENTER TIP

◆ ***Griselda GUIDONI, M. Swain and I. Jäger.*** *"Wear behaviour of enamel at the nano scale with a sharp and blunt indenter tip".* **Wear (2007) *Submitted*.**

4.1. Abstract

Two different diamond nanoindenter tips, a rounded conical (~ 400 nm radius) and a sharp cube corner (20-50 nm radius) were used to abrade bovine enamel. Square abraded areas (2 x 2 μm^2, 5 x 5 μm^2, 10 x 10 μm^2) were generated with loads that varied from 50 μN to 500 μN depending on the indenter tip. In addition normal and lateral forces were simultaneously measured along 10 μm single scratched lines with the sharp cube corner tip. SEM (Scanning electron microscopy) and TEM (Transmission electron microscopy) were also used to characterise the worn areas and debris. Two different wear mechanisms were observed depending on the geometry of the tip. The rounded tip generates a predominantly elastic contact that mainly compresses and plastically deforms the superficial material and generates severe shear deformation on the sub-surface material which, under certain conditions, fractures and removes material from the sample. The sharp tip cuts into and ploughs the enamel creating a wedge or ridge of material ahead of itself which eventually detaches. This sequence is repeated continuously for every passage of the sharp indenter tip. The different mechanisms are discussed in terms of abrading tip contact angle and enamel microstructure.

Key words: Attack angle, indentation strain-stress, abrasion, enamel.

4.2. Introduction

Wear of teeth, either during natural function or artificial testing regimes, is very complex. Besides normal loads, enamel (the outer and visible part of sound teeth) bears shear forces because of the sliding contact with opposing teeth, external objects during mastication and even the abrasive particles within toothpaste. Fernandes et al. (Fernandes et al., 2003) measured for three human females and three males of 57–72 years, bite forces from 60 N (in the central incisor region) to more than 120 N (bilaterally in the premolar regions). In general, enamel must sustain these contact events without failure and retain its shape while doing so. Unlike other calcified human structures, fracture of dental tissue is not self-repairing. One of the most important features of enamel is its good wear resistance, even under severe environmental conditions, such as: wide ranging loads, reciprocating grinding-like movements, temperature changes and acidic attacks.

The tribological response of human teeth depends strongly on:

- both microstructural orientation and location inside the same tooth (Zheng et al., 2003),
- environment: measurements under dry vs. artificial saliva conditions showed differences explained by the cooling and lubricant effect during wear process of the latter (Li and Zhou, 2002). In addition, fluid composition also plays a role, i.e. carbonated acidic drinks, which contain calcium and phosphate exhibit a lower enamel erosive potential than the same drinks without calcium and phosphate (Jandt, 2006, West et al., 1999),

- anatomic position in the dental arch (i.e. canines showed more wear than molar and premolars under similar testing conditions) (Pintado et al., 1997),
- pathology (i.e. bruxism) (Pintado et al., 1997) and
- several other physical and microstructural factors (Oh et al., 2002) and also ethnological ones (Dahl et al., 1993).

If not controlled, tooth wear results in poor masticatory function with a concomitant reduction in quality of life and possible deterioration of systemic health. Thus, understanding friction and wear behaviour of enamel would help the clinical treatment for teeth and may assist with the development of new dental restorative materials (Magne et al., 1999 , Li and Zhou, 2002, Kelly et al., 1996, Dahl et al., 1993).

Enamel is the highest mineralized tissue in the human body. It is composed of approximately 97 % by weight of mineral, essentially non stoechiometric hydroxyapatite (HAp), 1 % organic material, mostly protein, which is not collagen, and 2 % water (Currey, 2002). As with most biological materials, it has a hierarchical microstructure, which imparts order from the nm to mm scale.

Crystallites of enamel are roughly rectangular in cross section with mean width of 45 nm and mean thickness of 25 nm (Selvig and Halse, 1972), and are “glued” together by a thin protein layer of not more than 2 nm (Selvig and Halse (Selvig and Halse, 1972) reported a 1-2.5 nm electron translucent space between the crystals of completely mineralized rat incisor enamel). Besides the “glueing” of the microstructure with proteins, White and co-workers (White et al., 2001) highlighted the biomechanical importance of the protein phase for the outstanding mechanical performance of enamel. They pointed out that the remaining proteins define the three-dimensional cleavage planes along which cracks will be preferentially deflected. This could prevent catastrophic fractures from advancing straight through enamel, but instead spread the damage laterally over a much larger volume. In addition, they stated that the proteinaceous remnants may allow limited differential movement between adjacent rods limiting damage and preventing catastrophic failure.

At the micrometer scale of the hierarchical organization of enamel, apatite crystals are bound together in bundles called prisms or rods that form in a radial manner from the dentine enamel junction to the external surface. Each rod is 3-6 μm in diameter. There is little protein within the prisms, while it is mainly concentrated at the interprism regions (Currey, 2002). This region is also called enamel sheath, and consists also of apatite crystals that are not part of the prisms and have a certain degree of mis-orientation with the axis of the rods (White et al., 2001). The enamel prisms themselves are arranged in a crossed, plywood-like structure (Currey, 2002, Macho et al., 2003) which is thought to act as crack arrester.

Enamel has a truly 3D structure (Macho et al., 2003). When observing the microstructure of a cross sectional area of enamel, i.e. after a transversal cut along the main direction of the tooth, it begins with a plywood-like structure near the interface with dentine (DEJ) and ends up with almost parallel alignment of rods near the outer surface. Depending on the analyzed section, e.g. occlusal or transversal, the mechanical response is expected to be

different (Spears, 1997). In addition, differences in mineral content and arrangement lead to different mechanical properties from the DEJ to the outer surface (Cuy et al., 2002).

The majority of wear studies in enamel have been made at the micrometer scale (Zheng et al., 2003, Li and Zhou, 2002) and macroscopic scale (West et al., 1999, Sajewicz, 2006, DeLong, 2006, Pintado et al., 1997, Magne et al., 1999). The present wear study was done in order to investigate the response at a finer scale of the hierarchical structure of enamel. Jandt (Jandt, 2006) also used AFM and nanoindentation but to study the influence of acidic soft drinks on the erosion behaviour on enamel. However, these techniques were not used to abrade the surfaces but to quantify the lost material and the change in mechanical properties after immersing enamel into different drinks. It was anticipated that the present studies would provide details of the influence of the deformation mechanism under the indenter tip on the tribological response of enamel.

4.3. Material

For the investigation reported here one incisor of a 1.5 year old steer was used. The tooth was cut with a diamond saw into two sections along the crown-root direction, carefully avoiding any overheating. A second premolar from a 12 year old male individual and a wisdom tooth of a 26 year old male individual extracted for orthodontic reasons were prepared following the same procedure and also tested.

For handling purposes, the pieces were glued to a plastic stub with cyanoacrylate glue. In all cases, the transversal section of the samples, consisting of enamel and dentine, was accessible for preparation. The exposed area was ground and polished to a 2500 P grit finish with silicon carbide cloths, followed by polishing in 0.3 μm alumina suspension.

4.4. Tribological Tests

Wear tests were carried out using an add-on nanoindentation device (Hysitron Triboscope, Hysitron Inc., Minneapolis, MN, USA) mounted on the scanner head of an AFM stage (Veeco – Digital Instruments, Santa Barbara, CA, USA).

Two different diamond single crystal indenters were used: a conical indenter tip (nominal radius of ~ 400 nm) and a sharp cube corner indenter (nominal radius of ~ 20-50 nm).

Load-displacement data of single point indentations were used to ascertain the maximum penetration depth over the load range investigated. These indentations were done at higher loads than the ones used here, in general the resultant force-displacement curves are shown in Fig. 34 and Fig. 35.

Single scans at constant load were done with a Triboindenter with an additional lateral force measurement device. The sharp cube corner tip was used. The scratched distance was 10 μm and the scan speed was 2 μm/s. Loads of 50 μN (on the bovine incisor), and 300 μN (on the human premolar) were used. For the case of the sharp indenter tip, the penetration depths mentioned above were corroborated by point indentations immediately before the tests started.

Wear was carried out by scanning the diamond indenter tip over a certain area with a load higher than typical for surface imaging (2-4 μN). Feedback load controlled measurements were done, which enabled the normal displacement and normal load data to be recorded continuously. The indenter tip sliding speed varied from 4 μm/s to 20 μm/s. Preliminary studies showed that the wear rate is not sensitive to the tip velocity in the tested range (results not shown here). The abraded areas were 10x10 μm^2 for the sharp indenter tip and 5x5 μm^2 in the case of the rounded conical indenter tip. For the case of human enamel and conical rounded tip, 2x2 μm^2 areas were also worn.

Some terminology will be defined in order to avoid confusion. “Scan” is used to denote the constant rate movement of the indenter tip in one direction along one line. “Double scan” means the movement of the indenter tip forward and backward along the same line. “Area scan” is employed to indicate a certain amount of double scans placed one beside the other. The final shape of the area scan is a square. The space between double scans is determined by the chosen number of double scans in each particular test. Once one double scan is complete, the indenter head is drawn perpendicular to the scan movement one step down. If more than one area scan is done in one single test, the test is named “double area scan”, “triple area scan”, etc, depending on the number of area scans carried out. The second area scan begins where the first area scan terminated. This procedure is repeated for the successive area scans.

Most of the area scan tests consisted of 128 double scans corresponding to a spacing of (10/128) or (5/128) μm apart except those done on the human enamel with the conical rounded tip shown in Fig. 37. In this latter case, 256 lines were used or a spacing of (2/256) μm. In addition, in the latter case, after each single abrasion scan test, a control image of 5 x 5 μm^2 was taken with the nanoindenter tip at 2-4 μN imaging force. All the area scans started from the same side of the square.

4.5. Results

4.5.1. Conical indenter tip

The included angle of the conical rounded indenter tip, 2α, is 90º. The transition from the rounded tip to the conical shape occurs at ~120 nm. Using single indentations in the human wisdom molar done at a maximum of 2000 μN (Fig. 34), an estimation of the penetration depth at the loads used here was obtained and is presented in Table 3. Thus, under the forces used for the wear tests the semi contact angle was greater than 45º. This can be seen from the 2D scaled projection of the conical rounded tip presented in Fig. 36. The normal load is equal to,

$$W = P\pi a^2 \qquad \text{Eq. 24}$$

where *W* is the applied normal load, *P* is the contact pressure, *a* is the contact radius.

The radii of contact were calculated using the calibrated area function of the indenter tip and the penetration depth by means of,

$$A_{(h)} = \pi a^2 \quad \text{Eq. 25}$$

where $A_{(h)}$ is the calibrated area function and h is the maximum penetration depth.

The effective radius of the indenter, R_e, is given by (He and Swain, 2007d),

$$a^2 = 2R_e h - h^2 \quad \text{Eq. 26}$$

By geometric considerations of a contact between a spherical indenter and a flat specimen when a<<R (see for example (He and Swain, 2007d)) it is found that,

$$\frac{a}{R_e} = \sin(\beta) \approx \tan(\beta) \quad \text{Eq. 27}$$

where $\beta = 90^o - \alpha$, is the angle between the indenter flank and the original surface. Eq. 27 is also directly related to the strain generated by a spherical indenter.

Thus, using Eq. 24 to Eq. 27 the semi contact angle (α), contact pressure (P), radius of contact (a) and effective indenter radius (R_e) were calculated and presented in Table 3. In addition, an approximation of the strain associated with this indenter tip is presented also in the same Table 3 by means of tan(β).

Since the scanned areas were 5x5 μm^2 and there were 128 scanned lines, the perpendicular step movement of the indenter tip was 5μm/128 lines, in other words, ~40 nm. Thus there was a superposition of scans since the minimum contact radius was greater than 40 nm (Table 3). For the case of 2x2 μm^2 areas, the perpendicular steps between scanning lines were 2μm/256 lines (~8 nm).

A sequence of scans is shown in Fig. 37 (human premolar, 2x2 μm^2, 4 μm/s, 4 single area scans, 400 μN, 256 double scans). After one scan was complete, the nanoindenter tip was used to take an image of the worn area at low load (2 to 4 μN). In Fig. 37a, the surface deformed area is shown. There is almost no evidence of debris on the abraded area. Fig. 37b-d show some apparently higher regions not only outside the tested area, but also inside. When material is removed from the scanned area it mainly sticks on the tip. To prove the latter, two reference samples (polycrystalline silver and a copper mono-crystal), one polystyrene block (Styrofoam) and the dry enamel sample were placed on the device. First the indenter tip was cleaned by penetrating the polystyrene block; afterwards the reference sample was indented ("clean indent"). Subsequently, the enamel sample was moved under the tip and one abrasion measurement was carried out. The reference sample was again placed under the indenter tip and indented ("dirty indent"). The penetration depths of the indents in the reference sample were higher than the average penetration depth of the abrasion tests. This procedure was repeated in silver and in copper. The load-displacement curves of the reference material before ("clean indent") and after ("dirty indent") the wear tests were compared. In the latter, an abnormal convex shape of the load-displacement curve was observed at higher penetration depths. This is a typical characteristic of indenters with a dirty tip.

As the number of indenter tip scans increases, the amount of "extra material" or debris on the sides of the tested area increases, although the "debris" inside the tested area is reduced.

The same procedure was carried out with normal forces of 50, 100 and 200 μN (human premolar, 2x2 μm^2, 4 μm/s, 256 double scans). For the latter two normal forces, 4 scans areas were done while for the 50 μN normal force measurement 20 area scans were done. At none of the loads above was debris evident either outside or inside the tested area.

4.5.2. Sharp cube corner indenter tip

The radii of contact were calculated using the calibrated area function of the indenter tip and the penetration depth by means of Eq. 25. The contact pressure was obtained using Eq. 24. The results are presented in Table 4. The contact angle values shown in Table 4 correspond to the effective cone angle of the indenter. The strain associated with this indenter tip is constant and can be represented by $\tan\beta = \tan(90º-\alpha) = \tan(47.73º)$.

The abraded areas were chosen to be 10x10 μm^2 with 128 double scans. This gives (10/128) μm spacing between each double scans (~80 nm). Thus, there was no superposition of scans for the case of 50 μN but for only the 300 μN load.

The scanned areas were not imaged with the nanoindenter tip since preliminary studies showed that the removed material is pushed away to the borders of the image window, where also agglomerates formed (images not shown here). In Fig. 38a (Bovine incisor, 10x10 μm^2, 20 μm/s, 1 area scan, 50 μN), a SEM image of a scanned area without any post cleaning or sample preparation procedure is shown. All the removed material remains inside the tested area. It tends to agglomerate. Fig. 38b (Bovine incisor, 10x10 μm^2, 20 μm/s, 1 area scans, 50 μN) is a detailed image at higher magnification of the marked region of Fig. 38b. Some remaining ploughing furrows are shown along with chip like structures. The indenter tip path can also be clearly seen.

For the case of the human premolar, single scans at 300 μN were done at two different arbitrary orientations on the cross section. The friction coefficient vs. time shows the same trend as the lateral force vs. time, that is a stick-slip response (Fig. 39). No orientation dependant difference was detected in the above response. The average friction coefficient was 0.98 ± 0.133. For the arbitrarily called 0º orientation, the normal penetration depth decreases with time (Fig. 40). Fig. 41 shows an SEM image of the single scan tracks. The material removed by the indenter tip is also observed and consists mainly of one entire swarf of material. Fig. 41b shows a higher magnification SEM image of the bottom single scratch. The removed material presents a serrated surface.

On the contrary, the bovine incisor tested at 50 μN presents a continuous increment in normal penetration depth during the duration of the tests (Fig. 40). Both friction coefficient and lateral force vary linearly with time an increasing load (Fig. 39). Friction coefficients increase from ~ 0.1 at the beginning of the scan to ~ 0.6 at the end.

In addition, a TEM observation was made of the removed debris material of the human premolar sample tested at 300 μN (human premolar, 10x10 μm^2, 20 μm/s, 3 area scans, 300 μN)

and it is presented in Fig. 42. EDAX was done to confirm the observed material was the mineral phase of enamel. The remnant, highly broken grain like structures are ~10 nm in diameter.

4.6. Discussion

The tested surface of enamel was the cross section. For the following explanation, enamel can roughly be considered a long fibre reinforced composite at the tested scale, since the mineralized fibrils in enamel are known to be ~100 μm in length (Fox, 1980), and ~ 100 nm in diameter (White et al., 2001), long compared to the indenter tip and the scan distances. Thus, and according to the nomenclature found in literature (Friedrich, 1986, Stachowiak and Batchelor, 2001), the orientation of the HAp crystals with respect to the movement of the indenter tip varies between purely parallel and antiparallel, and in addition the exposed surface may be at a certain angle with respect to the main direction of the rods. This orientational arrangement is expected to have consequences with respect to the abrasion behaviour (Friedrich, 1986). However, since in our experiments the orientation of the prisms was not known a priori, it is not clear whether mechanical response variations with slight changes in orientation (i.e. from one rod to an adjacent one) can be detected with the device used and moreover, the antiparallel/parallel mechanical response difference is not expected to be high (Macho et al., 2003, Friedrich, 1986), the results shown here are thought to be representative of the nanometric response of the cross section of enamel

The indenter tip maybe considered as a hard asperity scratching the material.

4.6.1. Conical rounded indenter tip.

There is a threshold load for the removal of material with the indenter used and this load is about 400 μN. At low loads, 50 μN, and even after 20 scans of 256 double scratches each, there was no removed material could be detected. The same trend was found with 100 and 200 μN loads after 4 area scans. An extra test was done at 300 μN and 7 area scans, no material was removed (human premolar, 10x10 μm^2, 20 μm/s, 7 single area scans, 300 μN, 128 double scans). Only after the same conditions but with a load of 400 μN, removal of material was observed. In addition, a new test at 500 μN was done (human premolar, 10x10 μm^2, 20 μm/s, 7 single area scans, 500 μN, 128 double scans). There was removal of material although the area scans were done continuously and it is not possible to know when it started.

The existence of this threshold load is of considerable importance since it may provide an estimate of the shear strength of the protein phase in situ. In addition, removal of material was registered for the case of 400 μN, but not for the case of 300 μN, when both induce the same contact pressure on the sample (Table 3). However, the difference remains in their generated strain. Although additional experimental work is needed in order to generate more reliable data, a ~ 2º increment of the contact angle produced the necessary strain to generate damage and remove material from the sample at the same contact pressure.

The sheaths present a more deformable surface, as expected due to the greater protein content in this region, an example is shown in a nanoindenter image presented in Fig. 43 (human premolar, 10x10 μm^2, 20 $\mu m/s$, 7 area scans, 300 μN). Note the higher heights along the rod interfaces. The enrichment of protein component in the sheaths determines a different mechanical response of the sheaths as compared with the centre of the rods. Ge and coworkers (Ge et al., 2005) measured the nanohardness and elastic modulus of these two enamel areas. They found 73.6% and 52.7% lower H and E than those of the prisms, respectively. Fig. 44 shows a nanoindenter image where both, rod interface deformation and removal of material on these areas are observed (human premolar, 10x10 μm^2, 20 $\mu m/s$, 7 area scans, 500 μN). SEM observations of tests done in an aqueous environment show that the mineral phase beneath the removed zone remains intact (to be published elsewhere). The fibrils are clearly seen. Thus, the fracture runs along the protein layer in an interfibrilar manner.

Let us consider what happens when the indenter tip is drawn along the surface during a single scan. At the contact loads and stresses developed the mineral platelets do not appear to be broken. In addition they are surrounded by a thin layer of protein which may act as a lubricant. The protein layer is sheared and squeezed between the minerals.

Hutchings (Hutchings, 1992) presented two deformation mechanisms for the friction of polymers: friction due to deformation and friction due to adhesion. As it can be seen from Fig. 37, friction due to asperity deformation predominates at the early stages (Fig. 37a) and later on adhesion starts to play a role (Fig. 37 b-d).

Greenwood and Williamson (Greenwood and Williamson, 1966) derived an expression for the plasticity index, ψ, given by

$$\psi = \frac{E}{H}\left(\frac{\sigma^*}{r}\right)^{1/2} \qquad \text{Eq. 28}$$

where *E* is the indentation or reduced elastic modulus, *H* is the indentation hardness of the rough surface and σ^* is the standard deviation of the height distributions. When the plasticity index is greater than 1, most asperities will deform plastically under even the lightest of the loads. It was derived for the case of a contact between a rough surface and a rigid plane surface. In the present case, the rigid plane surface is taken as the indenter and the rough surface as enamel. AFM images give a roughness value of $\sim 4.5 \pm 1$ nm. If H is assumed to be 2.5 GPa and *E* is taken as 55 GPa (both mechanical properties were measured with a Berkovich indenter on the bovine sample) and the asperities are considered as spherical (assumption of Greenwood and Williamson (Greenwood and Williamson, 1966)), a plasticity index of ~ 10 is obtained. Thus, even though elastic contact is expected between a spherical indenter and a perfectly flat surface under this condition, the first scan of an area plastically deforms all the asperities.

Unless regions showing obvious removal of material are present, the “extra material” on the borders of the scanned area is more likely to be highly deformed material, generated during the plastic deformation and shearing of asperities originally present on the surface. Here a ridge of deformed material is pushed ahead of the tip. Once one single scan is done, the tip reaches

the opposite border and this "wave" of material remains on this side. This observation resembles the observation of Challen et al. (Challen et al., 1984) of fatigue wear during sliding of a hard wedge on a metal substrate. In Fig. 37 a-d, all the tests started on the bottom of the images. Fig. 37b is an example of the above behaviour in enamel. On the top of the scanned area, "extra material" is observed. This "debris" is more likely to be an accumulation of highly deformed material after the last double scan was done. This removal of surface asperities is responsible for the smoothness of the resultant surface and for the very high strains that are sustained for the "wave" which lead to cracking of the material in the wave (Stachowiak and Batchelor, 2001).

This smoothness contributes to an increase in the likelihood for the transfer of a film of material onto the counterface (indenter tip). The superficial layer is now highly deformed. Once the surface is smooth and full contact is established, the successive and superimposed double scans produce high tensile and shear stresses in both directions which may nucleate and propagate interfibril cracks within the protein layer leading to detachment of material. Some of the load-displacement data showed reduction in penetration depth with time. This latter observation may indicate that the transferred film is well attached to the tip and supports the total load applied. A fictitious reduction of penetration depth and/or a reduction in applied pressure (due to the increase in loading bearing area) with the consequent reduction in damaged depth may be the consequence. Thus, on further sliding the enamel continues to wear by adding material to the transferred film. At some point, this film falls from the indenter tip on to the tested surface (Fig. 37b-d). As shown in Fig. 37d, this material is further compressed into the enamel.

The existence of a transferred film was also verified by indentations in reference materials before and after the wear tests as already described in the Results section. For a transferred film to occur, more than one scan of the area is needed since extremely smooth surfaces are required and fatigue cracking due to successive sliding is presumably the damage mechanism playing a role.

4.6.2. Sharp cube corner indenter tip

A stick-slip like action was recorded as sudden drops in the friction coefficient during the single scans done with the lateral force transducer at 300 μN (Fig. 39). In addition, in Fig. 41b and Fig. 45 (human premolar sample, 10x10 μm^2, 20 μm/s, 3 area scans, 300 μN) are SEM images containing removed pieces of material. The serrated like appearance of this swarf debris agrees with the stick-slip observation and corresponds to the repeated sequence of formation and detachment of the wedge.

The strip of material ahead of the tip is deposited on the other side of the scanned area if the loads are high enough to produce thick strips. The single scratch tests done with 300 μN confirm this (Fig. 41). The existence of a continuous strip of material with this load is also detected in the normal penetration depth vs. time data, since the continuous pushing of a swarf of material ahead and in contact with the indenter tip leads to fictitious decrement of penetration

depth with scratched distance. However, at the very low load of 50 μN, the thickness of the strip is thin enough to produce rupture by self weight before the other side of the square area is reached. From Fig. 38a, it can be seen that almost all the removed material remained inside the scanned area. The strip is then destroyed by the posterior movement of the indenter tip, although some remnants of strips are also seen. The above mechanism is also confirmed by the registered increase in penetration depth with scratched distance of the single scratch tests at 50 μN.

The structures of the debris revealed by TEM (Fig. 42) show a highly broken mineral phase. There is no evidence of fibrils. This highly damaged yet bound structure is still being held together by the protein glue bonding the apatite crystallites.

In contrast to the round indenter tip, the wear mechanism lies between ploughing and cutting. According to Hutchings (Hutchings, 1992) it is called wedge formation and the deformation consists of the growth and eventual detachment of the raised ridge, a sequence which is repeated continuously. The experimental observations confirm this model.

4.6.3. Damage mechanisms: Rounded conical versus Sharp cube corner indenter tips

Material is removed continuously with the sharp cube corner indenter tip, unlike for the case of the rounded tip in which the removal of material is localized. Rabinowicz (Rabinowicz, 1995) presented a quantitative expression for the volume of material removed by abrasive wear in his book, namely

$$V = \frac{Wl\tan(90^\circ - \alpha)}{\pi P} \qquad \text{Eq. 29}$$

where the new variables are: *V*, the volume of material swept out; *l*, the distance covered by the indenter tip and the applied normal load, *W,* is taken from Eq. 24. The tip is considered conical. Thus, using the effective conical angle of the sharp cube corner indenter tip (42.7º), a first rough estimation of the removed material can be done.

A normalized damage depth, *d*, defined by Eq. 30 will be considered for the comparisons. In order to avoid the influence of superposition of scans, the calculation was done considering only one single scan. The area was calculated multiplying the covered distance by the diameter of contact (2*a*). Using Eq. 24, Eq. 27 and Eq. 29,

$$\frac{V}{A_{abraded}} = d = \frac{1}{2}a\tan(\beta) \qquad \text{Eq. 30}$$

Thus, sharper indenter tips lead to greater removal of material.

The height of damage is related to the height of penetration, although it is not a simple relation, since

$$\frac{d_1}{d_2} = \frac{a_1}{a_2} = \sqrt{\frac{A_{(h_1)}}{A_{(h_2)}}}$$

Examples of the damage depth under various conditions are given in Table 4.

If we consider the damage depth for the case of the rounded indenter tip using Eq. 30, despite the formally identical equation, the functional connection is completely different. For the case of the rounded indenter tip, Eq. 29 is no longer a measure of material removed but the depth of deformed material. Thus, for the case of the rounded indenter tip Eq. 29 can be re written as,

$$\frac{V}{A_{abraded}} = d = \frac{1}{2} a \tan(\beta) = \frac{1}{2}\frac{a^2}{R_e} \qquad \text{Eq. 31}$$

As expected, since the abrasion generated by the blunt tip is mainly a ploughing mechanism, its influence depends on the strains generated (tanβ) and the amount of material involved (*a*). Spheres with greater radii will lead to a decrease in deformation. Furthermore, Eq. 31 shows that abrasion with the same rounded conical indenter but different loads leads to a variation in damage height (described by Eq. 32) mainly due to the change in penetration depth. As already shown, the plastic index of this system leads to plastically deformed asperities even at the very low loads, thus as far as the indenter tip penetrates the sample there will be deformation induced damage. The latter is indicated in Eq. 32, and damage height values are given in Table 3.

$$\frac{d_1}{d_2} = \frac{a_1^2 R_{e2}}{R_{e1} a_2^2} \approx \frac{h_1}{h_2} \qquad \text{Eq. 32}$$

There is an evident change in wear mechanism depending of the indenter tip used, as described above, and this change depends mainly in the sharpness of the indenter tip. Zum Gahr (Zum-Gahr and Karl-Heinz, 1987) also reported that the ratio of micro-ploughing to microcutting depends to the attack angles of the abrasive particles. In addition, it was stated that the critical attack angle is a function of the material undergoing wear and the test conditions.

Friction and wear involves not only normal loads but also tangential forces. The expected mechanisms are closely linked to the microstructure of the worn surface and its behaviour. The sliding of a hard indenter tip on a soft surface generates tensile and shear forces. Jäger and Fratzl (Jäger and Fratzl, 2000) presented a tensile model for the deformation of mineral platelets of bone. The key result of the model is that the organic phase is mainly subjected to shear strains. He and Swain (He and Swain, 2007a) have recently published a work in which they proposed a simple microstructural model to illustrate the structure related contact deformation mechanisms of human enamel. They found that the shear strains supported by the thin protein layer are up to 16 times greater than the contact strain. Although both models deal with the orientation of the fibrils parallel to the loading direction, the assumption of shear deformation supported mainly by the protein layer is used.

The differences in deformation mechanisms depending on the indenter tip geometry for the case of single point indentations was previously studied (Guidoni et al., 2007c). In this previous work (Guidoni et al., 2007c), it was found that the sharp indenter tip generates a more distributed damage around the indenter tip which causes a reduction in the measured elastic modulus when compared with a Berkovich tip. This may indicate that in the case of wear with this indenter tip, the deformation is carried by both the mineral phase which at this normal load

plus the lateral movement is more likely to break and the shearing of the protein phase. The response of enamel under the sharp indenter tip is a cutting mechanism. The loads used and the sharpness of the tip were sufficient to locally damage the structure instantaneously leading to a continuous removal of material. Tensile stresses and strains are expected to be highly concentrated and therefore severe, for this case. On the contrary, for the case of the rounded conical indenter tip, the mainly compressive stresses generated beneath the indenter tip are more likely to compress the structure. The response of enamel under the rounded indenter tip is mainly a deformation mechanism. The contact pressures and strains seem to be low enough to shear and squeeze the protein between the mineral phase without breaking the mineral crystals. There is no expected instantaneous damage in this deformation mechanism, as for the case of the sharp indenter tip, since the mineral platelets are small enough and sufficiently tough to resist the deformation without breaking. However, the asperities, which at the penetration depth involved here, start to play an important role, deform locally plastically and upon successive sliding fatigue damage is promoted. The shear strains supported by the proteins are high enough to exceed the shear strength of this organic phase at some point, thus nucleating and propagating cracks through it. As presented in Table 3 and Table 4, the strain for each of the indenters is markedly different, supporting the model proposed above.

4.7. Conclusions

From the above observations the following conclusions can be drawn:

Scanning the indenter tip on the surface of enamel can be thought as a hard asperity sliding on a soft substrate.

Depending on the sharpness of the indenter, different wear mechanisms are found. For the case of the rounded conical tip, mostly asperity deformation and fatigue wear occur during sliding. On the contrary, for the case of the sharp indenter tip, the mechanism is ploughing and wedge formation. It is mainly a cutting mechanism.

Similar penetration depth but different angles of attack (i.e. round vs. sharp indenter tip) lead to different abrasion mechanisms. As contact angle is reduced, cutting effects -suffered by both the mineral and protein phase- are the predominant mechanism against the shearing of the organic phase at greater contact angles.

There is a critical contact angle of attack between 74º and 43º for the deformation and wear to change to cutting abrasion mechanism. In other words, there is a critical strain at which the mineral platelets can not sustain the deformation and break.

For the case of larger contact angles (rounded indenter tip in this case), there is a threshold strain at which the organic phase does not fail catastrophically under the tested conditions.

The expected response may vary depending on the orientation of the enamel fibrils in relation to the indenter tip movement, although this can not be distinguished at this point.

4.8. Acknowledgements

Financial aid through EC Contract No MEST-CT-2004-504465, „Marie Curie Host Fellowships for Early Stage Research Training", is gratefully acknowledged. Dipl.-Ing. Andreas Jaeger is kindly thanked for his help with the single scratch tests. People in charge of the Triboindenter (including Dipl.-Ing. Andreas Jaeger) from Institute for Mechanics of Materials and Structures from Vienna University of Technology are also acknowledge for allowing us to carry out the single scratch tests using their device.

FIGURES OF CHAPTER 4

Fig. 34

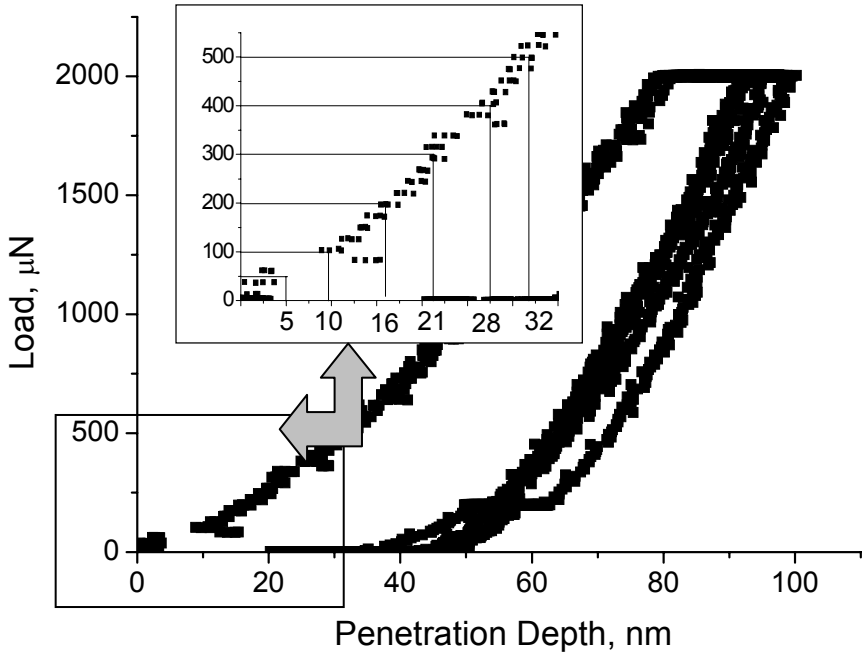

Fig. 34 Load-displacement curves of single point indentations done with the rounded conical indenter tip on a human wisdom tooth. Maximum load: 2000 μN. There were two load holding periods: 60s. at maximum load and the 20s. at 200 mN. In the upper left corner a magnified view at low penetration depth is shown. The corresponding penetration depths for the loads used are marked.

Fig. 35

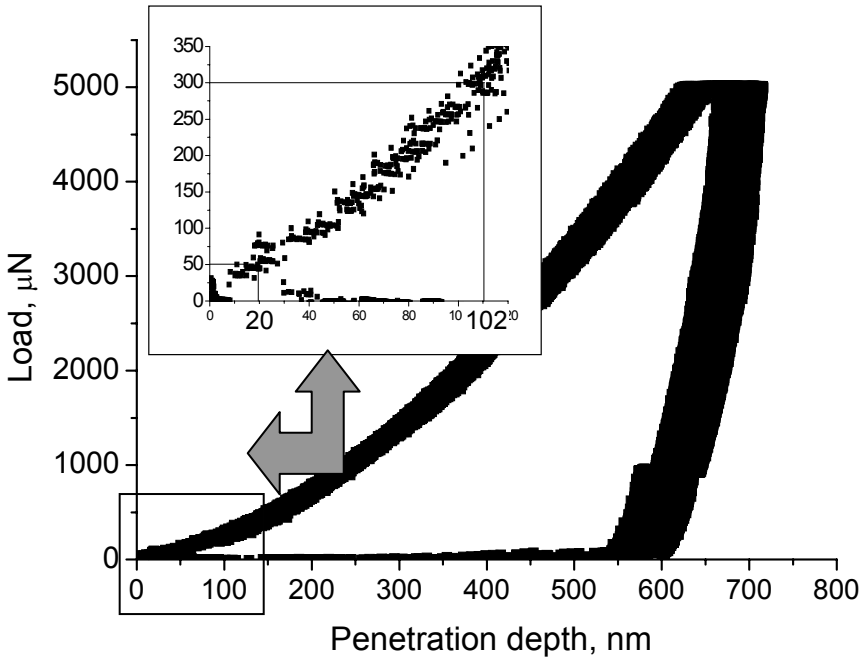

Fig. 35 Load-displacement curves of single point indentations done with the sharp cube corner indenter tip in a human premolar. Maximum load: 5000 μN. Maximum load: 2000 μN. There were two load holding periods: 60s. at maximum load and the 20s. at 1000 mN. In the upper left corner a magnified view at low penetration depth is shown. The corresponding penetration depths for the loads used are marked.

Fig. 36

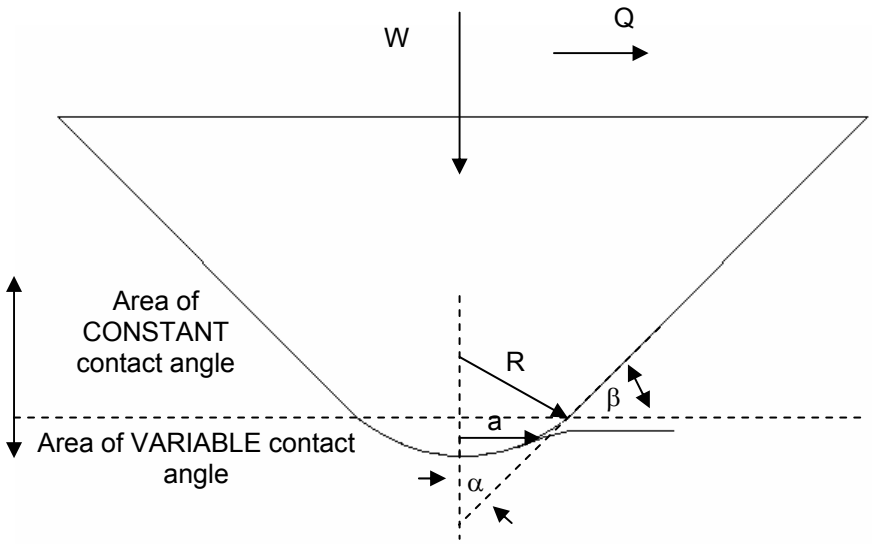

Fig. 36 Scaled projection of the conical rounded indenter tip. Two important parts are marked: the area at constant contact angle and the area of variable contact angle. *W* and *Q* are the normal and lateral applied forces, respectively. The variables defined in the text are also drawn. *R* is the nominal radius, *a* is the contact radius, α is the effective conical indenter semi angle, β is the contact angle.

Fig. 37

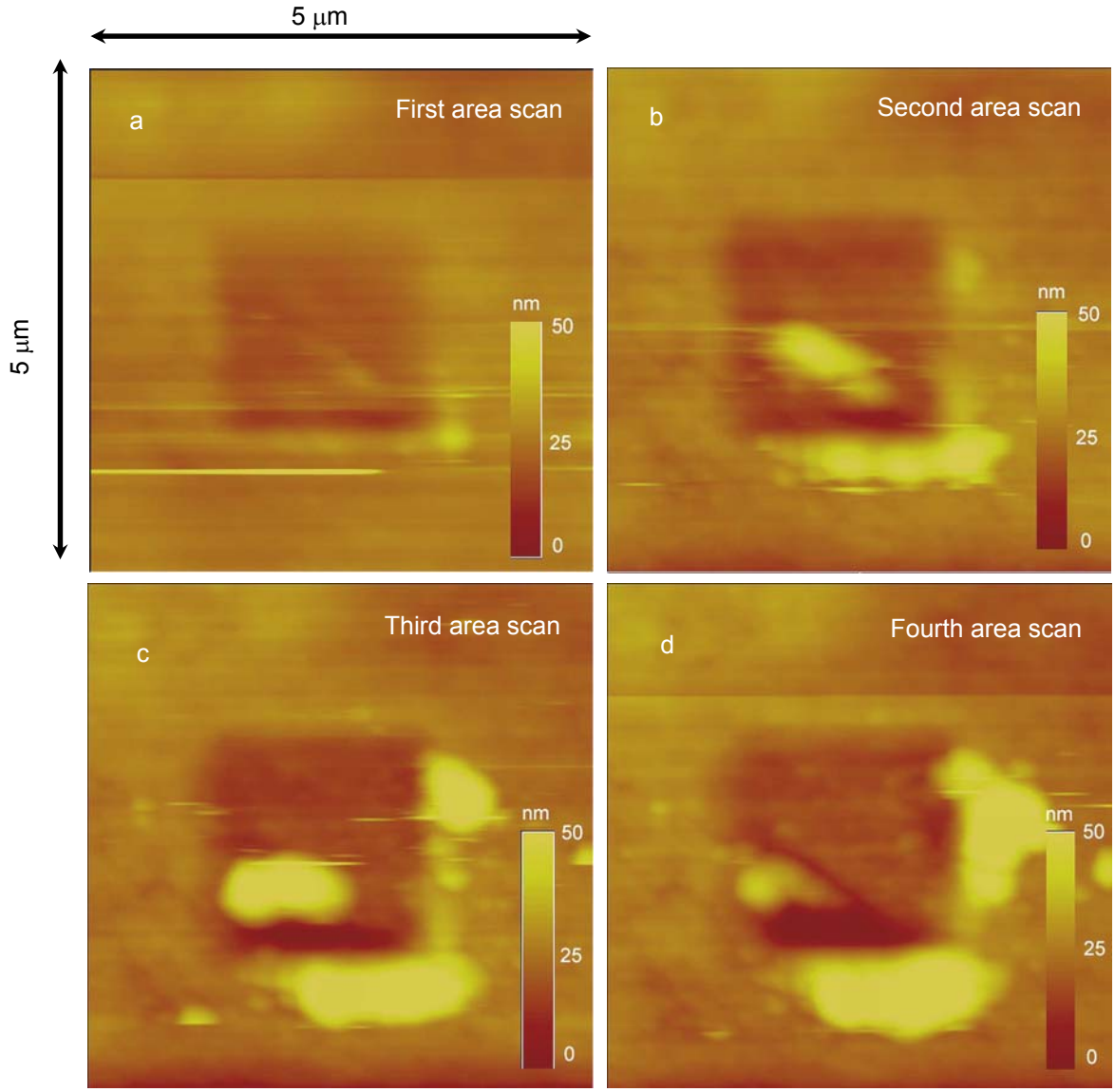

Fig. 37 Nanoindenter images of an abrasion test done on a human premolar with the rounded indenter tip. 2x2 μm^2 abraded area inside one single enamel rod, 4 μm/s scan speed, 4 single area scans, 400 μN load, 256 double scans. After one single area scan was carried out, the nanoindenter force was reduced to 2-4 μN in order to scan the area with a 5x5 μm^2 imaging window. All the area scans started from the top of the shown investigated areas.

Fig. 38

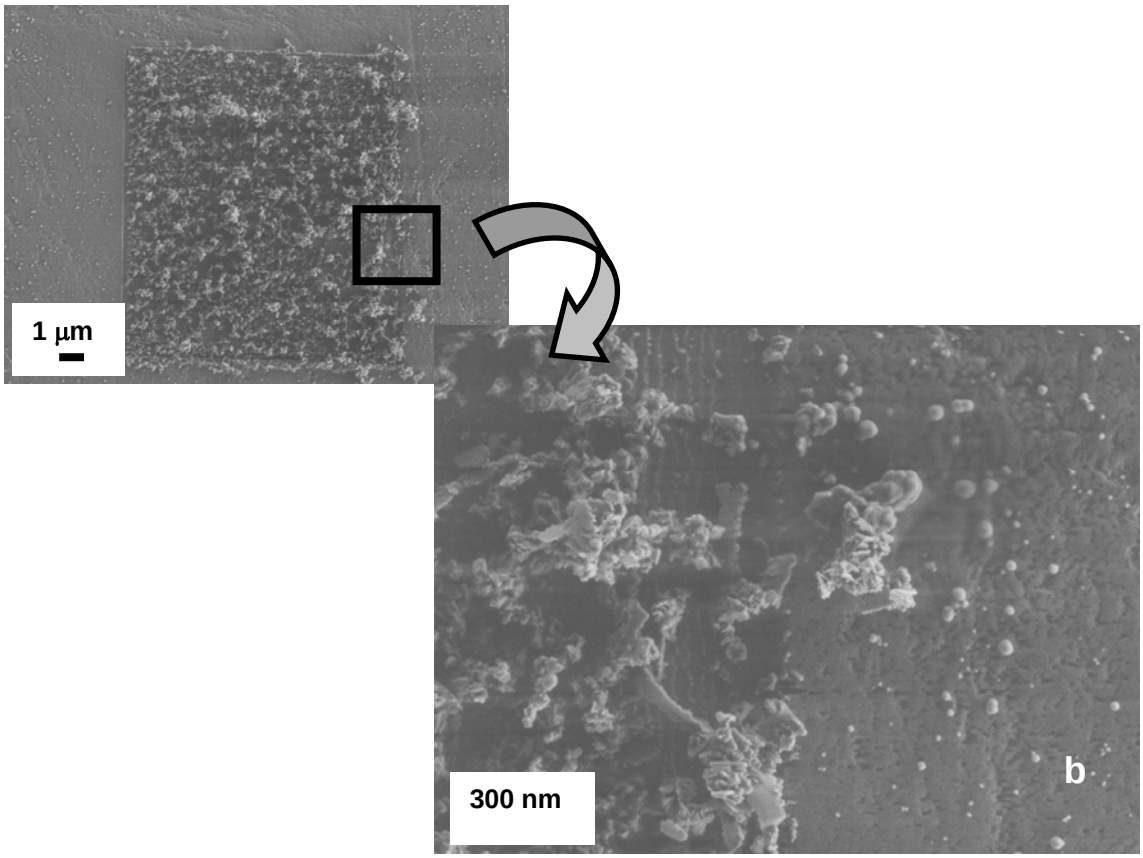

Fig. 38 SEM images of an abrasion test done in the bovine incisor with the sharp cube corner indenter tip. 10x10 μm^2 abraded area, 20 μm/s scan speed, 1 area scan, 50 μN load. b) shows a higher magnification SEM image of the square marked in a).

Fig. 39

Fig. 39

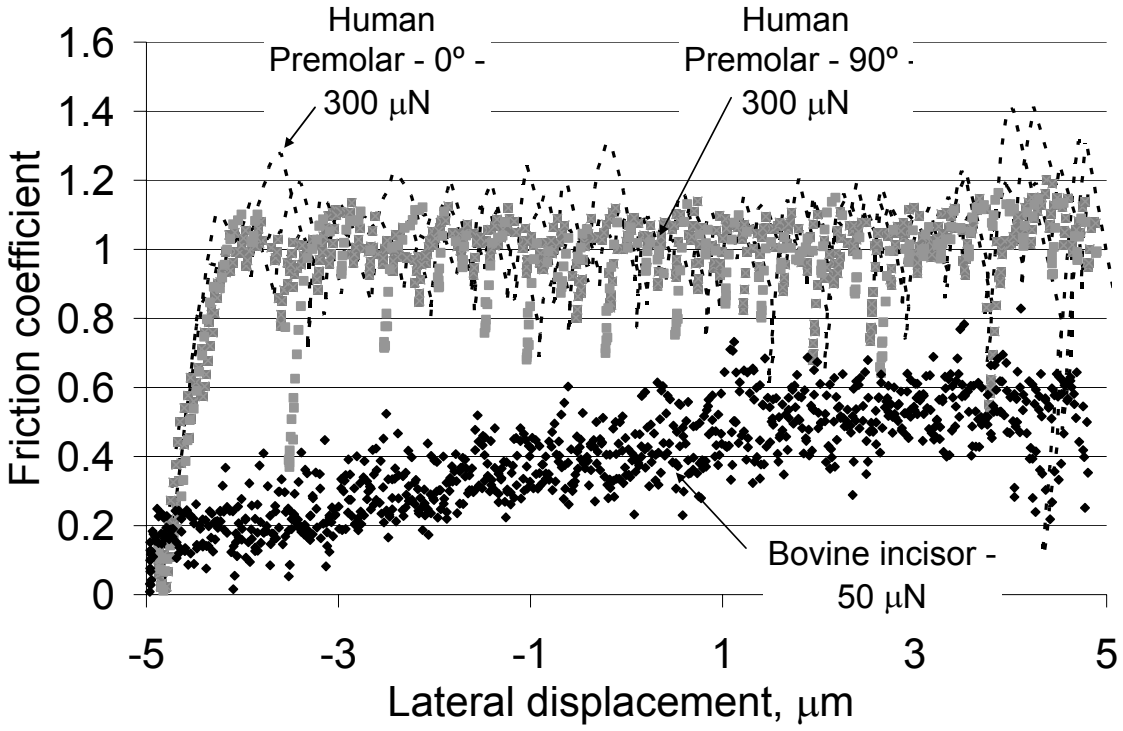

Fig. 39 Friction coefficient vs. lateral distance plot of the friction tests done with the sharp cube corner tip.

Fig. 40

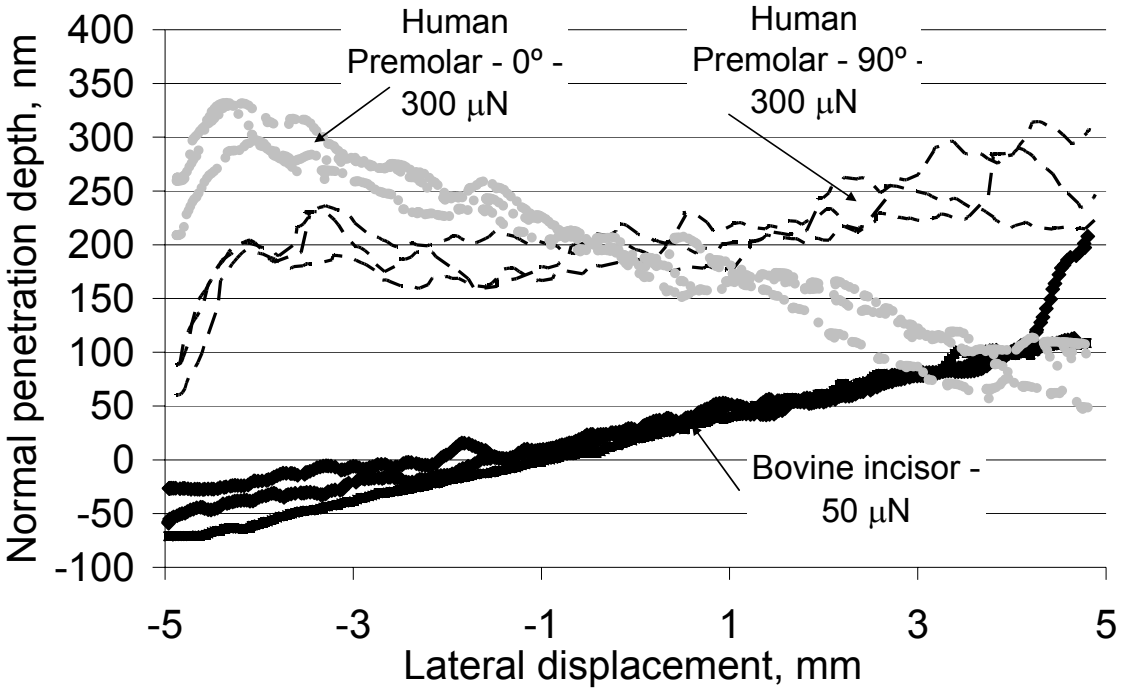

Fig. 40 Normal penetration depth vs. lateral distance plot of the friction tests done with the sharp cube corner tip.

Fig. 41

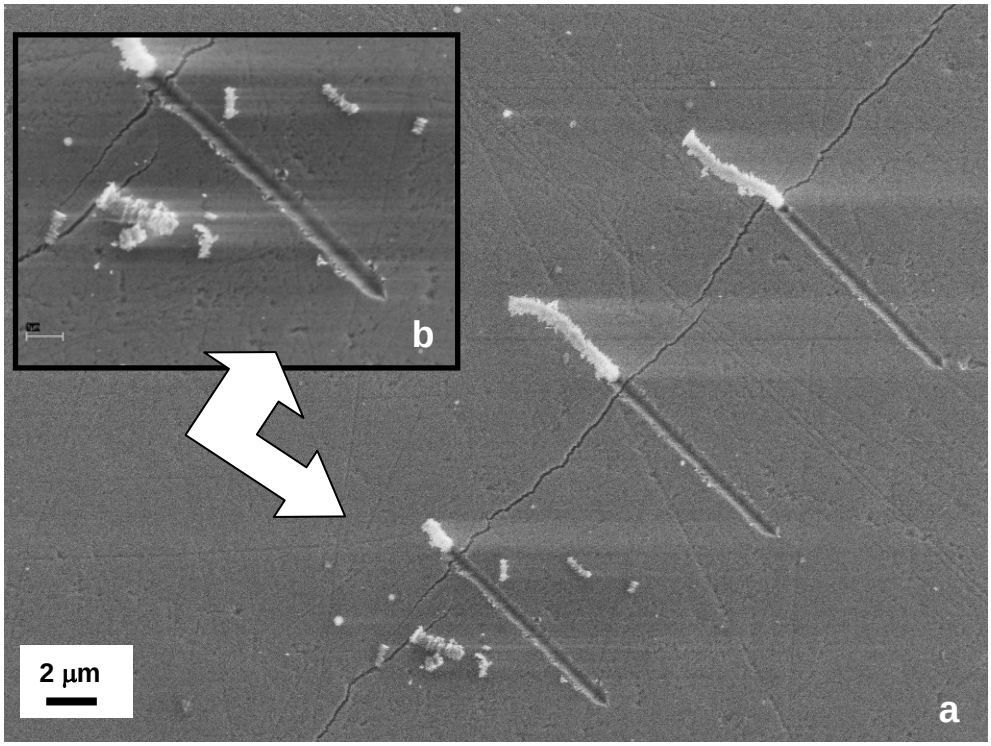

Fig. 41 SEM images of the friction tests done with the sharp cube corner tip on the human premolar. The load used for this case was 300 μN. Note the crack at the end of the scratched lengths which is believed to have occurred during desiccation of the samples for SEM observation. In the upper left corner a higher magnification of the bottom scratch test is shown.

Fig. 42

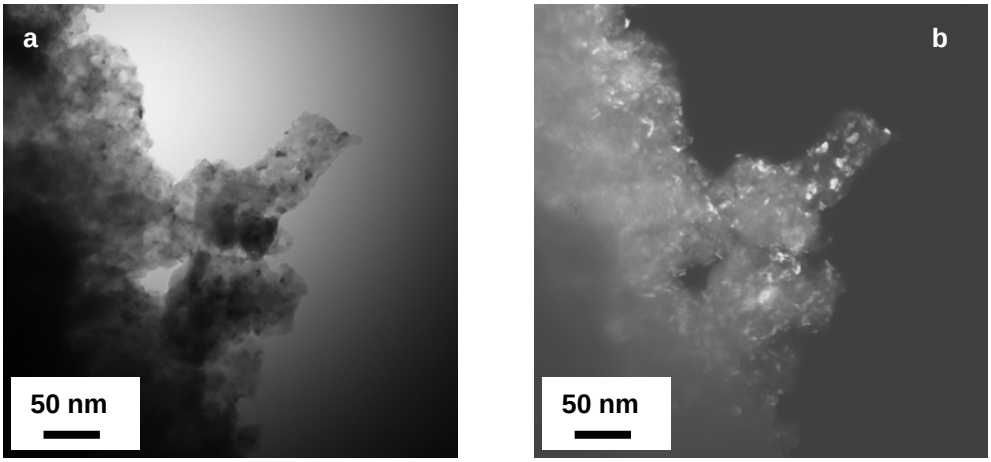

Fig. 42 TEM images of the debris found after scanning the human premolar with the sharp cube corner indenter tip with 300 μN. b) shows a dark field TEM image of Fig. 42a in which the size of the mineral phase can be deduced.

Fig. 43

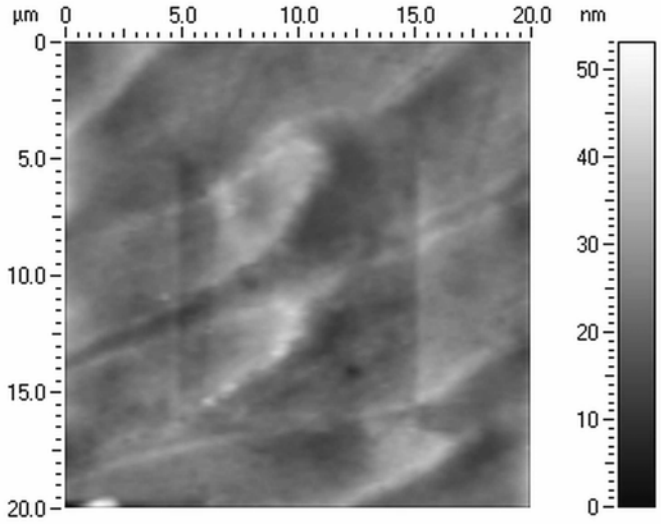

Fig. 43 Nanoindenter images of an abrasion test done in the human premolar with the rounded indenter tip. 10x10 µm^2 abraded area, 20 µm/s scan speed, 7 single area scans, 300 µN load, 128 double scans. The rods can be easily seen. Inside the abraded area there is a general depression, in comparison with the outer region. The height depression is around 7 nm.

Fig. 44

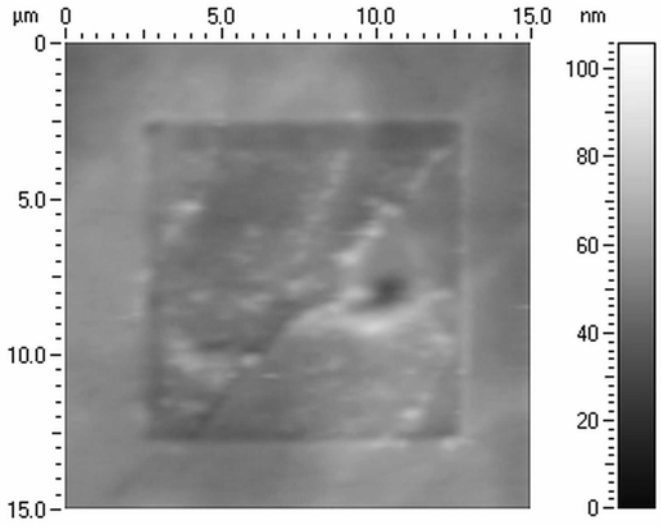

Fig. 44 15x15 µm^2 nanoindenter image of an abrasion test done in the human premolar with the rounded indenter tip. 10x10 µm^2 abraded area, more than one rod is crossed during the test, 20 µm/s scan speed, 7 single area scans, 500 µN load, 128 double scans. The removal of material seems to start at the interfaces of enamel rods. As in Fig. 43, the abraded region presents a depression in comparison with the outer region.

Fig. 45

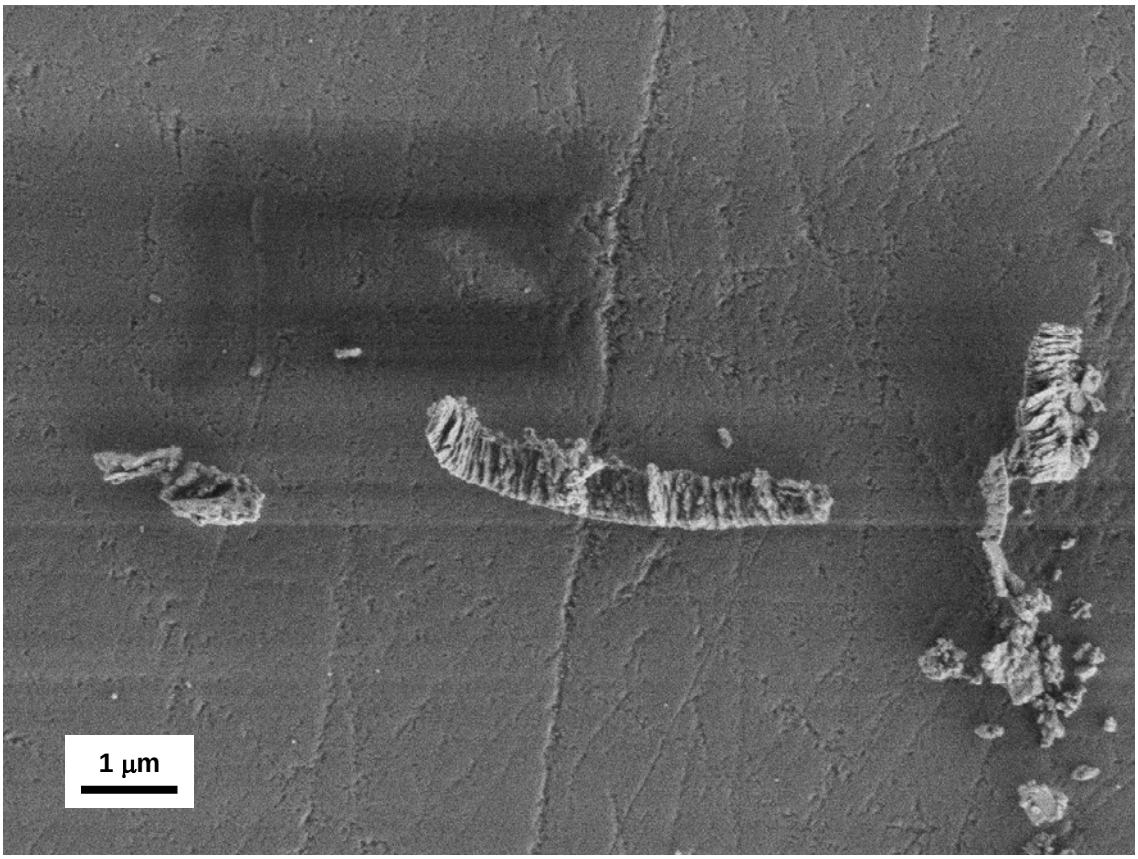

Fig. 45 SEM image of a piece of material removed from a human premolar sample with the sharp cube corner indenter tip. The load was 300 μN. The TEM image of Fig. 42 was also taken from this abrasion test.

TABLES OF CHAPTER 4

Table 3

Normal Force (W), μN	Maximum penetration depth (h), nm	Contact Radius (a), nm	Contact Pressure (P), GPa	Effective indenter radius (R_e), nm	tan(β) = a/R	α	Damage depth (d), nm. (Eq 35-36)
50	5	110.37	1.31	1220.65	0.09	84.83	4.99
100	10	156.25	1.30	1225.64	0.13	82.74	9.96
200	16	197.88	1.63	1231.64	0.16	80.87	15.90
300	21	226.93	1.85	1236.63	0.18	79.60	20.82
400	28	262.41	1.85	1243.63	0.21	78.09	27.68
500	32	280.76	2.02	1247.63	0.23	77.32	31.59

Table 3 Results for the rounded conical indenter tip and the human premolar sample.

Table 4

Normal Force (*W*), μN	Maximum penetration depth (*h*), nm	Contact Radius (*a*), nm	Contact Pressure (*P*), GPa	Effective conical semi contact angle (α), º	tan(β) = tan(90º-α)	Damage depth (*d*), nm. (Eq 34)
50	20	55.96	5.08	42.27	1.10	30.78
300	102	151.29	4.17	42.27	1.10	83.20

Table 4 Results for the sharp cube corner indenter tip and the bovine incisor sample.

CHAPTER 5

5. NANO-SCALE SLIDING CONTACT DEFORMATION BEHAVIOUR OF ENAMEL UNDER WET AND DRY CONDITIONS

◆ **Griselda GUIDONI, M. Swain and I. Jäger.** Nano-scale sliding contact deformation behaviour of enamel under wet and dry conditions, **Journal of Biomedical Research (2007)** ***Submitted.***

5.1. Abstract

Abrasion response of cross sectional areas of enamel was studied by sliding a rounded diamond conical nano-indenter tip along the surface. The nano-indenter tip was scanned over a specific square area with a load of 400 μN. The nominal indenter tip radius was ~ 400 nm. Two different environments were chosen: Hank's balanced salt solution (HBSS) and atmospheric laboratory condition. SEM (Scanning Electron Microscopy) and AFM (Atomic Force Microscopy) were used to characterize the final abraded areas. In addition, single scratches with linear incremented load were performed. The normal load and displacement data were utilized in a complementary manner to support the proposed deformation mechanisms. The latter is also involved in situ measurements of the depth profiles for single scratch tests. Greater orientation dependence for the case of the single scratches in relation to the abrasion tests was found. The latter results are discussed in terms of plastic deformation effects. The abrasion mechanisms were found to be the same for both wet and dry measurements and similar to that described in a previous study (Guidoni et al., 2007e). However, scratch deformation under fluid measurements shows greater recovery effects and abrasion resistance.

Key words: Abrasion, enamel, Hank's balanced salt solution (HBSS), Atomic Force Microscopy (AFM), nano-indentation.

5.2. Introduction

Enamel is the outer part of teeth and the highest mineralized tissue in human beings. Loss of hard tooth substance may be caused by factors other than caries and trauma. In modern man the factors contributing to tooth wear are many (Dahl et al., 1993, Oh et al., 2002). Tooth wear can be classified regarding the cause of wear: attrition, abrasion, erosion (Dahl et al., 1993). In particular, in the present work, abrasion will be treated. It is related to pathologic tooth wear caused by friction from a foreign body, independent of occlusion between the teeth. Tooth brushing could be an example of this type of wear.

Unlike other calcified human structures, fracture of dental tissue is not self-repairing. One of the most important features of enamel is its good wear resistance, even under severe environmental conditions, such as; wide ranging loads (Fernandes et al., 2003), reciprocating grinding-like movements, temperature changes and acidic attacks (West et al., 1999). On the other hand, saliva is thought to reduce wear (Dahl et al., 1993, Turssi et al., 2006). Abrasion may lead to a loss of essential anatomic form and possibly to a change in masticatory efficiency. Severe abrasion may also expose dentine (the layer below enamel) leading to an acceleration of the loss of hard tissue because of the inferior wear-resistance properties of dentine. Thus, understanding friction and wear behaviour of enamel may help the clinical treatment of teeth and may assist with the development of new dental restorative materials (Magne et al., 1999 , Li and Zhou, 2002, Kelly et al., 1996, Dahl et al., 1993)

To the best knowledge of the authors, tribological studies of enamel at the micrometer scale with the high-resolution positioning and testing capabilities a nanoindentation device in

combination with an AFM (Atomic Force Microscopy) have not been reported. In this work we chose to abrade enamel under Hank's balanced salt solution (HBSS) and atmospheric conditions. The latter, plus the scanning of a nano-indenter tip on selected areas of the enamel rod structure, allows us to evaluate the wear process a step further down the hierarchical structure of enamel, i.e. at a scale where mineral fibrils and protein layer responses may be discriminated.

5.3. Material and Methods

One healthy second premolar extracted for orthodontic reasons from a 12 years old human male together with an incisor of a 1.5 year old steer were examined. The samples were cut with a diamond saw in sections along the crown-root direction, carefully avoiding any overheating. One or more pieces of enamel from the same tooth were dehydrated in air ('dry'), the remainder were immersed in Hanks's balanced salt solution, HBSS, ('wet'). An antibacterial was added to HBSS (0.1 % by weight of sodium azide, NaN_3, Merck 888).

The transversal section of the premolar consisting of enamel and dentine was accessible for preparation. The exposed area was ground and polished to a 2500 P grit finish with silicon carbide cloths, followed by polishing in 0.3 μm alumina suspension. In the case of 'wet' conditions, the samples were continuously rinsed with HBSS while polishing, and stored under HBSS at all times to avoid accidental dehydration. This is essential especially in the last stages of preparation.

The nano-indenter tip was scanned across the samples using an add-on nano-indentation device (Hysitron Triboscope, Hysitron Inc., Minneapolis, MN, USA) mounted on the scanner head of an AFM stage (Veeco – Digital Instruments, Santa Barbara, CA, USA). Normal load and displacement data can be recorded and stored.

Two types of specimens were evaluated: 'dry', in which the samples were stored and tested under atmospheric conditions, and 'wet', in which samples were stored under HBSS and sample and indenter tip were immersed in HBSS during testing. For both cases a rounded conical diamond indenter tip (nominal radius of ~ 400 nm) was mounted at the end of a tungsten rod ca. 9.5 mm long in order to keep the transducer at a safe distance from the fluid.

Typical examples of the maximum penetration depth at 400 μN were obtained by making single point indentation tests under both wet and dry conditions.

5.3.1. Single scratches

Single scans with linearly increasing loads *on individual enamel rods* were made. The load was linearly increased from 4 μN to a defined maximum load over a distance of ~ 5 μm at a sliding velocity of 1.2 μm per sec. The maximum loads were 800, 900, 1000, 1200 and 2000 μN for the dry measurements and 400, 1000, 2000 and 4000 μN for the wet measurements. Normal load and displacement were recorded.

5.3.2. Wear tests

Wear tests were carried out by scanning the diamond indenter tip over a certain micrometer sized square area with 400 μN. In previous experiments (Guidoni et al., 2007e, Guidoni et al., 2007d), evidence for removal of material appeared within a reasonable number of scans when using a 400 μN load for both wet and dry experiments. For each test, the normal displacement data was recorded. The indenter tip velocity is determined by the scanning frequency and the dimension of the scanned area. Thus, it will be individually denoted for each particular test.

Window scan side dimension, scan frequency and number of lines (double scans) per abraded area were the experimental set up parameters. The indenter tip moves forward a distance equal to the side of the window (single scan) and then comes backwards on the same track, the same distance (double scan). The distance between two adjacent double scans is given by (size of the window/number of lines). Double scans are parallel among themselves. Once one abraded area is completed, in other words, once the set up number of lines per abraded area is done, the subsequent beginning of another test commences where the last abraded area terminated.

Some tests were deliberately placed inside one single enamel rod and others were chosen to be sufficiently large to incorporate more than one rod, in order to discriminate whether the enamel rod interfaces (also called sheaths) are influencing the wear behaviour of enamel.

Immediately after some of the wear tests, a control image of 5 x 5 μm^2 was taken with the nano-indenter tip in the AFM mode at low loads (2-4 μN). In addition, days after the wear experiments were done, some of the abraded areas were imaged with an AFM tip (under atmospheric conditions) and some were viewed with an SEM (under vacuum).

5.4. Results

The maximum conical tip penetration depth at 400 μN was obtained by making single point indentation tests on the human premolar sample. The penetration data was similar both for wet and dry conditions and it was ~25 nm.

5.4.1. Single scratches

The **single scratches** generated only deformed surfaces, even at the maximum loads tested. Fig. 46 shows AFM images of scratches in a wet condition. Depth profiles were taken across and along the main scanning direction from higher resolution AFM images. In contrast to the dry state, the scratches with maximum loads of 400 μN and 1000 μN in the wet condition were not found with the AFM.

In a previous study (Guidoni et al., 2007e), it was deduced that the damage depth (d) of single scratch tests done with a rounded conical indenter tip is approximately equal to the measured normal penetration depth (h), if $h<<R_e$, where R_e is the effective indenter radius. Since the normal penetration depth, h, was continuously measured in situ during the length of

each scratch test, the normal penetration depth data obtained with the transducer is a direct measurement of the scratch profile, including the elastic and plastic deformation.

The in situ normal penetration depths (*h*) together with the a posteriori AFM depth profiles of both dry and wet conditions are presented in Fig. 47 and Fig. 48, respectively. For all the conditions, except the scratch to 4000 μN maximum load in the wet condition, the start of a visible imprint with the AFM correlates with a lateral displacement equivalent to a normal applied force between 390 and 490 μN.

5.4.2. Area scans

For the case of the **area scans**, the normal penetration depth recorded may be used as an in situ measurement of abraded depth(Guidoni et al., 2007d) following the reasoning for single scratches.

The recorded penetration depths during the entire duration of the last area scan were averaged for each particular test and these values plus their standard deviation are presented in Table 1, in the “displacement data” column. In addition, the abraded areas were imaged with an AFM tip under atmospheric conditions. Profiles at 10 locations were taken along the slow scanning direction and these ten penetration depths for each single test were averaged and the standard deviation calculated. The latter values are shown in Table 1, in the AFM data column.

Human and bovine enamel are thought to be quite similar (see Discussion section below), so for the sake of comparison, Fig. 49 shows an abraded area of the bovine incisor sample (10x10 μm^2, 20 μm/s, 4 area scans, 400 μN, wet). The fibrils underneath the removed material can be observed, they are seen to remain intact.

An AFM image of an abraded area (human premolar sample, 2x2 μm^2, 4 μm/s, 7 area scans, 400 μN, wet) and a line profile are shown in Fig. 50 accompanied by a 3D visualisation. The test was deliberately done inside a rod (enamel sheaths are indicated by broken lines). The marked smoothness of the abraded surface is clearly seen by the general depression in relation with the surrounding region outside the abraded area. The central region in Fig. 50 was preferentially removed while cleaning (the AFM observations of this area during intermediate cleaning steps showed a still filled area). Cleaning was carried out by carefully wiping a tissue paper embedded in HBSS on the tested surface and/or softly polishing the sample in alumina suspension.This localized type of removal was only found for the wet measurements and it was seldom observed.

Two different representative abraded areas are presented in Fig. 51 and Fig. 52, including their 2D AFM images, line profiles and 3D presentation. Fig. 51 corresponds to a measurement done in a dry state and Fig. 52 to a wet measurement on the same sample (human premolar sample, 2x2 μm^2, 4 μm/s, 7 scan areas, 400 μN). In Fig. 52, smooth “strips” of material emerging towards the surface are present throughout the whole area. The same feature is also found in Fig. 49 and will be discussed later. Note the different surface finishes of both abrasion conditions (Fig. 51 and Fig. 52). The surface of the dry abraded area (Fig. 51) is rougher surface than the wet one (Fig. 52). Roughness measurements on selected areas show

an average rms roughness of 13 nm for the abraded area of Fig. 51 and a rms roughness of 3 nm for the abraded surface of Fig. 52. This suggests a more brittle behaviour in the dry state.

5.5. Discussion

Comparable single point indentation penetration depths (~25 nm) for both wet and dry conditions and the use of the same indenter tip leads to similar applied contact pressures during the area scan tests (see for instance (Johnson, 2003)), while the use of samples of only two different teeth rules out inter-sample scatter.

Although most of the literature dealing with mechanical properties of teeth studied human samples (Habelitz et al., 2002, Nalla et al., 2005, Cuy et al., 2002, Xu et al., 1998, Ge et al., 2005, Guidoni et al., 2006, Guidoni et al., 2007c, Guidoni et al., 2007e), there are investigations using bovine samples (Kahler et al., 2003, Kitasakoa et al., 2001, Schilke et al., 2000). No explicit differences were found in the literature in behaviour between these two different teeth origins. Furthermore, within the scope of the present study, they were found to behave comparatively similar.

It is remarkable that for the case of the single scratches, independent of the test conditions, the corresponding imprint became visible at loads around 400 μN (except for the 4000 μN wet single scratch). In previous studies done under similar experimental conditions (Guidoni et al., 2007d, Guidoni et al., 2007e), this load was found to be a threshold load for observing removal of material at a reasonable number of scans by fatigue damage. In the present study, it also appears to be related to the onset of “plastic” deformation.

The single scratch observations show signs of deformation recovery, as registered after imaging the samples with the AFM facility, in both wet and dry conditions. Even though not a decisive probe, the fact that the low load scratches were not found for the wet sample when AFM imaged, but were observed for the dry specimen indicates the influence that the environment has on the deformation and recovery processes in enamel.

The 4000 μN single wet scratch is a particular case since not only did the normal penetration depth exceed the transition between spherical and conical shape of the indenter tip (transition expected at around 120 nm height) but it was also accidentally placed close to the sheath of a rod (Fig. 46). The higher organic content of these regions leads to a different mechanical response with respect to the centre of the rods (Ge et al., 2005, He and Swain, 2006) and as also observed in (Guidoni et al., 2007e), the sheaths respond different to the cores with respect to abrasion. The influence of the transition between the spherical and conical shape of the indenter is presumably related to a change in abrasion mechanism. The abrasion mechanism is related to the effective angle of attack for the scratching body (Zum-Gahr and Karl-Heinz, 1987, Guidoni et al., 2007e, Hutchings, 1992) and is closely related to the indenter tip angle (Guidoni et al., 2007e).

Two different scratching responses are found in Fig. 48. The single scratches from 800 to 1200 μN showed higher normal penetration depth than the 2000 μN single scratch, the main difference being a 180º change in scanning direction between the former and the latter tests.

The orientation of the fibrils inside the rods is expected to gradually change from one rod to the adjacent one (Macho et al., 2003, White et al., 2001). A schematic scaled representation of the proposed mechanism is presented in Fig. 53 and Fig. 54. If the inclination of the fibrils for the low load single scratches of Fig. 48 is thought to be in the direction of the scanning movement (Fig. 53), the opposite orientation of the fibrils with respect to the indenter tip movement is more likely to occur for the fibrils of the rod tested to 2000 μN load and 180º difference in scanning direction (Fig. 54). In Fig. 53, the fibrils orientation results in a cooperative shear relative to the indenter moving direction, while in Fig. 54 it is not. Thus, the sliding resistance will be lower for the former case than for the latter one.

There were no significant differences in wear mechanism between wet and dry measurements, despite the final results being different. In a previous study (Guidoni et al., 2007e) the abrasion mechanism under the tested dry condition was found to be mainly a plastic asperity deformation process followed by sub-surface fatigue damage, which at a certain combination of load and scan cycles leads to removal of material. The same mechanism describes the abrasion response under the wet conditions tested.

Regarding the abrasion mechanisms, these are clearly evident in Fig. 49. The plastic deformation of the structure can not only be seen from the smoothness of the surface, but also from the remnant “wave” of deformed materials on the borders of the abraded area. The black arrow indicates the place where mineral fibrils appear to be moved by the indenter tip during the abrasion process, although they look to be displaced more than broken. Marked with an ellipse are regions where the sub-surface damage emerged to the surface, similar regions can be seen in Fig. 50 and Fig. 52. Those areas will be preferentially removed in further scans, or during cleaning of the sample.

The presence of inter-rod boundaries seems not to influence the abrasion mechanism after successive superimposed scannings, since no trace of them can be found inside the abraded area within the flattened surface layer (Fig. 49), in strong contrast to the results of single scratches. On the other hand, the inter-rod boundary zones are presumably not the loci of preferential damage, since the right damage area in Fig. 49 shows no indication of a boundary. In addition, the existence of a removed zone in Fig. 50, where the abraded area was placed inside one single rod also supports this statement.

According to Fig. 51, the superficial damage generated during the dry measurements seems more likely to be generally lost after the cleaning procedures. Note the smoothness of the outer region in Fig. 51, when comparing it with the abraded surface even though both surfaces experienced the same cleaning procedure. All the imaged tested areas presented the same feature. On the contrary, for the case of the wet measurement (Fig. 52) the highly deformed superficial layer seems to be still attached to the substrate after the abrasion tests and cleaning phase. For the dry tests, after the cleaning procedures, the removal of material appears to be related to a general detachment of the superficially deformed layer which also involves taking away material surrounding the abraded area. In Fig. 51, the size of the damaged area clearly exceeds the 2x2 μm^2 tested area. On the contrary, for the case of the wet samples,

removal of material after cleaning, when evident, was highly localized around an already visible damage region (Fig. 50) and was seldom observed. In general, the wet abraded areas were similar to those shown in Fig. 52, where the abraded deformed surface is smooth and where the "plastically" deformed structure emerges to the surface. The abraded area without cleaning resembles the final abraded area after cleaning, except for the elimination of debris.

It is notable that the results found for the displacement data and AFM profiles of the abrasion tests in the case of dry measurements are similar, as shown in Table 5, whereas in the wet state they are not. In addition, although the tests were done in different rods, the dependence in fibril orientation which was found for the single scratch tests could not be found in the case of the abrasion test. The first scans plastically deform the asperities and its resistance to the deformation will depend on the orientation of the fibrils with respect to the indenter movement. However, once the surface is plastically deformed, further scans will slide on a smooth, highly deformed surface. This smoothing or homogenization effect may explain the fibril orientation and scanning direction dependence for the single scratches and the independence of orientation effects for the abrasion tests.

5.6. Conclusions

- The abrasion mechanism under the tested dry and wet conditions is mainly a plastic asperity deformation process followed by sub-surface fatigue damage, which at a certain combination of load and scan cycles, leads to removal of material.
- A load of around 400 μN applied with this indenter tip appears to be related to the onset of "plastic" deformation of enamel.
- Single scratches are more sensitive to microstructural arrangement than abrasion tests. Once the surface is plastically deformed after the first scans, the following scans will slide on a smooth, highly deformed homogeneous surface. Thus, the microstructural native arrangement, including differences between rod- and inter-rod enamel does not play a role.
- Recovery effects are also present during sliding deformation in enamel for both wet and dry conditions, although HBSS favours this behaviour.
- While the highly deformed superficial layer is still visible after the cleaning procedures for the wet sample, it was removed for the dry ones exposing the underlying bulk material. This may indicate a better abrasion resistance for the former than for the latter condition.
- Within the scope of the present study, bovine and human enamel were found to behave comparatively similar.

5.7. Acknowledgements

Financial aid through EC Contract No MEST-CT-2004-504465, „Marie Curie Host Fellowships for Early Stage Research Training", is gratefully acknowledged.

FIGURES OF CHAPTER 5

Fig. 46

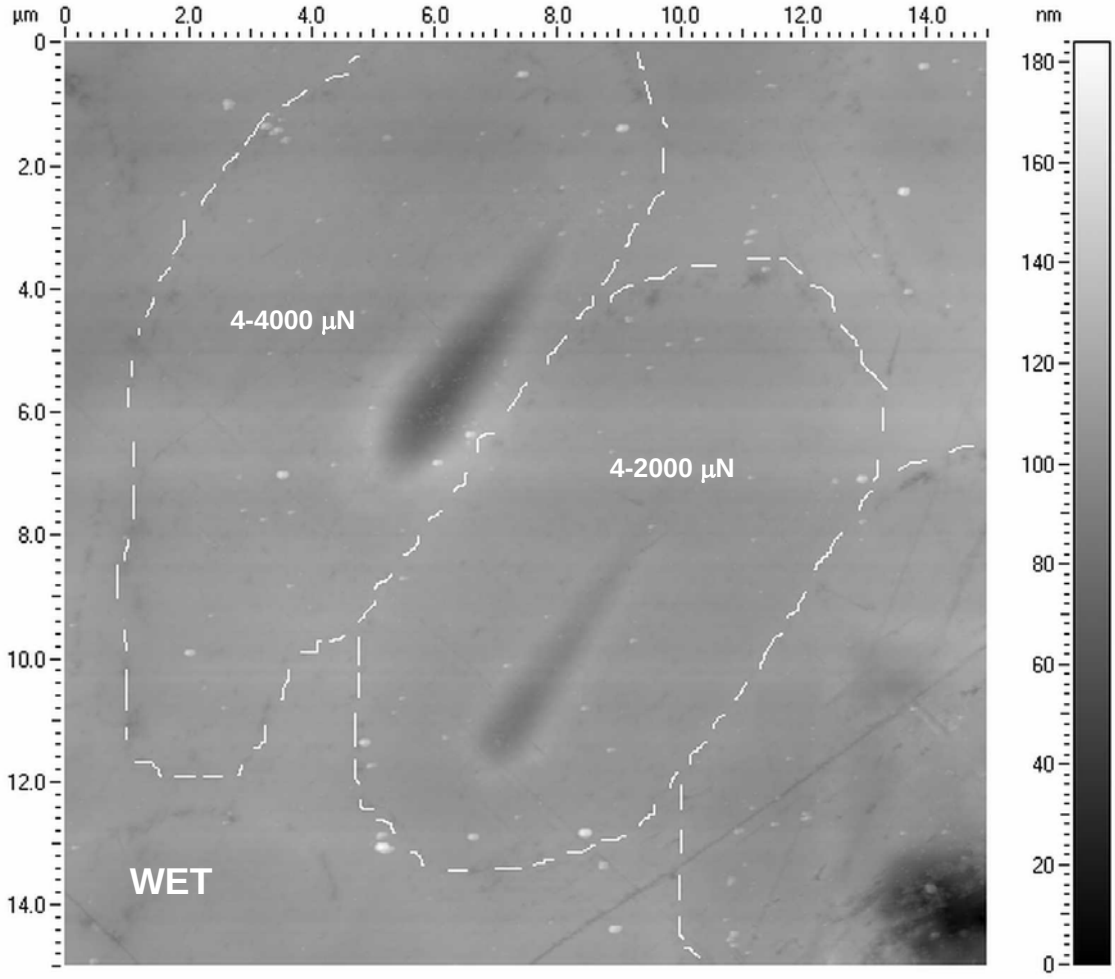

Fig. 46 15x15 µm^2 image of the wet single scratches taken with the nanoindenter tip in the AFM mode. The broken lines were drawn to show the enamel rod interfaces. Note the proximity of the 4000 µN single scratch to the enamel sheath.

Fig. 47

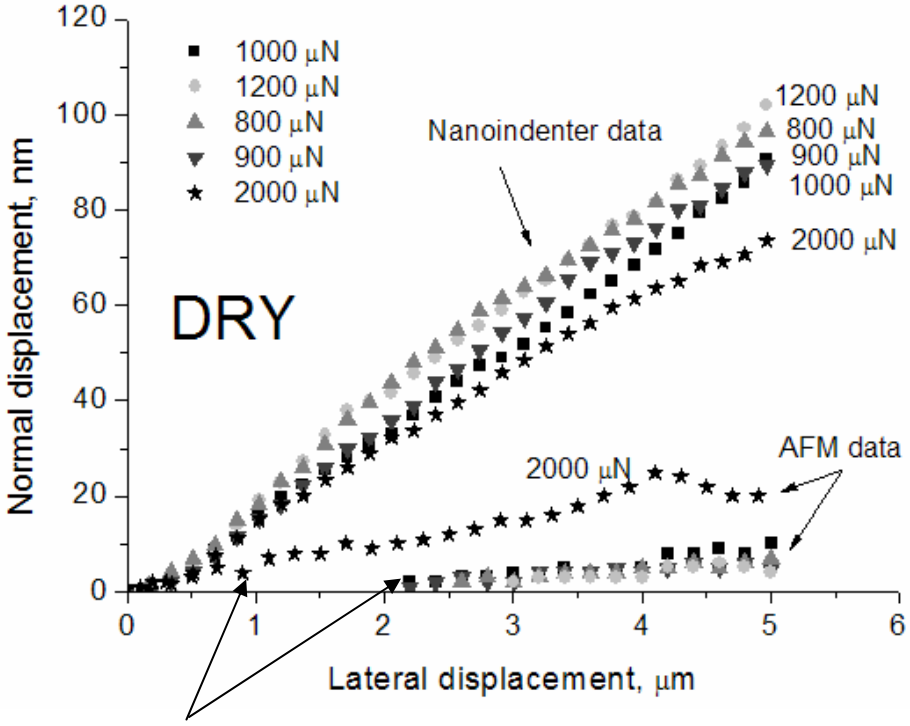

Equivalent normal load between 390 and 490 μN. Beginning of visible imprint.

Fig. 47 Normal displacement data versus lateral displacement of the dry single scratch tests. "Nanoindenter data" refers to the in situ normal displacement values obtained from the transducer which are equivalent to the damage depth, *d*. "AFM data" was measured after analysing the AFM line profiles along and across the direction of the scratch. The 2000 μN single scratch was done at a 180º change in scanning direction with respect to the remaining single scratches.

Fig. 48

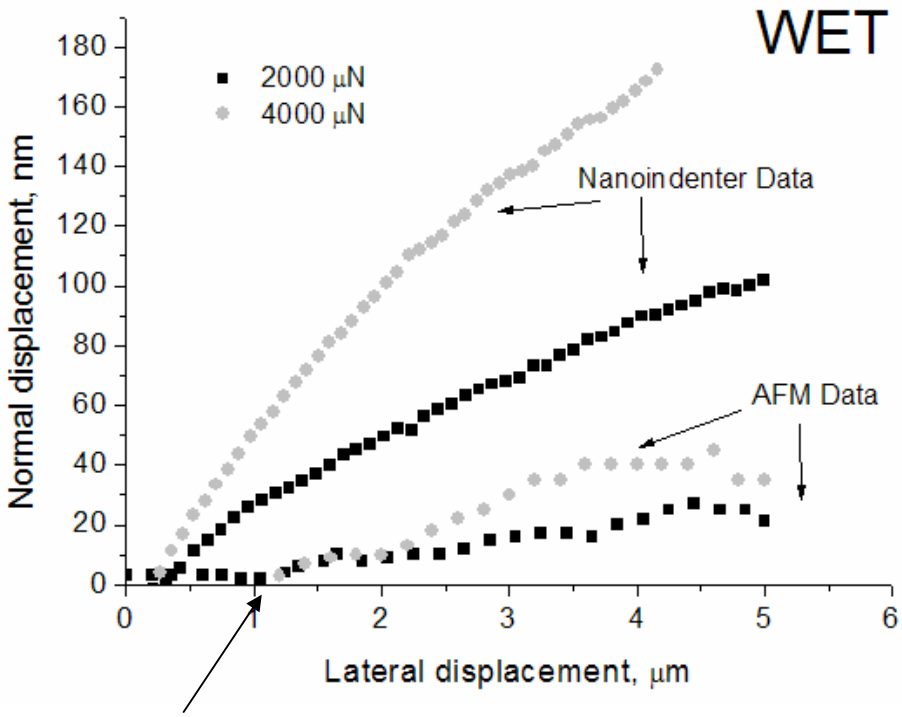

Fig. 48 Normal displacement data versus lateral displacement of the wet single scratch tests shown in Fig. 46. "Nanoindenter data" refers to the in situ normal displacement values obtained from the transducer which are equivalent to the damage depth, *d*. "AFM data" was measured after analysing the AFM line profiles along and across the direction of the scratch.

Fig. 49

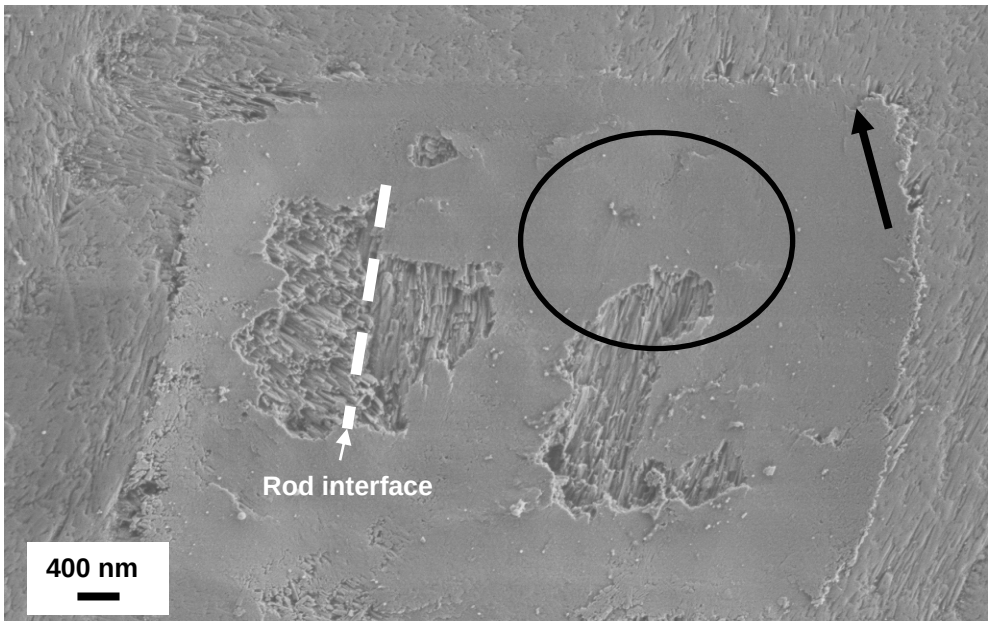

Fig. 49 High resolution SEM image of an abraded area of the bovine incisor sample (10x10 μm^2, 20 μm/s, 4 area scans, 400 μN, wet). The fibrils underneath the removed material can be observed, they are seen to remain intact. Note the different orientation of the fibrils in the abraded area where material was removed (left side removed area), presumably corresponding to a rod interface (marked with a discontinuous white line). Compare the smoothness of the abraded area with the outer surface. Moreover, compare the roughness of the fibrils underneath the right side removed area with the right side outer area, judging by this picture they belong to the same rod although only the former region was abraded. The plastically deformed surface is also observed along the borders of the abraded area as a "wave" of material approaching the borders. Marked with an ellipse is an area where the abrasion damage emerges to the surface. The arrow indicates a zone where the mineral fibrils seem to be pushed out of the tested area.

Fig. 50

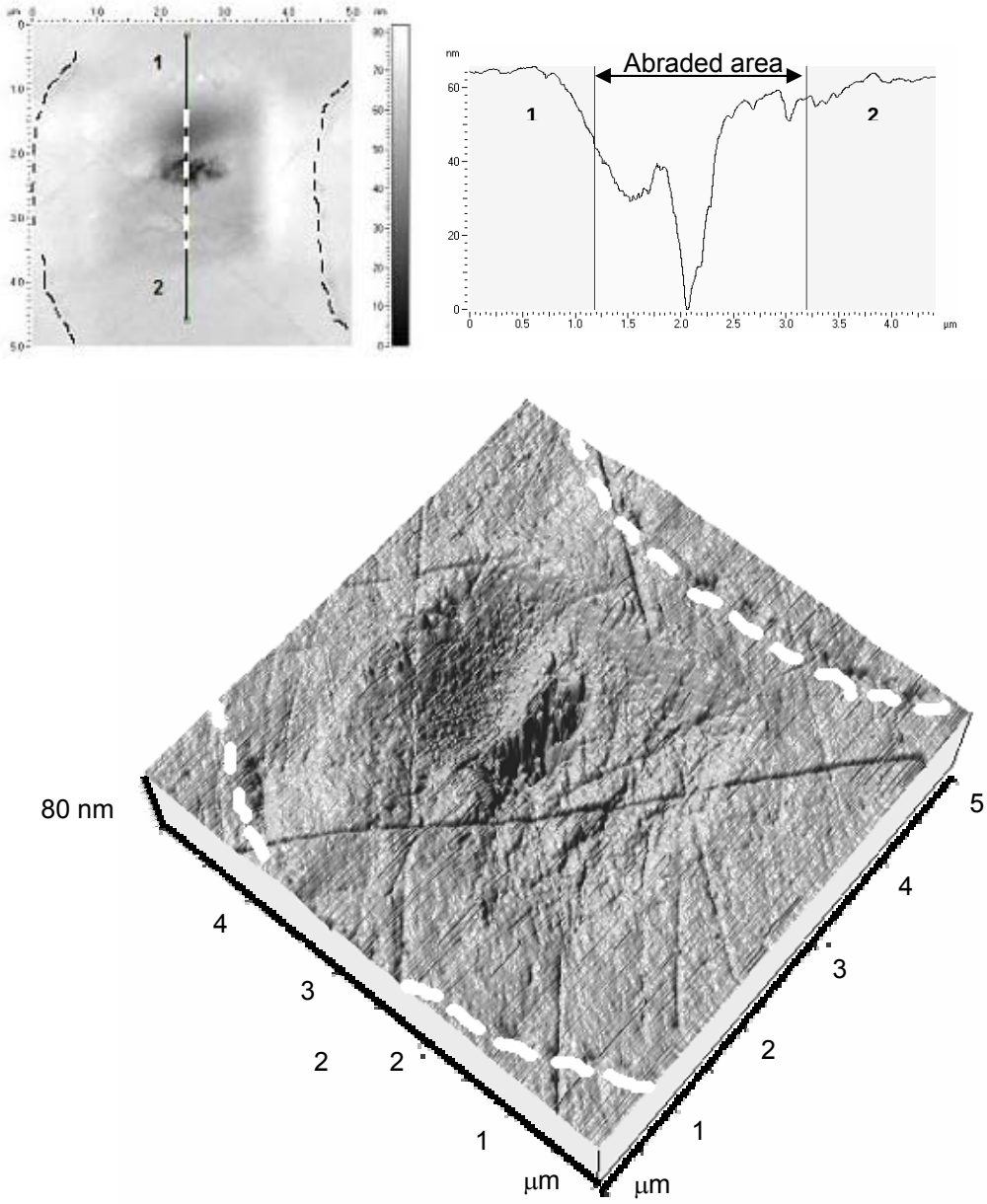

Fig. 50 5x5 μm^2 AFM image of an abraded area (human premolar sample, 2x2 μm^2, 4 μm/s, 7 area scans, 400 μN, wet). and its corresponding line profile. A 3D visualisation from the AFM image is shown in the bottom of the figure. Marked with dashed lines are the rod interfaces (or enamel sheaths). The test was deliberately done inside a rod. The central region was preferentially removed while softly wiping the sample with a tissue paper embedded in HBSS. This localized type of removal was only found for the wet measurements and it was seldom observed.

Fig. 51

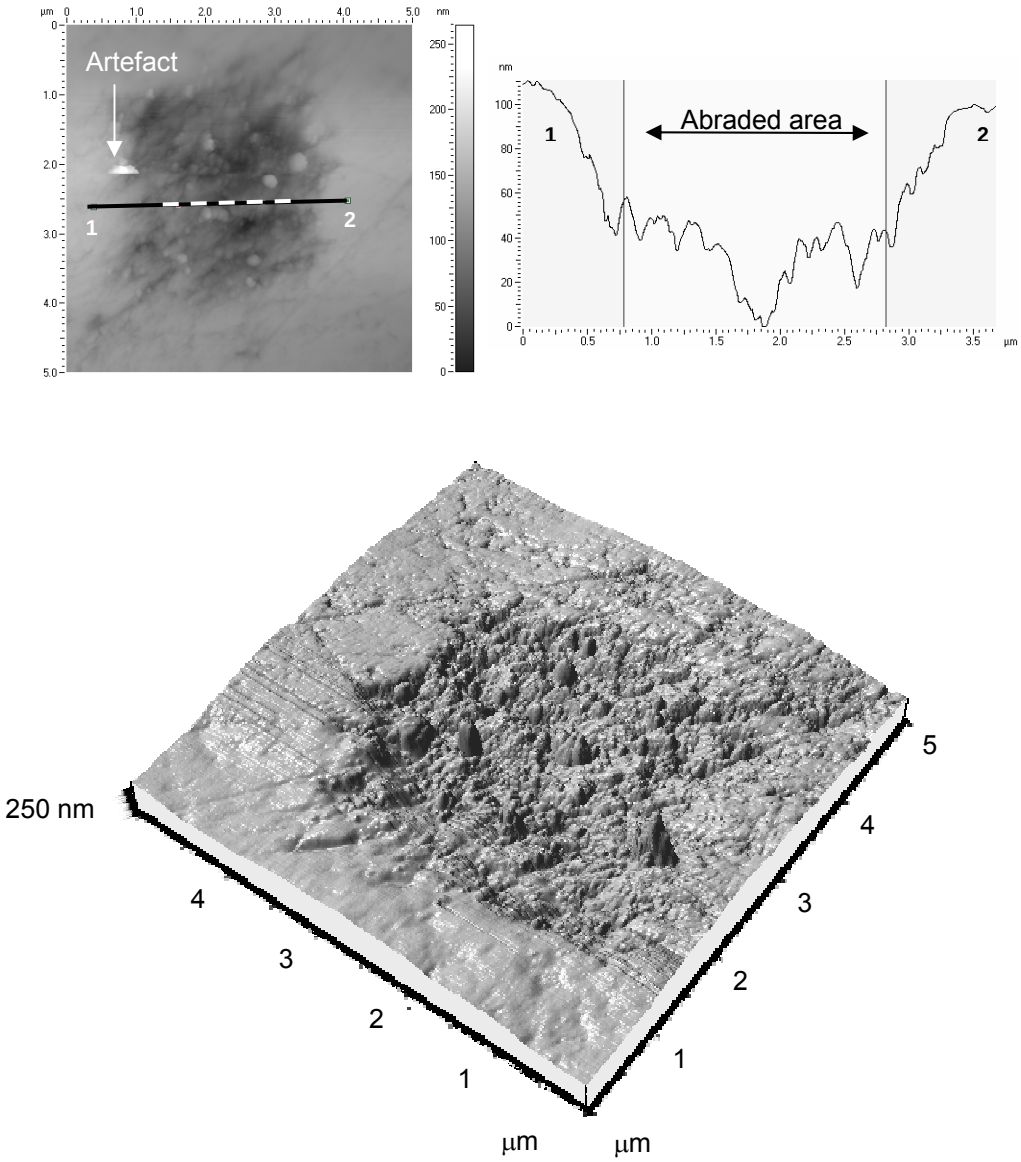

Fig. 51 5x5 μm^2 AFM image of an abraded area (human premolar sample, 2x2 μm^2, 4 μm/s, 7 area scans, 400 μN, dry) and its corresponding line profile. Due to an artefact pointed out in the figure the z-scale here goes up to 250 nm although the baseline is around 100 nm for the abrasion area. A 3D visualisation from the AFM image is shown in the bottom of the figure. The test was deliberately done inside a rod (rod interfaces not seen in this image).

Fig. 52

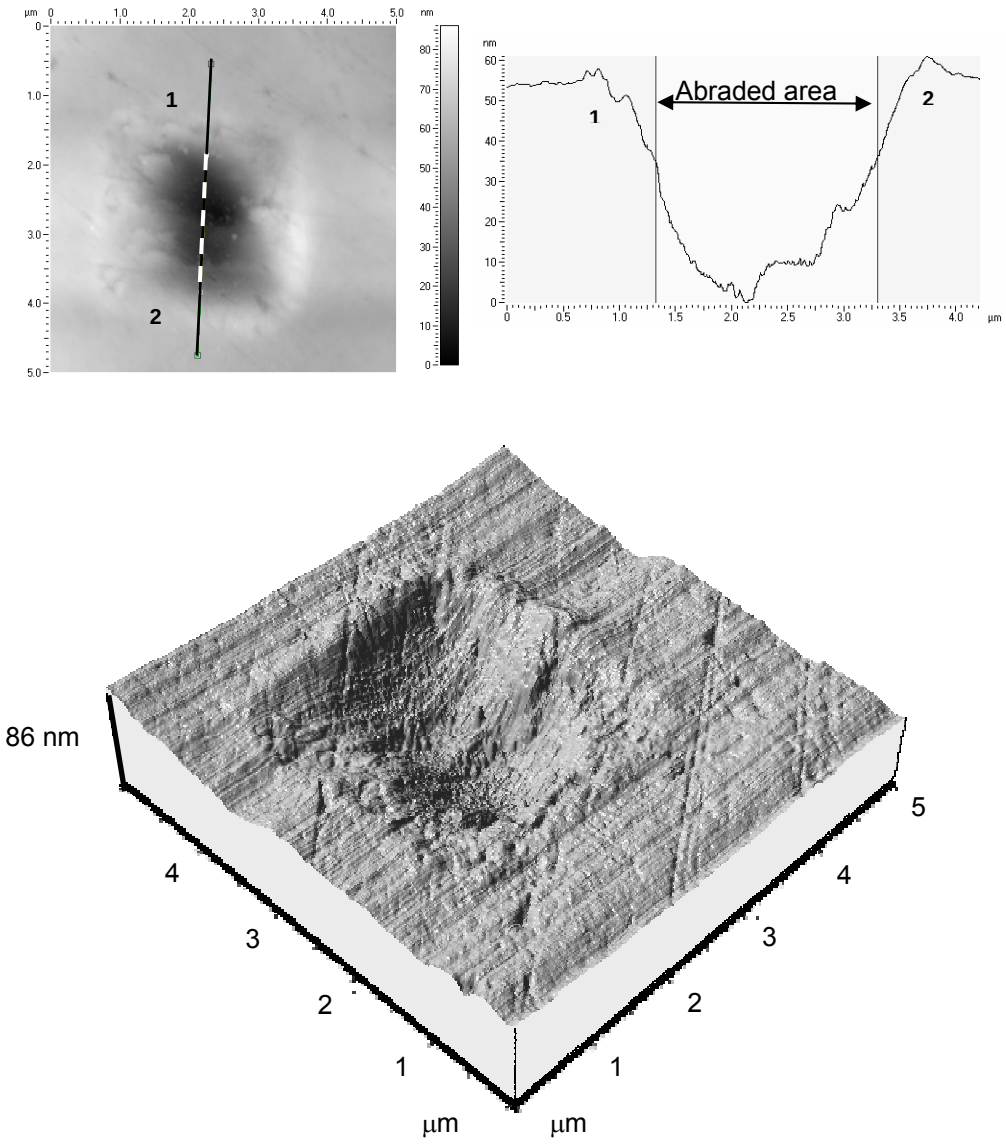

Fig. 52 5x5 μm^2 AFM image of an abraded area (human premolar sample, 2x2 μm^2, 4 μm/s, 7 area scans, 400 μN, wet) and its corresponding line profile. A 3D visualisation from the AFM image is shown in the bottom of the figure. The test was deliberately done inside a rod (rod interfaces not seen in this image).

Fig. 53

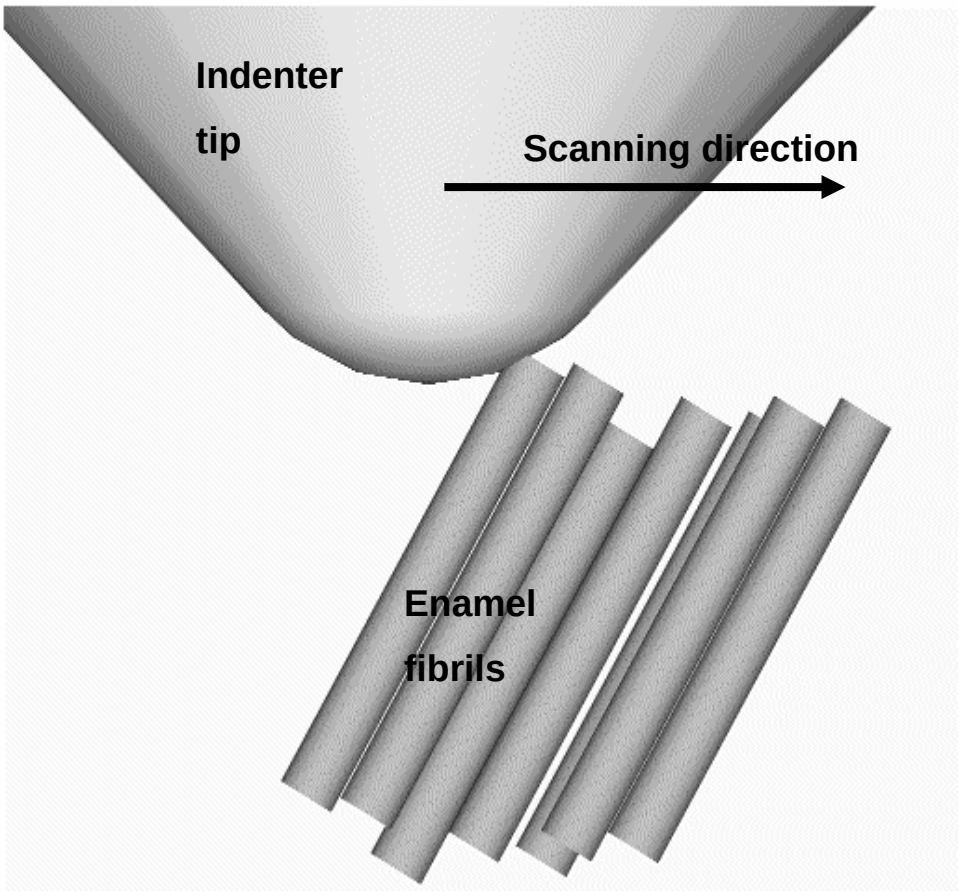

Fig. 53 Scaled representation of the proposed model of the dependence of scanning direction on the single scratch tests. Nominal tip radius = 400 nm; fibrils diameter = 100 nm. The arrangement shown in this picture corresponds to the proposed microstructural fibril orientation-indenter tip scanning direction combination of the single scratches done dry at 800, 900, 1000 and 1200 μN, presented in Fig. 47.

Fig. 54

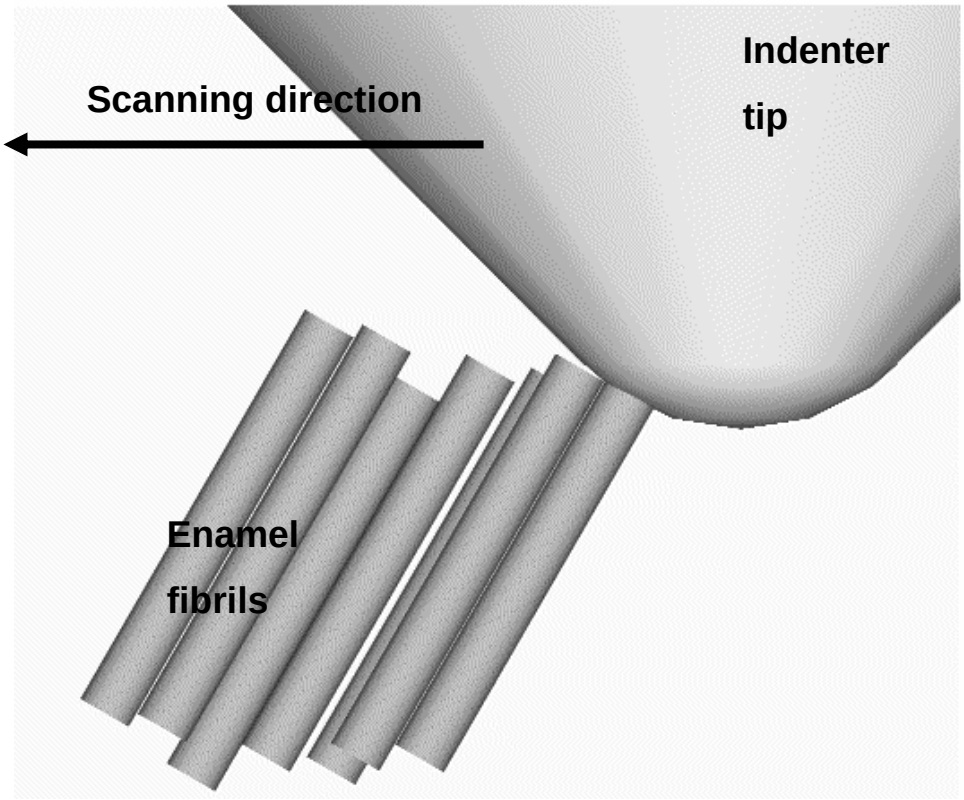

Fig. 54 Scaled representation of the proposed model of the dependence of scanning direction of the single scratch tests. Nominal tip radius = 400 nm; fibrils diameter = 100 nm. The arrangement shown in this picture corresponds to the proposed microstructural fibril orientation-indenter tip scanning direction combination of the single scratches done dry at 2000 μN, presented in Fig. 47.

TABLES OF CHAPTER 5

Table 5

	Displacement data	AFM
DRY1	88.6 ± 20.60	82 ± 19
DRY 2	81.9 ± 13.25	87 ± 18
DRY 3	97.5 ± 22.93	81 ± 15
DRY ABRA1	83.6 ± 23.79	141 ± 12*
DRY ABRA2	103.5 ± 26.64	120 ± 21*
WET1	54.6 ± 16.28	31 ± 16
WET 2	80.2 ± 6.38	49 ± 15
WET 3	136.7 ± 40.49	-
WET ABRA1	120.5 ± 17.82	23 ± 5**
WET ABRA2	78.0 ± 20.24	33 ± 6**

*** Other tests, not included in this report, where also done near this area and without the adding of new particles they presented AFM depths of 88 ± 12; 100 ± 8 and 127 ± 12 nm.**

**** Their profiles do not show a totally clean area.**

Table 5. Wear tests carried out at 400 μN. Seven scans of 256 scratches each. 2 x 2 μm^2 areas. Each value corresponds to one single test. For the "Displacement data" column, the mean values are the average penetration depth extracted from the load-displacement data throughout the 2 x 2 μm^2 area of the seventh scan follow by their standard deviation. In the case of the "AFM" column, mean values are the average depth of 10 profiles taken along the fast scanning direction follow by their standard deviation.

CHAPTER 6

6. ENAMEL: BRITTLE TO DUCTILE LIKE TRIBOLOGICAL RESPONSE

◆ ***Griselda GUIDONI, M. Swain and I. Jäger.*** *"Enamel: from brittle to ductile like tribological behaviour"* **Journal of dentistry (2008)** ***Submitted.***

6.1. Abstract

A sharp cube corner indenter tip (20-50 nm radius) was used to abrade glass, enamel as well as copper and silver mono-crystals. Square abraded areas (5 x 5 μm^2, 10 x 10 μm^2) were generated with loads of 50 μN for enamel and 100 μN for the remaining materials (2D abrasion). The normal load and displacement data were utilized in a complementary manner to support the comparison. In addition normal and lateral forces were simultaneously measured along 10 μm single scratched lines (1D abrasion). SEM (Scanning electron microscopy) and AFM (Atomic force microscopy) were also used to characterise the worn areas and debris. The sharp tip cuts into and ploughs the specimens creating a wedge or ridge of material ahead of itself which eventually detaches, for the ductile materials and high loads in enamel. For glass and enamel at low loads, the indenter tip ploughs into the material and the removed material is redistributed and pressed back into the abraded area. The role of the microstructural heterogeneity in the wear behaviour of enamel is considered in the discussion.

Key words: Attack angle, indentation strain-stress, abrasion, enamel.

6.2. Introduction

Enamel is the highest mineralized tissue in the human body. It is composed of approximately 97 % by weight of mineral, essentially non stoichiometric hydroxyapatite (HAp), 1 % organic material, mostly protein, which is not collagen, and 2 % water (Currey, 2002). As with most biological materials, it has a hierarchical microstructure, which imparts order from the nm to mm scale.

Crystallites of enamel are roughly rectangular in cross section with mean width of 45 nm and mean thickness of 25 nm (Selvig and Halse, 1972), and are “glued” together by a thin protein layer of not more than 2.5 nm. Besides the “glueing” of the microstructure with proteins, White and co-workers (White et al., 2001) highlighted that the remaining proteins spread the damage laterally over a much larger volume and may allow limited differential movement between adjacent rods, preventing thus catastrophic damage.

At the micrometer scale of the hierarchical organization of enamel, apatite crystals are bound together in bundles called prisms or rods that form in a radial manner from the dentine enamel junction to the external surface. Each rod is 3-6 μm in diameter. There is little protein within the prisms, while it is mainly concentrated at the interprism regions (Currey, 2002). This region is often called enamel sheath, and consists also of apatite crystals that are not part of the prisms and have a certain degree of mis-orientation with the axis of the rods (White et al., 2001). The enamel prisms themselves are arranged in a crossed, plywood-like structure (Currey, 2002, Macho et al., 2003) which is thought to act as a crack arrester.

The amount of enamel is limited in thickness to some millimetres per tooth sample. This latter situation, plus the complex hierarchical structure described above, make nanoindentation (Staines et al., 1981, Cuy et al., 2002, He et al., 2006, He and Swain, 2007d, He and Swain, 2007a, He and Swain, 2006, Habelitz et al., 2002, Ge et al., 2005) and nanoscratching (Guidoni

et al., 2007b, Guidoni et al., 2007d, Guidoni et al., 2007e, Habelitz et al., 2001b) suitable techniques for the characterization of this system. Regarding tribology, the majority of wear studies in enamel have been made at the micrometer scale (Zheng et al., 2003, Li and Zhou, 2002) and macroscopic scale (West et al., 1999, Sajewicz, 2006, DeLong, 2006, Pintado et al., 1997, Magne et al., 1999). However, there is some incipient literature on wear on enamel at the nanometre scale (Guidoni et al., 2007d, Jandt, 2006, Guidoni et al., 2007b, Guidoni et al., 2007e). Jandt et al. (Jandt, 2006) used AFM and nanoindentation to study the influence of erosion on enamel by measuring the change in mechanical properties after immersing enamel under different acidic soft drinks. Habelitz et al. (Habelitz et al., 2001b) studied the width of the dentine-enamel junction (DEJ) by nano-scratching. Guidoni et al. described the abrasion mechanism of enamel using the same indenter tip and different environments (Guidoni et al., 2007d, Guidoni et al., 2007b) and also comparing the wear mechanisms generated after using two different indenter tips: conical rounded and sharp cube corner tips (Guidoni et al., 2007e).

Thus, based on previous studies (Guidoni et al., 2007e) with a sharp cube corner indenter tip, the tribological response of enamel is compared with the abrasion response of an amorphous glass and two ductile materials, copper and silver mono-crystals. Since the mechanical properties of enamel are known to be viscoelastic (Guidoni et al., 2007c, Zhou and Hsiung, 2006a, He et al., 2006, He and Swain, 2007a, He and Swain, 2006), the chosen materials for comparison are considered to be at the two extremes of the expected mechanical behaviour of enamel, plus having the advantage of being well studied and homogenous systems.

6.3. Materials

For the investigation reported here one incisor of a 1.5 year old steer was used. The tooth was cut with a diamond saw into two sections along the crown-root direction, carefully avoiding any overheating. A second premolar from a 12 year old male individual and a wisdom tooth of a 26 year old male individual extracted for orthodontic reasons were prepared following the same procedure and also tested.

In all cases, the transversal section of the samples, consisting of enamel and dentine, was accessible for preparation. The exposed area was ground and polished to a 2500 P grit finish with silicon carbide cloths, followed by polishing in 0.3 μm alumina suspension.

The glass specimen was a borosilicate laboratory sample (optical microscope plate), which was cleaned and tested as received (50 x 20 x 5 mm plate). The single crystals of copper and silver, all with a (1 1 1) surface orientation, were wet ground and mechanically polished using alumina suspension with a grain size of 1 μm. Electropolishing was then performed in order to removed any deformation layer produced during the last polishing steps. A detailed description of these single-crystals may be found in (Rester et al., 2007).

6.4. Tribological Tests

Wear tests were carried out using an add-on nanoindentation device (Hysitron Triboscope, Hysitron Inc., Minneapolis, MN, USA) mounted on the scanner head of an AFM stage (Veeco – Digital Instruments, Santa Barbara, CA, USA).

The same sharp cube corner indenter tip (20-50 nm radius) was used for all the tests.

Load-displacement data of single point indentations (0D) were used to ascertain the maximum penetration depth over the load range investigated. The average penetration depths for all the materials are presented in Table 6.

Single scans (1D) at constant load were done with a Triboindenter with an additional lateral force transducer. The scratched distance was 10 μm and the scan speed was 2 μm/s. Loads of 50 μN (on the bovine incisor), and 100 and 300 μN (on the human premolar) were used. For the remaining materials, the chosen load was 100 μN. An indentation test at the starting point of the scratch was made immediately before the single scratches tests started.

Wear was carried out by scanning the diamond indenter tip over a certain area (2D) with a load higher than typical for surface imaging (Imaging load ≈ 2-4 μN). Feedback load controlled measurements were done, which enabled the normal displacement and normal load data to be recorded continuously. The indenter tip sliding speed varied from 10 μm/s to 20 μm/s. The abraded areas were 10x10 μm^2 and 5x5 μm^2.

Some terminology will be defined in order to avoid confusion. Single point indentations in which there is no lateral movement, only normal loading was applied are designated (0D). “Scan” is used to denote the constant rate movement of the indenter tip in one direction along one line (1D). “Double scan” means the movement of the indenter tip forward and backward along the same line. “Area scan” (2D) is employed to indicate a certain amount of parallel double scans placed one beside the other. The final shape of the scan area is a square. The space between double scans is determined by the chosen number of double scans in each particular test. If more than one area scan is done in the course of one single test, the test is named “double area scan”, “triple area scan”, etc, depending on the number of area scans carried out. The second area scan begins where the first area scan terminated. This procedure is repeated for the successive area scans. The area scan tests consisted of 128 double scans corresponding to a spacing of (10/128) or (5/128) μm apart.

6.5. Results

The effective radii of contact (a) of the indenter tip were calculated using the calibrated area function ($A_{(h)}$) and the penetration depth (h), by means of $A_{(h)} = \pi a^2$. The contact pressure (P) was obtained dividing the load (W) by the contact area ($A_{(h)}$), thus $P = W/A_{(h)} = W/\pi a^2$. The above parameters are presented in Table 6.

The indenter tip geometry will influence the wear response of the system (Guidoni et al., 2007e). Thus, the contact between indenter and sample was considered. Due to the anisotropy associated with the triangular pyramid of the indenter tip used, the analysis was made

considering effective cone angles (that is using the conical effective indenter tip which would generate the same contact area for the same penetration depths (Fischer-Cripps, 2004)). The indenter tip radius used lies between 20-50 nm, which indicates that the effective conical shape would start above 6-16 nm penetration depth. Thus, for all the cases presented in Table 6, the contact strain associated with this indenter tip can be represented by $\tan\beta = \tan(90º-\alpha)$, where β is the semi contact angle and it is equal to the complement of the indenter tip half angle (Tabor, 1970). The contact strain associated with the different scratching tests is therefore constant.

Included in Table 6 is the spacing between double scans for the area scans (2D abrasion) and whether there was superposition or not between adjacent double scratches. The abraded penetration depth was obtained from the displacement data obtained from the transducer. The normal displacement was averaged throughout the abraded area and the standard deviation from this data was calculated and presented as error bars.

6.5.1. Glass sample

The single scratches (1D) show a linear increment of lateral force with lateral distance. A constant normal force of 100 μN leads to a 60 μN lateral force at the beginning of the displacement to 90 μN at the end of the 10 μm single scratches. Two different arbitrary orientations were tested, no significant differences were found.

The area scans show a flat and homogenous abraded area. Fig. 55, in the left upper corner, shows an AFM image of one abraded area with its corresponding line profiles (Glass, 10 x 10 μm^2, 20 μm/s, 1 area scan, 100 μN). In the lower left corner a high resolution SEM image of the abraded area is shown. The nanoindenter path is distinguishable at higher resolution SEM. The AFM's from sectioned profiles corroborated the validity of the data obtained from the nanoindenter transducer (see Table 6).

6.5.2. Enamel sample

For the case of the human premolar, **single scans** at 300 μN were done at two different arbitrary orientations on the cross section. The friction coefficient vs. time shows the same trend as the lateral force vs. time, that is a stick-slip response. No orientation dependant difference was detected in the above response. For the arbitrarily (called 0º) orientation, the normal penetration depth decreases with time. Fig. 56 shows an SEM image of the single scan tracks. The material removed by the indenter tip is also observed and consisted primarily of one entire swarf of material. Fig. 56b shows a higher magnification SEM image of the lower single scratch. The swarf presents a serrated surface.

The single scans done on the enamel of the wisdom molar at 100 μN normal load also show stick-slip response. However, in this case, the swarf of material was more unstable and broke into small pieces, presumably due to the lower penetration depths with the consequent thinner stripes of material ahead of the indenter tip. On the contrary, the bovine incisor tested at 50 μN presents a continuous increment in normal penetration depth during the duration of the

tests. Both friction coefficient and lateral force vary linearly with time. Friction coefficients increase from ~ 0.1 at the beginning of the scan to ~ 0.6 at the end.

When the **scanned areas** were imaged with the nanoindenter tip after the abrasion tests the removed material is pushed away to the borders of the image window, where agglomerates of debris formed (Fig. 57. Human premolar, 5x5 μm^2, 10 $\mu m/s$, 3 area scans, 100 μN). These previous studies were not considered quantitatively, as they were done in order to find suitable testing conditions. However, qualitatively they may provide additional important information. Fig. 58 shows higher resolution SEM images of the agglomerates (Human premolar, 5x5 μm^2, 10 $\mu m/s$, 7 area scans, 300 μN). Note the thin form of the removed lamellas (debris) of material and how they become folded (left image) and form agglomerates.

On the contrary, Fig. 59a (Bovine incisor, 10x10 μm^2, 20 $\mu m/s$, 1 area scan, 50 μN) shows a SEM image of a scanned area without any post cleaning or sample preparation procedure. All the removed material remains inside the tested area. It displays a tendency to agglomerate. Fig. 59b (Bovine incisor, 10x10 μm^2, 20 $\mu m/s$, 1 area scan, 50 μN) is a detailed image, at higher magnification, of the marked region of Fig. 57b. Some remaining ploughing furrows are shown along with chip like structures. The indenter tip path can also be clearly seen.

6.5.3. Copper and Silver single-crystals

Most of the work was carried out on copper, although some data is presented on 2D abrasion of silver for comparison (Table 6). Silver and copper behaved similarly, although only Cu observations will be shown apart from the results presented in Table 6.

Single scratches (1D) on copper at 100 μN load show stick-slip behaviour. Regarding the **area scans** (2D) of copper these were evaluated both qualitatively and quantitatively. The quantitative results (QT) are shown in Table 6.

Qualitative results (QL):

- During the first area scan (or in general, odd area scan), the indenter tip ploughed and cut the material; during the second area scan (or in general, even area scans) the material was pressed into the abraded area. In the latter case the abraded area seemed smoother and cleaner. Fig. 60.
- Copper withstands large plastic deformation without breaking. Fig. 61 shows an extreme case tested with a 20 nm space between adjacent double scratches. Note the thickness of the copper lamellas (~ 20 nm). Dislocation patterns associated with this severe deformation can be seen on the lower right corner of the image.
- Even though the abraded areas were not imaged with the nanoindenter tip, the debris did not remain inside the abraded area. It was mostly relocated to the outer lateral borders.

6.6. Discussion

6.6.1. Glass like behaviour of enamel (low loads)

The stick-slip like action in the case of enamel was recorded as sudden drops in the friction coefficient during the single scans done with the lateral force transducer at 300 μN (Fig. 56) and 100 μN. In addition, in Fig. 57 (human premolar sample, 10x10 μm^2, 20 μm/s, 3 area scans, 100 μN) is an SEM image containing removed pieces of material. Although the spacing of the serrations could not be determined from the SEM images, the serrated like appearance of this swarf debris agrees with the stick-slip observation and may correspond to the repeated sequence of formation and detachment of the piled up wedge of material in front of the indenter.

The strip of material ahead of the tip is deposited on the other side of the scanned area if the loads are high enough to produce thick strips. The single scratch tests done with 300 μN confirm this (Fig. 56). The existence of a continuous strip of material with this load is also registered in the normal penetration depth vs. time data, as the continuous pushing of a swarf of material ahead and in contact with the indenter tip leads to frictional decrement of penetration depth with scratched distance. However, at the very low load of 50 μN, the thickness of the strip is thin enough to produce rupture by its own weight before the other side of the scan area is reached. From Fig. 57a, it can be seen that almost all the removed material remained inside the scanned area. The strip is then destroyed by the posterior movement of the indenter tip, although some remnants of strips are also seen. The above mechanism is also confirmed by the registered increase in penetration depth with scratched distance of the single scratch tests at 50 μN.

While the single scratches done on the wisdom tooth enamel at 100 μN load showed stick-slip response, the same initial conditions in glass (normal load and initial penetration depth, and hence contact pressure. Table 6) led to a linear increment of lateral force with lateral movement. However a 20 % reduction in contact pressure in enamel (equivalent to 50 μN load, Table 6) led to a glass like response of this system.

Interestingly, while the same behaviour is recorded in single scratches for enamel at 50 μN and glass at 100 μN, the same setup conditions as for area scan tests led to considerably differences in penetration depth (Table 6). The possible cause of this considerable difference is in the resultant lateral forces: from 60 to 100 μN in 10 μm for glass and 10 to 30 μN in 10 μm for enamel. While the pile up of debris ahead and on the side of the tip seems to be pressed back into the crater ground and therefore densified into the crater for the case of glass (leading therefore to higher lateral forces), the removed material in enamel disaggregates easily and is redistributed along the abraded area in enamel. This interpretation is also supported by Fig. 57a in which the removed enamel remains inside the abraded area and by Fig. 55, in which the abraded area of glass is clean and almost no removed material can be found.

Glass deforms plastically, as King and Tabor (King and Tabor, 1954) also reported. They suggested that the high hydrostatic pressures prevents brittle fracture, plastic deformation

occurs since the specific shear strength at the rubbing interface exceeds considerably the bulk shear strength of the material. Enamel does disaggregate, though.

6.6.2. Metal like behaviour of enamel (high loads)

As already pointed out above, at higher loads enamel presents stick-slip behaviour. The same effect is found for copper. However, while the contact pressures were higher in enamel, the penetration depths for the two tested metals were considerably greater than for enamel. If we consider the removed material shown for enamel (Fig. 57) and copper (Fig. 61), the stick-slip mechanism in both cases is related to different deformation mechanisms. For enamel it is presumably based on the propagation of damage along the organic phase instantaneously leading to removal of material. Tensile stresses and strains are expected to be highly concentrated and therefore severe. He and Swain (He and Swain, 2007a) have recently proposed a simple microstructural model to illustrate the structure related contact deformation mechanisms of human enamel. They suggest that the imposed shear strains are supported by the thin protein layer between the apatite crystallites and are up to 16 times greater than the averaged contact strains. Thus, while sliding a sharp indenter tip on enamel, the damage may occur preferentially within the protein phase. Damage is thought to be spread through the protein phase which it is thought to act by deflecting and arresting cracks (White et al., 2001) which may lead to the observed discontinuity in the removal of material. The serrated shape on the strips of material in Fig. 57 supports this mechanism. On the other hand, for the case of the metals, strain hardening and dislocation motion are the mechanisms involved. The evidence of dislocation motion and flat lamellas of removed material for the case of copper support the latter explanation.

If not controlled, tooth wear results in poor masticatory function with a concomitant reduction in quality of life and possible deterioration of systemic health. Thus, understanding friction and wear behaviour of enamel may help the clinical treatment of teeth and may assist with the development of new dental restorative materials (Magne et al., 1999 , Li and Zhou, 2002, Kelly et al., 1996, Dahl et al., 1993).

Human enamel will be ground down gradually with ageing, and the dentine might become exposed, causing high sensitivity to normal irritations. The present research shows that tribological behaviour of enamel resembles that of glass at low loads and metals at high loads. Removal of enamel occurred both at low and high loads. Thus, in order to preserve the integrity of sound enamel, a compromise between low abrasive prosthesis (i.e. metals, to avoid pathologic over-wear on the surface of the opposite healthy teeth) and restorative materials possessing mechanical properties similar to those of teeth (i.e. ceramic composites) should be considered for each dentistry treatment in particular.

6.7. Conclusions

From the above observations the following conclusions can be drawn:

- Even though the single scratch behaviour was similar at low loads, glass deformed plastically while enamel did not. While the incrementing lateral load with lateral displacement was related to plastically deformed and densified areas in glass, it corresponds to disaggregation and pressing and re-distribution of the removed material of enamel.
- On the other hand, the observed frictional behaviour of the single scratches on enamel at high loads and metals was a stick-slip one. However, strain hardening and dislocation motion are the involved mechanisms for the metal samples while for enamel it was the propagation of damage along the organic phase and the formation of a sufficiently thick swarf of removed material to remain as a entity. This strip of material was pushed ahead the indenter tip.

6.8. Acknowledgements

Financial aid through EC Contract No MEST-CT-2004-504465, „Marie Curie Host Fellowships for Early Stage Research Training", is gratefully acknowledged. Dipl.-Ing. Andreas Jaeger is kindly thanked for his help with the single scratch tests. People in charge of the Triboindenter (including Dipl.-Ing. Andreas Jaeger) from Institute for Mechanics of Materials and Structures from Vienna University of Technology are also acknowledge for allowing us to carry out the single scratch tests using their device.

FIGURES OF CHAPTER 6

Fig. 55

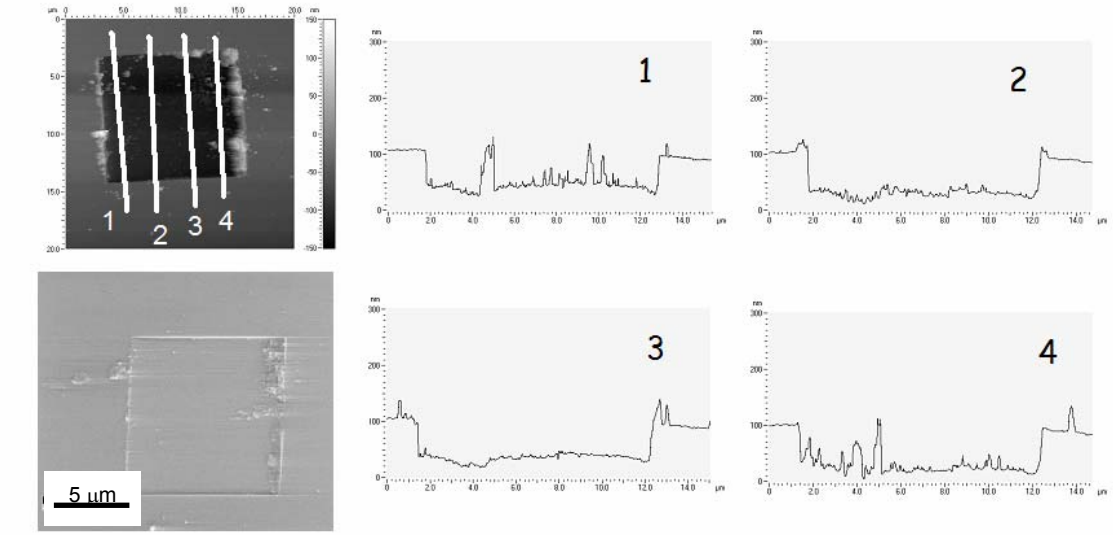

Fig. 55 Upper left: AFM image of the 2D abraded area of glass (20x20 µm^2 view window; 10x10 µm^2 abraded area, 150 nm max. height). The lines correspond to the 4 profiles on the right. Lower left: high resolution SEM image of the 2D abrasion on glass. Note the smoothness of the abraded area.

Fig. 56

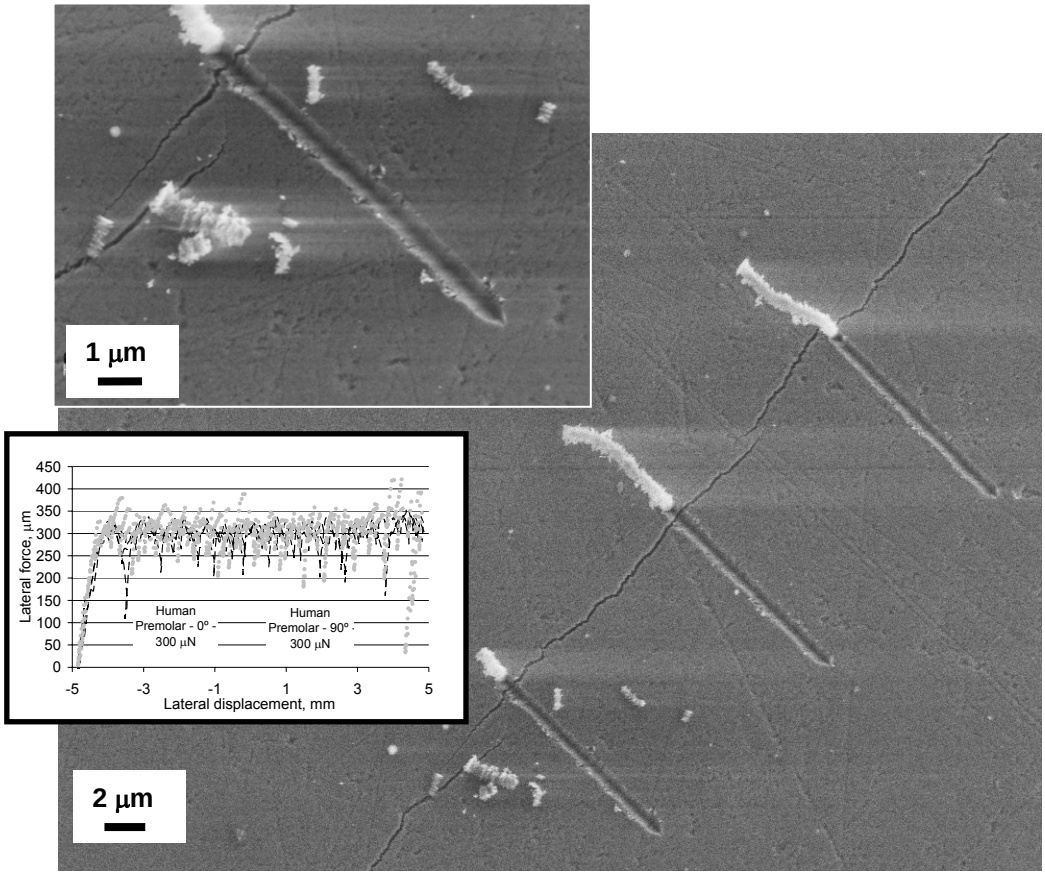

Fig. 56 SEM images of the 1D single scratches on enamel. Superimposed on the lower left side is the recorded lateral force vs. lateral displacement of the single scratches tests done at 300 μN. The fluctuations were related to a stick-slip behavior of the system. Note the serrated appearance of the removed strip of material. It remains also in one piece in front of the indenter tip.

Fig. 57

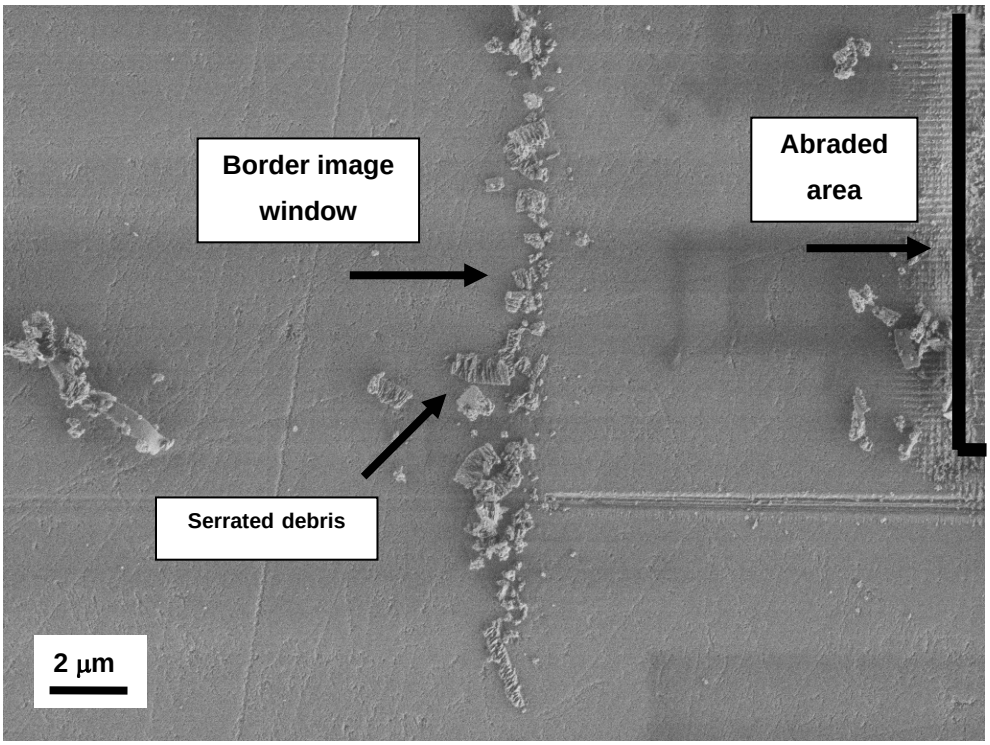

Fig. 57 SEM image of the removed material of a 2D abrasion test on enamel. The area was imaged with the nanoindenter tip immediately after the tests. The removed material is clearly moved to the borders of the scan windows.

Fig. 58

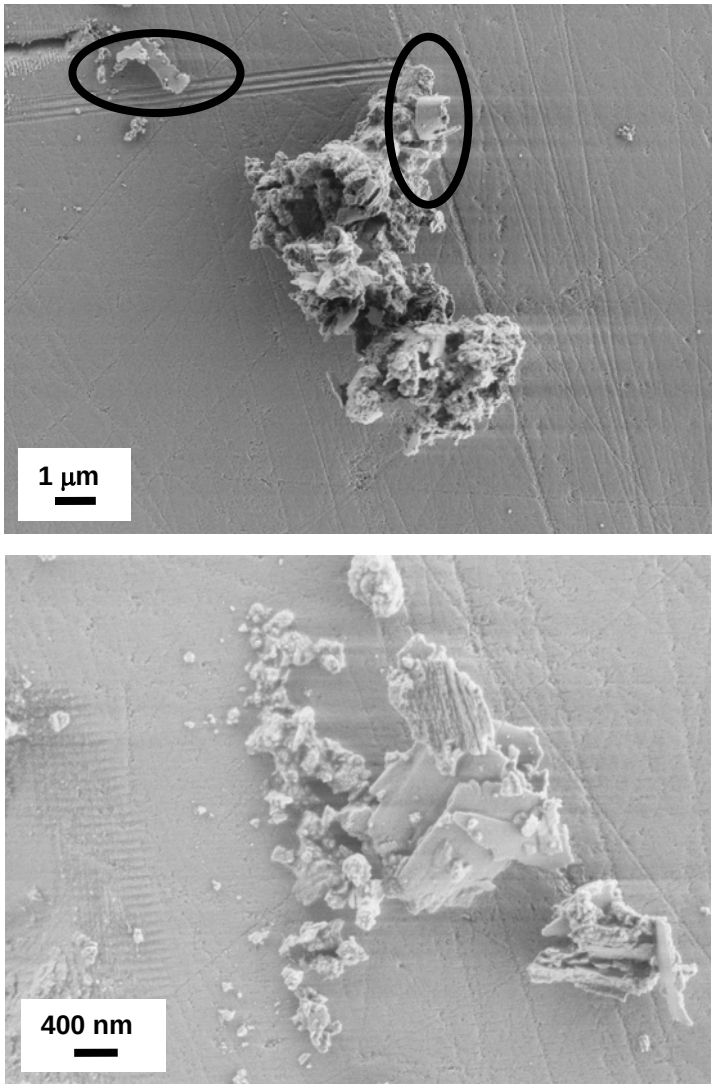

Fig. 58 SEM images of the removed material after 2D abraded tests were carried out. Ellipses mark highly deformed lamella of enamel. The removed material tends to agglomerate.

Fig. 59

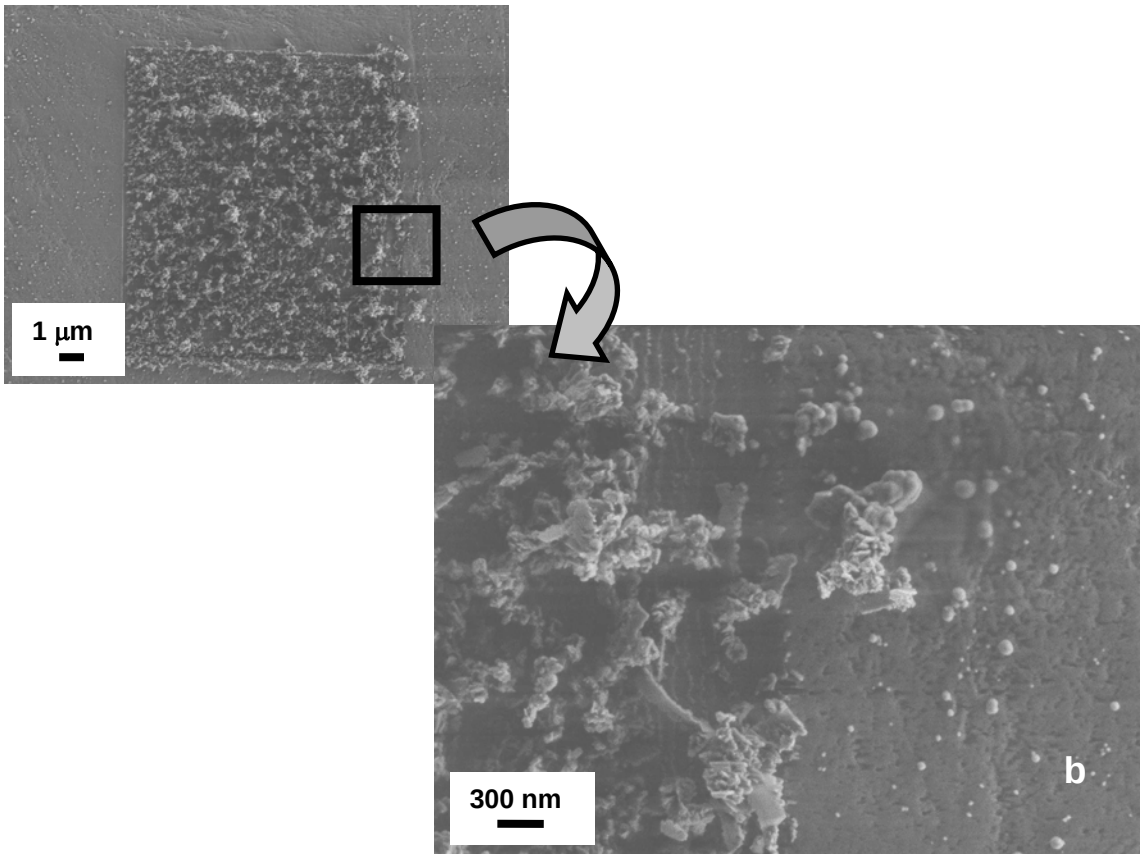

Fig. 59 SEM images of an abrasion test done in the bovine incisor with the sharp cube corner indenter tip. 10x10 μm^2 abraded area, 20 μm/s scan speed, 1 area scan, 50 μN load. b) shows a higher magnification SEM image of the square marked in a).

Fig. 60

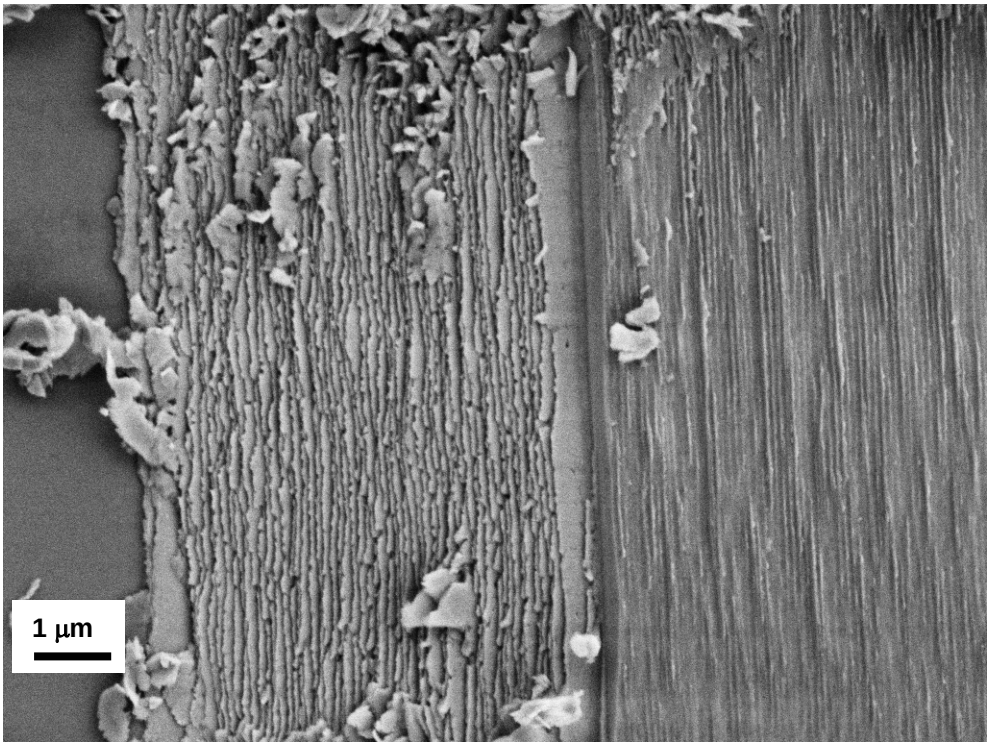

Fig. 60 SEM image showing a 2D abrasion test on copper single crystal. The test was deliberately stopped where the broader path is seen in the picture (middle). Note the different roughness of the abraded surface depending on the number of scans done on the surface.

Fig. 61

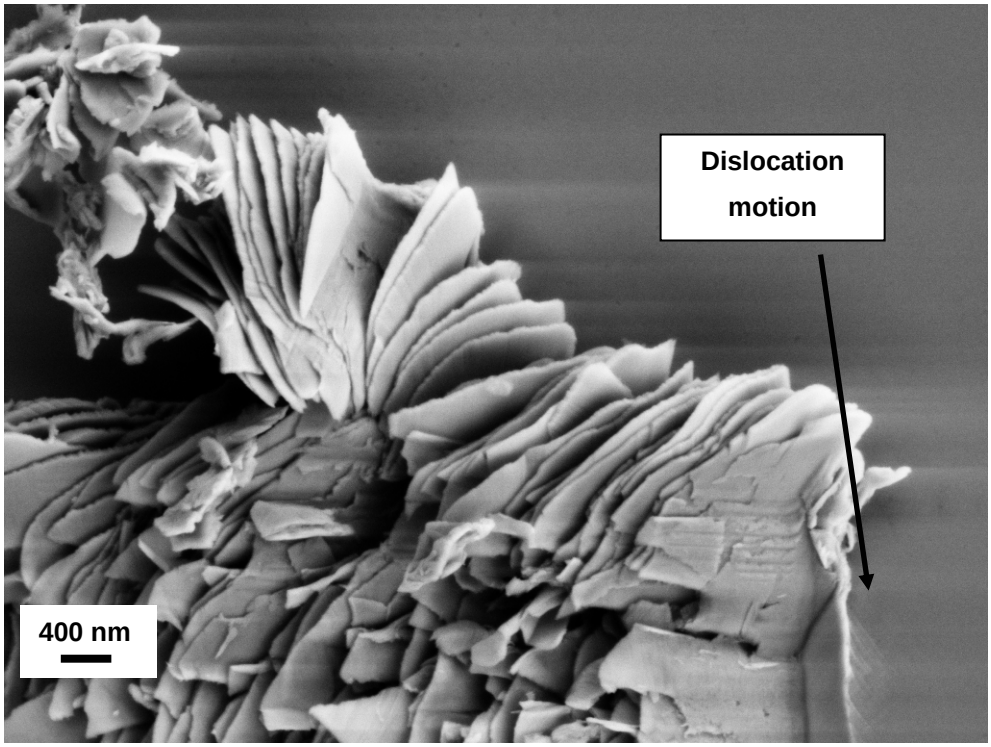

Fig. 61 SEM image of the removed material from a 2D abrasion test on copper singlecrystal. The image is located at one of the corners of an abraded area. Note the thickness of the laminated removed material. Patterns where dislocation motion has occured also seen.

TABLES OF CHAPTER 6

Table 6

QT=quantitative tests; QL = qualitative tests

Material	Load, μN	Penetration depth, nm	Contact area, nm^2	Contact radius, nm	Space between scratches, nm (2D, area scans)		Superposition	Mean Pressure, Gpa	Semi indenter angle α, º	Tan(90º–α)	Abrasion depth, nm (2D)
Glass	100	30	15534	70	78		NO	**6.44**	42.27	1.10	**60 ± 20**
Bovine Enamel	50	20	9836	56	78		NO	**5.08**			**170 ± 100**
Wisdom Enamel	100	30	15534	70	-		-	**6.44**			**-**
Molar Enamel	300	100	69981	149	-		-	**4.29**			**-**
Copper	100	80	51825	128	39 QT	78 QL	YES	**1.93**			**330 ± 100**
Silver	100	125	95602	174	39		YES	**1.05**			**500 ± 200**

Table 6 Comparative table with the data extracted after contact mechanics evaluation between indenter tip and surface. In addition, quantitative data of the 2d abrasion tests in presented in the last column.

CHAPTER 7

7. NANOINDENTATION IN TEETH: THE INFLUENCE OF EXPERIMENTAL CONDITIONS ON LOCAL MECHANICAL PROPERTIES

◆ ***Griselda GUIDONI, Julia Denkmayr, Thomas Schöberl, Ingomar Jäger.*** *"Nanoindentation in Teeth: the influence of experimental conditions in local mechanical properties"* **Philosophical Magazine. Volume 86 Number 33-35 (2006) 5705 – 5714**.

7.1. Abstract

The influence of various experimental conditions on the elastic modulus and hardness of human intertubular dentine was studied using instrumented nanoindentation at room temperature. The conditions studied were: dry (chemically dehydrated) versus wet (prepared and nanoindented under HBSS), the influence of long-term storage under HBSS at ca. 4°C, and the influence of deep-freezing under dry and wet conditions, respectively. The reversibility of chemical dehydration and the consequences of multiple deep-freezing cycles were also investigated. Two premolars of a twelve-years-old human male were chosen for evaluation. The absolute values of the mechanical properties differed by a factor of ~ 2 and ~ 3 between dry and wet state, whereas trends were conserved. Deep-freezing wet dentine samples deteriorated their mechanical properties by about 20 to 28%, whereas dehydrated samples suffered no damage. This may be due to the mechanical damage by the volume increase of water freezing inside the tubules.

Keywords: nanoindentation, biological materials, intertubular dentine, experimental conditions, Hank's balanced salt solution (HBSS).

7.2. Introduction

Storing teeth is an important matter concerning dental medicine. Keeping the integrity of these materials for further transplantation, replantation and restoration is an important issue for successful dental treatments (Moscovich and Creugers, 1998, Swartzl, 1986). In addition, in the case of research investigations, it is a crucial factor in order to measure the real mechanical response of such materials in a state as close to in-vivo as possible. Biological samples not studied immediately after harvesting, are usually stored in the laboratories until testing. Several storage solutions have been reported (HBSS; $CaCl_2$ solutions, water, etc) in order to simulate in vivo conditions and to try to keep the integrity of the teeth. However, these solutions can strongly influence the native properties of these systems (Pashley et al., 2003, Gustafson et al., 1996)

Nanoindentation is a technique able to detect the above deviations in the local mechanical properties of these materials, as Habelitz et al. (Habelitz et al.) also demonstrated with three different storage solutions. Although the penetration depth of nanoindentation is small (< 1 μm); the mechanical properties thus obtained are assumed to be representative of the whole sample and are comparable to one of the most accurate ways of determining elastic constants of a material, i.e. sonic measurements (Kinney et al.). Nanoindentation is a versatile, powerful and highly suitable technique for testing biomaterials, mainly because there is no need of vacuum condition and near in vivo condition can be attained quite easily.

Dentine is a mineralized tissue, containing approximately 50 % vol. mineral and 30 % vol. of collagen fibrils. Dentine contains many tubules typically radiating outwards from the root cavity, in which the dentinal fluid is located and the cytoplasmic processes of the cells that have formed the dentine, the odontoblasts, take place. In addition, tubules are surrounded by a thin,

hard, highly mineralized shell of peritubular dentine, the contribution of which to the overall mechanical properties of a tooth is not yet quite clear (Kinney et al., , Kinney et al., , Balooch et al., 2004). Local mechanical properties of the intertubular dentine (between the tubules) investigated here depend on mineral content and level of interpeptide hydrogen bonding. Most storage solutions are known to alter both characteristics (Habelitz et al., 2002, Nalla et al., 2005)

The present study investigates the difference in hardness and elastic stiffness between dehydrated samples and samples prepared and indented under HBSS. Furthermore the influence of the temperature of storage on the measured local mechanical properties is studied, since Panigh et al. (Panighi et al.) found an influence, albeit for the case of bond strength. The reversibility of chemical dehydration is tested, carrying out nanoindentations in the same sample first in wet and then in dried plus rewetted conditions. In addition the suitability of HBSS for long-term storing of teeth is studied by testing one premolar of the same human individual immediately after extraction, and another one after two years of storage in HBSS (plus Na-azid).

The method of nanoindentation is carried out on intertubular dentine after storing the corresponding samples from the same tooth under four different conditions: immersed in HBSS and room temperature, chemically dehydrated and room temperature, immersed in HBSS and deep frozen, and chemically dehydrated and deep frozen. Correspondingly, nanoindentations are done under atmospheric and fluid environments as appropriate.

7.3. Sample preparation

Preliminary experiments with a human tooth of unknown origin extracted at hospital ended with a thick, very soft surface layer of unknown composition in spite of the use of antibacterial agent and had to be discarded. Another investigated tooth had to be discarded because it had been cut in halves during extraction, which presumably lead to damage due to overheating. These facts prove that in order to get reliable values of mechanical properties of teeth it is of utmost importance to use healthy, freshly erupted specimens, extracted by a dental surgeon fully aware of the requirements of the experiments and thus avoiding predamage.

For the investigation reported here two second healthy premolars extracted from a 12 years old human male were examined. Each of them was extracted from each side of the jaw as part of an orthodontical treatment due to a lack of alveolar arch space distal to the second molar.

One of two premolars was mechanically tested immediately after extraction (1P) and the second one (2P) was studied after 2 years of storage immersed in HBSS and kept at $\sim 4^{o}$C.

The samples were cut with a diamond saw in two (1P) and four sections (2P) along the crown-root direction, carefully avoiding any overheating. Half of the samples of the same premolar were immediately dehydrated (‘DEH’), soaking it in different ethanol grading; the remainders were immersed in HBSS (‘HBSS’). In addition, the influence of two temperatures of storage were studied, in the case of 2P samples: room temperature and -15^{o}C (deep freezing), in combination with the ‘DEH’ and ‘HBSS’ condition described above.

After the indentation of the (2P) samples treated according to the first experimental conditions, the former dehydrated samples were rewetted (RW) in HBSS and stored at the

same temperature as at the beginning (RT or $-15^{\circ}C$) and the former HBSS samples were dehydrated ('DEH') in ethanol and stored at the same temperature as in the beginning. The later experiments were done to study the reversibility of chemical dehydration. In addition, one ('HBSS') sample was frozen and thawed 5 times (5x) to investigate the occurrence or not of additional damage with multiple freezing, on the local mechanical properties measured at room temperature.

For better understanding, all the conditions tested, including the nomenclature used, are summarized in Table 7.

For testing and handling purposes, some of the pieces were simply glued to a platform with cyanacrylate glue and some of them were embedded in a polymer resin. In all the cases, the transversal section of the premolar consisting of enamel, dentine and pulp, was accessible for preparation. The exposed area was ground and polished to a 2500 P grit finish with silicon carbide cloths, followed by polishing in 0.3 μm alumina suspension. In the case of 'wet' conditions, the samples were permanently rinsed with HBSS while polishing, and stored under HBSS all the time to avoid accidental dehydration. This is essential especially in the last stages of preparation.

7.4. Nanoindentation tests

Nanoindentation tests were carried out using an add-on nanoindentation device (Hysitron Triboscope, Hysitron Inc., Minneapolis, MN, USA) mounted on the scanner head of an AFM stage (Veeco – Digital Instruments, Santa Barbara, CA, USA).

Two kinds of configurations were used in the nanoindenter: on the one hand, 'dry indentations', in which the dehydrated samples were indented under atmospheric conditions with a cube-corner indenter, on the other hand, 'wet indentations', in which sample and part of the indenter were immersed in HBSS during testing. For the latter case the conical indenter tip is mounted at the end of a tungsten rod ca. 9.5 mm long in order to keep the transducer well away from the fluid cell. Unfortunately, it turned out that the long rod sometimes introduced a markedly higher level of noise into the measurements; therefore we preferred the standard tip with the standard short rod for the "dry" measurements. No remarkable influence, on the other hand, was found of the fluid itself on the results. So, all the 'wet' indentations were done with the same conical indenter on a long tungsten rod, whereas all the 'dry' indentations were done with the same cube corner indenter. This procedure is justified by a preliminary investigation (Tesch et al., 2001) showing that the shape of the indenter does not influence the results of H and E in dentine (results not shown here).

Nanoindentation tests were carried out in several loading-unloading steps, the first three steps were the same for (1P) and (2P) samples: first the specimen was linearly loaded to the maximum load in 5 seconds, secondly the load was maintained 50 seconds in order to eliminate most of the creep before unloading, thirdly the sample was unloaded to an intermediate load. In the case of 1P specimens and wet condition, after the third step, 5 cycles of unloading and loading between 10 % of maximum load and maximum load were included and for each

indentation, 5 elastic moduli were calculated from the unloading curves and averaged. Hardness was calculated from the first cycle. Since measurements from 1P samples showed no significant difference between E calculated from the five unloading curves, these cycles were not applied to the 2P samples. Regarding (2P) samples, the third unloading step was done until an intermediate load of 100 μN within 10 s, fourth step was to hold this load 20 s for control of thermal drift and, finally, unloading linearly to zero within 2 s.

Maximum load was 5000 μN in all the samples and conditions, except in the case of the 'dry' indentations of 2P samples, were maximum load was 2500 μN, in order to keep the penetration depth between 700 and 800 nm.

The temperature of testing was in all the cases room temperature. The samples stored in a deep-frozen ($-15^{o}C$) condition were defrosted before testing.

In the case of 1P specimens, the indentations were done along a line starting in the dentine-enamel junction (DEJ) and finishing in the root, far away from the pulp. On the other hand, in the case of 2P samples, the indentations were done randomly in the dentine zone, far away from the pulp and enamel. In the later, the tests were repeated daily during two weeks in order to check the stability of the measured mechanical properties with time. In both cases, the indented region was intertubular dentine, and the indents were carefully placed by means of the AFM mode scanning with the nanoindenter tip between the tubules to avoid any influence of the peritubular dentine and/or tubules on the results.

Elastic Modulus and Hardness were calculated by means of the load-displacements curves using the well known Oliver-Pharr method (Oliver and Pharr).

At least 30 measurements per storage condition were taken. In order to compare the results, ANOVA one way statistical analysis was used, with a confidence interval of 0.05.

7.5. Results

The ratio between the measured mechanical properties, E and H, in the wet and dry state is ~2 and ~3, respectively, as can be seen from Fig. 62a and Fig. 62b. However, although the absolute values of E and H differ, the trends, such as the typical gradient in E and H starting at the dentine-enamel-junction (DEJ) and extending for some hundreds of micrometers into the dentine are conserved, as shown in Fig. 63a and Fig. 63b. In addition a few indentations were made in the enamel, showing that even in this very highly mineralized material (up to 95 wt%, (Barbour et al., 2003)) a strong difference in the hardness exists between the dry and the wet state (≈ 2:1), whereas, strange enough, the elastic modulus remains unaltered. But since enamel was not the main aim of this investigation, this was not pursued further.

The measured mechanical properties in the case of 2P samples for each condition were significantly similar during the two weeks of testing. For this reason, all the presented results correspond to the average of the measurements (among 30 to 180 nanoindentations per condition) during the evaluated time.

The final median (average) data of all the initial conditions are shown in Table 8, followed by their standard deviation.

A result to point out is the similarity in the mechanical response of the 1P and 2P samples (denoted by dark and light grey cells for the corresponding wet and dry properties, respectively, in Table 8), where the main difference is the storage time (immediately tested and stored during 2 years in HBSS, respectively).

As shown in Table 8, for the 2P samples, the measured mechanical properties vary with the temperature of storage by 25 %, approx. in the case of wet conditions. This result was not observed in the dry conditions. From now, dry conditions will be denoted by simply 'DEH' (without specifying temperatures of storage) since E and H are not influenced by the temperature of storage in the dry state.

Fig. 64a and Fig. 64b show all the results of the wet and rewetted conditions of 2P samples. Independently of the storage conditions in the dehydrated state, after rewetting, their mechanical properties fit in with the mechanical properties of HBSS RT condition. A similar behaviour is found in the case of the re-dehydrated sample at RT, which mechanical response agrees with the response of the native dehydrated samples ('DEH'): 21.67 $\pm$ 0.67 GPa and 0.95 $\pm$ 0.03 GPa for E and H, respectively (Refer to Table 8 for comparison). In the case of frozen and defrosted several times, there is no observable extra damage in the mechanical properties after the first cycle, as it can also be seen in Fig. 64a and Fig. 64b.

7.6. Discussion

It is well known that the fluid for storing dental tissues can alter their mechanical properties (Habelitz et al., 2002, Nalla et al., 2005). Alcohol, e.g. produces shrinkage of the tissue because it increases the levels of interpeptide hydrogen bonding (Nalla et al., 2005). This leads to enhanced hardness and mechanical stiffness, compared with the case of storage in HBSS. HBSS, on the other hand, has a major percentage of water, with the necessary ions to prevent dentine demineralization (Habelitz et al., 2002, Nalla et al., 2005) and water plasticizes collagen by breaking interpeptide bonds (Habelitz et al., 2002), which is translated into lowered hardness and stiffness of the hydrated samples. As the results show, the difference is remarkable: E and H decrease to about half and one third of their values, respectively, on going from dry (alcohol) to wet (HBSS) conditions. Nevertheless, the fluid influences all the tooth structure and the tendencies like, e.g. local gradients, are kept even though the absolutes values differ considerably.

The fact that the mechanical properties were kept even after two years of storage in HBSS, supports the result presented by Habelitz et al. (Habelitz et al., 2002) that HBSS is a most suitable solution for storing teeth. However, in this study it was found that it is not only suitable for short periods (two weeks) as they stated, but also for longer ones (years).

In addition to the effects of different storing fluids discussed above, it was observed in this work that the temperature of storage is also important. HBSS is an aqueous buffer solution. Water is mainly located inside the tubules, so when the samples are deep frozen, the increase in volume of frozen water may introduce irreversible mechanical damage in the microstructure of the dentine tubules as well as in the surrounding dentine. This may explain the ~25 %

decrease in local mechanical properties obtained among the samples stored submersed under HBSS and kept at room temperature and the ones deep frozen, respectively. However, this phenomenon is not observed in chemically dehydrated samples because the water is replaced by alcohol, which at $-15^{o}C$ neither freezes nor experiences any volume increase. In contrast to our findings, Moscovich et al. (Moscovich et al., 1999) did not observe changes in the hardness of dentine after storing it at $-18^{o}C$ in water. However, their chosen method was macroindentations with loads of 30 kg in 2.1 mm thick disks, which may have hidden the microstructural changes introduced by the swelling of solidified water since due to the average size of the macroindentations, it averages the contributions of peritubular, intertubular dentine and tubules, and judging by the load used and specimen thickness its results may be influenced by the sample holder too. Nanoindentation, on the other hand, is a powerful technique to investigate biomaterials with hierarchical structure, because nanoindentation is capable to measure mechanical properties in the micrometer range, allowing researchers to understand and discriminate the influence of micrometer size structures on the mechanical behaviour.

After dehydrating the former wet samples and rewetting the former dehydrated samples, the measured local mechanical properties corresponded to the initially dehydrated and wet samples, respectively. It is remarkable that, independently of the initial storing temperatures in the dehydrated state, the E and H of the rewetted conditions fitted in with the measured properties of just wet and kept at room temperature ('HBSS RT Average', in Fig. 64a and Fig. 64b) samples. This is explained by the fact that initially, with the former dehydration process, the water is replaced by alcohol which does not freeze nor increase its volume. When again the ethanol is replaced by HBSS in the rewetting step, the resulting microstructure corresponds to the 'HBSS RT' condition since freezing the sample did not introduce any mechanical damage. This simple model explains why all the rewetted samples respond in a similar way as immersed in HBSS and kept at room temperature, independently of the temperature of storage in the dehydrated state.

The above observations indicate reversibility of chemical dehydration as already presented by Nalla et al. (Nalla et al., 2005) for the fracture resistance behaviour of dentine.

7.7. Conclusions

Nanoindentation is a valuable technique for studying biomaterials. Not only because vacuum environment is not a requirement, but also because near in vivo conditions are achievable allowing indentations to be done under fluids.

The several conditions investigated in this work led to the following conclusions:

- The temperature of storage is an important factor for storing teeth in HBSS, if it reaches the solidification point of water. This conclusion may be extrapolated to all aqueous fluids which preserve dentine mineralization, because it is the increase in water volume after freezing which introduces irreversible damage.
- Chemical dehydration seems to be a reversible process.
- Hank's balanced salt solution (HBSS) is a suitable fluid for storing teeth.

- The mechanical properties of dehydrated dentine considerably differ from the near in vivo condition (immersed in HBSS). In this case, the plasticizing role of water and the presence of the necessary ions to prevent demineralization in HBSS are the reason for obtaining lower mechanical properties than in the dehydrated state, where alcohol is thought to increase the levels of polypeptide bonds with the expected increase in E and H that is entailed.
- Deep-freezing not only is not needed when using HBSS for storing teeth, but even detrimental.
- Healthy teeth are necessary to distinguish the mechanical response differences among different storing conditions.

7.8. Acknowledgements

Griselda Guidoni acknowledges the financial support provided by the European Community under EC Contract No MEST-CT-2004-504465, „Marie Curie Host Fellowships for Early Stage Research Training". The authors thank Dr. Erich Klein and his team for the prompt and very competent delivery of two perfect premolars for the investigation.

FIGURES OF CHAPTER 7

Fig. 62a

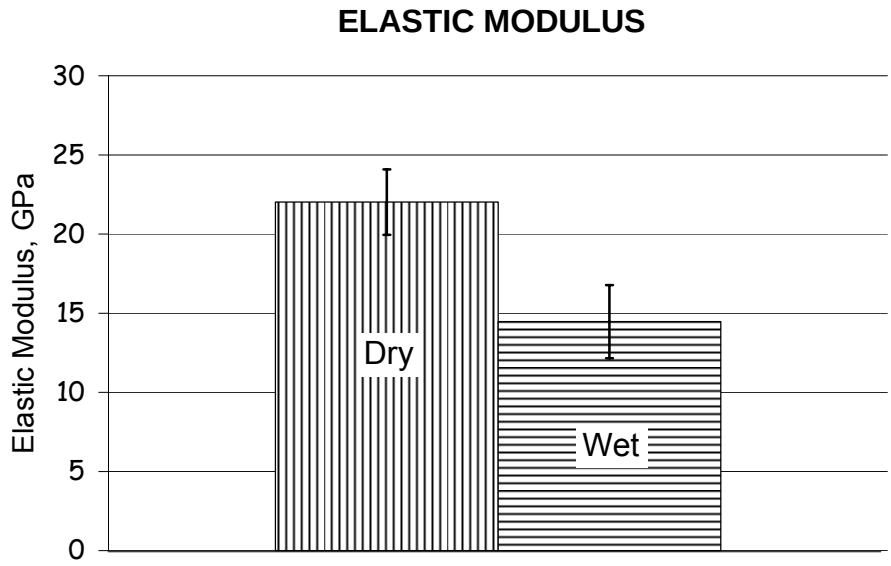

Fig. 62b

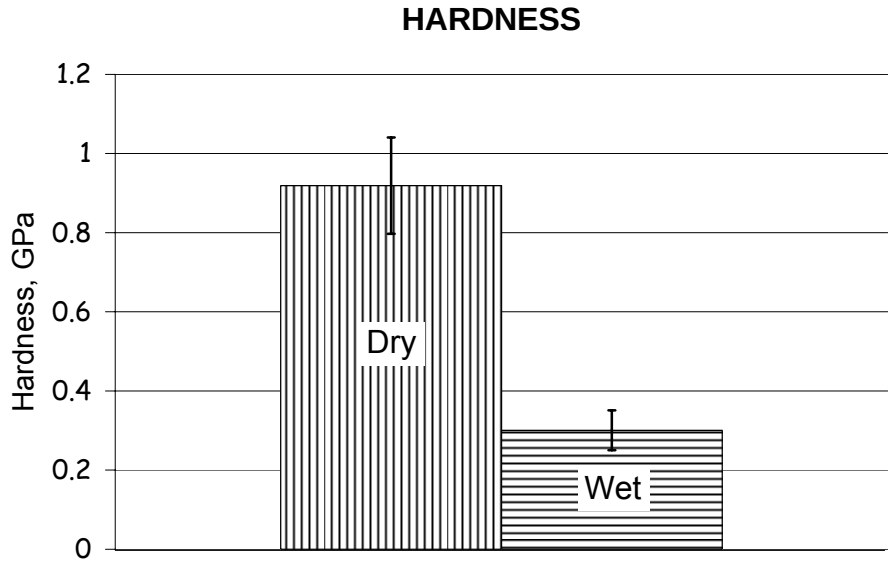

Fig. 62 Each column represents the averaged elastic modulus (E) and hardness (H) of the 1P sample, both in the dry and wet condition. E is presented in Fig. 62a and H in Fig. 62b. The difference in absolute values between both conditions can clearly be seen.

Fig. 63a

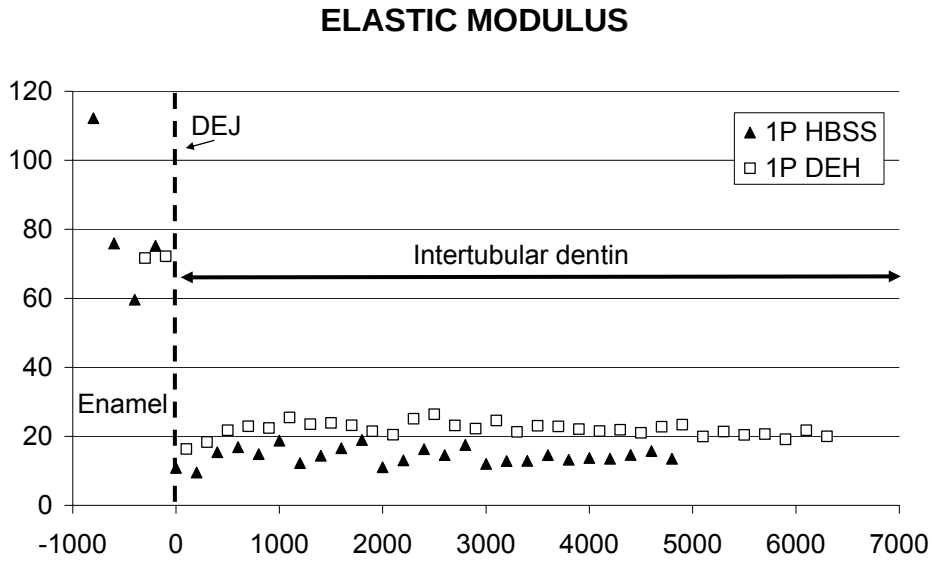

Fig. 63b

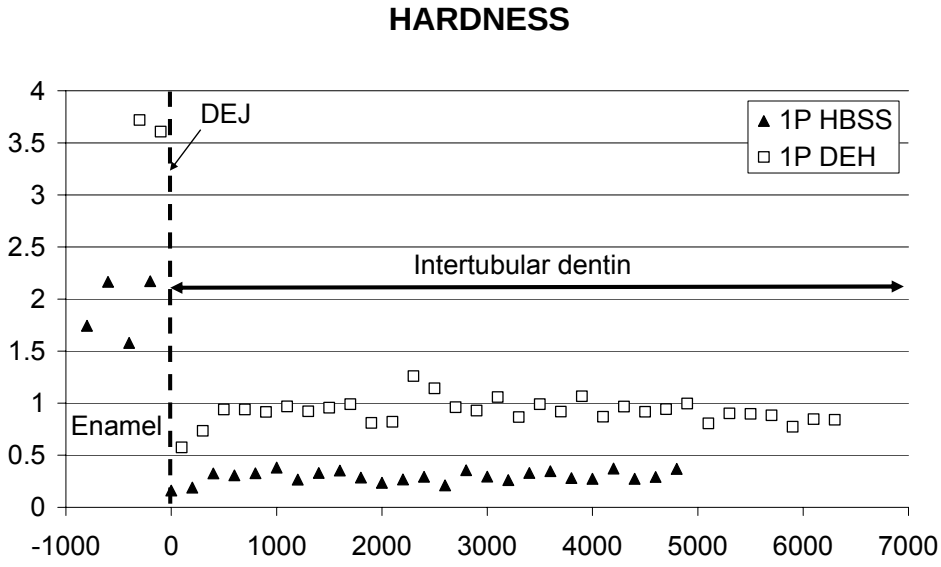

Fig. 63 Elastic modulus (E) and Hardness (H) of 1P sample are shown in Fig. 63a and Fig. 63b, respectively. In both graphs, left side of the figure corresponds to enamel, right side to intertubular dentine. Each point is a single measurement.

Fig. 64a

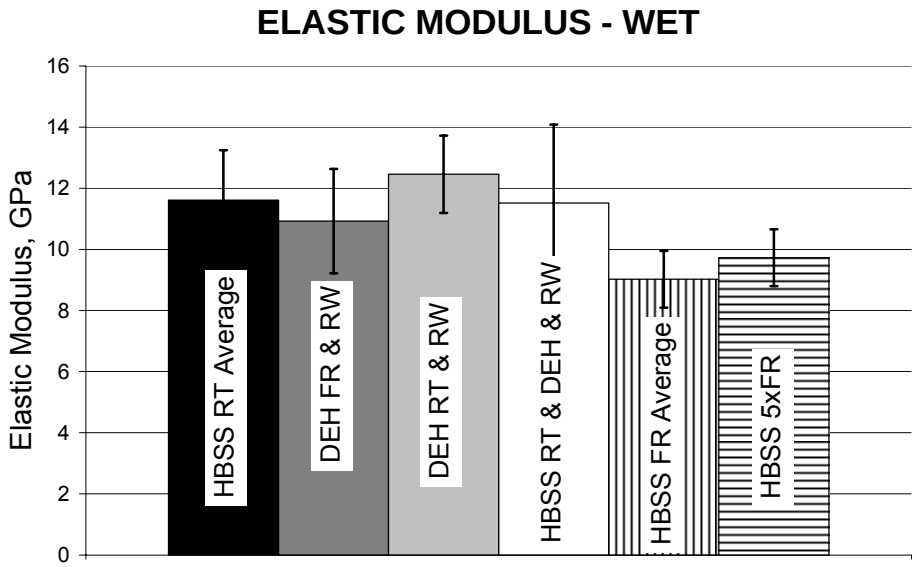

Fig. 64b

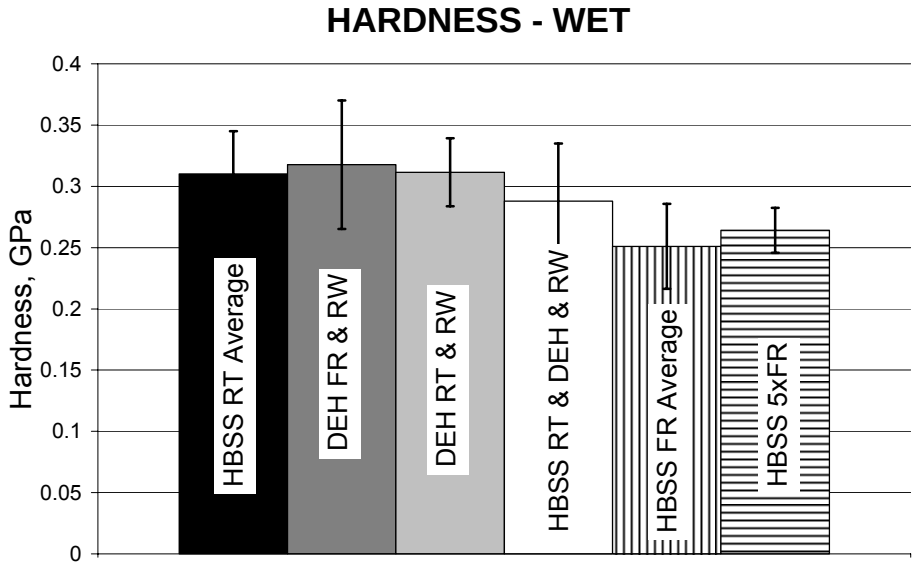

Fig. 64 Elastic Moduli of all the tested WET conditions of 2P samples are shown in Fig. 64a. On the other hand, hardness data of all the tested WET conditions of 2P samples are plotted in Fig. 64b. Columns values are average values. The error bars were calculated as the standard deviation (SD) of the measurements. HBSS RT and FR average are the average during the two week of testing of each of the conditions, respectively.

TABLES OF CHAPTER 7

Table 7

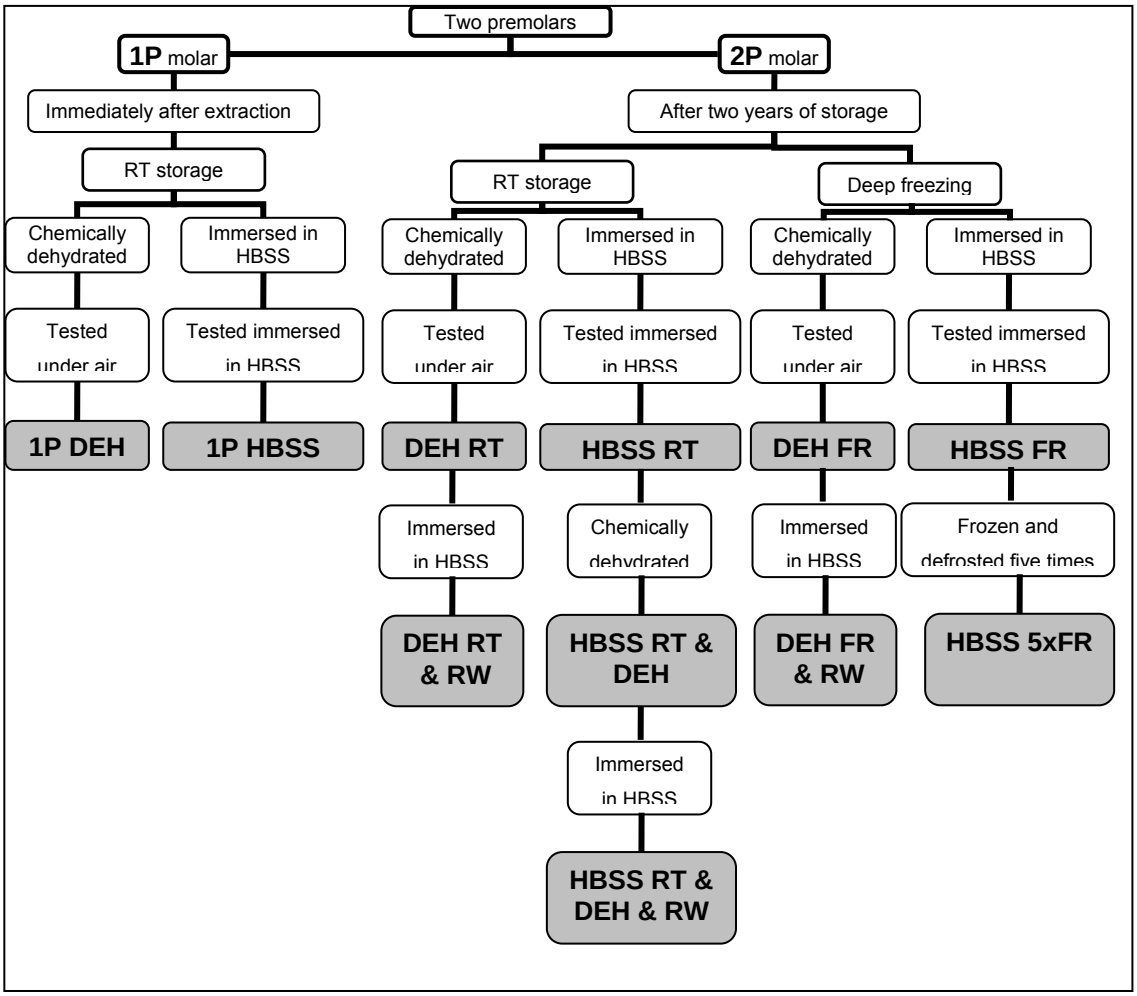

Table 7 Schema showing all the experimental conditions used (in white boxes) and the nomenclature chosen (grey boxes).

Table 8

Sample	Condition		Hardness, H (GPa)	Elastic Modulus, E (GPa)
1P	HBSS		0.30 ± 0.05	14 ± 2
	DEH		0.92 ± 0.12	22 ± 2
2P	HBSS	RT	0.31 ± 0.03	12 ± 2
		FR	0.25 ± 0.03	9 ± 1
	DEH RT & FR		0.96 ± 0.07	23 ± 2

Table 8 Local mechanical properties of the initial tested conditions of both 1P and 2 P samples.

CHAPTER 8

8. NANOINDENTATION OF WET AND DRY COMPACT BONE: INFLUENCE OF ENVIRONMENT AND INDENTER TIP GEOMETRY ON THE ELASTIC MODULUS

◆ ***Griselda GUIDONI, M. Swain and I. Jäger.*** *"Nanoindentation in wet and dry compact bone: influence of environment and indenter tip geometry on the elastic modulus"* **Journal of Biomechanics (2008)** ***Submitted.***

8.1. Abstract

The indentation derived elastic modulus, E, of dry bovine compact bone is 40 % higher than when measured wet. Although this difference is independent of orientation, there is 20 % difference in elastic modulus within the same tested environment between longitudinal and transversal directions. In addition, the estimated elastic modulus of the same samples when tested wet in buffer solution after deep freezing (-15ºC) was not affected. The discrepancy between wet and dry results was attributed to the non mineralized phase contribution and rationalized by a simple mechanical model (Jäger and Fratzl, 2000). Anisotropy effects could be explained in terms of deformation mechanisms with orientation. The effect of sub-zero storage temperatures could be clarified by the biomechanics of the helicoidal arrangement of lamellar bone. Viscoelastic effects were also considered and incorporated into the analysis of the force-displacement data.

Keywords: compact lamellar bone, nanoindentation, Hank´s balanced salt solution.

8.2. Introduction

Several authors reported mechanical anisotropy of compact bone (Fan et al., 2002, Espinoza-Orías, 2005, Hoffler et al., 2000, Yung, 1993) and moisture dependent properties (Rho and Pharr, 1999, Gupta et al., 2006a, Hengsberger et al., 2002), however the origin of such differences and the contribution of the involved hierarchical level on the measured total mechanical property of lamellar bone is still not well understood. In addition, deep freezing is normally used to store mineralized tissue like dentine (Moscovich et al., 1999, Panighi et al., 1997) and bone (Burr et al., 1998, Hoffler et al., 2000, Kang et al., 1997). No reports, to the best knowledge of the authors, are available on the effect of cryopreservation on the elastic modulus of compact bone.

Compact lamellar bone material is a composite material. It consists of an organic framework (mostly collagen) in which small particles of a mineral (mostly non-stoichiometric hydroxyapatite) are dispersed (Currey, 2002).

Collagen is formed by protein chains, which are self-arranged into fibrils. These fibrils are organized in a staggered way, having gaps and overlap zones (Fratzl and Weinkamer, 2007). The mineralized collagen fibre of about 100 nm in diameter is the basic building block of bone material and is composed of bundles of mineralized fibrils embedded in an extra cellular matrix. The mineral individual crystallites are exceedingly small and generally assumed to be platelets elongated along the c axis with average dimensions of 30 x 20 x 2 nm. Collagen behaves visco-elastically whereas hydroxyapatite is a brittle ceramic. The small size of the mineral crystals is thought to impart theoretical strength (Gao et al., 2003) to their structure.

The mechanical properties of a composite material depends not only on the composition, but also on the structure of bone (Yung, 1993). Compact bone lamellae consist of an extra-fibrillar matrix with collagen fibres interweaving each other running in longitudinal, transverse, and various oblique directions (Wagermaier et al., 2006a).

Although a detailed quantitative description of the deformation mechanisms of bone at the nanoscale remains unclear, several mechanisms have been proposed (Gupta et al., 2005, Thompson et al., 2001, Gupta et al., 2006a, Jäger and Fratzl, 2000). Less is understood about the influence of the environment on the mechanical properties of compact bone.

Jäger and Fratzl (Jäger and Fratzl, 2000) proposed a model with a staggered array of platelets that accounts for an increase of both elastic modulus and fracture stress with the amount of mineral in the fibril. This latter model includes shear stresses in the collagen phase between the overlapping mineral platelets. Although the mineral and organic phase arrangement resembles a parallel model, the deformation is assumed to be transmitted through shear of the organic phase into the mineral phase (tensile) leading to a simplified one-dimensional serial spring system. Some of the limitations of this model are that the stress must occur along the main axis of the mineral phase and the minerals are considered to be highly oriented. Gupta et al. (Gupta et al., 2006a) noted that this model could be applied to the next higher hierarchical level where the mineral phase and the organic phase arranged together into fibres (or fibrils) embedded in a ductile matrix. In particular, this is the level tested during nanoindentation.

The aim of this paper is to understand the mechanisms associated with nano-indenting lamellar compact bone. Microstructural anisotropy and, the influence of temperature of storage and environment were investigated. A rounded diamond conical indenter tip of 90º included angle and approximately 400 nm nominal radius was used. This particular indenter tip shape was chosen for its rotational symmetry avoiding indenter tip orientation effects and singularity effects associated with a sharp tip. Initially the contact follows an elastic response predicted by Hertz (Johnson) before the onset of elastic-plastic behaviour. Once the rounded tip portion of the truncated cone (~117 nm) is overcome a condition of effective constant contact strain prevails for further indentation penetration depths (Tabor, 1970).

8.3. Sample preparation

A femur of a 1.5 years old steer was obtained from a butcher. The bone samples tested here come from a young bullock therefore the bone is of the fast-growing type as described by, e.g., Currey (Currey, 2002). It had been refrigerated but never frozen. It had been dissected from the muscle just prior to purchase. It was immediately taken to the laboratory and prepared for testing and storage. The soft tissue was removed with a scalpel and the bone marrow was taken away with high pressure air. The cleaned compact bone parts were kept in the refrigerator immersed in Hank's balanced salt solution (HBSS) with 0.1 wt% of sodium azide (NaN_3, Merck 888) as an antibacterial.

Three main testing directions were defined: longitudinal (L), transversal (T) and radial (R). A schematic is presented in Fig. 65. Thus, the nomenclature was chosen as follows; BL for the bovine compact bone sample tested parallel to the longitudinal direction and BT for the bovine compact bone sample tested in the transversal direction.

Two pieces of approx. 8 x 8 mm^2 were cut with a saw along the longitudinal direction of the diaphysis a short time after receiving the bovine bone. One of them was prepared leaving the cross section exposed for testing (BL) and the other one the transversal section (BT).

The exposed area of the compact bone pieces was ground and polished to a 2500 P grit finish with silicon carbide cloths, followed by polishing in 0.3 μm alumina suspension. In the case of 'wet' conditions, the sample was continuously rinsed with HBSS while polishing, and stored under HBSS at all times to avoid accidental dehydration. This is essential especially in the last stages of preparation.

The tested bovine samples, when not under investigation, were always kept at 4 ºC immersed in HBSS. The first set of experiments was done under a wet condition. Afterwards, the buffer solution was removed with a syringe; the sample was wiped with a tissue paper and left to dry under laboratory conditions for more than 48 h and tested dry. The samples were then immersed in HBSS and stored at -15ºC for at least 12 hours. They were subsequently laboratory thawed over at least 8 hours and tested wet at room temperature. "FR" was added to the nomenclature to distinguish this new storing condition.

8.4. Nanoindentation Tests

Nanoindentation tests were carried out using an add-on nanoindentation device (Hysitron Triboscope, Hysitron Inc., Minneapolis, MN, USA) mounted on the scanner head of an AFM stage (Veeco – Digital Instruments, Santa Barbara, CA, USA).

Two kinds of configurations were tested: 'dry indentations', in which the samples were stored and indented under atmospheric conditions, and 'wet indentations', in which the sample and part of the indenter were immersed in HBSS during testing. For both cases the same rounded diamond conical indenter tip of 90º included angle and approximately 400 nm nominal radius, mounted at the end of a tungsten rod ca. 9.5 mm long was used.

The area function was calibrated with a fused quartz sample. Although the penetration depths during calibration are governed by the nature of the standard sample (fused quartz), the form of the area function is chosen to converge to the ideal area of the indenter at higher penetration depths (Fischer-Cripps, 2004) .

Nanoindentation tests were carried out in several loading-unloading steps: first the specimen was loaded at a constant loading rate to the maximum load (5000 μN) in 5 seconds, secondly the load was maintained 60 seconds in order to exhaust most of the creep before unloading, thirdly the sample was unloaded at a linear rate to an intermediate load of 1000 μN within 10 s, fourthly this intermediate load was held for 20 s to monitor recovery effects and, finally, complete linear unloading within 2 s. Testing in all cases was at room temperature.

Elastic modulus, E, and hardness, H, were calculated by means of the load-displacement curves using the well known Oliver-Pharr (Oliver and Pharr, 1992) method. Since Poisson´s ratio of the material is unknown and the material is highly anisotropic, the values of elastic modulus E given correspond to the reduced or indentation modulus (Oliver and Pharr,

1992). However, when indicated, the elastic modulus of the sample was derived using a Poisson's ratio of 0.3.

At least 15 measurements per condition were taken. The location for each nanoindentation was chosen by means of AFM imaging, done with the same indenter tip. The indentations were placed specifically in lamellar bone.

8.5. Results

The load-displacement data for the BL sample and the three tested conditions is shown in Fig. 66. Note the matching between the wet measurements (independent of the storage temperature) and the discrepancy of the dry measurements. The same behaviour is found for the BT samples.

Elastic moduli are presented in Fig. 67 as a function of contact penetration depth, h_c, for the BL sample (filled symbols) and BT sample (hollow symbols). Average values together with their corresponding error bars representing the standard deviation of the data are seen to overlap the individual values.

The penetration depth-time and load-displacement curves were studied individually in detail. All the extracted values (mean and standard deviation) are presented in Table 9. Although the viscoelastic creep effects seem to be slightly higher for the BT than for the BL samples, independently of the environment, the penetration depth during unloading is considerable higher in the former than in the latter condition.

The calculation of the elastic modulus depends on a fitting parameter, *m*, as described in (Oliver and Pharr, 1992). The *m* parameter has a physical meaning and is anticipated to be 2 for conical indenters (Oliver and Pharr, 1992). Thus, the sensitivity of the data to this parameter was studied by comparing the results obtained with the TriboScope software supplied with the nanoindenter. ("E, GPa (m = variable)" in Table 9) and by fixing m = 2 ("E, GPa (m = 2)" in Table 9).

The BT W indentation moduli data were the most affected by the above calculation and the corrected indentation moduli using m = 2 led to a constant difference between wet and dry measurements of 37%, independent of orientation. The difference between BL W and BT W and between BL D and BT D lies around 20 %.

Creep effects were corrected following the method of Ngan and co-workers (Ngan et al., 2005), although creep rates at the onset of unloading were in the range of the noise of the instrument (Table 9). As shown in Table 9 there were no remarkable differences after the viscoelastic creep correction, as anticipated. The values of the creep rate at the commencement of the first holding period are shown to emphasise the importance of the holding period at maximum load in order to exhaust most of the creep before unloading, even while carrying out dry measurements.

Recovery effects were more marked for the wet than for the dry conditions (Table 9). A discussion about recovery effects and nanoindentation can be found in (Guidoni et al., 2007c). The recovery correction proposed in (Guidoni et al., 2007c) was tried, but the relatively long

unloading times (10s) when compared with the second holding period time (20 s) and the higher recovery rates obtained for compact bone make the correction unreliable due to the extended extrapolation. Therefore, recovery was not incorporated into the calculation of the elastic modulus, although it is considered qualitatively in the interpretation and discussion of the data.

8.6. Discussion

Three different levels of bone hierarchical organization are thought to explain the effects of storage temperature, anisotropy effects, and environment dependence, as follows:

8.6.1. The influence of storage temperature on mechanical properties: lamellar level.

Storage of bone at -15ºC does not appear to significantly influence the local elastic properties of compact lamellar bovine bone (Fig. 67 and Table 9). The 4% volume dilatation of water when frozen seems to be accommodated by the structure without producing irreversible damage. This may be explained by the multidirectional structured model proposed by Ascenzi and coworkers (Ascenzi et al., 2003) in which they stated that the spiral oriented lamellae of the osteons are able to withstand multidirectional shearing forces effectively.

Simulations have been run in multilayer cylindrical concentric shafts subjected to torsion. Two conditions were considered: all the multilayers oriented at 10º with respect to the main longitudinal axis and the same multilayer but with an right-handed helicity orientation (Fratzl and Weinkamer, 2007) of each adjacent layer with respect to the main longitudinal axis. There is a dramatic decrement of strains and stresses (up to an order of magnitude) in most of the layers when comparing the former with the latter arrangement. Even though the bone structure is more likely to be loaded in a radial orientation after freezing rather than torsion; the above observations may indicate the basis for the damage insensitivity expected in a multistructural arrangement as bone.

Regarding moisture on the structure (beside the one filling the blood vessels, etc), not all the water surrounding collagen is thought to behave like bulk water (Chapman et al., 1971, Nyman et al., 2005). Chapman et al.(Chapman et al., 1971) stated that part of the hydration layer of collagen has a lower freezing point than bulk water, presumably due to the incompatibility of the ice structure with the neighboring structures. Moreover, water is also found in crystalline form, strongly bound to the apatite (Nyman et al., 2005). Thus, the effect of water expansion may be diminished.

Kang and coworkers (Kang et al., 1997) studied the influence of multiple thawing-freezing cycles on the indentation contact stiffness of bovine tibial cancellous bone. They found no considerable differences. Their discussion focused on the effects of freezing on the enzymatic activity, assuming the damage may come from a chemical degradation rather than a mechanical one. Since the use of an antibacterial agent minimizes chemical degradation, in the present work, the effect of freezing the sample was evaluated from a mechanical point of view.

Thus, the present work could be taken as a partially extension of the work of Kang (Kang et al., 1997) but for the case of compact bovine bone.

8.6.2. Anisotropy of the same type of compact bone: fibre level.

Zysset and coworkers (Zysset et al., 1999) found a marked variability of elastic modulus and hardness of cortical bone taken from selected sites within an individual. Thus in the present work, the samples were prepared from adjacent sites within the diaphysis to avoid this variability. The latter plus the specific sites tested (lamellar bone) leads us to assume that the differences in the mechanical properties stem, primarily, from the structural anisotropy of one type of bone.

Fig. 66 is shown to avoid the supposition of an area function calibration error associated with the measured final values. The different response of both orientations is clear.

The anisotropic trend found here is in good agreement with the measurements found in the literature (Rho and Pharr, 1999, Fan et al., 2002, Espinoza-Orías, 2005, Hoffler et al., 2000) and the absolute values agree within $\pm$ 30%. The discrepancy in absolute values between those measured here may be attributed to the different origin of the samples (bovine vs. human), specific environments and anatomical position.

Spears (Spears, 1997) developed a finite element model for enamel (the outer part of teeth) in which predicted marked differences between the elastic modulus in the direction parallel to the enamel rod orientation (in analogy, BL orientation) and perpendicular to the enamel rod orientation (in our case, BT orientation). Although the micro-structural arrangement of enamel differs from compact bone (White et al., 2001, Fincham et al., 1999), as does the volumetric fraction of mineral (between 0.88 and 0.91) the effect of orientation led a factor between 2 and 3 for the elastic modulus in the direction of the rod compared with the E parallel to the rods. On the other hand models for dentine, which bears a closer resemblance to compact bone, indicate an absence of anisotropic properties (Qin and Swain, 2004 , Kinney et al., 1999).

Even though not included in the above model, for the BL indentations, the load will be mainly carried by the fibres which may buckle or split. On the other hand, for the BT direction, the fibres would preferentially bend at small deformations. The differences in deformation mechanisms may also lead to an anisotropy effect.

8.6.3. The influence of the hydration state on mechanical properties: constituents' level.

From Fig. 66, it can be seen that there is a substantial difference between wet and dry measurements within the same sample.

In the present work, the penetration depth exceeded the zone of variable contact angle; thus the indentation strain was constant and directly related to the included cone angle of the indenter tip. Since the loading history and the indentation strain were the same for all the conditions; and the same sample was tested under the different environments, the differences

found between environments are mainly due to either genuine changes in elastic-plastic properties or to the occurrence of different deformation mechanisms depending on the tested environment.

If the arrangement between minerals and the organic matrix is simply represented by the modification of the staggered model (Gao et al., 2003, Jäger and Fratzl, 2000) as shown by Gupta et al.(Gupta et al., 2006a), then the elastic modulus of bone is given by

$$E = (1-\Phi)E_{matrix} + \Phi E_{mineral}\left(1+\frac{4(1-\Phi)D^2E_{mineral}}{\Phi L^2 G_{matrix}}\right)^{-1} \quad \text{Eq. 33}$$

$$\text{and } G_{matrix} = \frac{E_{matrix}}{2(1+\nu_{matrix})}, \text{ then } \partial G_{matrix} = \frac{1}{2(1+\nu_{matrix})}\partial E_{matrix}$$

where Φ is the volume fraction of the mineral phase (hydroxyapatite), E_{matrix} and $E_{mineral}$ are the elastic modulus of the organic phase (collagen) and of the inorganic phase (hydroxyapatite), respectively; D and L are the mineral thickness and length, respectively; and ν_{matrix} is the Poisson ratio of the organic matrix (collagen).

By differentiating Eq. 33 and rearranging it, a relation between the relative change of total elastic modulus and the necessary relative change in elastic modulus of the matrix can be obtained,

$$\frac{\partial E}{E} = \left(\frac{(1-\Phi)E_{matrix}}{E} + \frac{\Phi\beta}{E}\left(1+\frac{\beta E_{mineral}}{E_{matrix}}\right)^{-2}\frac{E^2_{mineral}}{E_{matrix}}\right)\left(\frac{\partial E_{matrix}}{E_{matrix}}\right) \quad \text{Eq. 34}$$

$$\text{where } \beta = \frac{8(1-\Phi)(1+\nu_{matrix})D^2}{\Phi L^2}$$

If it is assumed that the mineral volume fraction Φ is equal to 0.5, D/L (aspect ratio of the mineral platelets) = 0.03, assuming that the E of the mineral phase is 100 GPa and unaffected by moisture and demineralization is prevented by HBSS and using a Poisson ratio for the organic phase of 0.25, and considering only elastic deformations are involved in the differences between wet and dry measurements, then $\frac{\partial E_{matrix}}{E_{matrix}}$ may be estimated from the above equations.

Since other phenomenological studies on the effect of solvents on the response of the organic phase of compact bone were not found in the literature, and due to the similar composition of dentine and bone, dentine literature has been drawn upon for the discussion. Thus, based on (Pashley et al., 2003, Maciel et al., 1996, Angker et al., 2004, Angker et al., 2005), E_{matrix} of the wet matrix was chosen equal to 10-40 MPa.

Therefore, the measured 40% difference of E of BL orientation between wet and dry conditions is equivalent to a change in the elastic modulus of the organic matrix in bone, $\frac{\partial E_{matrix}}{E_{matrix}}$, of 4 to 16; according to Eq. 34.

Where may this change in elastic modulus of the organic phase come from? Water is known to plasticize collagen since it is the strongest known hydrogen bonding solvent, and together with its high molar concentration (55 mol/l) prevents H-bonds forming between peptides of adjacent triple helices leading to a more compliant structure. When drying, the absence of water molecules leaving free peptide bonds is the driving force to create new bonds between the peptide chains which are known to be stronger than the bond between Hydrogen and water. This interpretation is supported by the observation of shrinkage of the structure upon drying (Lee and Glimcher, 1991).

The simple uni-axial model proposed above based upon Jäger and Fratzl's approach (Jäger and Fratzl, 2000) results together with the present phenomenological explanation of the nanoindentation observations as follows. The fact that the wet measurements present higher penetration depths than their dry counter parts suggests a higher compliance for the former condition. Indenting bone may contribute to wedging open and breaking the weak bonds present while using HBSS due to the imposed tensile stresses, thereby increasing the measured penetration depths and resulting in a more compliant structure. Mullins and co-workers (Mullins et al., 2007) found that for Berkovich, Vickers and cube corner indenters of dry samples, only the latter generated cracks in their bovine compact bone samples. Upon removal of the load the bonds are restored as observed with the higher viscoelastic recovery of the wet condition. The fluid environment may contribute to a higher mobility of short range bonding between neighbour collagen chain groups and, hence faster restoration of the structure. Several studies on collagen showed the need of a small amount of residual water for maintaining the regularity of the structure (Lazarev et al., 1992, Lazarev et al., 1985, Ramachandran and Chandrasekharan, 1968). Thus, in the presence of water it seems the structure tends to form a better ordered arrangement and therefore recovery is favoured. This explanation also agrees with the proposed sacrificial bond theory (Fantner et al., 2005, Thompson et al., 2001).

The indentation strain is the same for the case of the dry measurements; however, the reduction in water content with the consequent increment of stronger peptide bonds (which are more difficult to shear) between collagen triple helices, shrinkage of the structure and the resultant compressive state leads to a stiffer structure reflected in the lower penetration depth measured under this condition.

8.7. Conclusions

- Indenter tip geometry and viscoelastic effects should be taken into account while analysing the nano-indentation of interstitial bovine compact lamellar bone with Oliver and Pharr method (Oliver and Pharr, 1992).
- Deep freezing the samples immersed in HBSS does not damage the elastic moduli of the samples.
- The measured 20% anisotropy between BL and BT orientation could be explained by different deformation mechanisms during nanoindentation.

- The measured 40 % difference in elastic modulus between wet and dry samples may be explained by a marked change in the elastic properties of the organic matrix.
- The change in the elastic modulus of the matrix with the chosen environment may be explained by the replacement and/or formation of inter-peptide bonds during hydration/dehydration.

8.8. Acknowledgement

Financial aid through EC Contract No MEST-CT-2004-504465, „Marie Curie Host Fellowships for Early Stage Research Training", is gratefully acknowledged. Griselda Guidoni wants to thank Dr. Himadri Gupta and Prof Peter Fratzl from Max Planck Institute of Colloids and Interfaces in Golm, Germany, for the discussions and literature given. Griselda Guidoni also kindly acknowledged Dr Markus Lengauer for the discussions and mechanical simulations provided.

FIGURES OF CHAPTER 8

Fig. 65

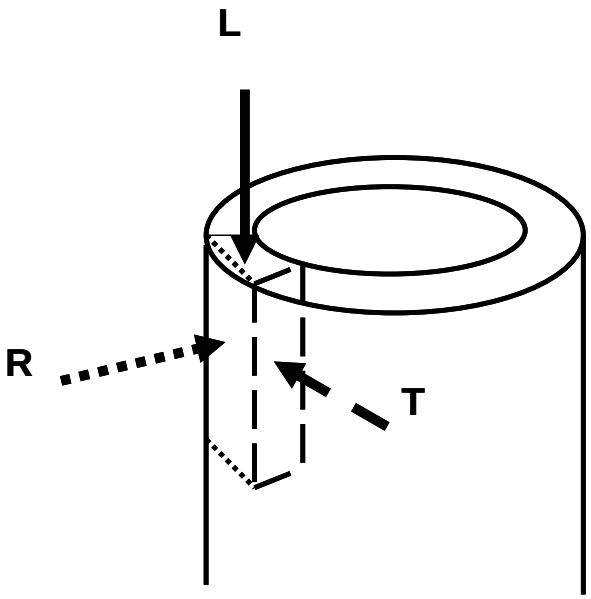

Fig. 65 Scheme showing the three different defined orientations in the long compact bone here tested.

Fig. 66

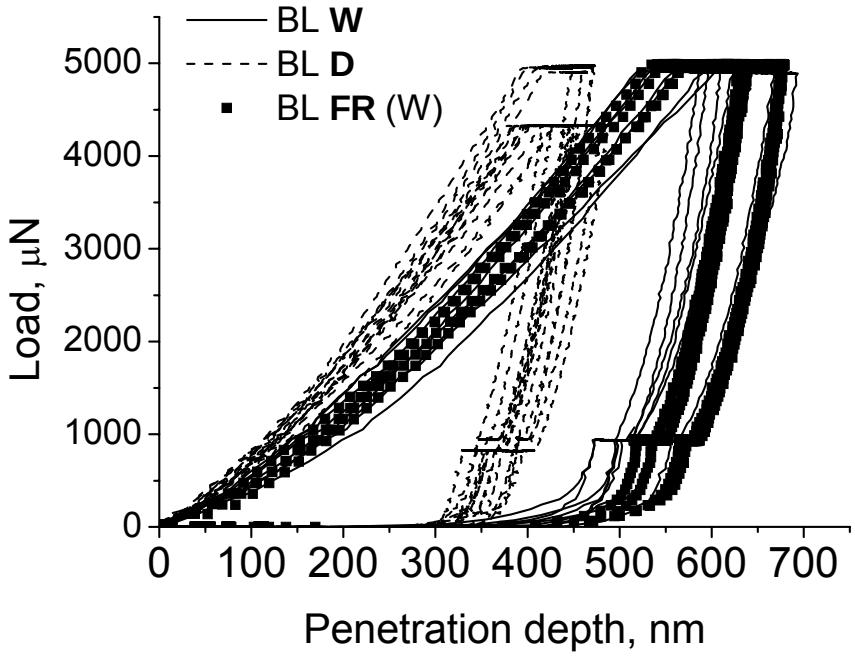

Fig. 66 Load-displacement curves of each individual test of the BL sample under the three different tested conditions: W, wet (under HBSS); D, dry and; FR (W) tested wet although stored under fluid and sub-zero temperature.

Fig. 67

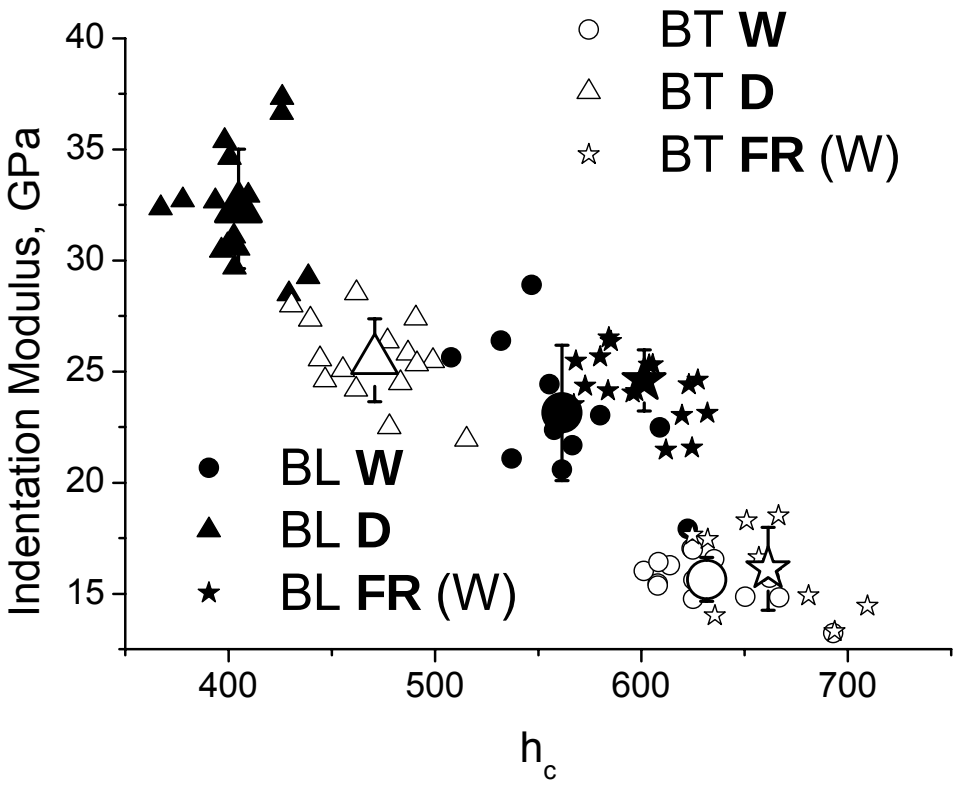

Fig. 67 Indentation moduli of the BL and BT samples under all the tested conditions as a function of the contact penetration depth, h_c.

TABLE OF CHAPTER 8

Table 9

	BLW	BTW	BLD	BTD	BLFR	BTFR
Creep rate initial, nm/s	4.7 ± 3.0	3.5 ± 0.7	4.2 ± 1.7	3.5 ± 1.2	4.1 ± 1.2	3.4 ± 1.6
Creep rate (unloading), nm/s	0.09 ± 0.2	0.09 ± 0.04	0.02 ± 0.05	0.11 ± 0.11	0.06 ± 0.05	0.33 ± 0.27
Creep distance	**69 ± 10**	**73 ± 14**	**46± 10**	**66 ± 13**	**75 ± 10**	**95 ± 17**
Initial penetration creep	557 ± 29	632 ± 25	407 ± 15	462 ± 21	572± 23	642 ± 17
Final penetration creep	627 ± 33	707 ± 29	453 ± 19	531 ± 25	647 ± 25	737 ± 30
Penetration during unloading	**107 ± 7**	**157 ± 43**	**76 ± 6**	**101 ± 5**	**99± 7**	**153 ± 14**
Initial penetration recovery	519 ± 29	549 ± 23	376 ± 18	430 ± 24	526 ± 23	554 ± 28
Final penetration recovery	498 ± 28	516 ± 23	362 ± 20	414 ± 25	548 ± 22	584 ± 25
Recovery, nm	**21 ± 8**	**33 ± 3**	**15 ± 3**	**17 ± 7**	**22 ± 3**	**29 ± 8**
E, GPa m = variable	**23 ± 3 (2.71 ± 0.32)**	**16 ± 1 (3.25 ± 0.25)**	**32 ± 3 (2.20 ± 0.20)**	**25 ± 2 (2.52 ± 0.22)**	**24 ± 2 (2.84 ± 0.27)**	**16 ± 2 (3.06 ± 0.40)**
E, GPa m = 2	**23 ± 4**	**20 ± 3**	**32 ± 3**	**27 ± 3**	**27 ± 3**	**20 ± 4**
E creep, GPa m = 2	**23 ± 4**	**19 ± 3**	**32 ± 2**	**26 ± 3**	**26 ± 3**	**19 ± 4**
E, GPa ν = 0.3	**21**	**17**	**30**	**24**	**24**	**18**

Creep rate initial: obtained by differentiating the exponential fitting of the first holding period in a displacement-time curve and calculating it at the beginning of the first holding period.

Creep rate (unloading): obtained by differentiating the exponential fitting of the first holding period in a displacement-time curve and calculating it at the onset of unloading.
Creep distance: average (creep) penetration during the first holding period (5mN, 60s).
Initial/final penetration creep: recorded penetration depth at the beginning/end of the first holding period. The range between initial and final penetration creep gives "creep distance".
Penetration during unloading: penetration depth during the first partial unloading period (0.4 mN/s, 10s).
Initial/final penetration recovery: recorded penetration depth at the beginning/end of the second holding period. The range between initial and final penetration recovery gives "recovery".
Recovery: average viscoelastic recovery depth during the second holding period (1mN, 20s).
E (m = variable): indentation modulus calculated using the Triboscope software.
E (m = 2): indentation modulus calculated by manually fitting the unloading curves fixing m = 2.
E creep (m = 2): indentation modulus having corrected viscoelastic creep at maximum load.
E ν = 0.3: elastic modulus of bone considering ν = 0.3 and correcting the compliance of the indenter.

Table 9 Visco-elastic and elastic parameter obtained from the analysis of the individual load-displacement curves. The data are the average value followed by their standard deviation.

APPENDIX A

A. NANOINDENTATION IN TEETH: THE INFLUENCE OF EXPERIMENTAL CONDITIONS ON LOCAL MECHANICAL PROPERTIES. VERIFICATION

Abstract

The influence of various experimental conditions on the elastic modulus and hardness of human intertubular dentin was studied using instrumented nanoindentation at room temperature in a previous work (Guidoni et al., 2006). One of the outputs was that deep-freezing wet dentin samples deteriorated their mechanical properties by about 20 to 28%, whereas dehydrated samples suffered no damage. Thus, the above damage was attempted to be corroborated using a fresh sample. No differences were found in this case. Possible explanations for this discrepancy were proposed.

Keywords: nanoindentation, biological materials, intertubular dentin, experimental conditions, Hank's balanced salt solution (HBSS).

Sample preparation

For the investigation reported here a healthy wisdom molar extracted from a 27 years old human male was examined. The sample was cut during extraction by the dentist as part of the treatment and immediately stored under HBSS (Hank's balanced salt solution) with 0.1 % by weight of sodium azide (antibacterial, Merck 888).

Thus, one of the received pieces was glued to a plastic stub with cyanoacrylate glue, for nanoindenter testing and handling purposes. The transversal section of the molar consisting of enamel and dentin was accessible for preparation. The exposed area was ground and polished to a 2500 P grit finish with silicon carbide cloths, followed by polishing in 0.3 μm alumina suspension. The sample was continuously rinsed with HBSS while polishing, and stored under HBSS at all times to avoid accidental dehydration. This is essential especially in the last stages of preparation.

After the first set of indentations (RT), the sample was immersed in HBSS and frozen at $-15^{o}C$ for more than 8 hours. The sample was let thaw for typically twelve hours and tested again under HBSS and room temperature. Several sample preparations were subsequently done before the second set of indentations were made: thawed without re-polishing (FR), soft polished (FR&Pol), deeper polished (FR&Pol2) and soft polished (FR&Pol2'). A new freezing and thawing cycle was made and was tested as the third set of indentations (FR2).

Nanoindentation tests

Nanoindentation tests were carried out using an add-on nanoindentation device (Hysitron Triboscope, Hysitron Inc., Minneapolis, MN, USA) mounted on the scanner head of an AFM stage (Veeco – Digital Instruments, Santa Barbara, CA, USA).

For the indentation, sample and part of the indenter were immersed in HBSS during testing. A conical rounded indenter tip was used (nominal radius ~ 400 nm) mounted at the end of a tungsten rod ca. 9.5 mm long in order to keep the transducer well away from the fluid cell.

Nanoindentation tests were carried out in several loading-unloading steps: first the specimen was linearly loaded to the maximum load of 5000 μN in 5 seconds, secondly the load

was maintained 50 seconds in order to exhaust most of the creep before unloading, thirdly the sample was unloaded to an intermediate load of 1000 μN within 10 s, fourth step was to hold this load 20 s, finally, unloading linearly to zero within 2 s.

The temperature of testing was in all the cases room temperature. The sample stored in a deep-frozen ($-15^{o}C$) condition was defrosted and allowed to equilibrate at ambient temperature before testing.

The indented region was intertubular dentin, and the indents were carefully placed by means of the AFM mode scanning with the nanoindenter tip between the tubules to avoid any influence of the peritubular dentin and/or tubules on the results.

Elastic Modulus and Hardness were calculated by means of the load-displacements curves using the well known Oliver-Pharr method (Oliver and Pharr, 1992).

At least 15 measurements per storage condition were taken. In order to compare the results, ANOVA one way statistical analysis was used, with a confidence interval of 0.05.

Results

The obtained, E and H, for all the tested conditions are shown in Fig. 68 and Fig. 69 respectively. No differences were found between the temperatures of storage.

Discussion

The temperature of storage did not influence the results in this verification, which raises the question whether freezing the sample plays a role in the mechanical integrity of intertubular dentin or not. The measured frozen data were in no case lower than the RT data.

In particular, the FR&Pol2' condition has a considerably higher value than the adjacent FR&Pol2 condition which indicates a possible mechanical property variation with position. Cuy and co-workers (Cuy et al., 2002) found a strong difference in elastic modulus and hardness of human enamel with position when measured by nanoindentation. They explained their results with the difference in composition among enamel. Tesch et al. (Tesch et al., 2001) found a decrement on elastic modulus of dentin towards the DEJ (Dentin enamel junction) from 26.5 to 19.5 GPa (26%). This output was explained by the increased tubular density as the pulp chamber was approached. In addition, they stated that there is a decrease in the amount of the intertubular dentin and an increase in the individual tubular diameter.

The microstructural heterogeneity of dentin (tubuli surrounded by peritubular dentin embedded in intertubular dentin matrix) makes nanoindentation a sensitive technique regarding the position of the underneath tubuli with respect to the indentation. Fig. 70 shows a scheme of a similar surface view but different conditions beneath the surface. The cylinders are oriented at 30º difference. For the case of indentations marked with the two arrows, depending on how deep the indentations are, the expected response will be different.

Hank's balanced salt solution (HBSS) is an aqueous buffer solution with the necessary ions to prevent demineralization (Habelitz et al., 2002, Nalla et al., 2005). Water is mainly located inside the tubules, so when the samples are deep frozen, the increase in volume of

frozen water may introduce irreversible mechanical damage in the microstructure of the dentin tubules as well as in the surrounding dentin. This may explain the ~25 % decrease in local mechanical properties obtained among the samples stored submersed under HBSS and kept at room temperature and the ones deep frozen under fluid, respectively. This latter was the explanation for the results presented in (Guidoni et al., 2006).

A rough estimation of the stresses occurring around the tubules after water freezing may be exercised. Only one tubule is considered and the water volume increment after freezing inside it is modelled as interference fit between two cylinders (Fig. 71). The change in dimension of the cylinder of liquid water due to the 4 % increment in volume of solid water leads to:

$$V_{water} = \pi a^2 l$$

$$V_{water+\Delta} = \pi(a+\Delta)^2 l$$

$$\frac{V_{water+\Delta}}{V_{water}} = \left(\frac{a+\Delta}{a}\right)^2 = 1.04$$

$$\Delta \approx 0.02a$$

where V_{water} is the volume of liquid water before freezing and $V_{water+\Delta}$ is the volume of solid water after freezing. Δ is the change in the radius of the water cylinder after freezing, and *a* is the original liquid water radius equal to the radius of the tubulus. It is assumed that the volume change occurs predominantly in the radial direction.

If no body forces act on the solids, the angular velocity is zero, the cylinders have uniform temperature, the shaft slides freely inside the bushing, the ends of the cylinder are free of force, both the shaft and cylinder have the same Young's modulus E and Poisson's ratio, the cylinder and shaft are sufficiently long to ensure that a state of generalized plane strain can be developed in each solid, then the strain and stresses induced can be described by (http://www.engin.brown.edu),

$$\varepsilon_{rr} = \frac{(1+\nu)a}{r^2}\frac{\Delta}{2}\left\{-1+(1-2\nu)\frac{r^2}{b^2}\right\} - \nu^2\frac{\Delta a}{b^2}$$

$$\varepsilon_{\theta\theta} = \frac{(1+\nu)a}{r^2}\frac{\Delta}{2}\left\{1+(1-2\nu)\frac{r^2}{b^2}\right\} - \nu^2\frac{\Delta a}{b^2}$$

$$\sigma_{rr} = \frac{E\Delta a}{2b^2}\left\{1-\frac{b^2}{r^2}\right\} \qquad \sigma_{\theta\theta} = \frac{E\Delta a}{2b^2}\left\{1+\frac{b^2}{r^2}\right\} \qquad \sigma_{zz} = 0$$

where ε and σ are strain and stresses, respectively and the sub-indexes rr and $\theta\theta$ denote radial and tangential directions respectively. E represents the elastic modulus; b is the external radius of the cylinder (tubulus), taking in this case as the outer radius of the peritubular dentin, r is the variable radius in which the stresses are evaluated and ν is the Poisson ratio.

Kruzic et al. (Kruzic et al., 2003) described the dentinal tubuli as being 1-2 μm in diameter and having a 1 μm thick peritubular dentin. Garberoglio and co-worker (Garberoglio and Brännström, 1976) reported a gradient in tubular diameter of intact human permanent teeth (24 premolars, 5 molars and one incisor. Sixteen teeth were from subjects aged 8-25 years and the remaining 14 from subjects aged 40 to 60 years.) from 2.5 μm near the pulp to 0.8 μm near the outer surface by scanning electron microscopy (SEM). Our own AFM observations with the nanoindenter tip showed diameters from 1 to 2 μm. The thickness of peritubular dentin is thought to be 1 μm (Balooch et al., 2004).

Kinney and co-workers (Kinney et al., 1996) measured by nanoindentation using a three-sided Berkovich diamond tip a 29.8 GPa elastic modulus for dry peritubular dentin of three unerupted human third molars. In a posterior work (Balooch et al., 2004), they measured an average of 48 GPa for the elastic modulus of dry peritubular dentin using a cube corner diamond tip. They argued that the higher values in the latter study could be a result of, but are not limited to, the age, race, location or gender of the samples. In this latter case they used three extracted non-carious human third molars.

Since the purpose of the present work is to obtain an estimation of the stresses generated after freezing temperatures inside the tubuli and after a previous work on the influence of the indenter tip geometry on the elastic modulus of enamel (Guidoni et al., 2007c), the chosen value for the elastic modulus of peritubular dentin was 30 GPa.

Thus, after all the considerations epressed above, if *b* is taken as *2a*, and the stresses are evaluated in the inner side of the tubule (*r*=*a*):

$$\sigma_{rr} = -\frac{3E\Delta}{8}$$

$$\sigma_{\theta\theta} = \frac{5E\Delta}{8}$$

which leads a tangential tensile stress of the order of 375 MPa. 670 MPa is obtained, if b is equal to 1.5a. The corresponding tangential deformations are 1.3 and 1.4 %. Although macroscopic values and not specifically for peritubular dentin, Konishi and co-workers (Konishi et al., 2002) found a ultimate shear strength of dentin ranging from 52.7 (range 29.0–73.1) MPa near the pulp to 76.7 (range 53.9–104.0) MPa near the dentin–enamel junction.

Therefore, in spite of all the simplifications used, mechanical damage due to freezing does seem feasible. Although here the tubules were thought as free cylinders when in fact, the surrounded intertubular dentin may act as a constraint.

The cylinders were model as free of residual stresses. Kishen and Vedantam (Kishen and Vedantam, 2007) studied the role of free water in the dentinal tubules on the mechanical integrity of bulk dentine by means of finite element analysis. They found in fact that the models with hydrostatic pressure demonstrated a residual tensile stress in dentin (at zero compressive load), which was higher in the inner dentine adjacent to the root canal. This could be taken as another argument for the possible damage after freezing dentin immersed in an aqueous solution.

Regarding water wetting the bulk material, it is found in literature that not all the water surrounding collagen is thought to behave like bulk water (Chapman et al., 1971). Chapman et al. (Chapman et al., 1971) stated that part of the hydration layer of collagen has a lower freezing point than bulk water, presumably due to the incompatibility with the ice structure of the neighboring structures. In addition, water is also found in crystal form (Nyman et al., 2005). Thus, the effect of water expansion may be diminished.

Moscovich et al. (Moscovich et al., 1999) did not observe changes in the hardness of dentin after storing it at $-18^{o}C$ in water. Their chosen method was macroindentations with loads of 30 kg in 2.1 mm thick disks and we did not find a change in the present work. We also did not find any deteriorating effect of deep freezing on the local mechanical properties of bovine compact bone (Guidoni et al., 2007a). Although it is true that even the composition of bone and dentin is similar, their microstructural arrangement is not.

The sample tested in (Guidoni et al., 2006) was not polished after freezing which may lead to the supposition of a surface film influencing the results. However the overlapping at low loads of the load-displacement curves between the RT and FR samples may rule out the formation of a film, besides the use of the AFM mode capability for checking the surface topography and appearance before testing. The FR and 5xFR results in this latter work gave also similar results and they were made in randomly chosen positions.

The sample tested here was cut during extraction. Shin and Yoon (Shin and Yoon, 2006) found that maximum temperatures during bone milling may rise over 100 ºC and that thermal induced cellular damage may occur to a depth of 1.9mm below the cut surface if there is no irrigation fluid. Thus, since the sample here tested was received as cut, a possible thermal damage of the sample may not be rejected. The elastic modulus and hardness were higher than the previous sample. Elastic modulus and hardness are well known to depend on mineral content (Tesch et al., 2001, Cuy et al., 2002). Since the sample came from a 26 year old individual, the degree of mineralization is expected to be higher than the former sample from 12 year old individual and thus, the mechanical properties are expected to be higher as they were found to be. However, since the degree of mineralization of both samples is unknown and there is no reliable correlation for the prediction of local mechanical properties with mineral content, the opposite effects of damaging and higher mineralization may have hidden a degree of thermal damage of the samples during extraction.

The comparison above should be taken with care since the samples come from different positions on the mouth and the mechanical properties need not necessarily be comparable (besides the different age of the individuals already discussed).

Conclusions

The several factors considered here together with the discrepancy of results lead us to suggest that the hypothesis of loss of mechanical integrity after freezing dentin immersed in an aqueous solution may be true and that the present sample may be damaged during extraction. However, a new test design in which the tested positions are close to one another to avoid intra-

sample scatter but distant enough to avoid interference is recommended, together with a careful extraction of the samples to avoid possible a priori damages.

FIGURES OF APPENDIX A

Fig. 68

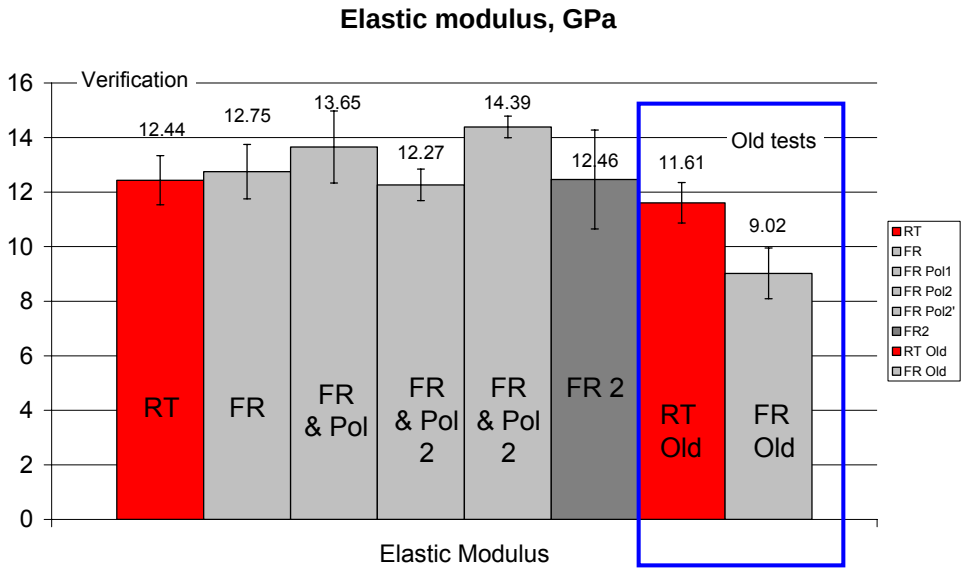

Fig. 68 Elastic modulus of the dentin verification sample followed by its standard deviation (error bars). The "old test" values refer to (Guidoni et al., 2006).

Fig. 69

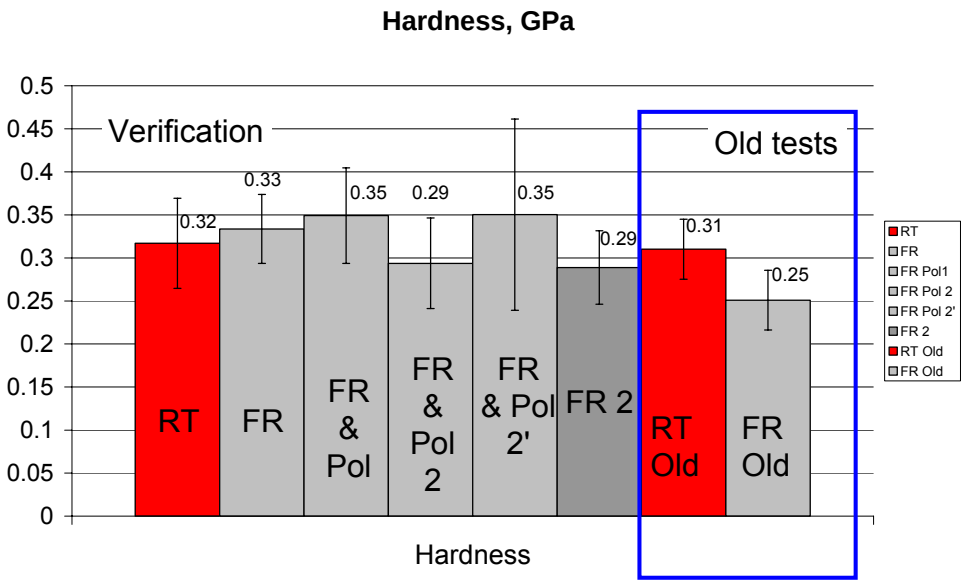

Fig. 69 Hardness of the dentin verification sample followed by its standard deviation (error bars). The "old test" values refer to (Guidoni et al., 2006).

Fig. 70

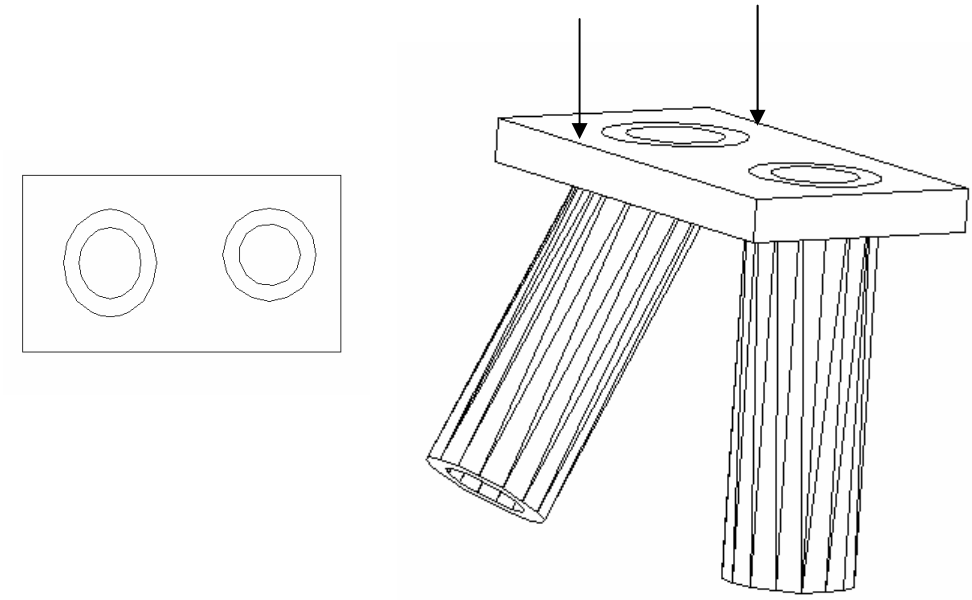

Fig. 70. Schematic top (left image) and lateral (right image) view of the effect of tubuli orientation on the indentation of this system.

Fig. 71

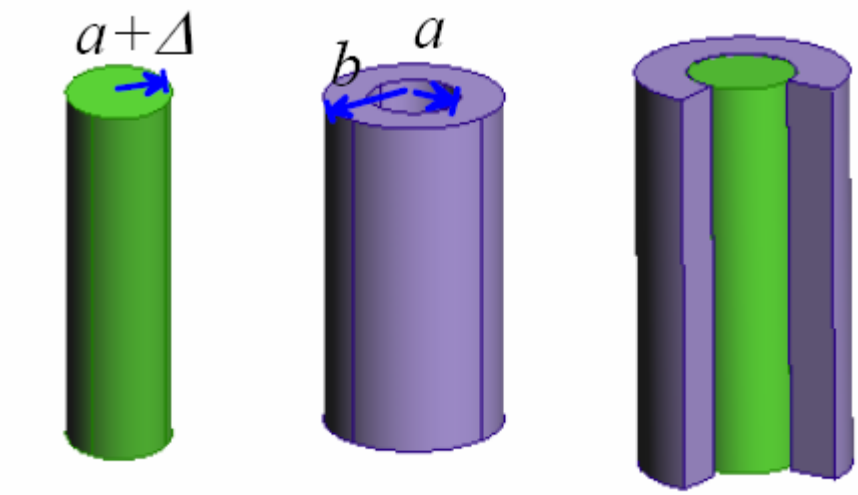

Fig. 71 Schematic representation and variables used for study the mechanics of inserting a solid cylinder of radius $a+\Delta$ into a hollow one with a radius a.

APPENDIX B

B. ABRASION TESTS ON HUMAN ENAMEL UNDER WET AND DRY CONDITIONS.

The fifth IASTED international conference on Biomedical Engineering ~Biomed 2007~

Innsbruck, Österreich (Austria). 14th to 16th February, 2007. (Talk)

- ***G. M. GUIDONI, T. Schöberl, G. Dehm and I. Jäger,*** *Abrasion tests on human enamel under wet and dry conditions,* **The fifth IASTED international conference on Biomedical Engineering "Biomed 2007" (2007)**

Abstract

Wear behaviour of the cross sectional area of human enamel at a micrometer scale was studied with a nanoindenter transducer mounted on an AFM stage. Wear was applied by scanning a diamond indenter tip over a certain area with a load higher than typical for surface imaging. A conical tip with a radius of ~ 400 nm was used. Single lines of linearly incremented load were also scratched. The rounded tip mainly compresses the near surface material, and under certain conditions, fractures and removes material from the sample. A threshold load of 400 μN for removing material was determined after scanning the sample with 50, 100 and 200 μN without observing any spalled material, but deformed areas. The area of the worn surfaces was 2 x 2 μm^2 since otherwise the tip crossed more than one mineral rod. Crossing a rod leads to a different condition under the tip due to the change in fibril orientation between the rods. For the 'rounded' tip the abrasion rate was larger under atmospheric conditions compared to the immersed in Hank's balanced salt solution (HBSS), when depth profiles were measured by Atomic Force Microscopy (AFM) imaging. However, similar results for both conditions were obtained when analysing the displacement data got from the transducer.

Key words: Nanoindentation, wear, enamel, Hank's balanced salt solution (HBSS), Atomic Force Microscopy (AFM).

Introduction

Enamel is the highest mineralized tissue in human body. It is composed of about 97 % by weight of mineral, essentially apatite, 1 % organic material, mostly protein, which is not collagen, and 2 % water (Currey, 2002). As most biological materials, it has a hierarchical structure, which imparts order from nm to mm level.

Many of the mineral crystals are bound together in bundles called prisms or rods. Each rod is 3-6 μm in diameter. There is little protein within the prisms, while it is mainly concentrated at the interprism boundaries (Currey, 2002). This region is also called enamel sheath, and consists also of apatite crystals that are not part of the prisms. The enamel prisms themselves are arranged in a decussating, plywoodlike structure (Currey, 2002, Macho et al., 2003) which is thought to act as crack arrester.

Several investigations have been reported on hydration, dehydration and rehydration of dentin (Guidoni et al., 2006, Habelitz et al., 2002, Nalla et al., 2005), the layer below enamel. Habelitz et al. (Habelitz et al., 2002) found a large decrease, even after 1 day, in reduced elastic modulus, E, and hardness, H, of dentin under deionized water or $CaCl_2$ solution when compared with HBSS. We measured reduced indentation modulus, E, and hardness, H, under HBSS and atmospheric conditions in dentin (Habelitz et al., 2002) and found a factor of ~ 2 and ~ 3 between the dry and wet state, respectively. To the knowledge of the authors, there are no investigations on these quantities in enamel at this scale. Staines et al. (Staines et al., 1981) did spherical indentations in human enamel with a 6.5 mm diameter tungsten carbide ball and 5 kN load. Their samples were kept under water until testing. Even though their indentations were

done under atmospheric conditions, the first set of indentations was carried out immediately after the sample was taken out from the fluid, state they called “wet”. Under these experimental conditions, they reported an increase in elastic modulus by some 15 % after 72 h drying. In this work we present the results of nanoindenting enamel under HBSS (where sample and indenter were always immersed under the fluid) and atmospheric conditions. We found a trend in the measured mechanical properties E and H when comparing atmospheric and HBSS conditions of human enamel and a significant difference in the absolute values.

Besides normal loads, enamel bears shear forces because of the direct contact with opposite teeth, external objects during mastication and even toothpaste hard aggregates. Fernandes et al. (Fernandes et al., 2003) measured in three human females and three males of 57–72 years, bite forces of 28 N to more than 120 N. In general, enamel is required to bear all these solicitations without failure and to retain its shape while doing so. Unlike other calcified human structure, fracture of dental tissue is not repairable. One of the most important features of enamel is its good wear resistance, even under bad working conditions, such as widely ranging load, reciprocating movements, temperature changes or possible acids attacks.

We searched and found some literature concerning this subject because understanding the wear mechanism of enamel is important to clinical tooth preparation and the development of tooth restorative materials. Several studies and reviews on wear at the millimetre scale were done (Dahl et al., 1993, Oh et al., 2002, West et al., 1999, Sajewicz, 2006). We are applying a technique to move a step further down on the hierarchical structure of enamel, i.e. to the micrometer scale. We produced observable wear by scanning a nanoindenter tip on selected areas and measuring the penetration depth in two different ways. By means of AFM depth profiles and in situ displacement data from the transducer we can estimate the worn depth of our samples. The AFM scanning mode allows us to choose and abrade areas inside the enamel rods.

Material

For the investigation reported here one healthy second premolar extracted for orthodontic reasons from a 12 years old human male was examined.

It was mechanically tested after 3 years of storage at 4 ºC immersed in HBSS plus antibacterial. Previous studies demonstrated that these storage conditions maintain the integrity of dentin (Guidoni et al., 2006) and the authors believe there are no reasons for expecting enamel degradation under these conditions.

The sample was cut with a diamond saw in two sections along the crown-root direction, carefully avoiding any overheating. Only one half of the premolar was tested. This half was again cut in two parts. One part was dehydrated in air (‘dry’), the remainder was immersed in HBSS (‘wet’). The pulp was cut away.

For testing and handling purposes, the pieces were glued to a platform with cyanacrylate glue. In all the cases, the transversal section of the premolar consisting of enamel and dentin was accessible for preparation. The exposed area was ground and polished to a

2500 P grit finish with silicon carbide cloths, followed by polishing in 0.3 µm alumina suspension. In the case of 'wet' conditions, the samples were permanently rinsed with HBSS while polishing, and stored under HBSS all the time to avoid accidental dehydration. This is essential especially in the last stages of preparation.

Nanoindentation and Tribological Tests

Nanoindentations and wear tests were carried out using an add-on nanoindentation device (Hysitron Triboscope, Hysitron Inc., Minneapolis, MN, USA) mounted on the scanner head of an AFM stage (Veeco – Digital Instruments, Santa Barbara, CA, USA).

Two kinds of configurations for both nanoindentations and wear tests were used: on the one hand, 'dry', in which the samples were nanoindented and abraded under atmospheric conditions, on the other hand, 'wet', in which sample and indenter were immersed in HBSS during testing. For both cases and types of tests a conical indenter tip (radius of ~ 400 nm) was mounted at the end of a tungsten rod ca. 9.5 mm long in order to keep the transducer at a safe distance from the fluid.

Nanoindentation tests were carried out in several loading-unloading steps: firstly the specimen was linearly loaded to the maximum load (5000 µN) in 5 s, secondly the load was maintained for 50 s in order to eliminate most of the creep before unloading, thirdly the sample was unloaded to an intermediate load of 1000 µN within 10 s, fourthly this load was held for 20 s for thermal drift correction and, finally, the sample was linearly unloaded to 0 µN within 2 s. More than 10 measurements per condition were taken.

Elastic modulus and hardness were calculated by means of the load-displacements curves using the well known Oliver-Pharr (Oliver and Pharr, 1992) method. Since Poisson´s ratio of the material is not widely known (He et al. (He et al., 2006) used 0.33 as Poisson ratio in their work, Cuy et al. (Cuy et al., 2002) chose 0.25, Ge et al. (Ge et al., 2005) mentioned a range from 0 to 0.5 for most materials but did not specify which value they used, if any) and the material is highly anisotropic anyway, the values of elastic modulus, E, are given as the reduced indentation modulus.

Single scratches with linearly increasing load were also done inside the rods. The ramps started from a pre load of 4 µN until maximum load. The length of the scratches was approx. 5 µm. Each scratch took 4 s.

Wear was applied by scanning the diamond indenter tip over a certain area with a load higher than typical for surface imaging. In previous experiments, a 400 µN load was determined by which, for both wet and dry experiments, measurable abrasion appeared within reasonable times. Feedback load controlled measurements were done, storing for each test the displacement data. The tip velocity was 4 µm/s in all the tests.

Due to enamel structure (mineral rods running along the whole structure), the area for the abrasion tests were chosen only inside the rods and avoiding crossing rod interfaces. Moving to a neighbour rod leads to scanning new areas with possibly different fibril orientations. At this point of early stage of technique development we had to reach a compromise: scanning

much bigger areas in order to average over different fibril orientations or reducing the abraded area as small as possible in order to remain inside one rod. We chose the last option as a first approach. For this reason and for the sake of comparison, areas of 2 x 2 μm^2 were abraded, both in wet and dry measurements, taking particular care of placing them inside the rods.

Due to the use of a long rod nanoindenter tip, it is not possible to choose the location of the abrasion areas by means of the attached optical microscope. Tip engagement is made in a blind way. Once the surface is reached, the AFM mode allows the user to image the surface with the nanoindenter tip and to find a suitable place for the abrasion tests (with the lateral resolution limited by the size of the nanoindenter tip). After each abrasion test, a control image of 5 x 5 μm^2 was taken with the nanoindenter tip in the AFM mode. In addition, after all the wear experiments were done, the sample was scanned and imaged with an AFM tip of ~ 2 nm radius.

In order to measure the remaining depth of the abraded areas by means of AFM imaging, it is important to carefully clean and move away the abraded particles from the interior of the worn areas. AFM imaging was a time consuming step due to the need of taking out the sample from the stage each time a new cleaning procedure was carried out and of finding again the desired areas. Several cleaning procedures were tried. For the dry samples and because of the sample mounting, a soft automatic polishing with 0.3 μm Al_2O_3 particles and a 20 N force was the best solution, judging from the profiles found. In the case of wet samples, they were manually cleaned with a cleaned alumina polishing cloth wetted with HBSS.

Two independent measurements were used to analyse wear: an average of 10 profiles measured by AFM imaging (noise <0.5 Å RMS in vertical (Z) dimension) and the average of the penetration depth obtained from the nanoindentation device (0.2 nm resolution).

Results

The reduced elastic modulus (E) and Hardness (H) are presented in Table 10, together with the ratios of properties and their combinations.

There were not enough scratches done for obtaining representative data. However, in contrast to the dry state, it is remarkable that the scratches done from 4 to 400 μN and 4 to 1000 μN in the wet condition were not found with the AFM. This fact probably corresponds to the stronger recovery expected in the wet state.

Preliminary experiments were carried out in order to find a suitable load for the wear tests. The results are shown in Table 11. Each scan corresponds to 512 scratches of 2 μm length done through the 2 x 2 μm^2 area. After each scan, the abraded zone was imaged with the nanoindenter tip in AFM mode with a 5 x 5 μm^2 window and a 4 μN imaging force. Each data belongs to one single test. The increased standard deviation at 400 μN may be explained by the explicit observation of spalling.

The results obtained after carrying out wear tests at 400 μN are presented in Table 12. As in the preliminary experiments, each data belongs to one single test. Seven continuous scans were carried out. Each scan corresponds to 256 scratches of 2 μm length done through

the 2 x 2 μm^2 area. After the end of the seventh set of scratches, an image of 5 x 5 μm^2 scan size with the nanoindenter tip in AFM mode was taken with a 4 μN imaging force.

In the tests labelled with the "ABRA" addition (Table 12), particles from previous tests were a priori distributed throughout the abraded area and subsequently new places were chosen close to the borders of previous tests. The influence of the incorporation of extra particles to the tests was studied with this configuration.

Discussion

Even though enamel contains less than 1 % of organic material in its structure, it also presents a considerable difference in mechanical properties when measured under dry or wet conditions. We already found the same trend in human dentin (Guidoni et al., 2006). We repeated the measurements in the enamel of a bovine permanent incisor and found a similar behaviour, although the ratio between dry and wet properties was higher in this case: 2.98 in Elastic modulus (83.5 $\pm$ 15.04 GPa 'dry' and 28.0 $\pm$ 7.29 GPa 'wet') and 2.01 in Hardness (3.8 $\pm$ 0.45 GPa 'dry' and 1.9 $\pm$ 0.39 GPa 'wet'), between dry and wet conditions, respectively.

Our measured 'dry' human E seems to be smaller than what we found in literature (Habelitz et al., 2002, Mahoney et al., 2004) presumable because Habelitz et al. (Atkins and Tabor, 1965) measured it in orthogonal directions to the rods with a sharp cube corner indenter of 20 nm radius and Mahoney et al. (Mahoney et al., 2004) measured by ultra micro indentation. Judging for their description of sample preparation, the indented places may have been chosen closer to the surface, where the reported E and H are higher (Habelitz et al., 2002). Our results fit within the values measured by Cuy et al. (Cuy et al., 2002) for the middle enamel of second molars near the buccal and lingual region, which are in fact, the areas we unintentionally indented.

Wear behaviour is definitively a very complex process where many variables are playing a role (Dahl et al., 1993). We are far way from being able to give a model for this system, but we have some insight which may contribute to further improvements on the experimental technique and understanding of abrasion processes.

With the round tip, the material is deformed under the nanoindenter tip. At low loads, 50 μN, and even after 20 scans of 512 scratches each, no spalled regions were found. The same trend was found with 100 and 200 μN loads after 4 scans. Only after the same conditions but with a load of 400 μN, abraded particles were observed. The spalled areas where occasionally seen with AFM, as shown in Fig. 72. For the sake of comparison, a 5 x 5 μm^2 area was abraded with 400 μN in the wet state with 4 continuous scans of 256 scratches each in the enamel of a bovine permanent incisor and observed in low energy mode scanning electron microscopy (SEM), as shown in Fig. 73. In Fig. 73 the different removal of material among different rods is clearly detectable.

He et al. (He and Swain, 2006) discussed the influence of the twisted orientation between adjacent rods in the nanoscale friction and interlocking at crystal level between two contact surfaces within the sheath (the protein rich layer which surrounds the rods) when they

were explaining the extra energy dissipated in enamel during nanoindentation. In our case, the slight disorientation between adjacent rods leads to different spalling responses, as observed in Fig. 73, which could also be interpreted as a mechanism of energy dissipation.

It is remarkable that the results found for the displacement data and AFM in the case of dry measurements are similar, as shown in Table 12. Surprisingly, this accordance was not found in the case of wet measurements. A frequently accepted theory for energy dissipation during the indentation (Thompson et al., 2001) and fracture (Fantner et al., 2005) of bone and nacre is the so-called “sacrificial bond”. He et al. (He and Swain, 2006) also used this theory to explain how the gradually unfolding of the proteins within the rods may absorb a large amount of deformation before the primary structure of the protein is directly stretched and may explain, in this way, the large energy dissipation they found during nanoindentation in enamel. We can not assure whether the large differences between our two independent depth measurements in the wet results is mainly caused by this behaviour, but the accordance between the dry measurements may support this statement.

West et al. (West et al., 1999) studied in situ and in vivo the influence of different low pH drinks on wear and stated that the addition of calcium to acidic fruit drinks can mitigate to a considerable degree the adverse effects of low pH. On the other hand, Fantner et al. (Fantner et al., 2005) reported that the energy dissipation in fracture of bone is also greater if calcium ions are present in the buffer while presenting their theory of sacrificial bonds. In our case, HBSS contains 186.58 mg/L of $CaCl_2 \cdot H_2O$. This fact may support the sacrificial bond theory also in wear of enamel and the difference we found between the two depth measurement methods for the wet results.

The sacrificial bond theory is also supported by the fact that the scratches made in a wet state with loads lower than 1000 μN were not detected with the AFM, even tough they were observed for the dry measurements.

Judging for the ratios between mechanical properties measured by nanoindentation (Table 10), the response of the material to abrasion tests should be the same under both conditions, at zero time. And this is what we measured with the in situ displacement data when comparing wet and dry measurements. Thus, the analysis with the displacement data is valid only at time zero, where the time dependant viscoelastic properties are not involved.

There is a higher scatter for the wet data, as shown in Table 12. Besides the possibly increase in thermal drift under wet conditions, the material is also more compliant (Table 10). Intuitively, this implies that the measured mechanical properties are the result of the influence of an increased volume of material under and surrounding the nanoindenter tip, compared with the one involved during drying measurements. He et al. (He et al., 2006) found that in the case of enamel, the measured elastic modulus is a function of contact area and effective volume of the contact stress field from which the elastic modulus is determined. Ge et al. (Ge et al., 2005) reported a decrease of 73.6 % and 52.7 % in H and E when comparing the sheaths with the prisms response. Even though the abraded areas where placed inside the rods, in the case of the wet measurements the influence of the sheaths may have contributed to the dispersion of

the data. Macho et al. (Macho et al., 2003) presented a computer model which recreates the 3D microstructure of prismatic enamel. This 3D anisotropy of enamel may also contribute to the dispersion in the wet data due to the increased involved volume during abrasion. Another contribution to the scatter, which is also present in the case of dry samples, is the inhomogeneity of biological samples. In the case of dry samples this location dependant response is observed in Table 12, where the same conditions but different places were chosen to abrade the material and a 10 to 40 % difference in penetration depth was obtained (comparing DRY and the table foot note results).

The removed material mainly remains inside the abraded area, a fact observed with the AFM mode with the nanoindenter tip and with low energy SEM, and also sticks on the tip. We carried out experiments to prove the latter. We place on our nanoindentation platform one reference sample (polycrystalline silver and a copper singlecrystal), one polystyrene block (Styrofoam) and the dry enamel sample. Firstly we cleaned the tip with the polystyrene block; afterwards we indented the reference sample ("clean indent"). Subsequently, we moved the tip indenter to the dry human enamel sample and carried out one abrasion measurement and went back to the reference sample and indented it again ("dirt indent"). The penetration depth in the reference sample was higher than the penetration depth of the abrasion tests. We repeated this procedure twice in silver and three times in copper. We compared the load-displacement curves of the reference material before ("clean indent") and after ("dirt indent") the wear tests. In the latter, a deviation from the "clean" load-displacement data was observed at higher penetration depths. This abnormal convex shape of the load-displacement curve is a typical characteristic of dirty tip indentations. We chose this method to prove the sticking of the material on the tip, because it is a reliable and easy to carry out check. Imaging the tip with low energy SEM between the checking steps would have been another option, with the disadvantage of extra manipulating the tip and increasing the experimental times. The effectiveness of cleaning the tip with Styrofoam was corroborated with a fused quartz sample.

The above statement, explains why there is no marked effect of adding extra particles from previous tests. In addition, even though we do not discuss here our results with a sharp cube corner tip, we measured with TEM the size of the inorganic particles after abrasion with the sharp tip and they presented a hexagonal shape with 2 to 3 nm in length. Lawn (Lawn, 1975) presented a wear mechanism for brittle solids in which he concludes that the calculated wear rate is independent of the number and size of indenting particles. Wear is proportional to the load on the indenting particle, not on its distribution. The apparent increase in wear observed in Table 12 for the ABRA dry measurements in comparison with the DRY tests is only due to the inherent inhomogeneity of biological samples. Wear tests, without the deliberately addition of previous abraded particles, were also made close to these regions and the results were similar (Table 12; compare foot note and ABRA results).

Conclusions

Unfortunately, we are not yet able to propose a wear mechanism for enamel. Nor can we provide quantitative reliable and repeatable data. However, we are on the step of developing a technique which may clarify an up to date not understood abrasive behaviour and can also give a qualitative description of our system. At this point some conclusions can be drawn:

- The measured mechanical properties of dehydrated enamel differ from the one measured immersed in HBSS.
- During abrasion tests with a rounded tip, the material is compressed and then spalled.
- There is a threshold load for starting abrasion.
- Abrasion inside the rods is a suitable compromise for understanding wear, if one can choose the orientation of the material under the tip. Larger areas are recommended when the orientation is not known a priori.
- The addition of abraded particles may not enhance wear due to the particle size-indenter tip ratio and because the abraded material remains inside the scanned area.
- In the case of wear tests, displacement data analysis may complement AFM imaging and allows in situ measurements, but does not take into account recovery effects.
- Difference in wear between the WET state and the DRY state is observed for AFM image analysis.

Acknowledgements

Financial aid through EC Contract No MEST-CT-2004-504465, „Marie Curie Host Fellowships for Early Stage Research Training", is gratefully acknowledged.

FIGURES OF APPENDIX B

Fig. 72

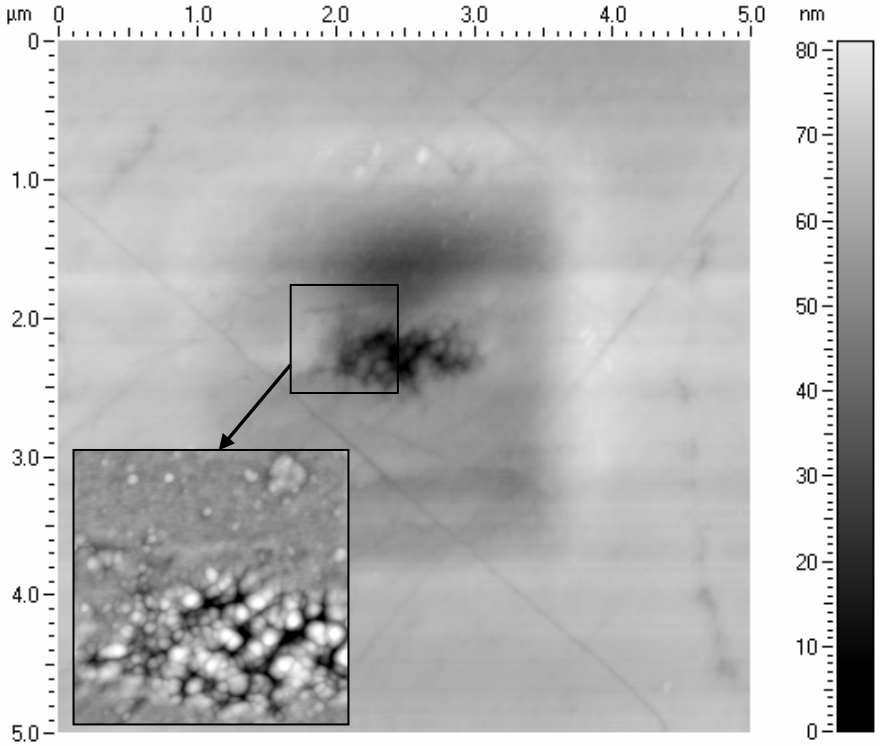

Fig. 72 5 x 5 µm^2 AFM image. Sample tested wet, 7 continuous scans with 256 scratches. 400 µN, 2 x 2 µm^2 abraded area. In the left bottom, a 1 x 1 µm^2 AFM image of the spalled area is shown.

Fig. 73

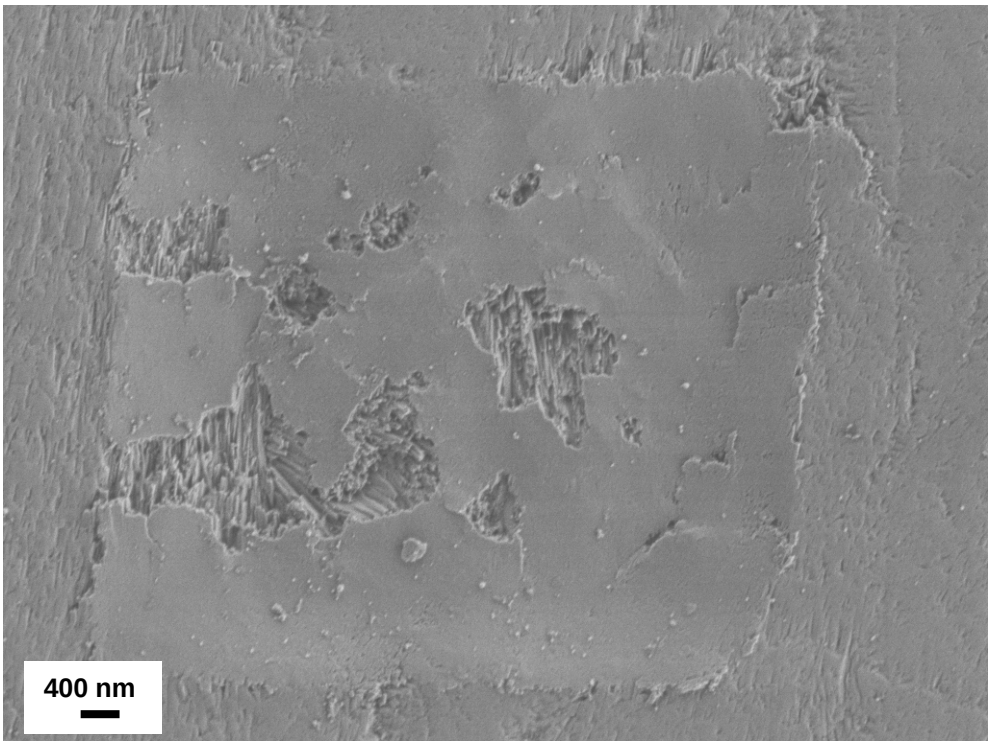

Fig. 73 Bovine incisor. WET. 4 continuous double scans, 400 μN, 5 x 5 μm^2. Low energy mode SEM image.

TABLES OF APPENDIX B

Table 10

	WET	DRY	Ratio Dry/Wet
E, GPa	30.73 ± 2.118	60.46 ± 7.279	**1.97 ± 0.508**
H, GPa	2.12 ± 0.180	3.98 ± 0.246	**1.59 ± 0.327**
Ratio H/E	0.08 ± 0.017	0.06 ± 0.020	**0.81 ± 0.584**

Table 10 Reduced elastic modulus (E) and hardness (H) of enamel measured by nanoindentation. The ratio between wet and dry properties is presented in the last left column. The usual parameter for predicting wear behaviour H/E is also included for comparison. The mean values are the average of 13 to 15 measurements and the errors correspond to the standard deviation of the data.

Table 11

	50 μN (WET)	100 μN (WET)	200 μN (WET)	400 μN (WET)	400 μN (DRY)
1st scan	9.2 ± 1.47	4.1 ± 2.66	21.2 ± 5.69	54.3 ± 22.2	-
4th scan	-	13.7 ± 3.19	18.3 ± 3.08	64.8 ± 33.71	35.8 ± 18.22
20th scan	8.8 ± 2.71	-	-	-	-
AFM	Not found	Not found	Not found	-	-

Table 11 Preliminary wear study in order to find a suitable load for wear measurements. Discontinuous scans. After each single scan an image was taken with the nanoindenter tip in AFM mode. Each scan contains 512 scratches of 2 μm length in a 2 x 2 μm^2 area. Each value corresponds to one single test. Mean values are the average penetration depth extracted from the displacement data throughout the 2 x 2 μm^2 area at the seventh scan follow by their standard deviation.

Table 12

	Displacement data	AFM
DRY1	88.6 ± 20.60	82 ± 19
DRY 2	81.9 ± 13.25	87 ± 18
DRY 3	97.5 ± 22.93	81 ± 15
DRY ABRA1	83.6 ± 23.79	141 ± 12*
DRY ABRA2	103.5 ± 26.64	120 ± 21*
WET1	54.6 ± 16.28	31 ± 16
WET 2	80.2 ± 6.38	49 ± 15
WET 3	136.7 ± 40.49	-
WET ABRA1	120.5 ± 17.82	23 ± 5**
WET ABRA2	78.0 ± 20.24	33 ± 6**

*** Other tests, not included in this report, where also done near this area and without the adding of new particles they presented AFM depths of 88 ± 12; 100 ± 8 and 127 ± 12 nm.**

**** Their profiles do not show a totally clean area.**

Table 12. Wear tests carried out at 400 μN. Seven scans of 256 scratches each. 2 x 2 μm^2 areas. Each value corresponds to one single test. For the "Displacement data" column, the mean values are the average penetration depth extracted from the load-displacement data throughout the 2 x 2 μm^2 area of the seventh scan follow by their standard deviation. In the case of "AFM" column, mean values are the average depth of 10 profiles taken along the fast scanning direction follow by their standard deviation

REFERENCES

.
ANDERSON, D. J. (1956) Measurement of stress in mastication. *Journal of Dental Research,* 35**,** 664-670.

ANGKER, L., NIJHOF, N., SWAIN, M. V. & KILPATRICK, N. M. (2004) Influence of hydration and mechanical characterization of carious primary dentine using an ultra-micro indentation system (UMIS). *European Journal of Oral Science,* 112**,** 231–236.

ANGKER, L., SWAIN, M. V. & KILPATRICK, N. (2003) Micro-mechanical characterisation of the properties of primary tooth dentine. *Journal of Dentistry,* 31**,** 261–267.

ANGKER, L., SWAIN, M. V. & KILPATRICK, N. (2005) Characterising the micro-mechanical behaviour of the carious dentine of primary teeth using nano-indentation. *Journal of Biomechanics,* 38**,** 1535–1542.

ASCENZI, M.-G., ASCENZI, A., BENVENUTI, A., BURGHAMMER, M., PANZAVOLTA, S. & BIGID, A. (2003) Structural differences between ''dark'' and ''bright'' isolated human osteonic lamellae. *Journal of Structural Biology,* 141**,** 22–33.

ATKINS, A. A. & TABOR, D. (1965) Plastic indentation in metals with cones. *Journal of Mech. Phys. Solids,* 13**,** 149-164.

BALOOCH, G., MARSHALL, G. W., MARSHALL, S. J., WARREN, O. L., ASIF, S. A. S. & BALOOCH, M. (2004) Evaluation of a new modulus mapping technique to investigate microstructural features of human teeth. *Journal of Biomechanics,* 37**,** 1223–1232.

BALOOCH, M., WU-MAGIDI, I. C., BALAZS, A., LUNDKVIST, A. S., MARSHALL, S. J., MARSHALL, G. W., SIEKHAUS, W. J. & KINNEY, J. H. (1998) Viscoelastic properties of demineralized human dentin measured in water with atomic force microscope (AFM)-based indentation. *Journal of Biomedical Materials Research,* 40**,** 539–544.

BARBOUR, M. E., PARKER, D. M. & JANDT, K. D. (2003) Enamel dissolution as a function of solution degree of saturation with respect to hydroxyapatite: a nanoindentation study. *Journal of Colloid and Interface Science,* 265**,** 9-14.

BEMBEY, A. K., OYEN, M. L., BUSHBY, A. J. & BOYDE, A. (2006) Viscoelastic properties of bone as a function of hydration state determined by nanoindentation. *Philosophical Magazine***,** 1-13.

BRALY, A., DARNELL, L. A., MANN, A. B., TEAFORD, M. F. & WEIHS, T. P. (2007) The effect of prism orientation on the indentation testing of human molar enamel. *Archives of Oral Biology,* 52**,** 856-860.

BURR, D. B., TURNER, C. H., NAICK, P., FORWOOD, M. R., AMBROSIUS, W., HASAN, M. S. & PIDAPARTI, R. (1998) Does microdamage accumulation affect the mechanical properties of bone? *Journal of Biomechanics,* 31**,** 337-345.

CURREY, J. D. (2002) *Bones,* Princeton (USA), Princeton University Press.

CUY, J. L., MANNA, A. B., LIVI, K. J., TEAFORD, M. F. & WEIHS, T. P. (2002) Nanoindentation mapping of the mechanical properties of human molar tooth enamel. *Archives of Oral Biology,* 47**,** 281-291.

CHALLEN, J. M., MCLEAN, L. J. & OXLEY, P. L. B. (1984) Plastic deformation of a Metal Surface in Sliding Contact With a Hard Wedge: Its Relation to Friction and Wear. *Proc. Roy. Soc. Lond.,* A394**,** 161-181.

CHAPMAN, G. E., DANYLUK, S. S. & MCLAUCHLAN, K. A. (1971) A model for collagen hydration. *Proc. R. Soc. London,* B. 178**,** 465-476.

DAHL, B. L., CARLSSON, G. E. & EKFELDT, A. (1993) Occlusal wear of teeth and restorative materials. *Acta Odontol. Scand,* 51**,** 299-311.

DELONG, R. (2006) Intra-oral restorative materials wear: Rethinking the current approaches: How to measure wear. *Dental Materials,* 22**,** 702–711.

DUGDALE, D. S. (1953) Wedge indentation experiments with cold worked metals. *Journal of the Mechanics and Physics of Solids,* 2**,** 14-26.

ELBAUM, R., TAL, E., PERETS, A. I., ORON, D., ZISKIND, D., SILBERBERG, Y. & WAGNER, H. D. (2007) Dentin micro-architecture using harmonic generation microscopy. *Journal of Dentistry,* 35**,** 150-155.

ESPINOZA-ORÍAS, A. A. (2005) The relationship between the mechanical anisotropy of human cortical bone tissue and its microstructure. *Graduate School of the University of Notre Dame.* Notre Dame, Indiana, Graduate School of the University of Notre Dame.

FAN, Z., SWADENER, J. G., RHO, J. Y., ROY, M. E. & PHARR, G. M. (2002) Anisotropic properties of human tibial cortical bone as measured by nanoindentation. *Journal of Orthopaedic Research,* 20**,** 806–810.

FANTNER, G. E., HASSENKAM, T., KINDT, J. H., WEAVER, J. C., BIRKEDAL, H., PECHENIK, L., CUTRONI, J. A., CIDADE, G. A. G., STUCKY, G. D., MORSE, D. E. & HANSMA, P. K. (2005) Sacrificial bonds and hidden length dissipate energy as mineralized fibrils separate during bone fracture. *Nature Materials,* 4**,** 612-615.

FERNANDES, C. P., GLANTZ, P. J., SVENSSON, S. A. & BERGMARK, A. (2003) A novel sensor for bite force determinations. *Dental Materials,* 19**,** 118-126.

FIELD, J. S., SWAIN, M. V. & DUKINO, R. D. (2003) Determination of fracture toughness from the extra penetration produced by indentation-induced pop-in. *Journal of Materials Research,* 18**,** 1412-1419.

FINCHAM, A. G., MORADIAN-OLDAK, J. & SIMMER, J. P. (1999) The structural biology of the developing dental enamel matrix. *Journal of Structural Biology,* 126**,** 270-299.

FISCHER-CRIPPS, A. C. (2004) *Nanoindentation,* New York (USA), Springer-Verlag.

FISCHER-CRIPPS, A. C. (2005) *The IBIS Handbook of Nanoindentation,* Forestville, Australia, Fischer-Cripps Laboratories Pty Ltd.

FONG, H., SARIKAYA, M., WHITE, S. N. & SNEAD, M. L. (2000) Nano-mechanical properties profiles across dentin–enamel junction of human incisor teeth. *Materials Science and Engineering C,* 7**,** 119–128.

FOX, P. G. (1980) The toughness of tooth enamel, a natural fibrous composite. *Journal of Materials Science,* 15**,** 3113-3121.

FRATZL, P. & WEINKAMER, R. (2007) Nature's hierarchical materials. *Progress in Materials Science,* 52**,** 1263-1334.

FRIEDRICH, K. (1986) *Friction and wear of polymer composites,* Amsterdam (The Netherlands), Elsevier Science.

GAO, H., JI, B., JÄGER, I. L., ARZT, E. & FRATZL, P. (2003) Materials become insensitive to flaws at nanoscale: lessons from nature. *Proceedings of the National Academy of Sciences of the United States of America,* 100**,** 5597–5600.

GARBEROGLIO, R. & BRÄNNSTRÖM, M. (1976) Scanning electron microscopic investigation of human dentinal tubules. *Archives of oral biology,* 21**,** 355-362.

GE, J., CUI, F. Z., WANG, X. M. & FENG, H. L. (2005) Property variations in the prism and the organic sheath within enamel by nanoindentation. *Biomaterials,* 26**,** 3333-3339.

GREENWOOD, J. A. & WILLIAMSON, J. B. P. (1966) Contact of nominally flat rough surfaces. *Proceedings of the Royal Society,* A295**,** 300-319.

GRUNZWEIG, J., LONGMAN, I. M. & PETCH, N. J. (1954) Calculations and measurements on wedge-indentation. *Journal of the Mechanics and Physics of Solids,* 2**,** 81-86.

GUIDONI, G., DENKMAYER, J., SCHÖBERL, T. & JÄGER, I. (2006) Nanoindentation in teeth: the influence of experimental conditions on local mechanical properties. *Philosophical Magazine,* 86**,** 5705 - 5714.

GUIDONI, G., SWAIN, M. & JÄGER, I. (2007a) Nanoindentation in wet and dry compact bone: influence of environment and indenter tip geometry on the elastic modulus. To be submitted.

GUIDONI, G., SWAIN, M. V. & JÄGER, I. (2007b) Nano-scale sliding contact deformation behaviour of enamel under wet and dry conditions. *Archives of Oral Biology***,** Submitted.

GUIDONI, G. M., HE, L. H., SCHÖBERL, T., JÄGER, I., DEHM, G. & SWAIN, M. (2007c) Influence of indenter tip geometry and environment on the elastic modulus of enamel. *Acta Biomaterialia***,** Submitted.

GUIDONI, G. M., SCHÖBERL, T., DEHM, G. & JÄGER, I. (2007d) Abrasion tests on human enamel under wet and dry conditions. *The fifth IASTED international conference on Biomedical Engineering "Biomed 2007".* Innsbruck (Austria).

GUIDONI, G. M., SWAIN, M. & JÄGER, I. (2007e) Wear behaviour of enamel at the nano scale with a sharp and blunt indenter tip. *Wear***,** Submitted.

GUPTA, H. S., SETO, J., WAGERMAIER, W., ZASLANSKY, P., BOESECKE, P. & FRATZL, P. (2006a) Cooperative deformation of mineral and collagen in bone at the nanoscale. *Proceedings of the National Academy of Sciences of the United States of America,* 103**,** 17741–17746.

GUPTA, H. S., STACHOWIAK, G. W., WAGERMAIER, W., ROSCHER, P., WAGNER, H. D. & FRATZL, P. (2006b) Mechanical modulation at the lamellar level in osteonal bone. *Journal Materials Research,* 21**,** 1913-1921.

GUPTA, H. S., WAGERMAIER, W., ZICKLER, G. A., AROUSH, D. R.-B., FUNARI, S. S., ROSCHGER, P., WAGNER, H. D. & FRATZL, P. (2005) Nanoscale deformation mechanisms in bone. *Nano Letters,* 5**,** 2108-2111.

GUSTAFSON, M. B., MARTIN, R. B., GIBSON, V., STORMS, D. H., STOVER, S. M., GIBELING, J. & GRIFFIN, L. (1996) Calcium buffering is required to maintain bone stiffness in saline solution 29**,** 1191-1194

HABELITZ, S., MARSHALL JR, G. W., BALOOCH, M. & MARSHALL, S. J. (2002) Nanoindentation and storage of teeth. *Journal of Biomechanics,* 35**,** 995-998.

HABELITZ, S., MARSHALL, S. J., MARSHALL JR, G. W. & BALOOCH, M. (2001a) Mechanical properties of human dental enamel on the nanometre scale. *Archives of Oral Biology,* 46**,** 173–183.

HABELITZ, S., MARSHALL, S. J., MARSHALL JR., G. W. & BALOOCH, M. (2001b) The Functional Width of the Dentino-Enamel Junction Determined by AFM-Based Nanoscratching. *Journal of Structural Biology,* 135**,** 294–301.

HE, L. H., CARTER, E. A. & SWAIN, M. V. (2007) Characterization of nanoindentation-induced residual stresses in human enamel by Raman microspectroscopy. *Anales of Bioanalitical Chemistry,* 389**,** 1185–1192.

HE, L. H., FUJISAWA, N. & SWAIN, M. V. (2006) Elastic modulus and stress–strain response of human enamel by nano-indentation. *Biomaterials,* 27**,** 4388-4398.

HE, L. H. & SWAIN, M. V. (2006) Energy absorption characterization of human enamel using nanoindentation. *Journal of Biomedical Materials Research,* A**,** 484-492.

HE, L. H. & SWAIN, M. V. (2007a) Contact induced deformation of enamel. *Applied Physics Letters,* 90**,** 171916/1-171916/3.

HE, L. H. & SWAIN, M. V. (2007b) Enamel—A ‘‘metallic-like’’ deformable biocomposite. *Journal of Dentistry,* 35**,** 431-437.

HE, L. H. & SWAIN, M. V. (2007c) Influence of environment on the mechanical behaviour of mature human enamel. *Biomaterials,* 28**,** 4512–4520.

HE, L. H. & SWAIN, M. V. (2007d) Nanoindentation derived stress-strain properties of dental materials. *Dental Materials,* 23**,** 814-821.

HENGSBERGER, S., KULIK, A. & ZYSSET, P. (2002) Nanoindentation Discriminates the Elastic Properties of Individual Human Bone Lamellae Under Dry and Physiological Conditions. *Bone,* 30**,** 178–184.

HILL, R., LEE, E. H. & TUPPER, S. J. (1947) The theory of wedge indentation of ductile materials. *Proceedings of the Royal Society,* A 188**,** 273-289.

HIRST, W. & HOWSE, M. G. J. W. (1969) The indentation of materials by wedges. *Proceedings of the Royal Society,* A311**,** 429-444.

HOFFLER, C. E., MOORE, K. E., KOZLOFF, K., ZYSSET, P. K., BROWN, M. B. & GOLDSTEIN, S. A. (2000) Heterogeneity of bone lamellar-level elastic moduli. *Bone,* 26**,** 603–609.

HUTCHINGS, I. M. (1992) *Tribology: friction and wear of engineering materials,* London (Great Britain), Edward Arnold.

JÄGER, I. & FRATZL, P. (2000) Mineralized collagen fibrils: a mechanical model with a staggered arrangement of mineral particles. *Biophysics Journal,* 79**,** 1737-1746.

JANDT, K. D. (2006) Probing the future in functional soft drinks on the nanometre scale—towards tooth friendly soft drinks. *Trends in Food Science & Technology,* 17**,** 263–271.

JI, B. & GAO, H. (2006) Elastic properties of nanocomposite structure of bone. *Composites Science and Technology,* 66**,** 1209–1215.

JOHNSON, K. L. (1970) The correlation of indentation experiments. *Journal of the Mechanics and Physics of Solids,* 18**,** 115-126.

JOHNSON, K. L. (2003) *Contact Mechanics,* Cambridge (United Kingdom).

KAHLER, B., SWAIN, M. V. & MOULE, A. (2003) Fracture-toughening mechanisms responsible for differences in work to fracture of hydrated and dehydrated dentine. *Journal of Biomechanics,* 36**,** 229–237.

KANG, Q., AN, Y. H. & FRIEDMAN, R. (1997) Effects of multiple freezing-thawing cycles on the ultimate indentation load and stiffness of bovine cancellous bone. *American Journal of Veterinary Research,* 58**,** 1171-1173.

KELLY, J. R., NISHIMURA, I. & CAMPBELL, S. D. (1996) Ceramics in dentistry: Historical roots and current perspectives. *The journal of Prosthetic Dentistry,* 75**,** 18-32.

KING, R. F. & TABOR, D. (1954) The strength properties and frictional behaviour of brittle solids. *Proceedings of the Royal Society of London,* A**,** 225-236.

KINNEY, J. H., BALOOCH, M., MARSHALL, G. W. & MARSHALL, S. J. (1999) A micromechanics model of the elastic properties of human dentine. *Archives of Oral Biology,* 44**,** 813-822.

KINNEY, J. H., BALOOCH, M., MARSHALL, S. J., MARSHALL JR, G. W. & WEIHS, T. P. (1996) Hardness and Young's Modulus of human peritubular and intertubular dentine. *Archives of Oral Biology,* 41**,** 9-13.

KINNEY, J. H., HABELITZ, S., MARSHALL, S. J. & MARSHALL, G. W. (2003a) The Importance of intrafibrillar mineralization of collagen on the mechanical properties of dentin. *Journal of Dental Research,* 82**,** 957-961.

KINNEY, J. H., MARSHALL, S. J. & MARSHALL, G. W. (2003b) The mechanical properties of human dentin: a critical review and re-evaluation of the dental literature. *Crit Rev Oral Biol Med,* 14**,** 13-29.

KISHEN, A. & VEDANTAM, S. (2007) Hydromechanics in dentine: Role of dentinal tubules and hydrostatic pressure on mechanical stress–strain distribution. *Dental materials,* 23**,** 1296–1306.

KITASAKOA, Y., BURROW, M. F., NIKAIDO, T. & TAGAMI, J. (2001) The influence of storage solution on dentin bond durability of resin cement. *Dental Materials,* 16**,** 1-6.

KONISHI, N., WATANABE, L. G., HILTON, J. F., MARSHALL, G. W., MARSHALL, S. J. & STANINEC, M. (2002) Dentin shear strength: effect of distance from the pulp *Dental Materials,* 18**,** 516-520.

KRUZIC, J. J., NALLA, R. K., KINNEY, J. H. & RITCHIE, R. O. (2003) Crack blunting, crack bridging and resistance-curve fracture mechanics in dentin: effect of hydration. *Biomaterials,* 24**,** 5209–5221.

LAKES, R. Viscoelastic Composite Materials

Viscoelasticity. Viscoelastic composites which exhibit internal friction.

LAWN, B. R. (1975) A model for the wear of brittle solids under fixed abrasive conditions. Short communication. *Wear,* 33**,** 369-372.

LAZAREV, Y. A., GRISHKOVSKY, B. A. & KHROMOVA, T. B. (1985) Amide I band of IR spectrum and structure of collagen and related polypeptides. *Biopolymers,* 24**,** 1449-1478.

LAZAREV, Y. A., GRISHKOVSKY, B. A., KHROMOVA, T. B., LAZAREVA, A. V. & GRECHISHKO, V. S. (1992) Bound water in the collagen-like triple helical structure. *Biopolymers,* 32**,** 189-195.

LEE, D. D. & GLIMCHER, M. J. (1991) Three-dimensional spatial relationship between the collagen fibrils and the inorganica calcium phosphate crystals of Pickerel (Americanus americanus) and Herring (Clupea harengus) bone. *Journal of Molecular Biology,* 217**,** 487.

LI, H. & ZHOU, Z. R. (2002) Wear behaviour of human teeth in dry and artificial saliva conditions. *Wear,* 249**,** 980–984.

LIPPERT, F., PARKER, D. M. & JANDT, K. D. (2004) In vitro demineralization/remineralization cycles at human tooth enamel surfaces investigated by AFM and nanoindentation. *Journal of Colloid and Interface Science,* 280**,** 442–448.

MACIEL, K. T., CARVALHO, R. M., RINGLE, R. D., PRESTON, C. D., RUSSELL, C. M. & PASHLEY, D. H. (1996) The effects of acetone, ethanol, HEMA, and air on the stiffness of human decalcified dentin matrix. *Journal Dental Research,* 75**,** 1851-1858.

MACHO, G. A., JIANG, Y. & SPEARS, I. R. (2003) Enamel microstructure—a truly three-dimensional structure. *Journal of Human Evolution,* 45**,** 81-90.

MAGNE, P., OH, W. S., PINTADO, M. R. & DELONG, R. (1999) Wear of enamel and veneering ceramics after laboratory and chairside finishing procedures. *The Journal of Prosthetic Dentistry,* 82**,** 669-679.

MAHONEY, E., HOLT, A., SWAIN, M. & KILPATRICK, N. (2000) The hardness and modulus of elasticity of primary molar teeth: an ultra-micro-indentation study. *J Dent,* 28**,** 589-594.

MAHONEY, E. K., ROHANIZADEHA, R., ISMAIL, F. S. M., KILPATRICK, N. M. & SWAIN, M. V. (2004) Mechanical properties and microstructure of hypomineralised enamel of permanent teeth. *Biomaterials* 25**,** 5091–5100.

MAROTTI, G. (1992) A New Theory of Bone Lamellation. *Calcified Tissue International,* 53**,** 47-56.

MARSH, D. M. (1964) Plastic flow in glass. *Proceedings of the Royal Society of London. Series A, Mathematical and Physical Sciences,* 279**,** 420-435.

MOSCOVICH, H. & CREUGERS, N. H. J. (1998) The novel use of extracted teeth as a dental restorative material—the 'Natural Inlay' *Journal of Dentistry,* 26**,** 21-24

MOSCOVICH, H., CREUGERS, N. H. J., JANSEN, J. A. & WOLKE, J. G. C. (1999) In vitro dentine hardness following gamma-irradiation and freezing. *Journal of Dentistry,* 27**,** 503–507.

MULLINS, L. P., BRUZZI, M. S. & MCHUGH, P. E. (2007) Measurement of the microstructural fracture toughness of cortical bone using indentation fracture. *Journal of Biomechanics,* 40**,** 3285–3288.

NALLA, R. K., BALOOCH, M., AGER III, J. W., KRUZIC, J. J., KINNEY, J. H. & RITCHIE, R. O. (2005) Effects of polar solvents on the fracture resistance of dentin: role of water hydration. *Acta Biomaterialia,* 1**,** 31-43.

NGAN, A. H. W., WANG, H. T., TANG, B. & SZE, K. Y. (2005) Correcting power-law viscoelastic effects in elastic modulus measurement using depth-sensing indentation. *International Journal of Solids and Structures,* 42**,** 1831-1846.

NTIM, M. M., BEMBEY, A. K., FERGUSON, V. L. & BUSHBY, A. J. (2006) Hydration effects on the viscoelastic properties of collagen. *Materials Research Society Symposium Proceedings,* 898E**,** 39-43.

NYMAN, J. S., REYES, M. & WANGA, X. (2005) Effect of ultrastructural changes on the toughness of bone. *Micron,* 36**,** 566-582.

OH, W., DELONG, R. & ANUSAVICE, K. (2002) Factors affecting enamel and ceramic wear: A literature review. *The journal of Prosthetic Dentistry,* 87**,** 451-459.

OLIVER, W. C. & PHARR, G. M. (1992) An improved technique for determining hardness and elastic modulus using load and displacement sensing indentation experiments. *Journal of Materials Research,* 7**,** 1564-1583.

OLIVER, W. C. & PHARR, G. M. (2004) Measurement of hardness and elastic modulus by instrumented indentation: Advances in understanding and refinements to methodology. *Journal of Materials Research,* 19**,** 3-20.

PANIGHI, M. M., ALLART, D., JACQUOT, B. M., CAMPS, J. & G'SELL, C. (1997) Influence of human tooth cryopreservation on dentin bond strength. *Dental Materials,* 13**,** 56-61.

PARIS, O., ZIZAK, I., LICHTENEGGER, H., ROSCHGER, P., KLAUSHOFER, K. & FRATZL, P. (2000) Analysis of the hierarchical structure of biological tissues by scanning X-ray scattering using a micro-beam. *Cellular molecular biology,* 46**,** 993-1004.

PASHLEY, D. H., AGEE, K. A., CARVALHO, R. M., LEE, K.-W., TAY, F. R. & CALLISON, T. E. (2003) Effects of water and water-free polar solvents on the tensile properties of demineralized dentin. *Dental Materials,* 19**,** 347-352.

PASHLEY, D. H., AGEE, K. A., NAKAJIMA, M., TAY, F. R., CARVALHO, R. M., TERADA, R. S. S., HARMON, F. J., LEE, W.-K. & RUEGGEBERG, F. A. (2001) Solvent-induced dimensional changes in EDTA-demineralized dentin matrix. *Journal of Biomedical Materials Research,* 56**,** 273–281.

PINTADO, M. R., ANDERSON, C., DELONG, R. & DOUGLAS, W. H. (1997) Variation in tooth wear in young adults over a two-year period. *The journal of Prosthetic Dentistry,* 77**,** 313-320.

POOLE, D. F. G. & BROOKS, A. W. (1961) The arrangement of cristallites in enamel prisms. *Archives of Oral Biology,* 5**,** 14-26.

POOLTHONG, S. (2000) Sydney, University of Sydney.

POOLTHONG, S., MORI, T. & SWAIN, M. V. (2001) Determination of the elastic modulus of dentin by small spherical diamond indenters. *Journal of Dental Materials,* 20**,** 227-236.

PORTER, A. E., NALLA, R. K., MINOR, A., JINSCHEK, J. R., KISIELOWSKI, C., RADMILOVIC, V., KINNEY, J. H., TOMSIA, A. P. & RITCHIE, R. O. (2005) A transmission electron microscopy study of mineralization in age-induced transparent dentin *Biomaterials,* 26**,** 7650–7660.

QIN, Q.-H. & SWAIN, M. V. (2004) A micro-mechanics model of dentin mechanical properties. *Biomaterials,* 25**,** 5081–5090.

RABINOWICZ, E. (1995) *Friction and wear of materials,* New York (USA).

RAMACHANDRAN, G. N. & CHANDRASEKHARAN, R. (1968) Interchain hydrogen bonds via bound water molecules in the collagen triple helix. *Biopolymers,* 6**,** 1649-1658.

REEH, E. S., DOUGLAS, W. H. & LEVINE, M. J. (1995) Lubrication of human and bovine enamel compared in an artificial mouth. *Archives of Oral Biology,* 40**,** 1063-1072.

RESTER, M., MOTZ, C. & PIPPAN, R. (2007) Stacking fault energy and indentation size effect: do they interact? *Scripta Materialia***,** In press.

RHO, J.-Y., KUHN-SPEARING, L. & ZIOUPOS, P. (1998) Mechanical properties and the hierarchical structure of bone. *Medical Engineering & Physics,* 20**,** 92–102.

RHO, J.-Y. & PHARR, G. M. (1999) Effects of drying on the mechanical properties of bovine femur measured by nanoindentation. *Journal of Materials Science: Materials in Medicine,* 10**,** 485-488.

RHO, J.-Y., TSUI, T. Y. & PHARR, G. M. (1997) Elastic properties of human cortical and trabecular lamellar bone measured by nanoindentation. *Biomaterials,* 18**,** 1325-1330.

SAJEWICZ, E. (2006) On evaluation of wear resistance of tooth enamel and dental materials. *Wear,* 260**,** 1256-1261.

SAJEWICZ, E. & KULESZA, Z. (2007) A new tribometer for friction and wear studies of dental materials and hard tooth tissues. *Tribology International,* 40**,** 885–895.

SARRETT, D. C., COLETTI, D. P. & PELUSO, A. R. (2000) The effects of alcoholic beverages on composite wear. *Dental Materials,* 16**,** 62–67.

SCHILKE, R., LISSON, J. A., BAUB, O. & GEURTSEN, W. (2000) Comparison of the number and diameter of dentinal tubules in human and bovine dentine by scanning electron microscopic investigation. *Archives of Oral Biology,* 45**,** 355-361.

SCHNEIDER, G. A., SCHOLZ, T., MUÑOZ-SALDAÑA, J. & SWAIN, M. V. (2005) Domain rearrangement during nanoindentation in single-crystalline barium titanate measured by atomic force microscopy and piezoresponse force microscopy. *Applied Physics Letters,* 86**,** 192903(1-3).

SELVIG, K. & HALSE, A. (1972) Crystal growth in rat incisor enamel. *Anatomical Records,* 173**,** 453-468.

SHIN, H. C. & YOON, Y. S. (2006) Bone temperature estimation during orthopaedic round bur milling operations. *Journal of Biomechanics,* 39**,** 33–39.

SIGMA & PRODUCT_INFORMATION Hank's balanced salts.

SNEDDON, I. N. (1965) The relation between load and penetration in the axisymetric Boussineq problem for a punch of arbitrary profile. *International Journal of Engineering Science,* 3**,** 47-57.

SPEARS, I. R. (1997) A three-dimensional finite element model of prismatic enamel: a re-appraisal of the data on the Young's Modulus of enamel. *Journal of Dental Research,* 76**,** 1690-1697.

STACHOWIAK, G. W. & BATCHELOR, A. W. (2001) *Engineering Tribology,* Woburn (USA).

STAINES, ROBINSON, W. H. & HOOD, J. A. A. (1981) Spherical indentation of tooth enamel. *Journal of Materials Science,* 16**,** 2551-2556.

SWADENER, J. G., RHO, J.-Y. & PHARR, G. M. (2001) Effects of anisotropy on elastic moduli measured by nanoindentation in human tibial cortical bone. *Journal of Biomedical Materials Research,* 57**,** 108-112.

SWARTZL, O. (1986) Cryopreservation as long-term storage of teeth for transplantation or replantation. *International Journal of Oral Maxillofacial Surgery,* 15**,** 30-32.

TABOR, D. (1970) The hardness of solids. *Review of Physics in Technology* 1**,** 145-179.

TAI, K., Q, H. J. & ORTIZ, C. (2005) Effect of mineral content on the nanoindentation properties and nanoscale deformation mechanisms of bovine tibial cortical bone. *Journal of Materials Science: Materials in Medicine,* 16**,** 947– 959.

TANG, B., NGAN, A. H. W. & LU, W. W. (2007) An improved method for the measurement of mechanical properties of bone by nanoindentation. *Journal Materials Science: Materials in Medicine,* 18**,** 1875–1881.

TESCH, W., EIDELMAN, N., ROSCHGER, P., GOLDENBERG, F., KLAUSHOFER, K. & FRATZL, P. (2001) Graded Microstructure and Mechanical Properties of Human Crown Dentin. *Calcified Tissue International,* 69**,** 147–157.

THOMPSON, J. B., KINDT, J. H., DRAKE, B., HANSMA, H. G., MORSE, D. E. & HANSMA, P. K. (2001) Bone indentation recovery time correlates with bond reforming time. *Nature,* 414**,** 773-776.

TURSSI, C. P., FARAONI, J. J., MENEZES, M. D. & SERRA, M. C. (2006) Analysis of potential lubricants for in vitro wear testing. *Dental Materials,* 22**,** 77-83.

VINCENT, J. F. V. (1990) *Structural Biomaterials: (Revised Edition),* UK, Princeton University Press.

WAGERMAIER, W., GUPTA, H. S., GOURRIER, A., BURGHAMMER, M., ROSCHGER, P. & FRATZL, P. (2006a) Spiral twisting of fiber orientation inside bone lamellae. *Biointerphases,* 1**,** 1-5.

WAGERMAIER, W., GUPTA, H. S., GOURRIER, A. L., PARIS, O., ROSCHGER, P., BURGHAMMER, M., RIEKEL, C. & FRATZL, P. (2006b) Scanning texture analysis of lamellar bone using microbeam synchrotron X-ray radiation. *Journal of Applied Crystallography,* 40**,** 115-120.

WEINER, S., VEIS, A., BENIASH, E., ARAD, T., DILLON, J. W., SABSAY, B. & SIDDIQUI, F. (1999) Peritubular dentin formation: crystal organization and the macromolecular constituents in human teeth. *Journal of Structural Biology,* 126**,** 27–41.

WEINER, S. & WAGNER, H. D. (1998) The material bone: structure-mechanical function relations. *Annual Review of Materials Science,* 28**,** 271–298.

WENK, H.-R. & HEIDELBACH, F. (1999) Crystal alignment of carbonated apatite in bone and calcified tendon: results from quantitative texture analysis. *Bone,* 24**,** 361–369.

WEST, N. X., HUGHES, J. A., PARKER, D. M., NEWCOMBE, R. G. & ADDY, M. (1999) Development and evaluation of a low erosive blackcurrant juice drink 2. Comparison with a conventional blackcurrant juice drink and orange juice. *Journal of Dentistry,* 27**,** 341-344.

WHITE, S. N., LUO, W., PAINE, M. L., H.FONG, SARIKAYA, M. & SNEAD, M. L. (2001) Biological organization of hydroxyapatite crystallites into a fibrous continuum toughens and controls anisotropy in human enamel. *Journal of Dental Research,* 80**,** 321-326.

WIKIPEDIA.

XIE, Z.-H., MAHONEY, E. K., KILPATRICK, N. M., SWAIN, M. V. & HOFFMAN, M. (2007) On the structure–property relationship of sound and hypomineralized enamel. *Acta Biomaterialia,* 3**,** 865–872.

XU, H. H. K., SMITH, D. T., JAHANMIR, S., ROMBERG, E., KELLY, J. R., THOMPSON, V. P. & REKOW, E. D. (1998) Indentation damage and mechanical properties of human enamel and dentin. *Journal of Dental Research,* 77**,** 472-480.

XU, J., RHO, J. Y., MISHRA, S. R. & FAN, Z. (2003) Atomic force microscopy and nanoindentation characterization of human lamellar bone prepared by microtome sectioning and mechanical polishing technique. *Journal of Biomedical Materials Research,* 67A**,** 719-726.

YUNG, Y. C. (1993) *Biomechanics. Mechanical properties of living tissues*, Springer Sciene+Business Media.

ZHENG, J., ZHOU, Z. R., ZHANG, J., LI, H. & YU, H. Y. (2003) On the friction and wear behaviour of human tooth enamel and dentin. *Wear,* 255**,** 967–974.

ZHOU, J. & HSIUNG, L. L. (2006a) Biomolecular origin of the rate-dependent deformation of prismatic enamel. *Applied Physics Letters* 89**,** 051904-051907.

ZHOU, J. & HSIUNG, L. L. (2006b) Depth-dependent mechanical properties of enamel by nanoindentation. *Journal of Biomedical Materials Research Part A***,** 67-74.

ZUM-GAHR, K. H. & KARL-HEINZ (1987) *Microstructure and wear of materials,* Amsterdam (The Netherlands), Elsevier Science Publishers.

ZYSSET, P. K., GUO, X. E., HOFFLER, C. E., MOORE, K. E. & GOLDSTEIN, S. A. (1999) Elastic modulus and hardness of cortical and trabecular bone lamellae measured by nanoindentation in the human femur. *Journal of Biomechanics,* 32**,** 1005-1012.